BREAKING THE CEILING OF CAPACITY LIMIT VIA ANION REDOX REACTIONS

by

YANFANG WANG

A thesis submitted to the University of Birmingham for the degree of

DOCTOR OF PHILOSOPHY

School of Chemistry

College of Engineering and Physical Sciences

The University of Birmingham

September 2023

UNIVERSITY OF
BIRMINGHAM

University of Birmingham Research Archive

e-theses repository

This unpublished thesis/dissertation is copyright of the author and/or third parties. The intellectual property rights of the author or third parties in respect of this work are as defined by The Copyright Designs and Patents Act 1988 or as modified by any successor legislation.

Any use made of information contained in this thesis/dissertation must be in accordance with that legislation and must be properly acknowledged. Further distribution or reproduction in any format is prohibited without the permission of the copyright holder.

ACKNOWLEDGEMENTS

Firstly, I would like to thank my supervisor, Dr. Phoebe Allan, for her guidance and encouragement throughout the past four years, always providing me penetrating instructions and inspiring advice. I have been always impressed by her richness of knowledge, curiosity for the unknown, and enthusiasms in research.

I would like to express my great appreciation to my co-supervisors Prof. Zhouguang Lu, and Prof. Fucai Zhang at SUSTech for their instruction and supervision, providing me the opportunity to work in a research environment at cutting edge of science without limitations. I would also like to thank Prof. Peter Slater and Dr. Joshua Makepeace for their mentorship during my studies.

I would like to thank my collaborators Dr. Yingzhi Li, Dr. Ning Qin, Dr. Zhiqiang Li, Dr. Cheng Li, Chun Zeng, Wen Luo. I would also like to thank other group members Rachel, Beatrice, Alex, Raquel, Javier at Birmingham, and Tao Liu, Huimin Yuan, Dexin Zhang, Zhiqiang Wang, Shuai Gu, Jingjing Chen, Yulin Cao, Hongzhi Wang, Qingmeng Gan, Fangchang Zhang, Xueting Shen, Yongcong Huang, Feng Wu at SUSTech.

Finally, I would like to express my deepest gratitude to my family for their love. Special thanks must go to my wife Yuexiang (Jessie) Li for her support and understanding in the past years. I would like to thank my dear daughter Mengliao (Merliah) Wang for giving me the power to keep going.

Dedicated to the Ones I Love

"Without a few steps, one cannot reach a thousand miles (不积跬步，无以至千里); without accumulating small streams, no river or sea can be formed (不积小流，无以成江海)."

Xuncius

313 BC - 238 BC

ABSTRACT

Anion redox reactions (ARRs) in lithium rich cathode materials (LRCMs) have attracted great attention due to their potential for delivering extra capacities beyond traditional cation redox activities. This thesis presents a study to stabilize the ARRs in LRCMs via developing the understanding of the nature of the oxygen redox activities and tailoring rational local structures to suppress the ARR-induced structural degradations (i.e., oxygen loss and transition metal (TM) migration).

Chapter 1 introduces a background to the field, including basic knowledge about lithium-ion batteries (LIBs), previous understanding of ARRs, and challenges for their future success in practical utilizations. The characterization techniques and experimental details are described in Chapter 2.

Monitoring the local coordination evolutions induced by ARRs and Ru redox reactions was carried out on the archetypal Li_2RuO_3 by using in-situ Raman spectroscopy. As detailed in Chapter 3, both the Raman-active Ru-Ru motions and the emergence of the O-O dimers were tracked and interpreted in combination with multimodal characterization techniques.

A F-doping study was conducted on Li_2RuO_3, as described in Chapter 4. Although F-dopants did not stabilize the ARRs, trace amount of F-doping improved the cycling stability of the Ru redox reactions. Such a performance enhancement was attributed

to the effects of F-dopants on relaxing the interlayer repulsions and altering the preferential orientations.

In Chapter 5, a metastable O6-phase was reported to demonstrate stable cation and anion redox reactions under long-term operation. The hidden mechanisms underneath its structural stability were investigated by using a plenty of techniques including ex-situ/ in-situ X-ray diffraction (XRD), ex-situ X-ray absorption spectroscopy (XAS), ex-situ/ in-situ Raman spectroscopy, ex-situ electromagnetic resonance spectroscopy (EPR), ex-situ X-ray photoelectron spectroscopy (XPS), and electrochemical analyses. Unlike the edge-sharing local structures in the traditional O3-phase, the O6-phase presented the face-sharing geometry between the TMO_2 and LiO_2 slabs, in which the interlayer TM migration was suppressed.

An interferometric scattering microscopy (iSCAT) setup was introduced in Appendix C, which was built to track the ARR-induced evolutions at the single particle level via using nondestructive visible light as the probe.

Table of contents

ACKNOWLEDGEMENTS i

ABSTRACT iii

CHAPTER 1. INTRODUCTION 1

1.1. Basic knowledge about LIBs 2
1.1.1. Main components of LIBs 2
1.1.2. Working mechanisms of LIBs 2
1.1.3. Key factors to evaluate LIBs 4
1.2. The development of LIBs 6
1.2.1. The emergence of $LiCoO_2$ 6
1.2.2. High-nickel NCA and NCM 7
1.2.3. Lithium-rich manganese oxides (LRMOs) 9
1.2.4. Olivine and spinel phases 10
1.2.5. From graphite to metallic lithium 11
1.2.6. Towards solid-state LIBs 12
1.2.7. The roadmap of LIBs 12
1.3. The origin of the extra capacity in Li-rich layered oxides 13
1.4. The nature of the anion redox reactions (ARRs) 16
1.5. Structural evolutions upon ARRs 18
1.6. Challenges of tapping into ARRs for practical applications 22
1.7. Aims 25
1.8. References 27

CHAPTER 2. EXPERIMENTS AND CHARACTERIZATION TECHNIQUES 32

2.1. Sample preparation 32
2.1.1. Synthesis of Li_2RuO_3 32
2.1.2. Synthesis of F-doped Li_2RuO_3 32
2.1.3. Synthesis of O3-phase $Li_{1.2}Ni_{0.2}Mn_{0.6}O_2$ 33
2.1.4. Synthesis of O6-phase $Li_{0.846}Ni_{0.190}Mn_{0.657}O_2$ 33
2.1.5. Synthesis of Li_2MnO_3 34
2.1.6. Synthesis of O6-phase $Li_{1.2}Mn_{0.8}O_2$ 34
2.2. Routine characterization techniques 35
2.2.1. X-ray diffraction (XRD) 35
2.2.2. Neutron diffraction (ND) 39
2.2.3. Rietveld refinement 41
2.2.4. Scanning electron microscope (SEM) 45
2.2.5. Transmission electron microscope (TEM) 47
2.2.6. X-ray photoelectron spectroscopy (XPS) 50
2.2.7. X-ray absorption spectroscopy (XAS) 53
2.2.8. Raman spectroscopy 55
2.2.9. Electron paramagnetic resonance (EPR) spectroscopy 58
2.2.10. Inductively coupled plasms-mass spectroscopy (ICP-MS) 60

2.2.11. Thermogravimetric analysis-differential scanning calorimetry (TGA-DSC) 61
2.3. Electrochemical evaluations 61
2.3.1. Electrode preparation 61
2.3.2. Electrolyte 61
2.3.3. Coin cell assembly 62
2.3.4. General electrochemical tests 62
2.3.5. Galvanostatic intermittent titration technique (GITT) 63
2.4. In-situ characterization techniques 64
2.4.1. In-situ XRD 64
2.4.2. In-situ Raman 65
2.5. References 67
CHAPTER 3. MONITORING THE LOCAL COORDINATION EVOLUTIONS IN LITHIUM RUTHENATE VIA IN-SITU RAMAN SPECTROSCOPY 68
3.1. Introduction 68
3.2. Physical characterization of Li_2RuO_3 72
3.3. General electrochemical properties of Li_2RuO_3 78
3.4. Structural evolutions of Li_2RuO_3 upon de-/lithiation 80
3.5. Chemical evolutions of Li_2RuO_3 upon de-/lithiation 82
3.6. Li^+ transfer dynamics of Li_2RuO_3 84
3.7. Local coordination evolutions in Li_2RuO_3 upon de-/lithiation 86
3.8. Summary and outlook 94
3.9. References 95
CHAPTER 4. MITIGATING STRAIN ACCUMULATION IN LITHIUM RUTHENATE VIA FLUORINE DOPING 98
4.1. Introduction 98
4.2. Structures of Li_2RuO_3 and $Li_{1.83}RuO_{2.83}F_{0.17}$ 101
4.3. Electrochemical properties of Li_2RuO_3 and $Li_{1.83}RuO_{2.83}F_{0.17}$ 105
4.4. The effect of trace amount of F-doping in $Li_{1.95}RuO_{2.95}F_{0.05}$ 111
4.4.1. Preparation of $Li_{1.95}RuO_{2.95}F_{0.05}$ 111
4.4.2. Morphology and structure of $Li_{1.95}RuO_{2.95}F_{0.05}$ 114
4.4.3. Electrochemical properties of $Li_{1.95}RuO_{2.95}F_{0.05}$ 116
4.5. The origin of stable Ru redox activities in F-doped Li_2RuO_3 118
4.6. Summary and outlook 120
4.7. References 121
CHAPTER 5. A METASTABLE O6-PHASE WITH STABLE CATION AND ANION REDOX REACTIONS 123
5.1. Introduction 124
5.2. Preparation and characterization of the O6-phase 127
5.2.1. Preparation in three steps 127
5.2.2. Formation mechanisms 132
5.2.3. Rietveld refined structure 136
5.2.4. Morphology 138

5.2.5. Electronic structures 140
5.3. Electrochemical properties of the O6-phase 148
5.4. Cation and anion redox mechanisms of the O6-phase 150
5.5. Structural evolutions of the O6-phase upon de-/lithiation 155
5.5.1. In-situ and ex-situ XRD results of the O6-phase upon de-/lithiation. 155
5.5.2. Interlayer interactions in O3- and O6-type structures 157
5.5.3. Structural evolutions upon the 1st charging to 4.5 V vs. Li/Li^+ 158
5.5.4. Structural evolutions upon the 1st charging from 4.5 V to 4.8 V vs. Li/Li^+ 159
5.5.5. Structural evolutions upon the 1st discharge to 2.0 V vs. Li/Li^+ 162
5.5.6. Structural evolutions upon the 2nd charging to 4.8 V vs. Li/Li^+ 165
5.5.7. Overall lattice changes of the O6-phase upon de-/lithiation 166
5.6. Electrochemical properties of O6-phase in the fluorinated electrolyte 169
5.6.1. Long-term cycling performance 170
5.6.2. The origin of the cycling stability in the fluorinated electrolyte 173
5.7. Summary and outlook 175
5.8. References 177
CHAPTER 6. CONCLUSIONS AND FUTURE WORK 181
6.1. Conclusions 181
6.2. Future work 184
Appendix A. Structural refinements of Li_2RuO_3 electrodes 186
Appendix B. Properties of O3-type $Li_{1.2}Ni_{0.2}Mn_{0.6}O_2$ 192
Appendix C. A taste of building interferometric scattering (iSCAT) microscopy to monitor single particle dynamics 196
C.1. Introduction 196
C.2. Fundamentals of visible light imaging 199
C.2.1. Extinction imaging 199
C.2.2. Fluorescence imaging 201
C.2.3. Interference imaging 202
C.3. Theory and applications of iSCAT 202
C.4. The possibility of tracking ARRs via iSCAT 204
C.5. Lab-made iSCAT setup 207
C.5.1. Illumination 207
C.5.2. 4f system 209
C.5.3. Imaging section 210
C.6. The sample designed for iSCAT test 211
C.6.1. Morphology and structure of O6-$Li_{1.2}Mn_{0.8}O_2$ 211
C.6.2. Electrochemical properties of O6-$Li_{1.2}Mn_{0.8}O_2$ 214
C.7. Summary and future work 215
C.8. References 215

CHAPTER 1. INTRODUCTION

Harnessing renewable energy (e.g., solar, wind, tide, etc.) and utilization of this electricity to replace the use of fossil fuels in sectors such as vehicular transport, play pivotal roles in realizing the sustainable future for mankind. However, the electricity generated by solar panels or wind plants is intermittent due to environmental fluctuations from time to time.[1-3] From this perspective, to maintain the stability of the grid, the electricity needs to be stored and integrated into the grid smartly, thereby promoting the development of all kinds of electrochemical energy storage (EES) devices (e.g., supercapacitors,[4,5] lithium-ion batteries (LIBs),[6-8] sodium-ion batteries (SIBs),[9,10] redox flow batteries,[11,12] and etc.).

Among them, lithium-ion batteries (LIBs) are the most successful in terms of commercialization and have drawn widespread attention due to the versatility for various applications. For instance, no matter whether in the traditional 3C market (i.e., computer, communication, and consumer electronic) or the burgeoning electric transportation market, LIBs are arguably the most favored candidates thanks to their high energy densities and high safety.[13] In spite of the remarkable improvements in the past, the ongoing demand for high-performance LIBs urges researchers to continuously investigate next-generation LIBs with cheaper prices, higher energy densities, better cyclabilities and superior safety.[14,15]

1.1. Basic knowledge about LIBs

1.1.1. Main components of LIBs

Generally, LIBs have four main components, i.e., the positive electrode (with cathode materials on current collectors), the negative electrode (with anode materials on current collectors), the electrolyte, and the separator.[16] Upon charging, the positive electrode undergoes anodic reactions and loses electrons, while the negative electrode undergoes cathodic reactions and accepts electrons, both are connected to the external circuit for electron transfer. Reversible reactions take place on discharging. For LIBs, both the positive and the negative electrodes are composed of active materials being able to store Li^+ ions, while conductive additives and binders are widely used to build the charge transfer framework between the active materials and current collectors (e.g., Al foils for cathode materials and Cu foils for anode materials). The internal charge transfer is achieved by the transportation of ions, whose pathways are provided by the electrolyte, consisting of inorganic or organic solvents and lithium salts. Specifically, the Li^+ ions flow from the positive electrode to the negative electrode in charging, while the reverse Li^+ transportation happens in discharging. The separator is usually immersed in the electrolyte and placed between the positive and the negative electrodes, providing pathways for Li^+ ions and avoiding the direct contact between the electrodes.

1.1.2. Working mechanisms of LIBs

Figure 1-1 schematically shows the working mechanisms of a typical lithium-ion

battery in which the layered $LiCoO_2$ (LCO) and the layered graphite function as the cathode material (positive electrode) and the anode material (negative electrode), respectively. Upon charging, the applied external voltage will drive the Li^+ ions to move out of the Li layers in $LiCoO_2$, to pass through the electrolyte and the separator, and to intercalate into the interlayer vacancies in the layered graphite, following the equations below.

Anodic process: $$LiCoO_2 \rightarrow Li_{1-n}CoO_2 + nLi^+ + ne^- \qquad (1-1)$$

Cathodic process: $$C_6 + nLi^+ + ne^- \rightarrow Li_nC_6 \qquad (1-2)$$

Full: $$LiCoO_2 + C_6 \rightarrow Li_nC_6 + Li_{1-n}CoO_2 \qquad (1-3)$$

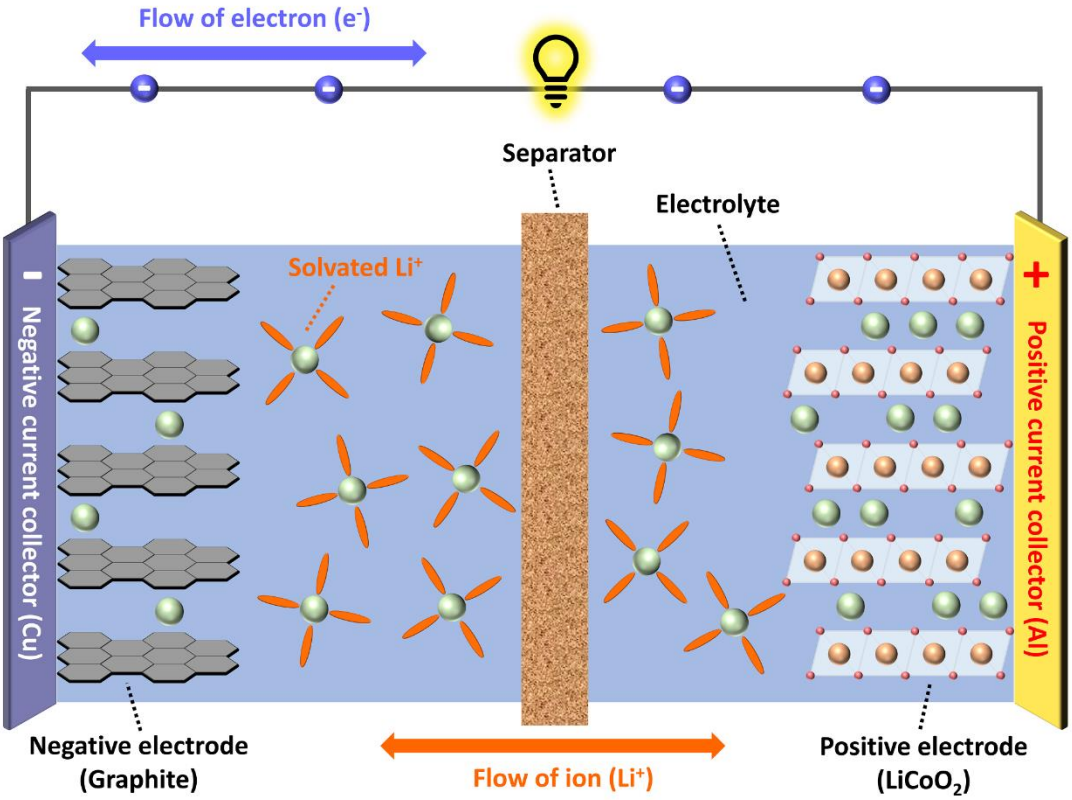


Figure 1-1. Schematic working mechanisms of the LIB ($LiCoO_2$-graphite).

1.1.3. Key factors to evaluate LIBs

Specific capacity. For a LIB, its specific capacity is usually determined by the amount of electric charge (Q) and its mass (m), following the equation:

$$C = \frac{Q}{m} = \frac{I \cdot t}{m} \qquad (1-4)$$

where I is the current, and t is the dis-/charging time.

Considering that a LIB is composed of many components and some of them are electrochemically inactive, the specific capacity is more widely used to describe the capability to take up charges for the active materials on either positive or negative electrodes. The specific capacity for the active material in the electrode could be calculated according to the Faraday's law,

$$C = \frac{nF}{3.6M} \qquad (1-5)$$

where n is the charge transfer number, F is the Faraday constant (96485.33 C/mol), M is the molecular weight of the active material. For example, in $LiCoO_2$, given that the largest amount of Li^+ that could be de-intercalated is 1 and the molecular mass is 97.873, its specific capacity is calculated to be 273.84 mAh/g. However, in practical tests, complete de-lithiation of $LiCoO_2$ is usually avoided for the purpose of preventing severe structural degradations. Therefore, as shown in **Figure 1-2a**, the charging capacity for $LiCoO_2$ is 226.7 mAh/g at the current density of 20 mA/g within the potential window of 2.0 - 4.7 V vs. Li/Li^+, meaning that the actual amount of the extracted Li^+ is around 0.83.

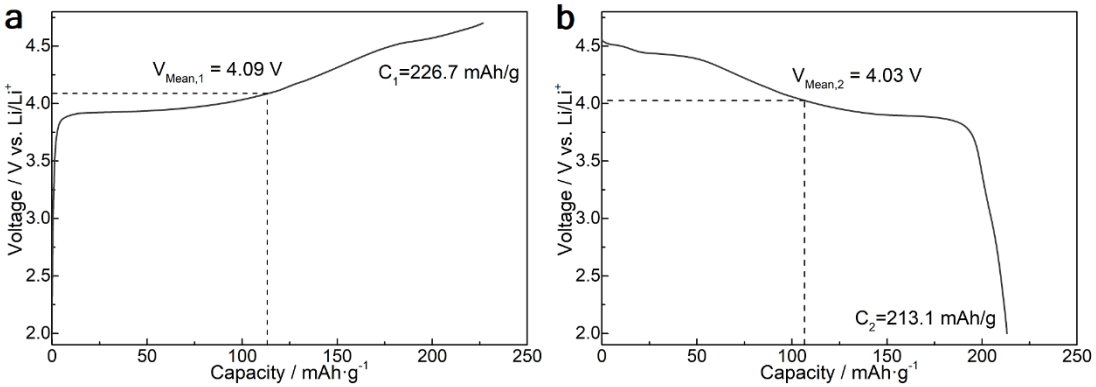


Figure 1-2. Voltage profiles of $LiCoO_2$ upon **(a)** the 2nd charging, and **(b)** the 2nd discharging. The current density is 20 mA/g and the potential window is 2.0 - 4.7 V vs. Li/Li^+.

Voltage. Voltage (V) of a LIB is determined by the potential difference between the positive and the negative electrodes, which is related to the change in Gibbs free energy.

$$V = \frac{\Delta G}{nF} \qquad (1-6)$$

As shown in **Figure 1-2**, the mean voltages (i.e., voltage at half of the capacity) of the $LiCoO_2$ electrode are 4.09 V and 4.03 V vs. Li/Li^+ in charging and discharging, respectively.

Coulombic efficiency. The coulombic efficiency (C.E.) of a LIB is a key factor to describe the reversibility between charging and discharging processes, which is the ratio between the discharging capacity and the charging capacity. As shown in **Figure 1-2b**, the discharging capacity of the $LiCoO_2$ electrode is 213.3 mAh/g, meaning that the C.E. is 94.0 % under such testing conditions.

Energy density. One of the most important factors to evaluate whether a LIB can be used or in what application scenarios can it be used is its energy density (E). Generally, portable 3C devices and electric vehicles require high-energy-density LIBs, whereas stationary energy storage devices have relatively lower requirements. It is determined by the specific capacity (C) and the voltage (V).

$$E = C \cdot V \qquad (1-7)$$

Cycling and rate performance. Cycling performance of a LIB refers to its capacity retention in long-term operation. Rate performance indicates its capability to store and release energy at large current densities, which is of particular interest when fast dis-/charging is required.

1.2. The development of LIBs

To cater for the growing demands for better LIBs, all key components of LIBs should be improved significantly to meet the requirements of high energy density, superior safety, low cost, long lifespan and so on.

1.2.1. The emergence of $LiCoO_2$

Considering first the cathode materials, the original concept of LIB proposed by Whittingham used TiS_2 as the cathode material in 1970s, which showed low voltage and poor cycling performance.[17] Later on, the discovery of $LiCoO_2$ by Goodenough and the replacement of the metallic Li with the layered graphite laid the foundation of the successful commercialization of the $LiCoO_2$-graphite cell by Sony in 1991.[18]

Ever since then, $LiCoO_2$ has been the dominant cathode material for LIBs in 3C devices thanks to its high compaction density and good electronic conductivity. In quite a long time, although $LiCoO_2$ has a theoretical capacity of 273.84 mAh/g upon the complete de-lithiation, the practical capacity is around 140 mAh/g within the potential window of 3.0 - 4.2 V vs. Li/Li^+, meaning that only 0.5 Li^+ is electrochemically active. Further removing more Li^+ ions out of the layered $Li_{0.5}CoO_2$ causes the detrimental O3-to-H1-3 phase transformation and oxygen release.[19,20] Recently, upon surface modification, bulk doping or the introduction of functional additives, the high-voltage $LiCoO_2$ has shown the potential of delivering capacities up to 200 mAh/g within the potential window of 3.0 - 4.6 V vs. Li/Li^+.[21-23] Nevertheless, because Co is expensive, $LiCoO_2$ is not economically competitive for LIBs in the automobile industry, not to mention the huge stationary energy storage market.

1.2.2. High-nickel NCA and NCM

A natural strategy to reduce the cost of the cathode material is to replace Co with cheaper transition metals, which leads to the innovation of the ternary materials of $LiNi_xCo_yAl_{1-x-y}O_2$ (NCA) and $LiNi_xCo_yMn_{1-x-y}O_2$ (NCM).[24] Thanks to the synergetic effects between different transition metals, both NCA and NCM have been prevailing in the LIBs for hybrid electric vehicles (HEVs) and electric vehicles (EVs). Specifically, Ni provides the high capacity via the redox pairs of Ni^{2+}/Ni^{3+} and Ni^{3+}/Ni^{4+}; Mn in the valence state of +4 favors the structural stability upon dis-/charging; Co or Al improves the electronic conductivity.[25] As to NCMs, the specific capacity of the first generation

$LiNi_{1/3}Co_{1/3}Mn_{1/3}O_2$ (NCM 111) is around 160 mAh/g, which increases to 170 mAh/g and 180 mAh/g in $LiNi_{0.5}Co_{0.2}Mn_{0.3}O_2$ (NCM 523) and $LiNi_{0.6}Co_{0.2}Mn_{0.2}O_2$ (NCM 622), respectively.[26-28] The state-of-the-art $LiNi_{0.8}Co_{0.1}Mn_{0.1}O_2$ (NCM 811) could deliver a reversible capacity up to 200 mAh/g. [29,30]

Further increasing the nickel content (> 0.8) in the ternary materials could contribute to higher capacities but might deteriorate their long-term stabilities. Firstly, the similar ionic radii of Li^+ (0.76 Å) and Ni^{2+} (0.69 Å) favors the Li/Ni mixing, meaning that the Ni^{2+} ions in the Li layers can block the 2-dimensional (2D) pathway of Li^+ ions and retard the ion diffusion.[31] Meanwhile, the irreversible transition metal (TM) migrations tends to induce the layered-to-rock salt/spinel phase transformations and cause both capacity decay and voltage fading.[32] Besides, the reactions between Ni^{4+} and the electrolyte can produce passivation layers on the surface and impede the ion transportation.[33] Moreover, from the perspective of safety concerns, the high ionicity of the Ni-O bond makes its cleavage easier than that of the high covalent Co-O bond. Thus, the high-nickel ternary cathode materials are liable to decompose and release gaseous oxygen at lower temperatures, thereby increasing the risk of thermal runaways.[34] Numerous attempts have been made to improve the stability of high-nickel NCMs, which could come down to surface coating,[35,36] doping,[37,38] building nanostructures with concentration gradients,[39,40] and so on. Anyhow, considering the economical and electrochemical advantages of NCMs, they are destined to be the dominant cathode materials in LIBs for HEVs and EVs in the foreseeable future.

1.2.3. Lithium-rich manganese oxides (LRMOs)

To break the ceiling of the capacity limit of cathode materials, lithium rich manganese oxides (LRMOs, $xLiTMO_2 \cdot (1-x)Li_2MnO_3$, TM=Ni, Co, Mn, etc.) have attracted widespread research interests thanks to their high theoretical capacities (> 250 mAh/g).[41-43] Generally, LRMOs could be regarded as the intergrowth (i.e., mixed uniformly in single particles) of a trigonal $LiTMO_2$ phase (R-3m) and a monoclinic Li_2MnO_3 phase (C2/m), in which the additional capacity is contributed by the lithium rich phase. Considering that Mn is environmentally benign and cheaper than Co/Ni, the high-capacity Li-rich Mn-based oxides are promising candidates for cathode materials in next-generation LIBs.

However, their practical applications are impeded by two major challenges, namely fast capacity decay and voltage fading upon cycling.[44] Firstly, removing more Li^+ ions out of the layered structure promotes the irreversible migration of TM ions, meaning that the detrimental layered-to-spinel phase transformation is inevitable in the long-term de-/lithiation.[45,46] Besides, because the Mn^{4+} is unlikely to be oxidized to higher valence states in the octahedral MnO_6, the extraction of Li ions from the Li_2MnO_3 domain induces the oxidization of the lattice oxygen (O^{2-}) for charge compensation.[47] Unfortunately, triggering the oxygen redox activities eases the O-O dimerization, the formation of gaseous O_2 and its release. In addition, both the sluggish kinetics of anion redox reactions (ARRs) and the low electronic conductivity of Mn^{4+} ions hinder the fast de-/lithiation of LRMOs.[48] Therefore, albeit promising, the future success of LRMOs is

determined by whether the following requirements could be met: i) rigid local structures to suppress the TM migration and oxygen loss, ii) effective cathode electrolyte interphases (CEIs) to prevent the TM dissolution and side reactions with the electrolyte, and iii) good electron and ion transfer networks to facilitate fast charge transfers.

1.2.4. Olivine and spinel phases

In addition to the above-mentioned layered oxides (i.e., LCO, NCM/NCA, and LRMOs), the olivine $LiFePO_4$ (LFP) and high voltage cathode materials such as the spinel $LiNi_{0.5}Mn_{1.5}O_4$ (LNMO) are also suitable for LIBs in EVs and stationary energy storage devices due to their advantages of low-cost and environmental friendliness. Since the first report in 1997, olivine LFP has been regarded as a promising candidate for EVs due to its high thermal stability and safety.[49] Yet, its wide application is still hindered by the low voltage (3.45 V vs. Li/Li^+) and poor low-temperature performances. On the contrary, the high-voltage (5 V-class) spinel LNMO, derived from spinel $LiMn_2O_4$, is estimated to deliver higher gravimetric energy densities. However, at such a high voltage (5 V vs. Li/Li^+), the strong reactivity between the oxidized Ni^{4+} ions and the electrolyte can easily lead to the decomposition of conventional $LiPF_6$-based carbonate electrolytes, resulting in Mn/Ni dissolution-migration-deposition and serious loss of active lithium (especially at graphite electrode).[50]

1.2.5. From graphite to metallic lithium

With respect to the anode materials, graphite has been dominating in the commercial LIBs since its initial implementation, which has a theoretical capacity limit of 372 mAh/g.[51] To push the boundary of capacity, tremendous efforts have been dedicated to finding alternative anode materials with low potentials vs. Li/Li^+. For instance, silicon-based materials (e.g., Si with hierarchical 3D structures, amorphous Si alloys, composites of SiO_x/C and nano-Si/C) have been investigated intensely because of their high capacities (> 500 mAh/g).[52-55] However, because the large volume expansion of Si upon lithiation usually leads to the pulverization and performance degradation, precisely tailoring the nanostructures in the composites of nano-Si and carbon matrix is the prerequisite for their practical applications.

Given that metallic Li has the lowest potential and the highest capacity, the final goal in future LIBs is to replace the graphite or Si-based composites with a Li metal anode.[56] However, several problems hinder its wide utilization. Firstly, Li metal could continuously react with the organic liquid electrolyte (OLE), forming dense solid electrolyte interphases (SEIs) to block the ion diffusion, to increase the impedance and to cause the gradual voltage decay.[57] Besides, the inhomogeneous Li deposition leads to the growth of Li dendrites, which either pulverize to form the “dead lithium” or penetrate the separator to cause short circuits.[58]

1.2.6. Towards solid-state LIBs

To circumvent the above mentioned issues, although designing nanostructures for uniform Li plating/stripping or building artificial SEIs have been proven to be effective,[59,60] developing solid state batteries (SSBs) is arguably the ultimate solution.[61] For example, inorganic solid-state electrolytes (SSEs), solid polymer electrolytes (SPEs) and composite polymer electrolytes (CPEs) have demonstrated their potentials for future SSBs.[62-64] However, realistically speaking, building all solid-state LIBs without OLEs still faces challenges such as incompatible electrode/electrolyte interfaces, large interfacial impedances, sluggish ionic conductivities, and poor mechanical properties.[65] Therefore, using hybrid electrolytes with trace amounts of OLEs might be the transitional stage towards the all-solid-state future.

1.2.7. The roadmap of LIBs

In summary, although other components such as the electrolytes and functional additives are non-negligible, the development of LIBs largely relies on the advances of the active materials. **Figure 1-3** displays the roadmap for LIBs in the following years. Specifically, the high-voltage $LiCoO_2$ is believed to be the dominant cathode material for 3C devices, while the high-Ni NCM and NCA are deemed to be the mainstream candidates for LIBs in HEVs and EVs. Besides, the olivine LFP and the high-voltage spinel LNMO have their roles to play in the stationary energy storage market and also in the e-mobility market. On the other hand, graphite and Si-based composites are supposed to continue to be the main anode materials, while the Li metal anode will gradually

step on to the stage. Finally, SSBs with the LRMOs cathode and the Li metal anode could potentially achieve desirable energy densities (> 500 Wh/kg) and eradicate the safety concerns of LIBs (e.g., thermal runaway and explosion).

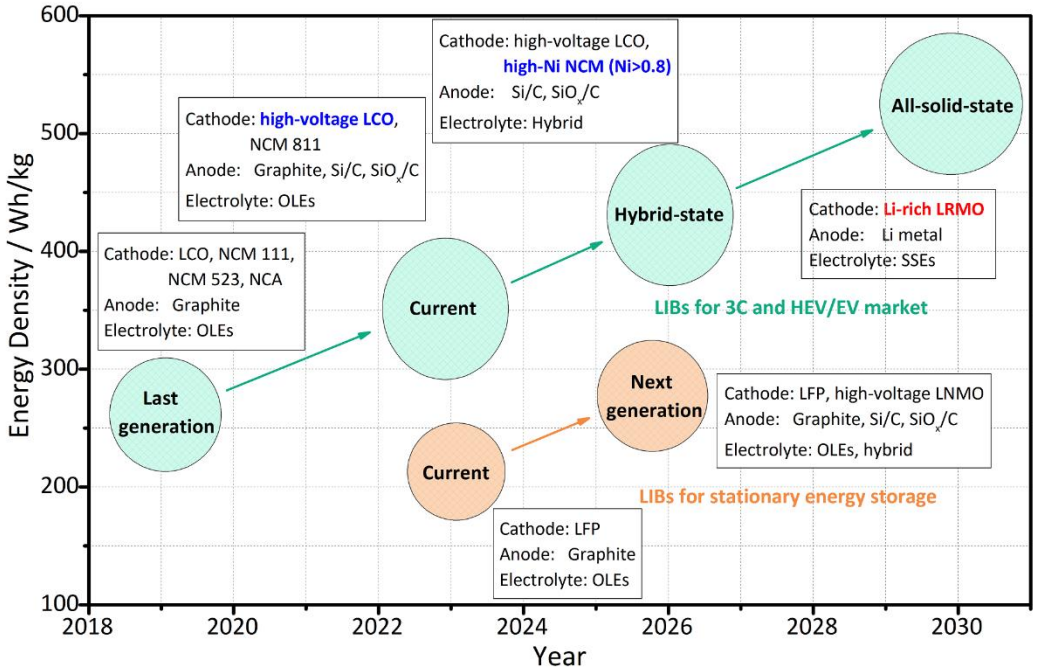


Figure 1-3. The roadmap of LIBs in the following decade.

1.3. The origin of the extra capacity in Li-rich layered oxides

Simply put, as the promising candidates for next-generation LIBs, Li-rich cathode materials (LRCMs) could deliver ultra-high capacities (>250 mAh/g) because of the larger amounts of the extractable Li^+ ions. Meanwhile, in addition to the conventional cation redox reactions, the emergence of anion redox reactions (ARRs) is believed to be responsible for the additional charge compensation.[66] In this section, to better understand the origin of the extra capacity, both the structural and chemical differences between the Li-stoichiometric and Li-rich layered oxides are compared.

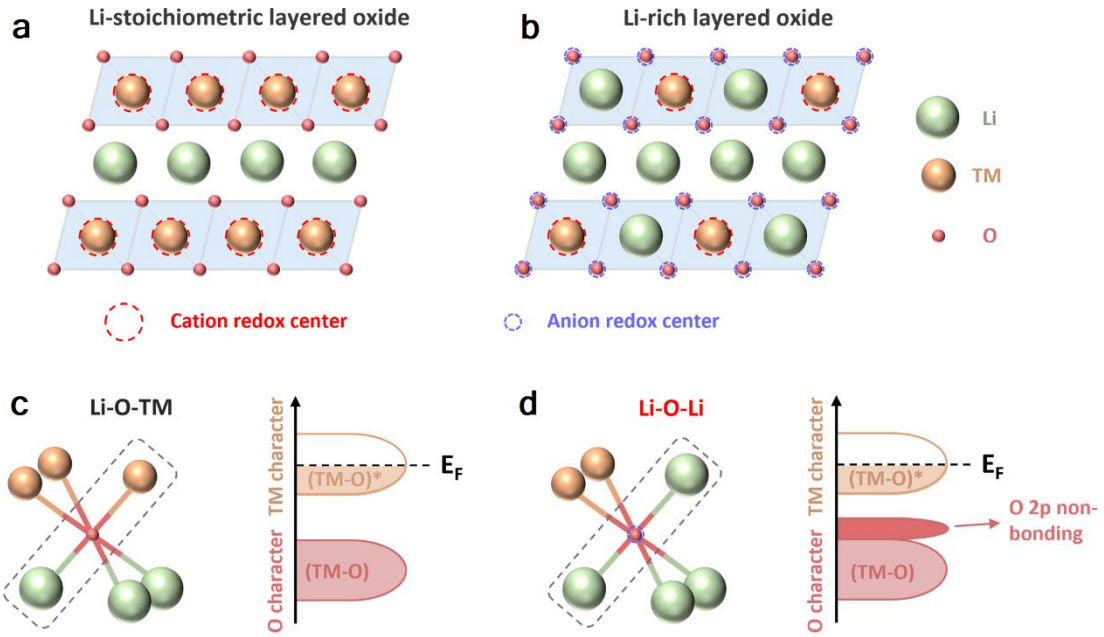


Figure 1-4. Differences between Li-stoichiometric and Li-rich layered oxides. **(a)** The structure of Li-stoichiometric layered oxides, such as $LiCoO_2$. **(b)** The structure of Li-rich layered oxides, such as Li_2MnO_3. **(c)** Local atomic coordination around O and schematic band structures in Li-stoichiometric layered oxides. **(d)** Local atomic coordination around O and schematic band structures in Li-rich layered oxides. E_F refers to the Fermi energy level. Reproduced according to ref 70 and 72.

From the perspective of general structures, Li, TM and O stack layer by layer along the *c*-axis to form the Li-stoichiometric layered oxides (**Figure 1-4a**), while Li ions not only occupy the Li layers but also occupy some sites in the TM layers in the Li-rich layered oxides (**Figure 1-4b**).[67] The Li-rich local environment alters the coordination around oxygen and reshapes the band structures of TM and O, which are believed to the key factors determining the charge compensation mechanisms.

Generally, whether the TM or the O ions are activated for charge compensation is determined by the relative positions of their energy bands to the Fermi level (E_F).[68,69] Specifically, in the conventional Li-stoichiometric cathode materials (e.g., $LiCoO_2$ and

NMCs), each O coordinates with three TM ions and three Li ions, forming Li-O-TM configurations along all of the three directions (**Figure 1-4c**). According to the molecular orbital theory, the O 2p orbitals could hybridize with the TM d/s/p orbitals to form the split bonding states (TM-O, e_g^b, a_{1g}^b and t_{1u}^b) and the anti-bonding states (TM-O*, e_g^*, a_{1g}^* and t_{1u}^*), which are thought to have O and TM characters, respectively.[70] Meanwhile, the overlap between the TM d_{xy}, d_{yz} and d_{xz} orbitals and the O 2p orbitals is negligible, resulting in the non-bonding t_{2g} state (TM character). Therefore, in the traditional layered oxides, because the E_F lies in the e_g^* or the t_{2g} band, TM ions are more liable to lose electrons. On the contrary, the TM-O bonding states usually lie at very low energies, meaning that the oxidation of the hybridized oxygen is unlikely to take place.

However, in Li-rich layered oxides (e.g., Li_2MnO_3), having Li ions in the TM layers creates both the Li-O-TM and the Li-O-Li configurations (**Figure 1-4d**).[71] In the Li-O-Li configuration, the O 2p orbitals are unlikely to hybridize with Li 1s orbitals because of the large energy difference between them. In the band structure, the orphaned O 2p orbitals (non-bonding states) lie at relatively higher positions than those of the TM-O bonding states.[72] Therefore, upon further de-lithiation, electrons can be removed from the orphaned O 2p orbitals. In summary, the ultra-high capacities of Li-rich cathode materials are contributed by multiple factors: i) the larger amounts of Li ions available for charge transfer, ii) the conventional cation redox reactions, and iii) the liable oxygen redox activities for the extra charge compensation.

1.4. The nature of the anion redox reactions (ARRs)

Although consensus has been reached that ARRs are responsible for the extra capacities in Li-rich cathode materials, it is still debatable as in what ways do anionic activities occur or to what extent could oxygen lattices evolve. To decipher the nature of the oxygen redox activities, tremendous efforts have been paid and multiple mechanisms have been proposed in the past decade (**Figure 1-5**).

The initial observation of ARRs in the layered oxides can be traced back to the late 1990s, when the shortened interplanar O-O pairs were captured in the deeply de-lithiated Li_xCoO_2.[73] However, it was not until a decade later that the oxygen redox activities started to attract widespread research interests, along with the bloom of Li_2MnO_3 and Li-rich NCMs. For instance, via using the soft X-ray absorption spectroscopy (sXAS) and conventional resonant inelastic X-ray scattering (RIXS), Luo et al. observed the formation of electron holes on the O 2p orbitals in the de-lithiated $Li_xNi_{0.2}Mn_{0.6}O_2$, yet no band belonging to the peroxide O_2^{2-} (O-O, 1.45 Å) was observed.[74] However, it was contradictory that, by using the operando differential electrochemical mass spectrometry (DEMS), they detected the release of gaseous O_2 in the highly charged ^{18}O-labelled $Li_x(Ni_{0.13}Co_{0.13}Mn_{0.54})O_2$, in which O was partially extracted from the lattice.[75] Considering the high reactivity between the oxidized O and the electrolyte, it was puzzling that whether the formation of O_2 was a surface activity or a bulk activity.

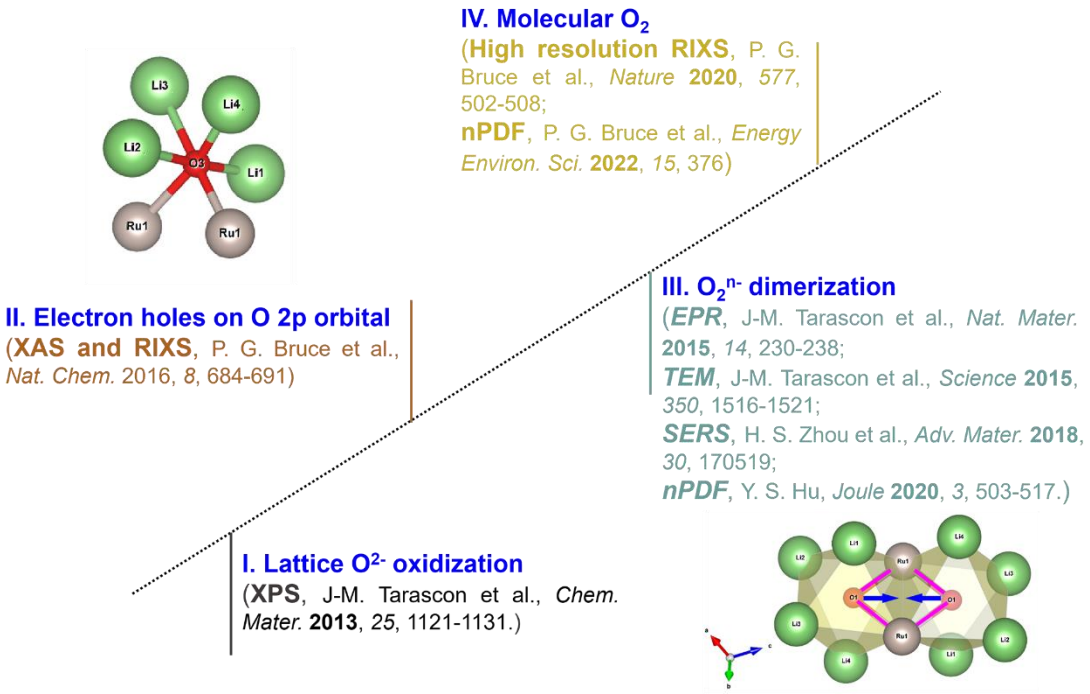


Figure 1-5. The developing mechanisms of the oxygen redox activities.

In the 4d and 5d TM-based Li-rich layered oxides (e.g., $Li_2Ru_{0.5}Sn_{0.5}O_3$ and Li_2IrO_3),[76-78] Tarascon et al. captured the O-O dimerization upon ARRs with the help of X-ray photoelectron spectroscopy (XPS), electron paramagnetic resonance (EPR) and transmission electron microscopy (TEM). Therefore, they suggested that the reversible reactions between the lattice O^{2-} and O_2^{n-} dimers ($0 < n < 2$) were accountable for the extra charge compensation. Besides, the signature Raman vibrations of the peroxide (O_2^{2-}) species were captured in the de-lithiated LRMOs by using the *operando* surface enhanced Raman spectroscopy (SERS).[79]

Recently, thanks to the technical advances, a converged understanding about ARRs has been proposed.[80] Specifically, the formation of bulk O_2 was proven across 3d, 4d, and 5d transition metal oxides by using the high resolution RIXS.[81-83] Besides, the bulk

sensitive solid-state ^{17}O magic-angle-spinning nuclear magnetic resonance (MAS-NMR) revealed the appearance of the confined O_2 molecules in the de-lithiated $Li_xNi_{0.13}Co_{0.13}Mn_{0.54}O_2$. Moreover, the O-O pair (1.2 Å) identical to the O_2 molecule was detected in the charged $Li_{0.1}Ni_{0.13}Co_{0.13}Mn_{0.54}O_2$ via low-temperature neutron pair distribution function (NPDF), indicating that the formation of O_2 was a bulk activity.[84]

In summary, in Li-rich layered oxides, the lattice oxygen (O^{2-}) can be oxidized ultimately to molecular O_2. Firstly, removing electrons from the Li-O-Li configuration creates holes on the non-bonding O 2p orbitals, signifying the emergence of ARRs. The coalescence of electron holes favors the formation of the O_2^{n-} dimers. Thereafter, depending on the covalency of the adjacent TM ions and the local structures, the dimerized O-O pairs might either localize in the bulk environment or de-coordinate from the octahedral TMO_6 framework. If the latter is the case, molecular O_2 appears, and the risk of oxygen loss increases.

1.5. Structural evolutions upon ARRs

Given that triggering the oxygen redox activities could inevitably induce local distortions around O, a natural question is in what ways do they take place? Generally, monitoring local structure changes is challenging because either the widely used X-ray diffraction (XRD) or the neutron diffraction (ND) mainly reveals the long-range orderings.[85,86] Pair distribution function (PDF) is potentially an ideal technique to probe short-range patterns because it take advantages of both Bragg diffraction and

the diffuse scattering signals.[87,88] For example, both distortions of TMO_6 octahedra and TM migrations were observed upon de-/lithiation of the archetypical Li_2MnO_3 by using the ex-situ X-ray PDF (XPDF).[89] However, directly capturing the evolution of the O-O pairs in XPDF is challenging due to the weak scattering effect of oxygen.

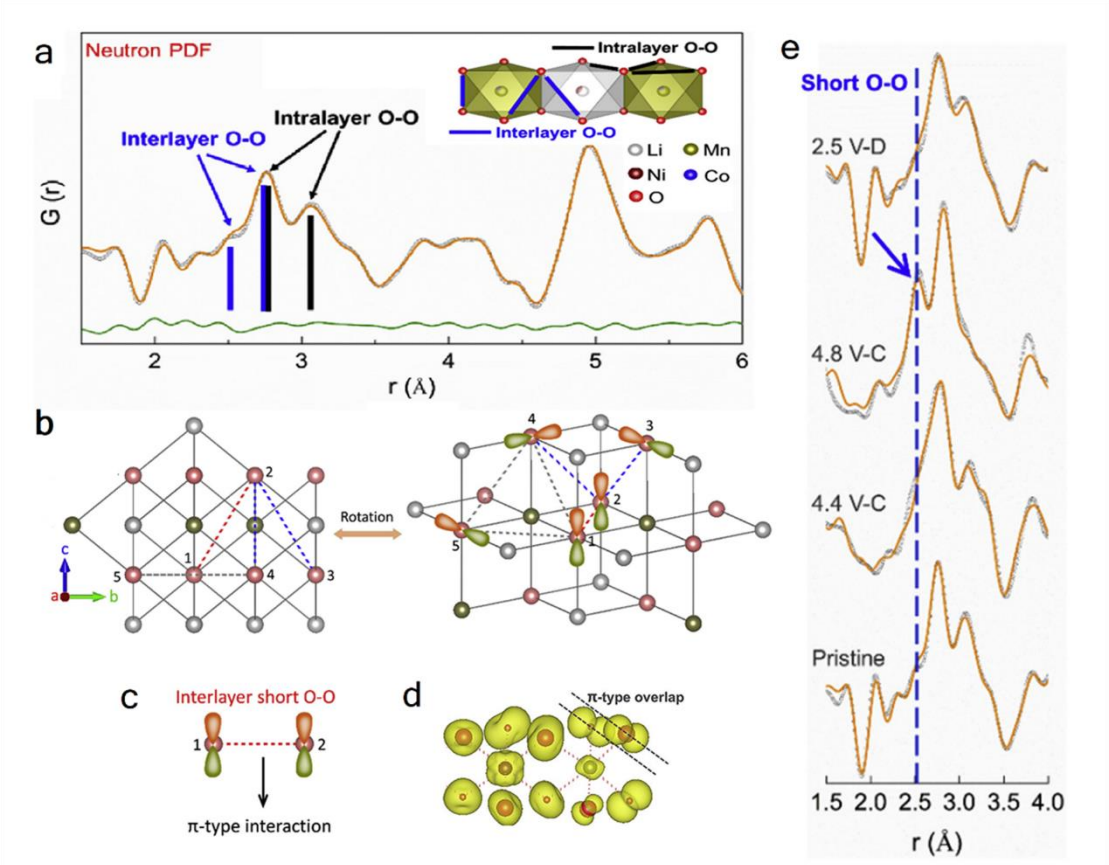


Figure 1-6. (a) NPDF data of the pristine $Li_{1.2}Ni_{0.13}Mn_{0.54}Co_{0.13}O_2$. The inset shows the interlayer and the intralayer O-O pairs in TMO_6 octahedra. **(b)** Crystal lattices showing the nonbonding O 2p orbitals along the Li-O-Li configurations. **(c)** The π-type interaction between the interlayer O-O pair. **(d)** Electron density iso-surface contour plots illustrating the π-type overlap. The energy ranges from -0.5 to 1.5 eV, where E_F = 0 eV. **(e)** Ex-situ NPDF results collected at different voltages. Adapted from ref 90.

Fortunately, thanks to the high scattering length of oxygen for neutron, Zhao et al. firstly captured the distorted oxygen lattices in the deeply de-lithiated $Li_{1.2}Ni_{0.13}Mn_{0.54}Co_{0.13}O_2$ via neutron PDF (NPDF).[90] As shown in **Figure 1-6**, the

interlayer O-O pairs shrink and dimerize through π-type overlap of the orphaned O 2p orbitals, yet the intralayer O-O pairs without the coplanar 2p orbitals are largely maintained, meaning that the structural evolution induced by ARRs is highly selective. Moreover, the local environment around oxygen further contributes to the selectivity, e.g., O-O dimers are more likely to form in the MnO_6 octahedra rather than in the NiO_6 octahedra because the stronger ionicity of Mn-O bonds allows them to distort more flexibly. It is noteworthy that the shortest interlayer O-O pair (~2.39 Å) is much longer than the length of the real peroxide (~1.45 Å), not to mention the molecular O_2. However, at extremely low temperatures (2 K), the O-O pair (1.2 Å) identical to the O_2 molecule was detected in the $Li_{0.1}Ni_{0.13}Mn_{0.54}Co_{0.13}O_2$ by using NPDF. [84]

In addition to the average techniques based on scattering, scanning transmission electron microscopy (STEM) with local probes has also demonstrated the capability to capture the local patterns induced by ARRs. For instance, McCalla et al. observed the distortion of the octahedral IrO_6 in the de-lithiated Li_2IrO_3.[78] Specifically, upon removing 1.5 Li^+, the shape of the IrO_6 octahedra changes asymmetrically and the O-O dimers with shorter O-O distances (~ 1.56 Å) appear in the $Li_{0.5}IrO_3$. Initially, it was believed that using STEM to visualize the atomic displacements of O in the 3d TM-based materials was not feasible because the inevitable cation disordering/mixing might make finding the right projections of the TMO_6 octahedra difficult and complicate the simulation of the O-O distances. However, thanks to the development of phase retrieval algorithms, electron ptychography (also known as 4D STEM) enables

the imaging of the oxygen shift at atomic resolutions in $Li_{1.2}Ni_{0.13}Mn_{0.54}Co_{0.13}O_2$, thereby providing new opportunities to probe lattice distortions even in disordered structures. [91]

On the other hand, upon the removal of Li^+ ions, TM ions are prone to migrate to the nearby Li vacancies either within the TM layers or in the Li layers (**Figure 1-7**), both of which are thermodynamically favorable.[92,93] Specifically, for the intralayer migration, TM ions tend to migrate to the adjacent octahedral Li vacancies, thereby destroying ordered local patterns (e.g., honeycomb-like superstructures). For the interlayer TM migration, once TM ions have entered the intermediate tetrahedral sites in the Li layers, their migration into the adjacent octahedral sites to form TM_{Li}-V_{TM} anti-site defects is

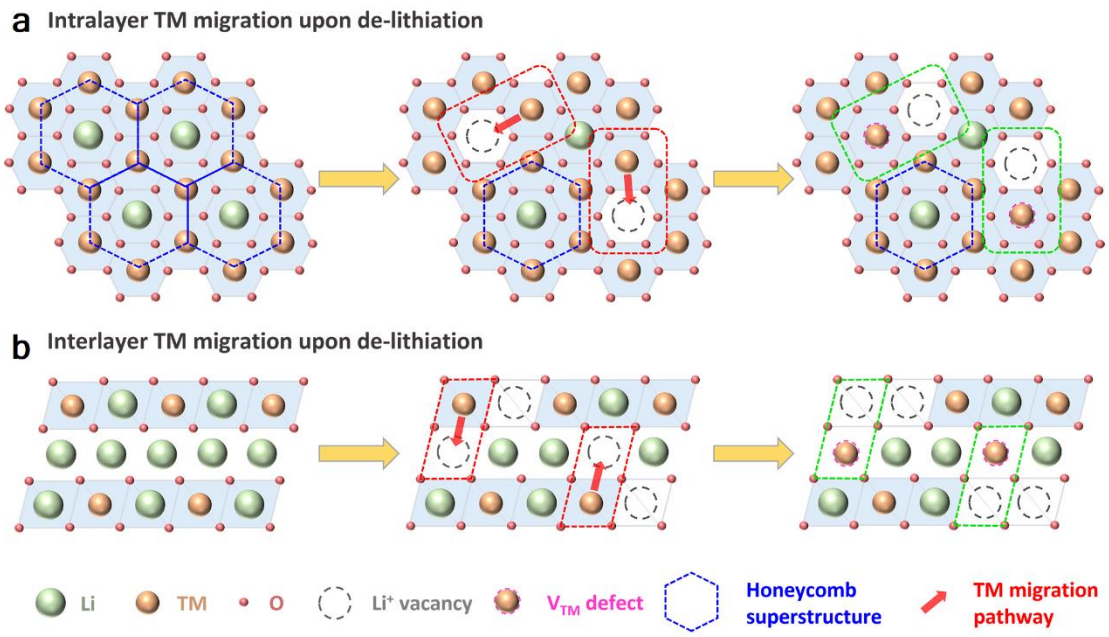


Figure 1-7. Diagrams of TM migrations in the Li-rich layered oxides upon de-lithiation**. (a)** The intralayer TM migration. The order-to-disorder arrangement destroys the pristine honeycomb-like superstructures. **(b)** The interlayer TM migration inducing the layered-to-rock salt/spinel phase transformations. The trapped TM ions block the 2D pathway of Li+ ions and retard the ion transfer kinetics.

inevitable and irreversible, therefore leading to the detrimental layered-to-rock salt/spinel phase transformations. Besides, considering that the layered oxides are built by the network of TM and O ions, the oxidation of oxygen and the O-O dimerization can weaken the TM-O bonding and lead to the TM-O de-coordination. Therefore, under the circumstance of ARRs, TM migration is supposed to take place more easily.[94]

1.6. Challenges of tapping into ARRs for practical applications

Currently, there is a consensus that exploiting ARRs in the Li-rich cathode materials provides a new paradigm to develop next-generation LIBs thanks to their high capacities (>250 mAh/g). Meanwhile, technical advances have largely enriched our understanding about the hidden mechanisms of oxygen redox activities. However, from the perspective of practicability, their real-world applications still face two major challenges, namely rapid capacity decay and voltage fading upon cycling.

Such performance declines originate from the ARRs-induced structural degradations, i.e., the irreversible TM migrations and oxygen loss. Commonly, the irreversible TM migrations are believed to be the origin of voltage drops in both the initial cycle and long-term cycles. Specifically, in the 1st cycle, the intralayer TM migration can destroy any superstructures within the TM layers (as evidenced by TEM images and also the decreasing XRD peaks in the Ti/Sn doped Li_2RuO_3), thereby inducing order-to-disorder transformation and voltage hysteresis.[95] Besides, the interlayer TM migration can lead

to the layered-to-rock salt/spinel phase transformations (as observed in Li-rich NCM), which destroy 2D Li^+ transfer pathways and cause gradual voltage decay.[96]

On the other hand, upon the oxidation of oxygen, the lattice oxygen (O^{2-}) ultimately transforms to molecular O_2 via the O-O dimerization. Ideally, no matter to what form the O ions are oxidized, they are expected to be stable in the TM-O framework and to be reduced reversibly upon discharging. It is generally true in the bulk because there are no easy pathways for the transfer of the O-O dimers or the gaseous O_2. However, TM migration creates isolated O_2 molecules no longer anchoring to the nearby TM sites, which thereafter escape from the lattice and cause capacity loss.[97] It is noteworthy that the oxygen loss further eases the detrimental TM migration and vice versa. In addition, in the near-surface areas, those activated oxygen can react with the organic electrolyte, lead to the formation of O vacancies, and induce the lattice densifications in the subsurface areas.[98] Upon cycling, such defects are prone to spread inward and result in nanovoids in the bulk. Consequently, the accumulation of those defects could increase the micro-strains and cause collapse or cracks, as evidenced by TEM images in cycled $Li_{1.2}Ni_{0.2}Mn_{0.6}O_2$.[99]

Great progress has been made to tackle the above-mentioned issues. For example, approaches to tuning TM/Li arrangement, e.g., tailoring the arrangement of local patterns to build ordered superstructures in 3d Mn-based materials and building totally disordered $LiRu_2$ layers as in 4d Ru-based Li_2RuO_3, have been demonstrated to

be effective in mitigating the intralayer TM migration.[100,101] For the interlayer TM migration, it is energetically favorable and inevitable even in the de-lithiated Li-stoichiometric layered oxides. Although preventing the unfavorable interlayer TM migration is challenging, multiple strategies (e.g., cation/anion doping and surface coating) have been demonstrated to be helpful.[102-105] A recent tactic of designing face-sharing local structures between LiO_6 and TMO_6 octahedra in an O2-type structure turns out to be effective because the repulsive Li^+-Mn^{4+} interaction at the face-sharing sites increases the energy penalty for the interlayer Mn migration.[106] To suppress the oxygen loss, no matter via conducting artificial surface modifications or introducing additives in the electrolytes, building uniform and dense CEIs is the key.

The future success of taking advantages of ARRs in Li-rich cathode materials is determined by whether they can systematically compete with the existing ones not only in terms of capacity but also from various aspects (e.g., energy efficiency, cost, rate capability, etc.). For instance, although the ARRs-induced O-O dimerization provides a new paradigm for extra charge compensation, the cleavage of O-O dimers is energy consuming and sluggish.[107,108] From this perspective, although the basic theories about ARRs have matured and the arsenal to mitigate performance degradations has been enriched, the inferior electrochemical kinetics of the oxygen redox activities needs to be improved.

1.7. Aims

As outlined in above sections, triggering the ARRs in LRCMs contributes to extra capacities beyond traditional cation redox reactions, thereby making them promising candidates as cathode materials in next-generation LIBs. However, although consensus has been made that the lattice oxygen (O^{2-}) can be oxidized to O-O dimers and ultimately to molecular O_2 upon oxygen redox activities, monitoring the local structure evolutions around oxygen is still challenging, especially under electrochemical conditions. In addition, from the perspective of practical applications, although tapping into ARRs results in high capacities, the parasitic oxygen loss and TM migration unfortunately lead to rapid performance degradation, namely capacity decay and voltage fading, which need to be tackled for their future success.

Therefore, the overarching objective of this thesis is to improve the stability of ARRs in LRCMs through (i) developing better understanding of the nature of ARRs, (ii) developing in situ/operando techniques to monitor the ARR-induced changes during electrochemical processes, and (iii) using these insights and those from the literature to design LRCMs with improved stability.

Accordingly, to gain more knowledge about ARRs, in Chapter 3, a thorough in-situ Raman study was conducted on the archetypal Li_2RuO_3 to investigate the local coordination evolutions around oxygen, which were interpreted with multimodal characterizations including in-situ/ ex-situ XRD, ex-situ XPS, ex-situ XAS, Rietveld

refinements, and electrochemical experiments; in Appendix C, an interferometric scattering microscopy (iSCAT) setup was designed for the purpose of tracking ARRs at the single particle level. On the other hand, to improve the stability of ARRs, in Chapter 4, F-doping was introduced to Li_2RuO_3 and its effects on electrochemical properties were investigated; in Chapter 5, a metastable O6-phase material with stable cation and anion redox activities was designed, and it exhibited excellent cycling performance thanks to its face-sharing local structures being able to suppress the interlayer Mn migration and the reversible O6-to-O2 phase transformation with less lattice changes with respect to the O3-to-O1 phase transformation in traditional O3-phase LRCMs.

1.8. References

1. A. A. Kebede, T. Kalogiannis, J. Van Mierlo, and M. Berecibar, *Renew. Sust. Energy Rev.*, 2022, **159**, 112213.
2. S. Shivashankar, S. Mekhilef, H. Mokhlis, and M. Karimi, *Renew. Sust. Energy Rev.*, 2016, **59**, 1170-1184.
3. S. D. Ahmed, F. S. M. Al-Ismail, M. Shafiullah, F. A. Al-Sulaiman, and I. M. El-Amin, *IEEE Access*, 2020, **8**, 10857-10878.
4. F. Wang, X. Wu, X. Yuan, Z. Liu, Y. Zhang, L. Fu, Y. Zhu, Q. Zhou, Y. Wu, and W. Huang, *Chem. Soc. Rev.*, 2017, **46**, 6816-6854.
5. Poonam, K. Sharma, A. Arora, and S. K. Tripathi, *J. Energy Storage*, 2019, **21**, 801-825.
6. B. Dunn, H. Kamath, and J.-M. Tarascon, *Science*, 2011, **334**, 928-935.
7. J. B. Goodenough, and Y. Kim, *Chem. Mater.*, 2009, **22**, 587-603.
8. J. B. Goodenough, and K. S. Park, *J. Am. Chem. Soc.*, 2013, **135**, 1167-1176.
9. H. Pan, Y.-S. Hu, and L. Chen, *Energy Environ. Sci.*, 2013, **6**, 2338-2360.
10. Y. Li, Y. Lu, C. Zhao, Y.-S. Hu, M.-M. Titirici, H. Li, X. Huang, and L. Chen, *Energy Storage Mater.*, 2017, **7**, 130-151.
11. K. Lin, Q. Cheng, M. R. Gerhardt, L. Tong, S. B. Kim, L. Eisenach, A. W. Valle, D. Hardee, R. G. Gordon, M. J. Aziz, and M. P. Marshak, *Science*, 2015, **349**, 1529-1532.
12. P. Alotto, M. Guarnieri, and F. Moro, *Renew. Sust. Energy Rev.*, 2014, **29**, 325-335.
13. M. Li, J. Lu, Z. Chen, and K. Amine, *Adv. Mater.*, 2018, **30**, e1800561.
14. T. Kim, W. Song, D.-Y. Son, L. K. Ono, and Y. Qi, *J. Mater. Chem. A*, 2019, **7**, 2942-2964.
15. F. Wu, J. Maier, and Y. Yu, *Chem. Soc. Rev.*, 2020, **49**, 1569-1614.
16. H. Zhang, H. Zhao, M. A. Khan, W. Zou, J. Xu, L. Zhang, and J. Zhang, *J. Mater. Chem. A*, 2018, **6**, 20564-20620.
17. M. S. Whittingham, *J. Electrochem. Soc.*, 1976, **123**, 315-320.
18. K. Mizushima, P. C. Jones, P. J. Wiseman, and J. B. Goodenough, *Solid State Ionics*, 1981, **3/4**, 171-174.
19. R. Yazami, Y. Ozawa, H. Gabrisch, and B. Fultz, *Electrochim. Acta*, 2004, **50**, 385-390.
20. J. Li, C. Lin, M. Weng, Y. Qiu, P. Chen, K. Yang, W. Huang, Y. Hong, J. Li, M. Zhang, C. Dong, W. Zhao, Z. Xu, X. Wang, K. Xu, J. Sun, and F. Pan, *Nat. Nanotechnol.*, 2021, **16**, 599-605.
21. X. Tan, Y. Zhang, S. Xu, P. Yang, T. Liu, D. Mao, J. Qiu, Z. Chen, Z. Lu, F. Pan, and W. Chu, *Adv. Energy Mater.*, 2023, **13**, 2300147.
22. Y. Huang, Y. Zhu, H. Fu, M. Ou, C. Hu, S. Yu, Z. Hu, C. T. Chen, G. Jiang, H. Gu, H. Lin, W. Luo, and Y. Huang, *Angew. Chem. Int. Ed.*, 2021, **60**, 4682-4688.
23. H. Huang, Z. Li, S. Gu, J. Bian, Y. Li, J. Chen, K. Liao, Q. Gan, Y. Wang, S. Wu, Z. Wang, W. Luo, R. Hao, Z. Wang, G. Wang, and Z. Lu, *Adv. Energy Mater.*, 2021, **11**, 2101864.
24. P.-C. Tsai, B. Wen, M. Wolfman, M.-J. Choe, M. S. Pan, L. Su, K. Thornton, J. Cabana,

and Y.-M. Chiang, *Energy Environ. Sci.*, 2018, **11**, 860-871.
25. W. Luo, F. Zhou, X. Zhao, Z. Lu, X. Li, and J. R. Dahn, *Chem. Mater.*, 2009, **22**, 1164-1172.
26. N. Yabuuchi, and T. Ohzuku, *J. Power Sources*, 2003, **119-121**, 171-174.
27. S.-K. Jung, H. Gwon, J. Hong, K.-Y. Park, D.-H. Seo, H. Kim, J. Hyun, W. Yang, and K. Kang, *Adv. Energy Mater.*, 2014, **4**, 1300787.
28. H. Kim, M. G. Kim, H. Y. Jeong, H. Nam, and J. Cho, *Nano Lett.*, 2015, **15**, 2111-2119.
29. Y. Xia, J. Zheng, C. Wang, and M. Gu, *Nano Energy*, 2018, **49**, 434-452.
30. J. Xu, F. Lin, M. M. Doeff, and W. Tong, *J. Mater. Chem. A*, 2017, **5**, 874-901.
31. H. Li, A. Liu, N. Zhang, Y. Wang, S. Yin, H. Wu, and J. R. Dahn, *Chem. Mater.*, 2019, **31**, 7574-7583.
32. X. Liu, G. L. Xu, L. Yin, I. Hwang, Y. Li, L. Lu, W. Xu, X. Zhang, Y. Chen, Y. Ren, C. J. Sun, Z. Chen, M. Ouyang, and K. Amine, *J. Am. Chem. Soc.*, 2020, **142**, 19745-19753.
33. X. Wang, Y. L. Ding, Y. P. Deng, and Z. Chen, *Adv. Energy Mater.*, 2020, **10**, 1903864.
34. X. Feng, M. Ouyang, X. Liu, L. Lu, Y. Xia, and X. He, *Energy Storage Mater.*, 2018, **10**, 246-267.
35. K. Yuan, N. Li, R. Ning, C. Shen, N. Hu, M. Bai, K. Zhang, Z. Tian, L. Shao, Z. Hu, X. Xu, T. Yu, and K. Xie, *Nano Energy*, 2020, **78**, 105239.
36. R. Qian, Y. Liu, T. Cheng, P. Li, R. Chen, Y. Lyu, and B. Guo, *ACS Appl. Mater Interfaces*, 2020, **12**, 13813-13823.
37. C. H. Jung, D. H. Kim, D. Eum, K. H. Kim, J. Choi, J. Lee, H. H. Kim, K. Kang, and S. H. Hong, *Adv. Funct. Mater.*, 2021, **31**, 2010095.
38. Q.-Q. Qiu, S.-S. Yuan, J. Bao, Q.-C. Wang, X.-Y. Yue, X.-L. Li, X.-J. Wu, and Y.-N. Zhou, *J. Energy Chem.*, 2021, **61**, 574-581.
39. J. L. Shi, R. Qi, X. D. Zhang, P. F. Wang, W. G. Fu, Y. X. Yin, J. Xu, L. J. Wan, and Y. G. Guo, *ACS Appl. Mater. Interfaces*, 2017, **9**, 42829-42835.
40. G.-T. Park, H.-H. Ryu, T.-C. Noh, G.-C. Kang, and Y.-K. Sun, *Mater. Today*, 2022, **52**, 9-18.
41. W. He, W. Guo, H. Wu, L. Lin, Q. Liu, X. Han, Q. Xie, P. Liu, H. Zheng, L. Wang, X. Yu, and D. L. Peng, *Adv. Mater.*, 2021, **33**, e2005937.
42. X. Ji, Q. Xia, Y. Xu, H. Feng, P. Wang, and Q. Tan, *J. Power Sources*, 2021, **487**, 229362.
43. M. Zhang, D. A. Kitchaev, Z. Lebens-Higgins, J. Vinckeviciute, M. Zuba, P. J. Reeves, C. P. Grey, M. S. Whittingham, L. F. J. Piper, A. Van der Ven, and Y. S. Meng, *Nat. Rev. Mater.*, 2022, **7**, 522-540.
44. M. Li, T. Liu, X. Bi, Z. Chen, K. Amine, C. Zhong, and J. Lu, *Chem. Soc. Rev.*, 2020, **49**, 1688-1705.
45. X. Liu, G.-L. Xu, V. S. C. Kolluru, C. Zhao, Q. Li, X. Zhou, Y. Liu, L. Yin, Z. Zhuo, A. Daali, J.-J. Fan, W. Liu, Y. Ren, W. Xu, J. Deng, I. Hwang, D. Ren, X. Feng, C. Sun, L. Huang, T. Zhou, M. Du, Z. Chen, S.-G. Sun, M. K. Y. Chan, W. Yang, M. Ouyang, and K. Amine, *Nat. Energy*, 2022, **7**, 808-817.
46. W. Hua, S. Wang, M. Knapp, S. J. Leake, A. Senyshyn, C. Richter, M. Yavuz, J. R.

Binder, C. P. Grey, H. Ehrenberg, S. Indris, and B. Schwarz, *Nat. Commun.*, 2019, **10**, 5365.
47. E. Hu, X. Yu, R. Lin, X. Bi, J. Lu, S. Bak, K.-W. Nam, H. L. Xin, C. Jaye, D. A. Fischer, K. Amine, and X.-Q. Yang, *Nat. Energy*, 2018, **3**, 690-698.
48. Z. Zhu, D. Yu, Y. Yang, C. Su, Y. Huang, Y. Dong, I. Waluyo, B. Wang, A. Hunt, X. Yao, J. Lee, W. Xue, and J. Li, *Nat. Energy*, 2019, **4**, 1049-1058.
49. J. Wang, and X. Sun, *Energy Environ. Sci.*, 2015, **8**, 1110-1138.
50. G. Xu, C. Pang, B. Chen, J. Ma, X. Wang, J. Chai, Q. Wang, W. An, X. Zhou, G. Cui, and L. Chen, *Adv. Energy Mater.*, 2017, **8**, 1701398.
51. H. Zhang, Y. Yang, D. Ren, L. Wang, and X. He, *Energy Storage Mater.*, 2021, **36**, 147-170.
52. M. Ge, C. Cao, G. M. Biesold, C. D. Sewell, S. M. Hao, J. Huang, W. Zhang, Y. Lai, and Z. Lin, *Adv. Mater.*, 2021, **33**, e2004577.
53. B. Chen, L. Chen, L. Zu, Y. Feng, Q. Su, C. Zhang, and J. Yang, *Adv. Mater.*, 2022, **34**, e2200894.
54. H. Li, H. Li, Y. Lai, Z. Yang, Q. Yang, Y. Liu, Z. Zheng, Y. Liu, Y. Sun, B. Zhong, Z. Wu, and X. Guo, *Adv. Energy Mater.*, 2022, **12**, 2102181.
55. L. Sun, Y. Liu, R. Shao, J. Wu, R. Jiang, and Z. Jin, *Energy Storage Mater.*, 2022, **46**, 482-502.
56. D. Lin, Y. Liu, and Y. Cui, *Nat. Nanotechnol.*, 2017, **12**, 194-206.
57. J. Liu, Z. Bao, Y. Cui, E. J. Dufek, J. B. Goodenough, P. Khalifah, Q. Li, B. Y. Liaw, P. Liu, A. Manthiram, Y. S. Meng, V. R. Subramanian, M. F. Toney, V. V. Viswanathan, M. S. Whittingham, J. Xiao, W. Xu, J. Yang, X.-Q. Yang, and J.-G. Zhang, *Nat. Energy*, 2019, **4**, 180-186.
58. X. Cao, X. Ren, L. Zou, M. H. Engelhard, W. Huang, H. Wang, B. E. Matthews, H. Lee, C. Niu, B. W. Arey, Y. Cui, C. Wang, J. Xiao, J. Liu, W. Xu, and J.-G. Zhang, *Nat. Energy*, 2019, **4**, 796-805.
59. W. Liu, D. Lin, A. Pei, and Y. Cui, *J. Am. Chem. Soc.*, 2016, **138**, 15443-15450.
60. Y. Sun, N. Liu, and Y. Cui, *Nat. Energy*, 2016, **1**, 16071.
61. L. Xu, J. Li, W. Deng, H. Shuai, S. Li, Z. Xu, J. Li, H. Hou, H. Peng, G. Zou, and X. Ji, *Adv. Energy Mater.*, 2020, **11**, 2000648.
62. J. Xiang, Y. Zhang, B. Zhang, L. Yuan, X. Liu, Z. Cheng, Y. Yang, X. Zhang, Z. Li, Y. Shen, J. Jiang, and Y. Huang, *Energy Environ. Sci.*, 2021, **14**, 3510-3521.
63. H. Zhang, J. Zhang, J. Ma, G. Xu, T. Dong, and G. Cui, *Electrochem. Energy Rev.*, 2019, **2**, 128-148.
64. A. Manthiram, X. Yu, and S. Wang, *Nat. Rev. Mater.*, 2017, **2**, 16103.
65. L. W. Tian, J. W. Kim, S.-B. Hong, H.-H. Ryu, U.-H. Kim, Y.-K. Sun, and D.-W. Kim, *Chem. Eng. J.*, 2022, **450**, 138043.
66. Y. Yu, P. Karayaylali, D. Sokaras, L. Giordano, R. Kou, C.-J. Sun, F. Maglia, R. Jung, F. S. Gittleson, and Y. Shao-Horn, *Energy Environ. Sci.*, 2021, **14**, 2322-2334.
67. E. Hu, Q. Li, X. Wang, F. Meng, J. Liu, J.-N. Zhang, K. Page, W. Xu, L. Gu, R. Xiao, H. Li, X. Huang, L. Chen, W. Yang, X. Yu, and X.-Q. Yang, *Joule*, 2021, **5**, 1-17.
68. Z. Zhang, S. Zhao, B. Wang, and H. Yu, *Cell Rep. Phys. Sci.*, 2020, **1**, 10061.
69. A. Manthiram, *Nat. Commun.*, 2020, **11**, 1550.

70. D. H. Seo, J. Lee, A. Urban, R. Malik, S. Kang, and G. Ceder, *Nat. Chem.*, 2016, **8**, 692-697.
71. M. Ben Yahia, J. Vergnet, M. Saubanere, and M. L. Doublet, *Nat. Mater.*, 2019, **18**, 496-502.
72. G. Assat, and J.-M. Tarascon, *Nat. Energy*, 2018, **3**, 373-386.
73. G. G. Amatucci, J.-M. Tarascon, and L. C. Klein, *J. Electrochem. Soc.*, 1996, **143**, 1114-1123.
74. K. Luo, M. R. Roberts, N. Guerrini, N. Tapia-Ruiz, R. Hao, F. Massel, D. M. Pickup, S. Ramos, Y. S. Liu, J. Guo, A. V. Chadwick, L. C. Duda, and P. G. Bruce, *J. Am. Chem. Soc.*, 2016, **138**, 11211-11218.
75. K. Luo, M. R. Roberts, R. Hao, N. Guerrini, D. M. Pickup, Y. S. Liu, K. Edstrom, J. Guo, A. V. Chadwick, L. C. Duda, and P. G. Bruce, *Nat. Chem.*, 2016, **8**, 684-691.
76. M. Sathiya, G. Rousse, K. Ramesha, C. P. Laisa, H. Vezin, M. T. Sougrati, M. L. Doublet, D. Foix, D. Gonbeau, W. Walker, A. S. Prakash, M. Ben Hassine, L. Dupont, and J. M. Tarascon, *Nat. Mater.*, 2013, **12**, 827-835.
77. M. Sathiya, K. Ramesha, G. Rousse, D. Foix, D. Gonbeau, A. S. Prakash, M. L. Doublet, K. Hemalatha, and J.-M. Tarascon, *Chem. Mater.*, 2013, **25**, 1121-1131.
78. E. McCalla, A. M. Abakumov, M. Saubanère, D. Foix, E. J. Berg, G. Rousse, M.-L. Doublet, D. Gonbeau, P. Novák, G. Van Tendeloo, R. Dominko, and J.-M. Tarascon, *Science*, 2015, **350**, 1516-1521.
79. X. Cao, H. Li, Y. Qiao, M. Jia, X. Li, J. Cabana, and H. Zhou, *Adv. Mater.*, 2021, **33**, e2004280.
80. R. A. House, J.-J. Marie, M. A. Pérez-Osorio, G. J. Rees, E. Boivin, and P. G. Bruce, *Nat. Energy*, 2021, **6**, 781-789.
81. R. A. House, U. Maitra, M. A. Perez-Osorio, J. G. Lozano, L. Jin, J. W. Somerville, L. C. Duda, A. Nag, A. Walters, K. J. Zhou, M. R. Roberts, and P. G. Bruce, *Nature*, 2020, **577**, 502-508.
82. R. A. House, G. J. Rees, M. A. Pérez-Osorio, J.-J. Marie, E. Boivin, A. W. Robertson, A. Nag, M. Garcia-Fernandez, K.-J. Zhou, and P. G. Bruce, *Nat. Energy*, 2020, **5**, 777-785.
83. R. A. House, J. J. Marie, J. Park, G. J. Rees, S. Agrestini, A. Nag, M. Garcia-Fernandez, K. J. Zhou, and P. G. Bruce, *Nat. Commun.*, 2021, **12**, 2975.
84. R. A. House, H. Y. Playford, R. I. Smith, J. Holter, I. Griffiths, K.-J. Zhou, and P. G. Bruce, *Energy Environ. Sci.*, 2022, **15**, 376-383.
85. P. P. Ewald, *Nature*, 1942, **150**, 450-451.
86. G. E. Bacon, *Nature*, 1955, **176**, 895-896.
87. P. K. Allan, J. M. Griffin, A. Darwiche, O. J. Borkiewicz, K. M. Wiaderek, K. W. Chapman, A. J. Morris, P. J. Chupas, L. Monconduit, and C. P. Grey, *J. Am. Chem. Soc.*, 2016, **138**, 2352-2365.
88. J. M. Stratford, A. K. Kleppe, D. S. Keeble, P. A. Chater, S. S. Meysami, C. J. Wright, J. Barker, M. M. Titirici, P. K. Allan, and C. P. Grey, *J. Am. Chem. Soc.*, 2021, **143**, 14274-14286.
89. Y. Yang, H. Su, T. Wu, Y. Jiang, D. Liu, P. Yan, H. Tian, and H. Yu, *Sci. Bull.*, 2019, **64**, 553-561.

90. E. Zhao, M. Zhang, X. Wang, E. Hu, J. Liu, X. Yu, M. Olguin, T. A. Wynn, Y. S. Meng, K. Page, F. Wang, H. Li, X.-Q. Yang, X. Huang, and L. Chen, *Energy Storage Mater.*, 2020, **24**, 384-393.
91. W. Song, M. A. Pérez-Osorio, J.-J. Marie, E. Liberti, X. Luo, C. O'Leary, R. A. House, P. G. Bruce, and P. D. Nellist, *Joule*, 2022, **6**, 1049-1065.
92. H. Liu, C. Zhao, Q. Qiu, B. Hu, F. Geng, J. Li, W. Tong, B. Hu, and C. Li, *J. Phys. Chem. Lett.*, 2021, **12**, 8740-8748.
93. D. Eum, B. Kim, S. J. Kim, H. Park, J. Wu, S. P. Cho, G. Yoon, M. H. Lee, S. K. Jung, W. Yang, W. M. Seong, K. Ku, O. Tamwattana, S. K. Park, I. Hwang, and K. Kang, *Nat. Mater.*, 2020, **19**, 419-427.
94. J. Hong, W. E. Gent, P. Xiao, K. Lim, D. H. Seo, J. Wu, P. M. Csernica, C. J. Takacs, D. Nordlund, C. J. Sun, K. H. Stone, D. Passarello, W. Yang, D. Prendergast, G. Ceder, M. F. Toney, and W. C. Chueh, *Nat. Mater.*, 2019, **18**, 256-265.
95. M. Sathiya, A. M. Abakumov, D. Foix, G. Rousse, K. Ramesha, M. Saubanère, M.-L. Doublet, H. Vezin, C. P. Laisa, A. S. Prakash, D. Gonbeau, G. Van Tendeloo, and J.-M. Tarascon, *Nat. Mater.*, 2015, **14**, 230-238.
96. C. Cui, X. Fan, X. Zhou, J. Chen, Q. Wang, L. Ma, C. Yang, E. Hu, X. Q. Yang, and C. Wang, *J. Am. Chem. Soc.*, 2020, **142**, 8918-8927.
97. K. Nakayama, R. Ishikawa, S. Kobayashi, N. Shibata, and Y. Ikuhara, *Nat. Commun.*, 2020, **11**, 4452.
98. W. Yin, A. Grimaud, G. Rousse, A. M. Abakumov, A. Senyshyn, L. Zhang, S. Trabesinger, A. Iadecola, D. Foix, D. Giaume, and J. M. Tarascon, *Nat. Commun.*, 2020, **11**, 1252.
99. P. Yan, J. Zheng, Z. K. Tang, A. Devaraj, G. Chen, K. Amine, J. G. Zhang, L. M. Liu, and C. Wang, *Nat. Nanotechnol.*, 2019, **14**, 602-608.
100. X. Cao, H. Li, Y. Qiao, P. He, Y. Qian, X. Yue, M. Jia, J. Cabana, and H. Zhou, *Joule*, 2022, **6**, 1-14.
101. F. Ning, B. Li, J. Song, Y. Zuo, H. Shang, Z. Zhao, Z. Yu, W. Chu, K. Zhang, G. Feng, X. Wang, and D. Xia, *Nat. Commun.*, 2020, **11**, 4973.
102. Q. Li, D. Zhou, L. Zhang, D. Ning, Z. Chen, Z. Xu, R. Gao, X. Liu, D. Xie, G. Schumacher, and X. Liu, *Adv. Funct. Mater.*, 2019, **29**, 1806706.
103. X. Ding, D. Luo, J. Cui, H. Xie, Q. Ren, and Z. Lin, *Angew. Chem. Int. Ed.*, 2020, **59**, 7778-7782.
104. Z. Zhu, R. Gao, I. Waluyo, Y. Dong, A. Hunt, J. Lee, and J. Li, *Adv. Energy Mater.*, 2020, **10**, 2001120.
105. B. Zhang, L. Wang, X. Wang, S. Zhou, A. Fu, Y. Yan, Q. Wang, Q. Xie, D. Peng, Y. Qiao, and S.-G. Sun, *Energy Storage Mater.*, 2022, **53**, 492-504.
106. Z. Yang, J. Zhong, J. Feng, J. Li, and F. Kang, *Adv. Funct. Mater.*, 2021, **31**, 2103594.
107. M. Okubo, K. Kawai, Z. Ma, and A. Yamada, *Acc. Mater. Res.*, 2021, **3**, 33-41.
108. K. Kawai, X.-M. Shi, N. Takenaka, J. Jang, B. M. de Boisse, A. Tsuchimoto, D. Asakura, J. Kikkawa, M. Nakayama, M. Okubo, and A. Yamada, *Energy Environ. Sci.*, 2022, **15**, 2591-2600.

CHAPTER 2. EXPERIMENTS AND CHARACTERIZATION TECHNIQUES

This chapter introduces the experimental details and characterization techniques used in this thesis.

2.1. Sample preparation

2.1.1. Synthesis of Li_2RuO_3

Li_2RuO_3 was prepared via a solid-state method. Typically, anhydrous ruthenium dioxide (RuO_2, Sigma-Aldrich, 99.99 %) was mixed with lithium carbonate (Li_2CO_3, Sigma-Aldrich, 99.0 %) in a molar ratio of 1: 1.05. Then, the mixture was ground by hand and annealed in a muffle furnace. The programmed heating process included a water removal step at 350 °C for 3h (5 °C/ min), a burn-in period at 800 °C for 12 h (2 °C/ min), an annealing period at 1000 °C for 12 h (2°C/ min) and a cooling period to 100 °C (2 °C/ min) in air.

2.1.2. Synthesis of F-doped Li_2RuO_3

To prepare $Li_{1.83}RuO_{2.83}F_{0.17}$, stoichiometric amounts of RuO_2, Li_2CO_3 and LiF (Sigma-Aldrich, 99.9 %) were mixed and ground by hand. The mixture was annealed following similar processes as above, and the final annealing temperatures were 800, 900 and 1000 °C. To prepare $Li_{1.95}RuO_{2.95}F_{0.05}$, stoichiometric amounts of RuO_2, Li_2CO_3 and LiF were mixed and ball-milled in acetone. The mixture was dried in vacuum oven at 120 °C for 12 h, transferred into a muffle furnace and annealed at 800, 825, 850, 875, or 900°C for 12 h (2 °C/min), and gradually cooled to 100 °C (2 °C/min).

2.1.3. Synthesis of O3-phase $Li_{1.2}Ni_{0.2}Mn_{0.6}O_2$

The O3-phase $Li_{1.2}Ni_{0.2}Mn_{0.6}O_2$ was prepared via a traditional solid-state reaction. Typically, bimetallic carbonate ($NiMn_3(CO_3)_4$, Hai-An Zhi Chuan Co. Ltd.) was mixed with lithium carbonate (Li_2CO_3, Aladdin) in a molar ratio of 1: 3.09. Then, the mixture was ground by hand and annealed in a muffle furnace. The programmed heating process included a water removal step at 450 °C for 5 h (5 °C/ min), an annealing period at 800 °C for 12 h (2°C/ min) and a cooling period to 100 °C (2 °C/ min) in air.

2.1.4. Synthesis of O6-phase $Li_{0.846}Ni_{0.190}Mn_{0.657}O_2$

Firstly, the P2-type precursor ($Na_{0.745}[Li_{0.153}Ni_{0.19}4Mn_{0.626}]O_2$) was prepared via a solid-state method. Typically, bimetallic carbonate ($NiMn_3(CO_3)_4$, Hai-An Zhi Chuan Co. Ltd.) was mixed with lithium carbonate (Li_2CO_3, Aladdin) and sodium carbonate (Na_2CO_3, Aladdin) in a molar ratio of 2: 1.03: 4.12. Then, the mixture was ground by hand and annealed in a muffle furnace. The programmed heating process includes a water removal step at 450 °C for 5 h (5 °C/ min), an annealing period at 800 °C for 12 h (2°C/ min) and a cooling period to 100 °C (2 °C/ min) in air. The as-prepared P2-type precursor was transferred into the argon-filled glove box for storage.

Via a facile Na^+/Li^+ ion-exchange method, the O2+T2-type $Li_{0.673}[Li_{0.162}Ni_{0.188}Mn_{0.650}]O_2$ was synthesized from the sodium-deficient P2-phase. Typically, the P2-type precursor was mixed with $LiNO_3$ and LiCl in a weight ratio of 1: 8.2: 1.8 and annealed in a muffle furnace at 280 °C for 4 h in air. The as-obtained product was washed thoroughly with

distilled water and dried at 80 °C overnight. To evaluate its thermal stability, the dried O2+T2 mixture was annealed in air at 250, 350, 450, 550, 650, 750, 850, and 950 °C, respectively. Finally, to get the metastable O6-type $Li_{0.693}[Li_{0.153}Ni_{0.190}Mn_{0.657}]O_2$, the dried O2+T2 mixture was annealed at 550 °C for 12 h.

2.1.5. Synthesis of Li_2MnO_3

The Li_2MnO_3 was prepared via a traditional solid-state reaction. Typically, manganese carbonate $MnCO_3$ **(**Hai-An Zhi Chuan Co. Ltd.) was mixed with lithium carbonate (Li_2CO_3, Aladdin) in a molar ratio of 1: 1.05. Then, the mixture was ground by hand and annealed in a muffle furnace. The programmed heating process included a water removal step at 450 °C for 5 h (5 °C/ min), an annealing period at 800 °C for 12 h (2°C/ min) and a cooling period to 100 °C (2 °C/ min) in air.

2.1.6. Synthesis of O6-phase $Li_{1.2}Mn_{0.8}O_2$

The O6-phase $Li_{1.2}Mn_{0.8}O_2$ was prepared in similar ways as introduced in the preparation of the O6-phase $Li_{0.846}Ni_{0.190}Mn_{0.657}O_2$. Firstly, the P2-type precursor was prepared via a solid-state method. Typically, manganese carbonate $MnCO_3$ (Hai-An Zhi Chuan Co. Ltd.) was mixed with lithium carbonate (Li_2CO_3, Aladdin) and sodium carbonate (Na_2CO_3, Aladdin) in a molar ratio of 8: 1.03: 4.12. Then, the mixture was ground by hand and annealed in a muffle furnace. The programmed heating process includes a water removal step at 450 °C for 5 h (5 °C/ min), an annealing period at 800 °C for 12 h (2°C/ min) and a cooling period to 100 °C (2 °C/ min) in air. The as-

prepared P2-type precursor was transferred into the argon-filled glove box for storage. For Na^+/Li^+ ion-exchange, the P2-type precursor was mixed with $LiNO_3$ and LiCl in a weight ratio of 1: 8.2: 1.8 and annealed in a muffle furnace at 280 °C for 4 h in air. The as-obtained product was washed thoroughly with distilled water and dried at 80 °C overnight. Finally, the O6-phase $Li_{1.2}Mn_{0.8}O_2$ was obtained by annealing the ion-exchanged sample at 500 °C for 12 h.

2.2. Routine characterization techniques

2.2.1. X-ray diffraction (XRD)

X-rays, firstly discovered by Roentgen in 1895, are a kind of electromagnetic radiation, whose wavelengths are in the same order with that of the distances between atoms, i.e., 10^{-10} m. Generally, for X-ray diffraction (XRD) experiment, X-rays could be generated in two ways. Traditionally, in the lab X-ray diffractometer, via applying a potential gradient, the electrons produced by the thermionic emission of a tungsten filament are accelerated to hit the target (usually Cu, Mo, etc.). As illustrated in **Figure 2-1a**, the high energy electron beam dislodges the inner shell electrons in the target via inelastic scattering and produces inner shell vacancies. Then, the electrons at higher energy levels fall into the lower energy vacancies, emitting the characteristic X-rays. The energy of the generated X-rays is determined by the type of orbital decay and the target element. Nowadays, thanks to the development of advanced synchrotron radiation facilities, high-coherence and high-flux X-rays could also be generated by the high-speed electron beams accelerated by the magnetic field (**Figure 2-1b**).

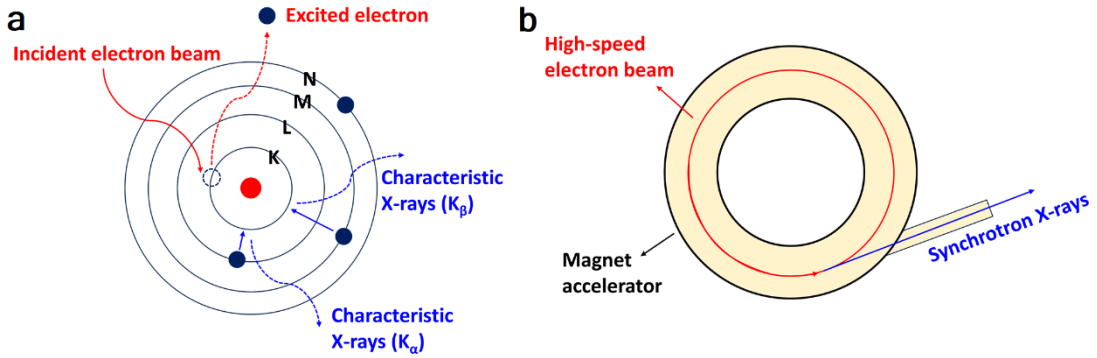


Figure 2-1. Schematic of the generation of X-rays from **(a)** traditional X-ray diffractometers and **(b)** synchrotron light sources.

For XRD tests, no matter generated by the traditional lab X-ray diffractometer or synchrotron light sources, X-rays need to be collimated and monochromatically filtered before being directed to the sample. Generally, XRD relies on the elastic scattering between the incident X-rays and the electron clouds of the atoms. As depicted in **Figure 2-2**, when interacting with the sample, the constructive interference could be achieved at specific angles, i.e., the Bragg's law:[1]

$$2dsin\theta = n\lambda \qquad (2-1)$$

where d is the spacing between different lattice planes, θ is the glancing angle, n is an integer, and λ is the wavelength of the incident X-rays.

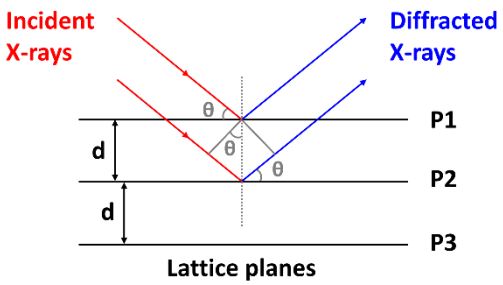


Figure 2-2. Diagram of X-ray diffractions. P1-P3 refer to different lattice planes.

Generally, the diffraction intensity of the hkl plane (I_{hkl}) is determined by types and positions of the scattering atoms via the structure factor (F_{hkl}):

$$F_{hkl} = \sum_j f_j \cdot \exp\left[2i(hx_j + ky_j + lz_j)\right] \qquad (2-2)$$

where x_j, y_j, and z_j describe the position of atom j, and f_j is its scattering factor.

For crystalline samples, the XRD patterns could be indexed to determine space groups of their unit cells and to calculate the lattice parameters. Standard powder diffraction files (PDF) for indexing could be obtained from the International Centre for Diffraction Data (ICDD) and the Inorganic Chemical Structure Database (ICSD). More structural information could be derived via Rietveld refinements.

In this thesis, the XRD tests for the Li_2RuO_3 sample were performed on a D8 X-ray diffractometer (Bruker, Germany), while all the other samples were tested on a Rigaku X-ray diffractometer with a Cu target (Rigaku, Japan). The Cu K_α X-rays (λ = 1.54184 Å) were used as the incident beams with a foil filter to remove the Cu K_β X-rays. Specifically, the Cu K_α X-rays are composed of $K_{\alpha1}$ (λ_1 = 1.54056 Å) and $K_{\alpha2}$ (λ_2 = 1.54439 Å), wherein the former's intensity is twice as that of the latter. For powder samples, they were ground by hand in a mortar and placed flatly into a silicon holder. The PXRD measurements were performed in reflection mode (Bragg-Brentano geometry). Both optic and height calibrations were conducted before every single θ-2θ scan. Commonly, the scanning ranges were between 2θ = 5-90° and the step size was 0.02°. The powder

of O6-phase was also tested on I15-1 at Diamond Light Source (λ = 0.16167 Å) in transmission mode (Debye–Scherrer geometry).

For ex-situ XRD tests, the cycled electrodes were disassembled in the argon protected glove box, washed with dimethyl carbonate (DMC), and naturally dried in argon flow, before being put onto a flat sample stage. Because the electrodes were collected from a series of cells at multiple voltages, they might be different in Z values. As illustrated in **Figure 2-3**, in the typical Bragg-Brentano diffraction geometry, an offset of ΔZ in the sample stage results in a peak shift of Δ2θ in the XRD patterns. Considering the thin thickness (~ 100 μm) and surface curvature of the electrode, proper Z calibration is the prerequisite for further analysis.

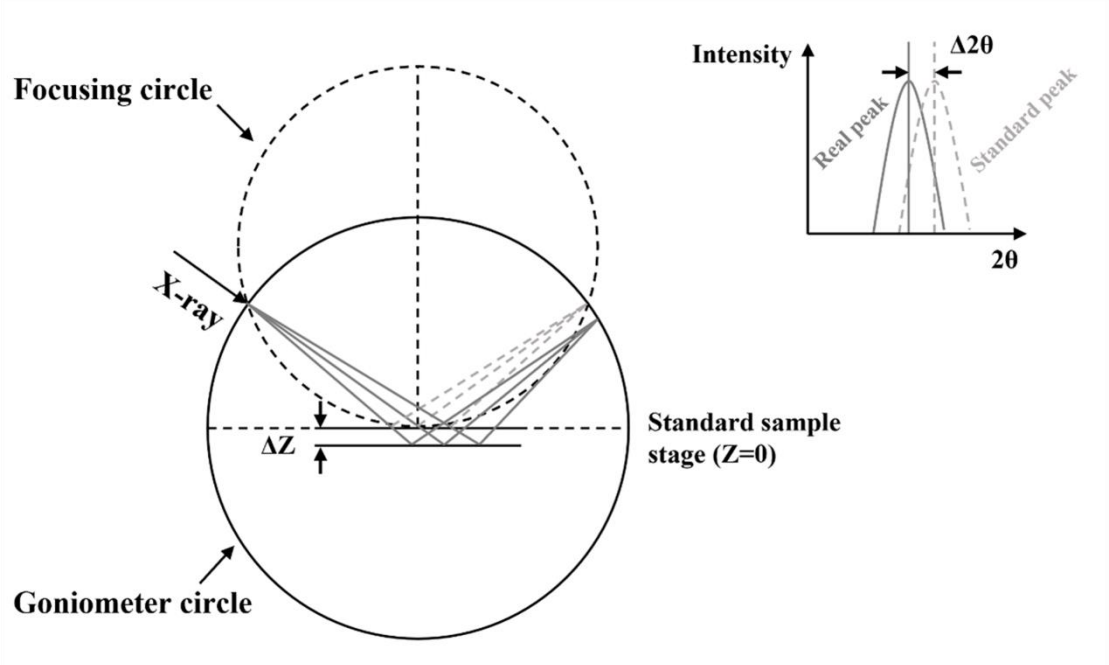


Figure 2-3. Schematic illustration of the Bragg-Brentano diffraction geometry.

To achieve the precise Z calibration, an automatic height calibration was performed before every single XRD test (denoted as the pre-test Z calibration method). Firstly, to

avoid surface curvatures, all electrodes collected from cycled cells were flattened and put on a flat sample stage. Then, as illustrated in **Figure 2-4a**, the incident X-ray was fixed at the position in parallel with the flat sample surface (2θ = 0°). The sample stage was moved down to out of the X-ray pathway and the maximum intensity (I_{max}) was achieved on the detector. Upon moving up the sample stage, the position where the detected intensity was half of the maximum was regarded as the standard position Z_0 (**Figure 2-4b**). The following θ-2θ scanning was done without changing the height. It is noteworthy that the above pre-test Z calibration should be done every time after changing the sample.

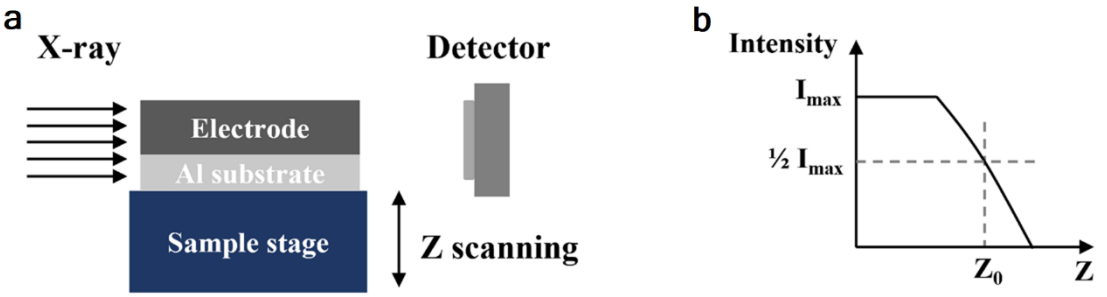


Figure 2-4. Schematic illustration of **(a)** the setup for automatic Z calibration, and **(b)** simulated signals upon Z scanning.

2.2.2. Neutron diffraction (ND)

Neutrons, initially proposed by Rutherford and experimentally proven by Chadwick, have a mass of 1.6749×10^{-27} kg and diameters of around 1.7×10^{-15} m. The mechanism of using neutron diffraction to study the structural information of samples also follows the Bragg's law, as introduced in the X-ray diffraction. However, unlike the elastic scattering between the X-rays and the electron clouds of the atoms in XRD, neutrons are diffracted by the nuclei of the atoms. Therefore, even light atoms could produce

strong scattering, meaning that neutron diffraction has the advantage to decipher the positions of light atoms such as lithium and oxygen. Besides, although neutrons have no net charge, they have magnetic moments with spin because they are composed of charged quarks. Therefore, neutron diffraction has the potential to reveal the microscopic magnetic properties of the samples.[2]

Generally, there are two ways to generate neutrons, namely nuclear fission, and spallation. The first way produces continuous neutron flows, which are extracted and monochromatically filtered before interacting with the samples. Because the wavelength of the neutrons is fixed, the diffraction angle changes during the tests and the neutron diffraction data is usually plotted in the form like that of the XRD patterns (i.e., intensity vs θ/2θ). On the other hand, via nuclear spallation, neutrons are generated by hitting the metal target with high energy protons. Specifically, the negative hydrogen ions (H^-) are accelerated firstly in a linear accelerator (LINAC) and converted to proton beams by passing through a stripping foil, which are accumulated and further accelerated in a rapid cycling synchrotron (RCS) to high-speed (~ 90 % of the speed of light). The high-speed proton beams are then directed out of the RCS by a target beam transfer line to hint the tungsten target, generating pulses of hot neutrons. For neutron diffractions, the as-generated high-energy neutrons need to be cooled down to become thermal or cold neutrons (λ = 0.1-3 Å), whose wavelengths are in the same order with the distances between atoms. Because the pulsed neutron beams consist of neutrons with different wavelengths, the travel time of the neutrons

between the neutron source and the detector varies Therefore, their elastic scattering with the samples is termed as time-of-flight (TOF) neutron diffraction.

In this thesis, TOF neutron diffraction was performed on a multi-purpose neutron reflectometer (BL02) at China Spallation Neutron Source (CSNS). A vanadium can was used to load the powder samples because it hardly scatters neutrons. For every single experiment, the data were collected from seven banks fixed at different angles in the space. The TOF neutron diffraction patterns are plotted in the form of intensity vs d-spacing (d). The d is calculated according to the equation:[3]

$$t = difC \times d + difA \times d^2 + Zero \qquad (2-3)$$

where t is time-of-flight (μs), d is the d-spacing (Å), difC, difA and Zero are instrumental parameters.

2.2.3. Rietveld refinement

Although having XRD or ND patterns of a sample allows the possibility to index its structures in the established crystal databases, the actual structure might be slightly different from the reported ones due to various factors, e.g., synthesis conditions, particle sizes, strain, defects, preferential orientations, etc. Therefore, to obtain a more accurate structure of a crystalline sample, Rietveld refinement is widely used, which is basically a least square method.[4,5] According to the Bragg's law, for a certain lattice plane with the Miller indices (hkl), the distance (d_{hkl}) between two adjacent parallel planes could be calculated if the peak position (2θ) and the wavelength of the incident wave (λ) are known. Therefore, once the symmetry of the unit cell is determined via

indexing, both the size and the shape of the unit cell could be obtained after calculating d-spacings of multiple planes. However, except for the position, other factors of a diffraction peak such as the intensity, the shape, and the full width at half maximum (FWHM) are related to more complicated properties of the sample and need to be analyzed systematically.

Other than the structure factor (F_{hkl}), several other factors also affect the intensity I_{hkl}, following the equation:

$$I_{hkl} = I_0 \cdot \frac{e^4}{m^2c^4} \cdot \frac{\lambda^3}{32\pi R} \cdot \left(\frac{V}{V_0}\right)^2 \cdot |F_{hkl}|^2 \cdot P \cdot \varphi(\theta) \cdot e^{-2M} \cdot A(\theta) \qquad (2-4)$$

where I_0 is the intensity of the incident wave, e is the charge of an electron, m is the mass of an electron, c is the speed of light, λ is the wavelength of the incident wave, R is the radius of the diffractometer, V is the size of the irradiated area on the sample, V_0 is the volume of the unit cell, $|Fhkl|^2$ is the structure amplitude, P is the reflection multiplicity, ϕ(θ) is the Lorentz polarization factor, e^{-2M} is an isotropic correction, and A(θ) is the absorption factor.

The ϕ(θ) could be written as:

$$\varphi(\theta) = \frac{1 + \cos^2(2\theta)}{sin^2(\theta)\cos(\theta)} \qquad (2-5)$$

where the denominator is caused by the non-monochromaticity of the incident wave and the nominator is related to its polarization.

The e^{-2M} could be expressed as:

$$e^{-2M} = e^{-2B(\frac{sin^2(\theta)}{\lambda^2})} = e^{-16\pi^2u^2(\frac{sin^2(\theta)}{\lambda^2})} \qquad (2-6)$$

where B is the atomic displacement parameter and u is the root mean squared displacement. Usually, the atomic vibration around the average position weakens the intensity I_{hkl} and broadens the peak. Such a broadening effect becomes more severe with increasing θ, which explains why the high angle peaks are usually weak for XRD patterns collected in the Bragg-Brentano geometry.

For a single data point i, the calculated intensity $y_{calc,i}$ is a sum of intensities from all lattice planes:

$$y_{calc,i} = \sum_i I_{hkl,i} + b_i \qquad (2-7)$$

where $I_{hkl,i}$ is the intensity at the point i and b_i is the background.

The calculated intensity $y_{calc,i}$ is then compared with the observed intensity $y_{obs,i}$, and a least-squares refinement is done to minimize the difference between them,

$$\Delta = \sum_i w_i(y_{obs,i} - y_{calc,i}(\alpha))^2 \qquad (2-8)$$

where w_i is weight (usually $1/y_{obs,i}$) and α is the parameter to be refined. In practical trials, one or several parameters are selected at once for least-squares refinements to reduce the residual difference (Δ). During those processes, the profile R factor (R_p) and the weighted profile R factor (R_{wp} or wR_p) are monitored.

$$R_p = \frac{\sum_i |y_{obs,i} - y_{calc,i}(\alpha)|}{\sum_i y_{obs,i}} \qquad (2-9)$$

$$R_{wp} = \sqrt{\frac{\sum_i w_i (y_{obs,i} - y_{calc,i}(\alpha))^2}{\sum_i w_i (y_{obs,i})^2}} \qquad (2-10)$$

The expected weighted profile R factor (R_{exp}) is also calculated:

$$R_{exp} = \sqrt{\frac{n-p}{\sum_i w_i (y_{obs,i})^2}} \qquad (2-11)$$

where n is number of data points and p is the number of parameters.

The quality of a refinement is usually evaluated by the goodness of fit (GOF, χ), and the value of χ should close to 1 for a good refinement.[6]

$$\chi = \frac{R_{wp}}{R_{exp}} = \sqrt{\frac{\sum_i w_i (y_{obs,i} - y_{calc,i}(\alpha))^2}{n-p}} \qquad (2-12)$$

In this thesis, Rietveld refinements were performed by using GSAS-EXPGUI and GSAS-II software.[7,8] Instrumental parameters of the lab X-ray diffractometer were obtained by refining a standard Si sample and used as the initial values for further refinements. Instrumental parameters of the spallation neutron source were obtained from the beamline scientist and were fixed during the refinements. The initial structure files were obtained from crystal databases or built by using VESTA based on previous reports. For all samples, the roughness, absorption, and micro-strain were not refined; the preferential orientations were refined by using spherical harmonics. For multi-phase samples, the fractions of different phases were refined.

2.2.4. Scanning electron microscope (SEM)

Electrons, originally discovered by Thomson in 1897, are negatively charged (q=1.602 × 10^{-19} C) and have a mass of 9.1096 × 10^{-31} kg. When interacting with the samples, the incident electrons could either transmit through the atoms or be elastically scattered by the atoms, producing transmitted electrons (**Figure 2-5a**) and backscattered electrons (**Figure 2-5b**), respectively. In both scenarios, the energy of the electrons is unchanged. On the other hand, the incident electrons could collide with and excite the outer shell electrons, producing secondary electrons (**Figure 2-5c**).

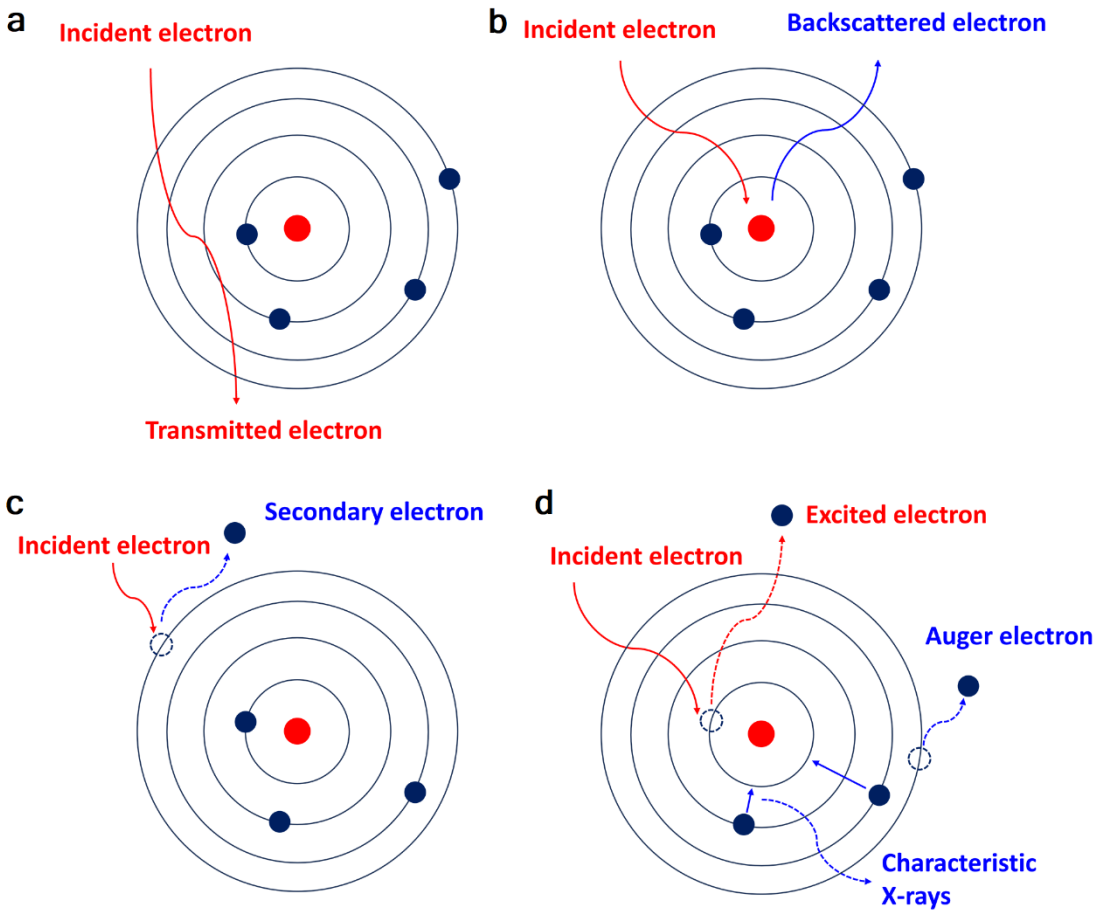


Figure 2-5. Schematic of the productions of **(a)** the transmitted electron, **(b)** the backscattered electron, **(c)** the secondary electron, and **(d)** the characteristic X-rays and Auger electron.

In addition, as mentioned above, once the inner shell electrons are dislodged, the high energy electrons naturally drop down to lower energy vacancies, producing characteristic X-rays to keep the energy balance. Alternatively, such an energy difference could free the outer shell electrons and emit Auger electrons (**Figure 2-5d**).

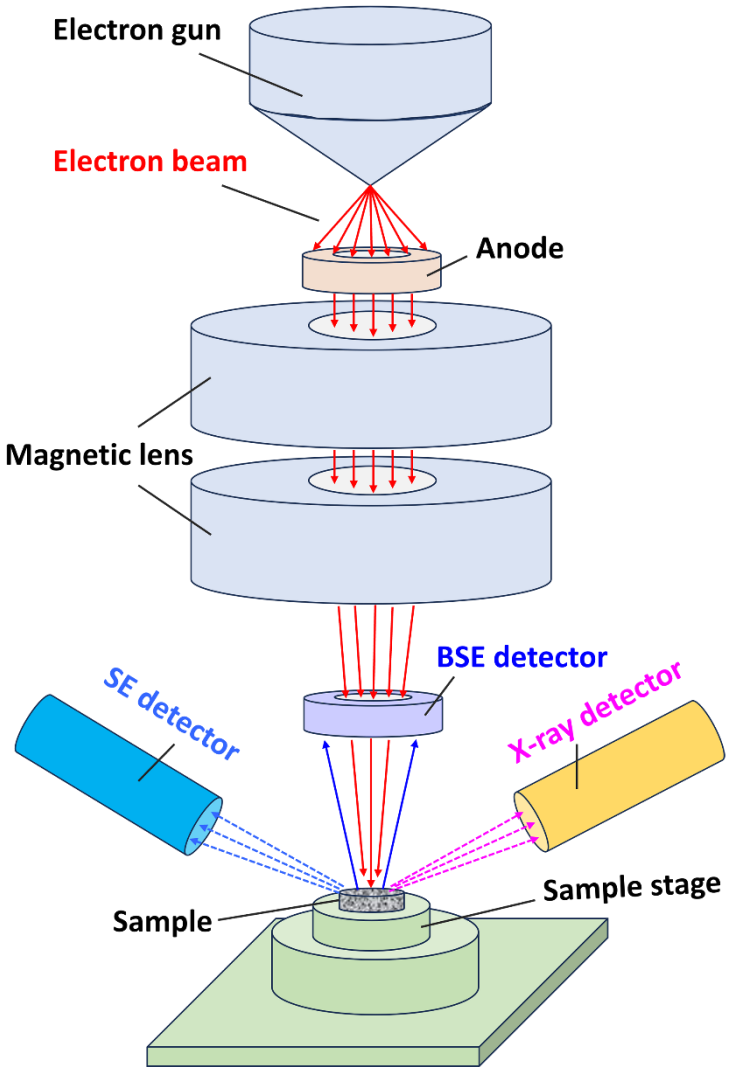


Figure 2-6. Schematic of scanning electron microscope (SEM).

As illustrated in **Figure 2-6**, in a typical scanning electron microscope (SEM), the electrons are used as the probe to scan over the surface of the sample in a regular manner. The incident electrons could be thermally emitted from tungsten or

lanthanum hexaboride (LaB_6) wires or via a field emission (FE) gun. The as-generated electron beams are accelerated in the vacuum chamber by the applied potential field, focused by the magnetic lens (condenser) and directed to scan the sample. After interacting with the sample, both the secondary electrons and the backscattered electrons carry information about the surface morphology of the sample, which therefore are collected by the detectors to produces SEM images. Given that the inelastic scattering also generates electromagnetic radiation (i.e., characteristic X-rays), SEM is usually equipped with an X-ray detector, which allows elemental analysis of the sample, also known as energy dispersive X-ray spectroscopy (EDX).

In this thesis, SEM analyses were performed on a TESCAN MIRA 3 with the accelerating voltages in the range of 15-30 kV. The secondary electrons were mainly used for imaging. The powder samples were put onto conductive tapes and stuck on the aluminum sample stage before transferring into the vacuum chamber. Alternatively, the samples were dispersed in ethanol, dropped onto silicon substrates, and vacuum dried, before being attached to the sample stage for test. No sputtering was used to deposit conductive layers on the samples.

2.2.5. Transmission electron microscope (TEM)

In a typical transmission electron microscope (TEM), the interactions between the incident electrons and the samples are no different from those in the SEM. Specifically, as illustrated in **Figure 2-7**, the emitted electrons are accelerated and focused by a

potential field and a magnetic lens (condenser) to hit the sample, like the process in SEM. The difference is that the transmitted electrons are used for imaging. After passing through the objective lens, a real intermediate image is produced, which is then magnified and projected by the projector lens onto the detector, e.g., a charge-coupled device (CCD) camera or a fluorescent screen.

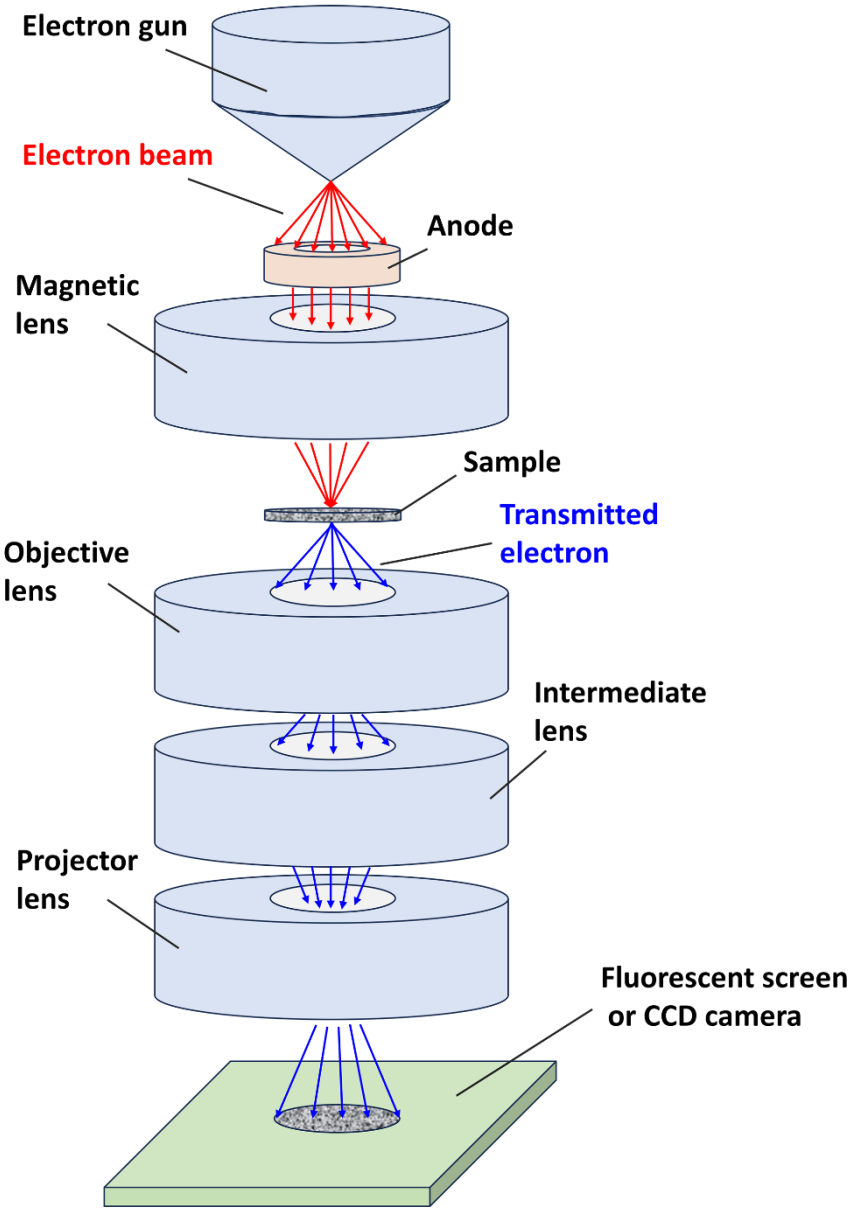


Figure 2-7. Schematic of transmission electron microscope (TEM).

Because higher accelerating voltages are usually used in TEM, the electron beams with shorter wavelengths could produce high-resolution (sub-angstrom) images, meaning that TEM is an ideal tool to study local patterns, defects, interfaces, grain boundaries, etc. The high-resolution transmission electron microscope (HR-TEM) and the scanning transmission electron microscope (STEM) could even resolve the positions of groups of atoms. Similarly, TEM is usually equipped with an EDX detector, which allows the analysis of the elemental compositions. Besides, selected-area electron diffraction (SAED) is available in TEM, during which the electrons are focused onto a small area of the sample and the diffracted patterns are recorded. For single crystals, the SAED patterns could be used to study the crystallography of the sample via indexing the dots in the reciprocal space (Fourier space).

In this thesis, TEM and EDX tests for the Li_2RuO_3 and F-doped Li_2RuO_3 samples were performed on Talos F200X (Thermo-Fisher) with an accelerating voltage of 200 kV. STEM and EDX tests for the O6-type samples were carried out on Titan Themis G2 (FEI) with an accelerating voltage of 300 kV. The powder samples were dispersed in ethanol and ultra-sonicated for several minutes. Then, several droplets of the dispersion were dropped on the TEM grid (Cu mesh) and vacuum dried before being transferred into the vacuum chamber for TEM test. No mechanical grinding was involved during the sample preparation. All TEM and STEM images were saved in Gatan EMD files, which were used to produce SAED patterns via Fast Fourier transform (FFT) by using the Gatan software.

2.2.6. X-ray photoelectron spectroscopy (XPS)

X-ray photoelectron spectroscopy (XPS) is widely used to characterize compositions of sample surfaces and the binding environments of different elements in subsurface areas (~ 10 nm). The principal theory for XPS tests is the photoelectric effect proposed by Einstein in 1905. As illustrated in **Figure 2-8**, when being directed onto samples, X-rays could not only be elastically scattered by the electron clouds of the atoms (i.e., XRD) but also collide with the electrons. If the energy of the incident X-rays is high enough to excite the inner shell electrons to the vacuum level, the electrons could escape from the atoms to become photoelectrons. It is noteworthy that once the inner shell electrons are excited, the outer shell electrons could drop into the lower energy vacancies, during such a process, the released energy could either be emitted in the form of X-ray fluorescence or excite the outer shell electrons to produce Auger electrons. In a typical XPS test, both the photoelectrons and the Auger electrons are detected.[9]

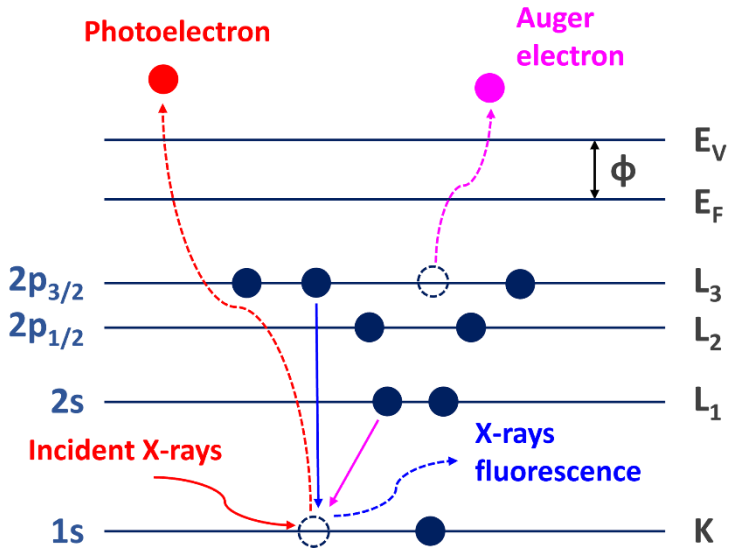


Figure 2-8. Interaction between incident X-rays and core-level electrons.

Generally, the binding energy (E_b) of the inner shell electrons could be obtained following the equation,

$$E_b = E_{hv} - E_k - \varphi \qquad (2-13)$$

where E_{hv} is the energy of the incident X-rays, E_k is the kinetic energy of the photoelectrons, and ϕ is the constant work function, i.e., the energy difference between the Fermi level (E_F) and the vacuum level (E_V). Both the kinetic energies (E_k) and the counts of the photoelectrons are measurable by using a hemispherical sector analyzer and an electron detector, meaning that both qualitative and semi-quantitative analyses of the binding energies are available in XPS.

Considering that the binding energy of the electron is identical to the electron orbital (e.g., s, p, d, and f) in a specific element, it could be used to analyze the chemical environments around the element, e.g., valence states, coordination, electronic structures, etc. Because of the spin-orbit splitting, all orbitals in core-levels other than the s orbitals split into doublets, meaning that XPS spectra of p, d, or f orbitals have two peaks at different binding energies. Specifically, the XPS spectra of p-levels split into $p_{1/2}$ and $p_{3/2}$ peaks in the area ratio of 1: 2; the XPS spectra of d-levels split into $d_{3/2}$ and $d_{5/2}$ peaks in the area ratio of 2: 3; the XPS spectra of f-levels split into $f_{5/2}$ and $f_{7/2}$ peaks in the area ratio of 3: 4.

In this thesis, XPS tests were carried out on a PHI5300 X-ray photoelectron spectrometer using Mg K_α radiation (E_{hv} = 1253.4 eV, 250 W, 14 kV). For all powder

samples, they were put onto conductive tapes/ indium foils and stuck on the aluminum sample stage before transferring into the vacuum chamber. To prepare samples for ex-situ XPS tests, the electrodes were dis-/charged to different voltages and maintained at corresponding voltages for 30 min in coin cells, before being disassembled in the argon protected glove box, washed with dimethyl carbonate (DMC), and naturally dried in argon flow. The obtained electrodes were put onto conductive tape, stuck on the aluminum sample stage, and vacuum transferred to chambers for XPS tests. To get depth profiling XPS spectra of the O6-type electrodes, they were etched by Ar^+ beam for 0, 10, 20, 30, 40 and 50 s, respectively. The etching speed was estimated to be around 0.2 nm/s.

For each sample, a scan of the full XPS spectrum was first performed in the survey mode in the range of 0-1100 eV. Thereafter, a detailed scan was done to get fine structures of specific peaks. The National Institute of Standards and Technology (NIST) XPS database could be used to initially identify the as-obtained spectra. All raw XPS data were calibrated based on the C 1s peak (284.8 eV). After that, the backgrounds were subtracted with linear/ Shirley functions and the spectra were deconvoluted into multiple peaks with Gaussian-Lorentzian curves by using Avantage or XPSPEAK41 software. Specifically, when fitting the p XPS spectra, the energy differences between the $p_{1/2}$ and $p_{3/2}$ peaks were set to be the same for a specific element in different valences. The area ratio between the former and the latter was fixed at 1: 2. The full width at half maximum (FWHM) for the split peaks was equivalent to each other.

2.2.7. X-ray absorption spectroscopy (XAS)

X-ray absorption spectroscopy (XAS) is a technique to measure the property of samples to absorb X-rays of different energies, commonly available in advanced synchrotron X-ray facilities. As shown in **Figure 2-9**, for a typical X-ray absorption fine structure (XAFS) obtained by XAS test, it is composed of two parts, namely the X-ray absorption near-edge structure (XANES) and the extended X-ray absorption fine structure (EXAFS).

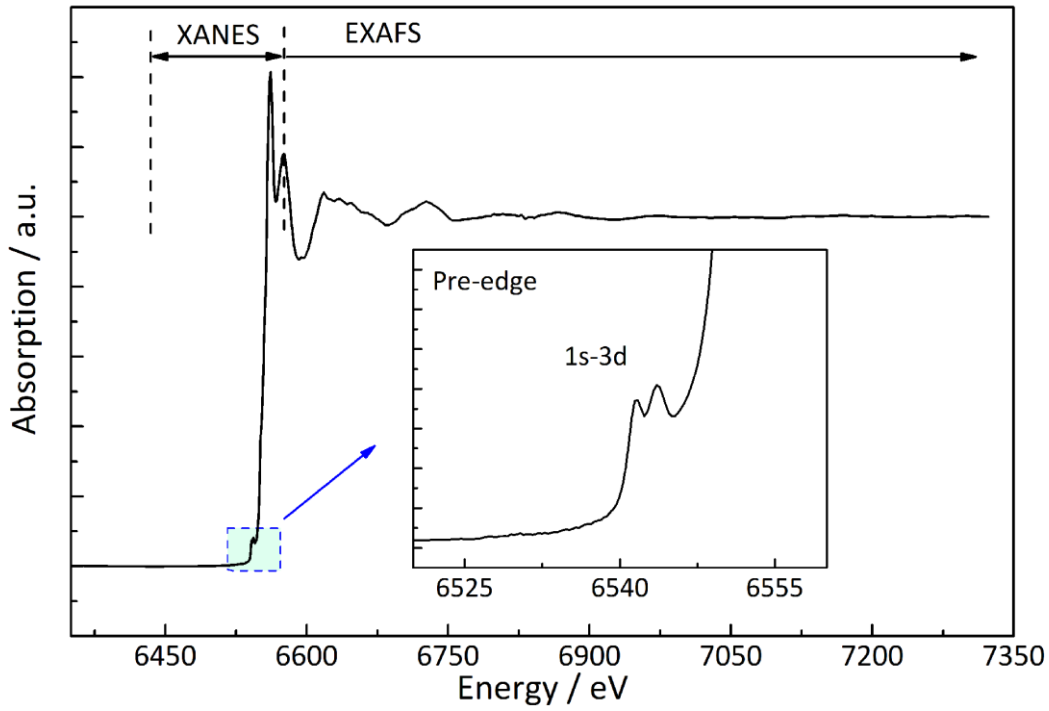


Figure 2-9. A typical XAS spectra with XANES and EXAFS results (Mn K-edge absorption spectra collected at BL11B, SSRF). The inset shows the enlarged image of the pre-edge peaks.

When interacting with a sample, the energy of the incident X-rays could be absorbed by its inner shell electrons. The absorption follows the equation:

$$I_1 = I_0 \cdot e^{-\mu t} \qquad (2-14)$$

where I_0 is the incident intensity, I_1 is the exiting intensity, t is the thickness of the sample, μ is the x-ray absorption coefficient. The value of μ is related to properties of the sample and varies with the energy of the incident X-rays.

Once the energy matches with the ionization energy of the core electrons in a certain shell, the absorption increases sharply, known as an absorption edge. Besides, after absorbing the energy of the incident X-rays, the inner shell electrons could not only be excited to be become free photoelectrons but also be excited to vacancies in higher energy shells. Therefore, even at energies lower than that of the edge (i.e., pre-edge regions), absorption peaks might appear (e.g., the 1s-to-3d jump in 3d transition metals). Generally, in the pre-edge and edge regions, the XANES is sensitive to the oxidation state of the absorbing atom in the sample. In addition to the absorption -related features revealed by XANES, in the post-edge regions (i.e., energies higher than that of the edge), the photoelectrons could be scattered by the neighboring atoms, resulting in oscillations in the absorption spectrum, known as EXAFS. The EXAFS could reveal the coordination between the absorbing atom and the neighboring atoms (e.g., bond distances, species of the neighbors).[10]

In this thesis, all XAS tests were conducted at Shanghai Synchrotron Radiation Facility (SSRF). All raw data were processed (normalization and energy calibration) by using Athena software and only XANES results were analyzed. For ex-situ O K-edge XAS tests of Li_2RuO_3, they were performed on a soft X-ray beamline (BL02U) with a scanning

energy range of 300-1000 eV. To prepare the samples, the electrodes were dis-/charged to different voltages and maintained at corresponding voltages for 30 min in coin cells, before being disassembled in the argon protected glove box, washed with dimethyl carbonate (DMC), and naturally dried in argon flow. The obtained electrodes were pressed on to indium foils, stuck on the aluminum sample stage and transferred into the vacuum chambers.

For ex-situ Ni/Mn K-edge XAS tests of O6-type materials, they were performed on a hard X-ray beamline (BL11B) with scanning energy ranges of 6200-6900 eV for Mn and 8000-8700 eV for Ni. To prepare the samples, the electrodes were disassembled from coin cells in similar ways as above mentioned. However, because the hard X-ray experiments were performed in the transmission mode, laminations with materials of interest needed to be peeled off from the aluminum substrates, sandwiched by X-ray transparent Kapton tapes, and put in the path of the X-rays. For powder samples, they were directly sandwiched in Kapton tapes for tests.

2.2.8. Raman spectroscopy

With light as the probe, Raman spectroscopy is a technique to measure vibrations of chemical bonds in a sample. At temperatures higher than absolute zero (0 K), atoms in any materials move all the time rather than stay in fixed positions. Therefore, chemical bonds vibrate constantly, while their vibration frequencies are determined by many factors such types of the bonds and the local coordination chemistry.

Generally, vibrational energies of chemical bonds are at the same level with the energy of visible light. Therefore, in the light-matter interaction, the energy of the incident photons could be absorbed to excite the bond vibrations from the ground state to the virtual state (**Figure 2-10**). The virtual state is unstable and quickly relaxes back to the ground state, emitting photons in the same energy with the incident ones, known as elastic scattering or Rayleigh scattering. On the other hand, the light might be inelastically scattered, and the released photons gain or lose energies during the relaxation, known as Raman scattering. There are two types of Raman scattering. Firstly, vibrations at the ground state are excited to the virtual state, which then relax to the excited state via emitting photons in energies lower than the original ones, i.e., Stokes Raman scattering. Inversely, the released photons might have higher energies if the incident photons are absorbed by vibrations at the excited state and the relaxation makes them fall back to the ground state, i.e., anti-Stokes Raman scattering. Stokes and anti-Stokes Raman spectra are identical in term of the energy. Yet, because most vibrations are in the ground state at room temperatures, Stokes scattering is dominant and is mainly measured in practical tests.

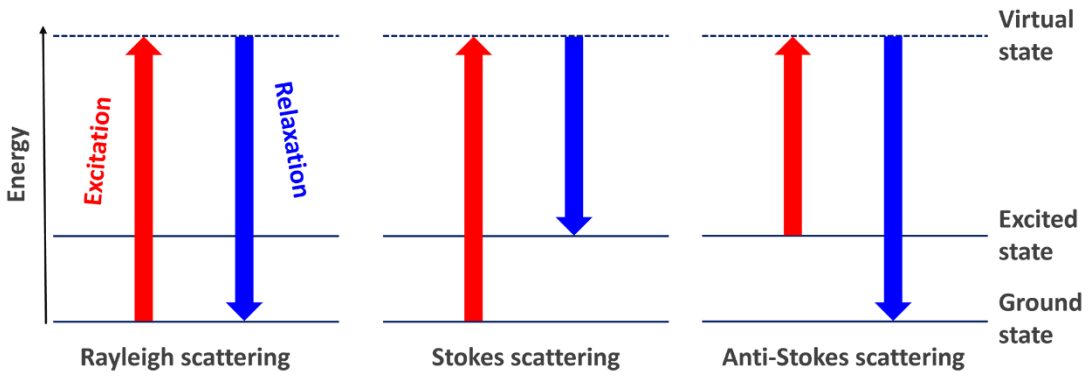


Figure 2-10. Schematic of Rayleigh, Stokes, and anti-Stokes scatterings.

In Raman spectroscopy, wavelengths of both the incident light and the Raman scattered light are measurable, thereby allowing the calculation of their frequency differences according to the equation:

$$\Delta v = \frac{1}{\lambda_0} - \frac{1}{\lambda_{Stokes}} \qquad (2-15)$$

where λ_0 and λ_{Stokes} are wavelengths of the incident light and the Stokes scatted light, respectively. Such frequency shifts, widely termed as Raman shifts, are unique to the vibrational modes and types of the bonds, thereby allowing them to be used as characteristic fingerprints to figure out chemical and structural details of the sample. In solid state materials, thanks to its high sensitivity to lattice vibrations, Raman spectroscopy is an ideal tool to investigate short-range patterns and local coordination evolutions.

In this thesis, Raman tests were performed on an inVia Raman spectrometer (Renishaw, UK) with multiple solid-state lasers (532 nm, 633 nm, and 785 nm). For powder samples, they were put onto a glass substrate and fixed on the multi-axis translation stage. For ex-situ Raman tests, the cycled electrodes were dissembled from coin cells and pre-treated as introduced in previous sections before being transferred onto the sample stage. For each test, the chosen laser was focused onto sample surfaces with the help of an affiliated optical microscope. Raman signals were collected in a reflective mode. Instrumental calibration was performed by using a single-crystal Si plate, during which the Si-Si vibrational peak was calibrated to 520 cm^{-1}. The power of the laser, the exposure time and the accumulation times were modified to avoid

sample damage and to get good signal-to-noise ratio spectra. If not specified, a green laser (532 nm) was used, and the scanning range was 100-3000 cm^{-1}. All raw spectra were used without data processing expect for the one of Li_2RuO_3 powder. The Raman spectrum of the Li_2RuO_3 powder sample was fitted by using the LabSpec software.

2.2.9. Electron paramagnetic resonance (EPR) spectroscopy

Electron paramagnetic resonance (EPR) is a technique that detects the unpaired electrons in paramagnetic species, also known as electron spin resonance (ESR). EPR is a powerful tool to investigate electronic properties of paramagnetic substances because it provides direct evidence of the presence of unpaired electrons and information about the local environments around them. When an external magnetic field is applied, the unpaired electrons could either orient in parallel or antiparallel with the magnetic field, creating two energy states (i.e., E_α and E_β), known as the Zeeman effect (**Figure 2-11**).[11]

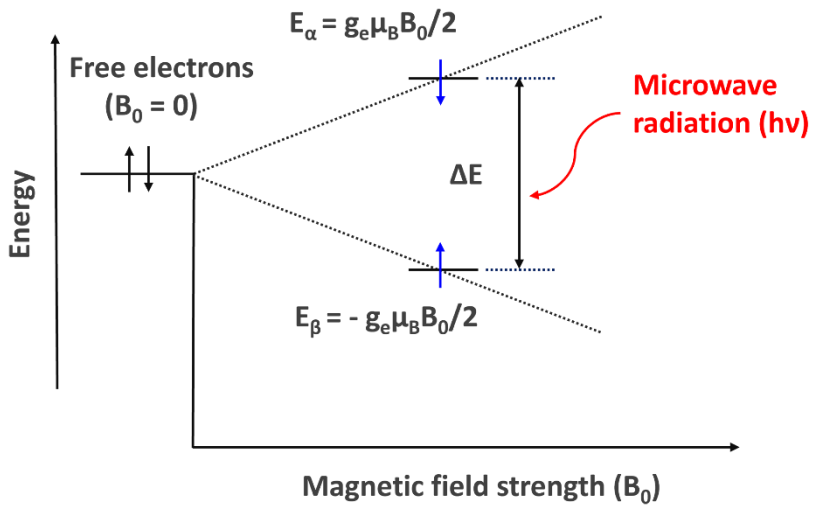


Figure 2-11. Diagram of the split of spin energy states.

The energy difference (ΔE) between the split states follows the equation:

$$\Delta E = E_{\alpha} - E_{\beta} = g_e \mu_B B_0 \qquad (2-16)$$

where g_e is the g-factor, μB is the Bohr magneton, and B_0 is the strength of the magnetic field. Via absorbing energy from the electromagnetic radiation (hv), the electron in the lower energy state could be excited to the higher energy state, during which the spin flips. The energy required for such an electron spin transition is at the same level with that of the microwave. Therefore, in a typical EPR test, a microwave is applied on the sample and the absorption spectrum is collected.

When the energy of the microwave matches with the energy for the electron spin transition, an absorption peak appears in the spectrum. Usually, the 1st derivative of the absorption spectrum is used as the EPR spectrum for easier interpretation. In real tests, either the magnetic field or the microwave is fixed, while the rest one changes to satisfy the resonance condition (ΔE = hv).

In this thesis, continuous wave (CW)-EPR tests were performed on an EMX-plus 10/12 spectrometer of the X-band (Bruker, Germany). Typically, the frequency of the incident microwave was fixed, and the strength of the magnetic field was changed in a range across the absorption peak. To prepare ex-situ EPR samples, the cycled electrodes were dissembled from coin cells and pre-treated in similar ways as above mentioned. Laminations with active materials were peeled off from aluminum foils, weighed, transferred into paramagnetic tubes, sealed tightly in an argon protected glove box,

and put into the resonant cavity. All EPR spectra were normalized by the mass of the active material.

2.2.10. Inductively coupled plasms-mass spectroscopy (ICP-MS)

Inductively coupled plasms-mass spectroscopy (ICP-MS) is a technique designed for trace elemental analysis of solutions. In the typical test, the sample solution is pumped and dispersed into small droplets, which are then introduced in to the ICP source and ionized into a beam of charged and neutral particles. Thereafter, the positive ions are separated and directed into the mass spectrometer equipped with a quadrupole filter for mass analysis. Basically, ions with selected m/z ratios are transmitted by the mass spectrometer and collected by a detector. Because different ions have different m/z ratios, the ICP-MS results could quantitively reveal the amounts of multiple elements in the solution.[12]

In this thesis, ICP-MS tests were performed on ICP-MS 7700 X (Agilent, USA). All solid samples were ultrasonically digested in HNO_3 and diluted in deionized (DI) water. For every element of interest, its concentration in the final diluted solution for ICP-MS tests was in the range of 10 to 1000 ppb (μg/L). Standard solutions were prepared by diluting the mother solutions (purchased from Agilent) with 2 % HNO_3, consisting of gradient concentrations of 0, 10, 20, 50, 100, 200, 500, 1000 ppb.

2.2.11. Thermogravimetric analysis-differential scanning calorimetry (TGA-DSC)

Thermogravimetric analysis (TGA) measures the weight loss of a sample upon being heated, while differential scanning calorimetry (DSC) detects the change of differential heat flow between the sample of interest and the reference sample. In this thesis, TGA-DSC tests were performed on a NETZSCH STA449 F3 Thermal Analyzer. The sample (~10 mg) was placed in an alumina pan and another alumina pan was used as the reference sample. Typically, the heating rate was 5 °C/min and the atmosphere was nitrogen.

2.3. Electrochemical evaluations

2.3.1. Electrode preparation

The as-prepared materials, carbon black and polyvinylidene fluoride (PVDF) in the weight ratio of 8: 1: 1 were mixed homogeneously in N-methyl pyrrolidone (NMP) by using Thinky for 15 min. The as-obtained slurry was then coated uniformly on an aluminum foil (12 μm in thickness) with a doctor blade (150 μm in thickness). The as-prepared laminate (electrode materials on the Al foil) was vacuum dried at 80°C for 12 h before being cut into pieces (1.2 cm in diameter) for coin cell assembly.

2.3.2. Electrolyte

The commercial electrolyte was purchased from Canrd (Guangdong, China). It is a solution of 1 M $LiPF_6$ in ethylene carbonate (EC)/ dimethyl carbonate (DMC) binary solvent (1:1 in volume). The all-fluorinated electrolyte was self-made in the argon-filled glove box. Typically, it is a solution of 1 M $LiPF_6$ (Battery grade, Innochem) in a

mixture of fluoroethylene carbonate (FEC, Innochem), 3,3,3-fluoroethylmethyl carbonate (FEMC, Macklin), and 1,1,2,2-tetrafluoroethyl-2′,2′,2′-trifluoroethyl ether (HFE, Innochem) (2:6:2 in volume) with the additive of 2 wt% lithium difluoro(oxalato)borate (LiDFOB, Macklin).

2.3.3. Coin cell assembly

CR2016-type coin cells were assembled in an argon-filled glovebox by using the as-prepared electrodes (cathode, ~50 μm in thickness), lithium metal plates (anode, 200 μm in thickness) and Celgard membranes (separator, 25 μm in thickness). The areal mass loading of active material is around 2.0 mg/ cm^2. The amount of electrolyte injected for each coin-cell was around 40 μL in volume.

2.3.4. General electrochemical tests

Electrochemical tests including galvanostatic charge-discharge (GCD) tests, cyclic voltammetry (CV) and electrochemical impedance spectroscopy (EIS) were performed on a Biologic electrochemical workstation (VMP3). To evaluate evolution of resistance upon de-/lithiation, in-situ EIS results of the O6-type electrode were collected at different potentials during the initial 5 cycles. Typically, before EIS test, the electrode was charged or discharged to a specific potential and rested for 30 min to stabilize the open circuit voltage (OCV). The as-obtained Nyquist plots were fitted by using ZView 4. Long time cycling and rate performance were tested on the Neware battery cycler (CT-4008-5V-10mA-164, Shenzhen, China). All tests were performed at 25 °C.

2.3.5. Galvanostatic intermittent titration technique (GITT)

GITT tests were performed on a Biologic electrochemical workstation. As shown in **Figure 2-12**, each step in GITT consists of a current pulse (10 min) to break the equilibrium state (from E_0 to E_1) and a relaxation (3 h) to reach the new equilibrium state (E_2). Here, nanoparticles are simplified to spherical models and the Li^+ diffusion coefficient (D, cm^2/s) could be calculated according to the following equation derived from the one reported by Weppner and Huggins:[13]

$$D = \frac{4}{\pi\tau}\left(\frac{R_S}{3}\right)^2\left(\frac{\Delta E_S}{\Delta E_t}\right)^2 \qquad \tau << L^2/D \qquad (2-17)$$

where R_s (cm) represents the diameter of a spherical particle, τ (s) is the duration of current pulse (600 s), ΔE_t (V) is the potential change after one pulse excluding the iR drop (V), ΔE_s (V) is the potential change after relaxation and L (cm) is the diffusion length.

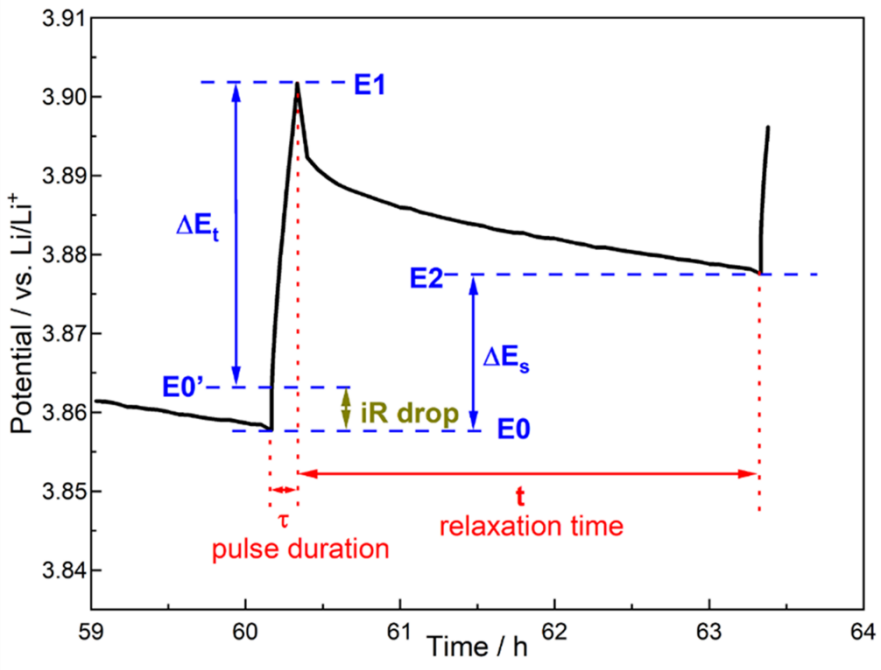


Figure 2-12. Diagram of GITT.

2.4. In-situ characterization techniques

2.4.1. In-situ XRD

An in-situ cell was made to perform in-situ XRD tests, whose configuration is shown in **Figure 2-13**. Specifically, to prepare the electrodes for in-situ tests, the active materials, carbon black and polyvinylidene fluoride (PVDF) in the weight ratio of 8: 1: 1 were mixed homogeneously in N-methyl pyrrolidone (NMP) and coated on directly on aluminum or beryllium foils. The mass of the active materials was calculated by weighing the foils before and after coating. The as-prepared electrodes, lithium metal plates (anode, 200 μm in thickness) and Celgard membranes (separator, 25 μm in thickness) were assembled in an argon-filled glovebox. The electrolyte was 1 M $LiPF_6$ in EC/DMC (1:1 in volume) and the amount of electrolyte injected was around 100 μL.

All in-situ XRD tests were carried out on a Rigaku X-ray diffractometer with a Cu target (Rigaku, Japan), in which the Cu K_α X-rays (λ = 1.54184 Å) were used as the incident beams with a foil filter to remove the Cu K_β X-rays. In a typical in-situ XRD test, the diffraction patterns were collected in the Bragg-Brentano geometry. Before the first scan, the height of the in-situ cell was calibrated in similar ways as above mentioned, which was an indispensable process to get reliable results. Thereafter, during the entire in-situ test, no further Z calibration was needed because the height of the electrode was unchanged. The electrochemical performance of the in-situ cell was evaluated on a battery tester (Land-CT, Wuhan, China) via GCD tests. Commonly, the scanning ranges were between 2θ = 10-90° and the step size was 0.02°.

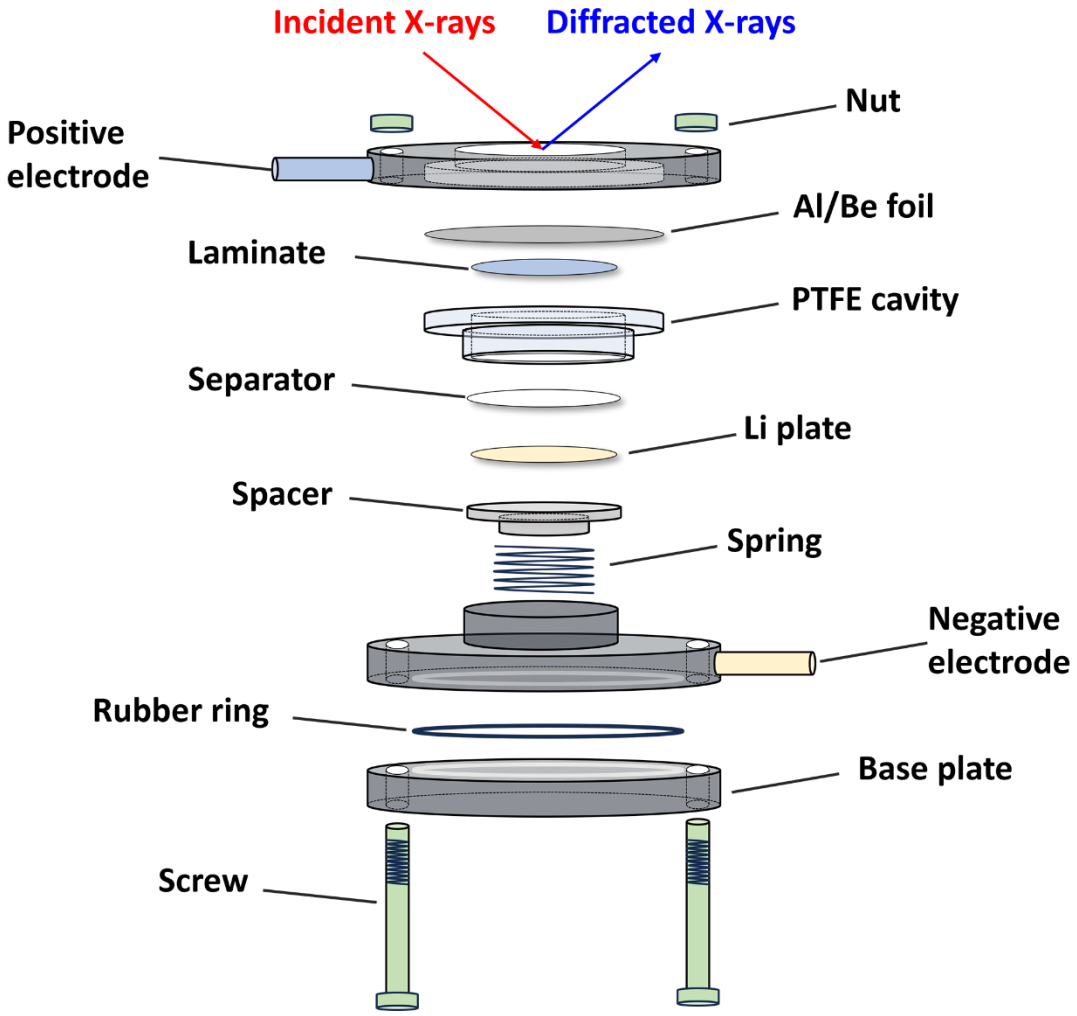


Figure 2-13. Exploded view of the in-situ cell for XRD tests.

2.4.2. In-situ Raman

The in-situ cell used for in-situ Raman tests was adapted from conventional coin cells, while a glass window was attached on the base for light penetration, as shown in **Figure 2-14**. Generally, the electrode preparation and the cell assembly were in no difference with those in making coin cells for ordinary electrochemical tests. However, both the Li plate and the separator were punched to form holes, so that the incident light could reach and interact with the electrode-of-interest.

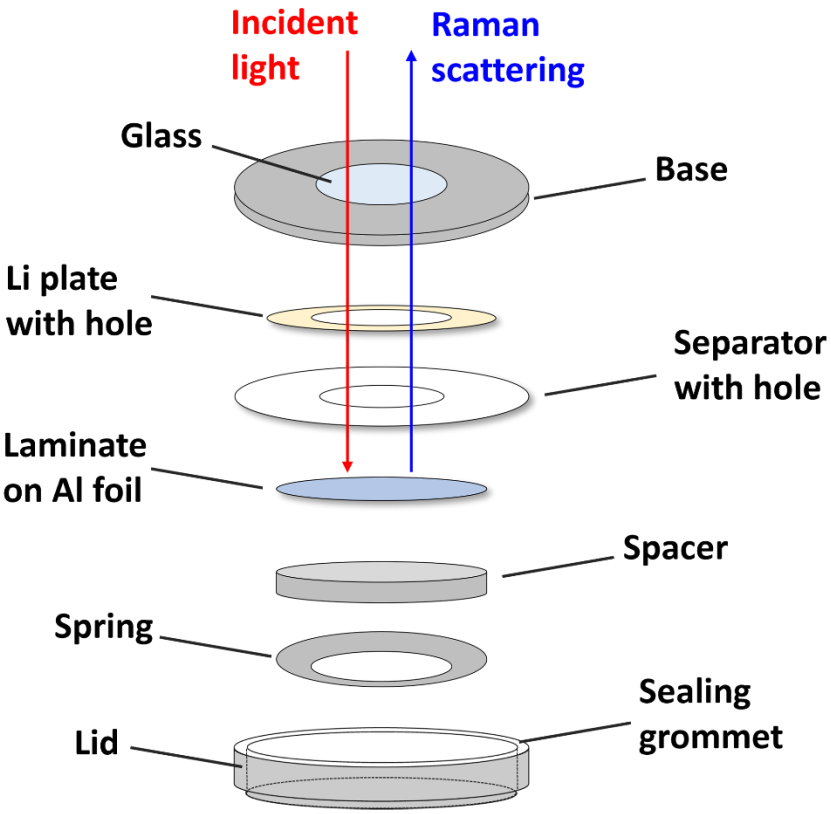


Figure 2-14. Exploded view of the in-situ cell for Raman tests.

To avoid possible damage caused by the laser, the power of the laser and the exposure time were chosen deliberately upon multiple trials. It is noteworthy that even the same sample presents different tolerance towards different lasers. Also, fluorescence is another thing should be considered for in-situ Raman tests because strong fluorescence could induce very broad peaks and make the background subtraction difficult. The fluorescence might come from different components in the in-situ cell (e.g., the electrode and the electrolyte), which are usually sensitive to different lasers. Therefore, the choice of laser for in-situ Raman tests should be considered case by case. Herein, the green laser (532 nm) was used for all in-situ Raman tests. Typically, for a single Raman spectrum, the exposure time was 10 s, the accumulation time was

10, and the scanning range was 100-2000 cm^{-1}. The corresponding electrochemical performance of the in-situ cell was recorded by using an electrochemical workstation (CHI660E, Shanghai, China). For data processing, the very sharp lines from the cosmic radiation were extruded automatically by the software of the Raman spectrometer. Background subtraction and fitting were done on LabSpec or Origin software.

2.5. References

1. W. L. Bragg, *Proc. Cambr. Phil. Soc.*, 1917, **17**, 43-57.
2. S. Mühlbauer, D. Honecker, E. A. Périgo, F. Berger, S. Disch, A. Heinemann, S. Erokhin, D. Berkov, C. Leighton, M. R. Eskildsen, and A. Michels, *Rev. Mod. Phys.*, 2019, **91**, 015004.
3. N. C. Popa, and B. T. M. Willis, *Acta Cryst.*, 1994, **A50**, 57-63.
4. H. Rietveld, *J. Appl. Cryst.*, 1969, **2**, 65-71.
5. J. A. Kaduk, S. J. L. Billinge, R. E. Dinnebier, N. Henderson, I. Madsen, R. Černý, M. Leoni, L. Lutterotti, S. Thakral, and D. Chateigner, *Nat. Rev. Methods Primers*, 2021, **1**, 77.
6. B. H. Toby, *Powder Diffr.*, 2006, **21**, 67-70.
7. B. H. Toby, *J. Appl. Cryst.*, 2001, **34**, 210-213.
8. B. H. Toby, and R. B. Von Dreele, *J. Appl. Cryst.*, 2013, **46**, 544-549.
9. C. S. Fadley, *J. Electron. Spectrosc.,* 2010, **32**, 178-179.
10. J. J. Rehr, and R. C. Albers, *Rev. Mod. Phys.*, 2000, **72**, 621.
11. P. Zeeman, *Phil. Mag.*, 1897, **43**, 226-239.
12. T. V. Acker, S. Theiner, E. Bolea-Fernandez, F. Vanhaeche, and G. Koellensperger, *Nat. Rev. Methods Primers*, 2023, **3**, 52.
13. W. Weppner, and R. A. Huggins, *J. Electrochem. Soc.*, 1977, **124**, 1569-1578.

CHAPTER 3. MONITORING THE LOCAL COORDINATION EVOLUTIONS IN LITHIUM RUTHENATE VIA IN-SITU RAMAN SPECTROSCOPY

Although consensus has been reached that the lattice oxygen (O^{2-}) could be ultimately oxidized to molecular O_2 in lithium rich cathode materials (LRCMs), monitoring the local coordination evolutions around oxygen in real-time is still demanding. In this chapter, we demonstrate the potential of using in-situ Raman spectroscopy to decipher the local environment changes upon de/ lithiation in the archetypal Li_2RuO_3. Evolutions of both the Ru-Ru motions and the Ru-O vibrations have been captured by in-situ Raman tests and interpreted in combination with multimodal characterizations.

3.1. Introduction

Lithium ruthenate (Li_2RuO_3), firstly synthesized by Dulac in 1970,[1] was reported to have a monoclinic structure (C2/c), in which 1/3 of Ru sites in the Ru layers are occupied by Li ions to form the ordered honeycomb-like patterns ($LiRu_6$). However, it was until nearly two decades later that Li_2RuO_3 was revisited due to the period enthusiasm of finding suitable layered oxides for lithium de-/ intercalation. In 1988, James and Goodenough confirmed the structure proposed by Dulac and indicated that Li_2RuO_3 was paramagnetic via magnetic susceptibility tests.[2] Also, they tentatively tried to test its electrochemical properties, yet the de-lithiated phases showed poor crystallinity for structural analysis.

Later in 1995, Kobayashi et al firstly investigated the structural evolutions of Li_2RuO_3 upon electrochemical de-lithiation.[3,4] According to XRD patterns, they proposed that the pristine monoclinic phase (Li_2RuO_3, C2/c) transformed into the rhombohedral phase ($Li_{1.0}RuO_3$, R-3) via a distorted monoclinic intermediate ($Li_{1.3}RuO_3$, C2/c), during which the arrangement of oxygen arrays changed from the cubic close packing (ccp) to the hexagonal close packing (hcp). However, because of the limit of the electrolyte back in that time, the Li_2RuO_3 electrode was only charged to 4.0 V vs. Li/Li^+, roughly corresponding to the extraction of half Li^+ (i.e., the 1^{st} Li^+).

Again, during the following two decades, although there were several trials to improve its electrochemical performance via doping or surface coating,[5-7] Li_2RuO_3 was generally out of the interest of electrochemists. Luckily, physicists were persistently interested in its magnetic properties and their efforts enriched the knowledge about it.[8,9] Remarkably, in 2007, via neutron diffraction patterns, Miura et al discovered that the bond lengths of two of the six Ru-Ru pairs in the $LiRu_6$ hexagon could reduce to form unique Ru-Ru dimers, thereby suggesting that it was more accurate to use a $P2_1/m$ phase to describe the structure of Li_2RuO_3.[10] In the following two years, theoretical calculations revealed that the Ru-Ru dimerization was induced by the formation of the Ru-Ru molecular orbit,[11-13] which actually had been predicted by James and Goodenough twenty years previously.[2] Such a statement was supported experimentally by later pair distribution function (PDF) analysis and ^{17}O and ^{7}Li nuclear magnetic resonance (NMR) results.[14,15]

Finally, in 2010s, along with the development of high-voltage electrolyte and the intense research interest in LRCMs, Li_2RuO_3 regained the spotlight as the cathode material for lithium-ion batteries and soon became an archetypal model to investigate the underlying mechanisms of the oxygen redox activities.

Sathiya et al pioneered this round of investigation and thoroughly studied both the Ru and O redox activities in the pristine Li_2RuO_3 and a series of transition metal (TM) doped $Li_2Ru_{1-y}TM_yO_3$ (TM = Mn, Sn and Ti, $0.2 \leq y \leq 0.8$).[16-18] Specifically, via multimodal characterization techniques, such as ex-situ XPS and ex-situ EPR spectroscopy, they demonstrated that the Ru^{4+}-to-Ru^{5+} oxidation was responsible for the charge compensation during removing the 1st Li^+ to form $Li_{1.0}RuO_3$. On the contrary, during the extraction of the 2nd Li^+, electrons were extracted from the lattice oxygen (O^{2-}), and the oxidized oxygen (O^-) tended to dimerize to form super-/peroxide like species (O_2^{n-}, $0 < n \leq 2$), witnessed by the higher binding energy in O 1s XPS spectra and the CaO_2-type signals in EPR spectra for the deeply de-lithiated samples. Therefore, they proposed that the reversible reactions between O^{2-} and O_2^{n-} dimers contributed to the extra capacities beyond the Ru redox reactions (i.e., 164 mAh/g for the Ru^{4+}-to-Ru^{5+} oxidation). Such processes were also suggested in theoretical calculations by Yu et al.[19,20]

However, via the operando differential electrochemical mass spectrometry (DEMS)

tests, Sathiya et al also detected the release of gaseous O_2 during the final stage of the charging process, probably indicating that the lattice O^{2-} could be oxidized ultimately to molecular O_2. Later, the formation of O_2 molecules was proven to be a bulk activity via high-resolution resonant inelastic X-ray scattering (RIXS) tests by House et al.[21]

Although pioneering work has largely enriched our knowledge about the hidden mechanisms underneath the oxygen redox activities in Li_2RuO_3, monitoring the local structure evolutions around the lattice oxygen in real time is challenging. For instance, most of the above-mentioned techniques require rigorous experimental conditions, making them difficult to be performed in situ, e.g., EPR requires low temperature to get high signal-to-noise ratio and RIXS using soft X-rays needs high vacuum chambers.

In this chapter, we demonstrate the use of in-situ Raman spectroscopy to decipher the local coordination evolutions upon both cation and anion redox activities in the archetypal Li_2RuO_3. Firstly, because of the unique Ru-Ru dimerization in Li_2RuO_3, it presents Raman active Ru-Ru motions in the region of 150-300 cm^{-1}. The evolutions of such Ru-Ru dimers have been monitored and interpreted in combination with multiple structural and chemical characterizations including in-situ/ ex-situ X-ray diffraction (XRD), ex-situ XPS, ex-situ XAS, Rietveld refinements, and electrochemical experiments. Moreover, we have captured the emergence of a Raman band at around 500 cm^{-1} upon triggering the oxygen redox activities, which is suggested to originate from the Ru-O_2^{n-} ($0 < n < 4$) coordination and could be regarded as the indicator of O-O dimerization.

Accordingly, a general picture about the redox activities in Li_2RuO_3 has been drawn, which is consistent with present theories, thereby manifesting the capability of the Raman spectroscopy to study local environment changes under electrochemical conditions.

3.2. Physical characterization of Li_2RuO_3

The Li_2RuO_3 used in this chapter was prepared via a solid-state reaction, as detailed in Chapter 2. **Figure 3-1** shows the morphology of the as-prepared material. Generally, it is composed of polyhedrons with smooth surfaces and sizes of several micrometers.

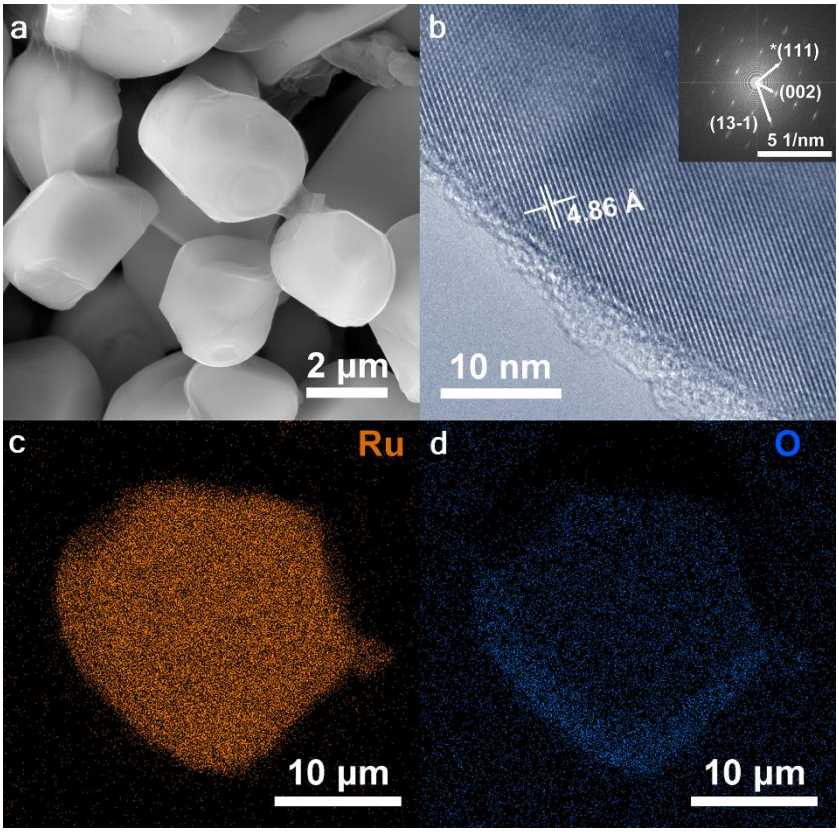


Figure 3-1. Morphology of Li_2RuO_3. **(a)** SEM image. The scale bar is 2 μm. **(b)** TEM image. The scale bar is 10 nm. The inset is the SAED patterns with a scale bar of 5 1/nm. EDX mappings of **(c)** Ru, and **(d)** O. The scale bars are 10 μm.

The TEM image reveals its layered structure, while the interlayer spacing is measured to be 4.86 Å. The SAED patterns indicate that it is a single crystal whose diffraction spots can be indexed to a monoclinic phase (C2/c). The EDX mappings show that both Ru and O disperse uniformly within a single particle.

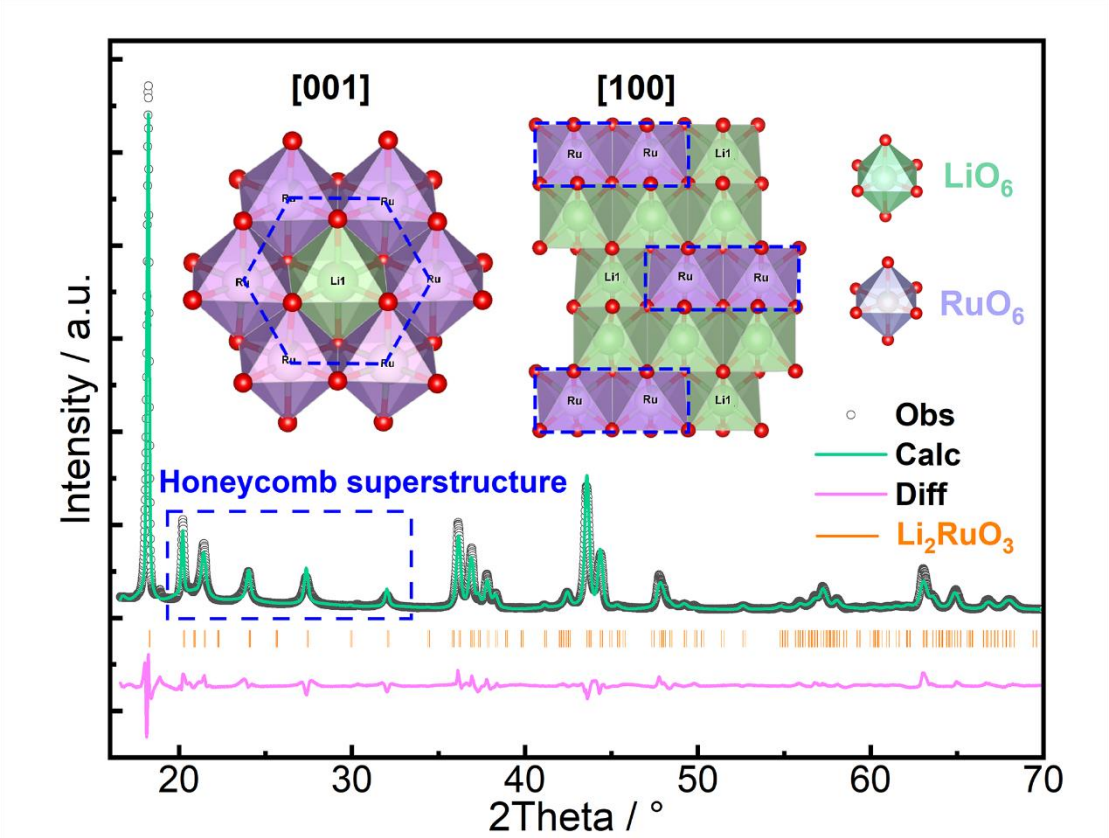


Figure 3-2. XRD patterns and Rietveld refinement results of Li_2RuO_3 (C2/c symmetry). The inset shows the stacking arrangements of RuO_6 and LiO_6 octahedra in the *ab*-plane ([001] projection) and in the *bc*-plane ([100] projection).

The as-prepared material was further indexed to the monoclinic Li_2RuO_3 (C2/c) according to its XRD patterns. As shown in **Figure 3-2**, the sharp peak at 2θ = 18.2° (Cu K_α, λ=1.54 Å) represents the typical (002) peak, and peaks in the region of 2θ = 20-35° are attributed to the honeycomb-like superstructure (e.g., *(020), *(11-1) and *(111) at 20.2°, 21.4°, and 24.0°, respectively). It is noteworthy that both the interlayer Li/Ru

mixing (4e/8f sites, ~4 %) and the intralayer Li/Ru mixing (4d/8f sites, ~7 %) were considered (details in **Table 3-1**). The inset of **Figure 3-2** displays the typical structure of Li_2RuO_3 in the C2/c symmetry. Generally, it has ordered $LiRu_6$ patterns within the basal plane (*ab*-plane), which follows a (0, 1/2, 1/2) stacking displacement along the *c*-axis.

Table 3-1. Structural parameters of pristine Li_2RuO_3 - C2/c symmetry

Phase: Li_2RuO_3	**Space group: C2/c**				
Atom	Fractional coordinates			Wyckoff symbol	Occupancy
	x	y	z		
Li1	0.25	0.25	0.50	4d	0.86
Ru1	0.25	0.25	0.50	4d	0.14
Li2	0	0.07	0.25	4e	0.96
Ru2	0	0.07	0.25	4e	0.04
Li3	0	0.4034(8)	0.25	4e	1.00
Ru3	0	0.4034(8)	0.25	4e	0.00
Li4	0	0.7345(1)	0.25	4e	0.96
Ru4	0	0.7345(1)	0.25	4e	0.04
Ru5	0.2400(6)	0.7937(7)	-0.0026(8)	8f	0.90
Li5	0.2400(6)	0.7937(7)	-0.0026(8)	8f	0.10
O1	0.135(1)	0.2508(1)	0.118(1)	8f	1.00
O2	0.1223(1)	0.5768(1)	0.120(1)	8f	1.00
O3	0.118(1)	0.907(1)	0.118(1)	8f	1.00

Lattice parameters:

a=4.95060(22) Å, b=8.77370(32) Å, c=9.87665(21) Å; α=90°, β=100.035(4)°, γ=90°;

$V_{unit\ cell}$=422.430(27) $Å^3$, R_p=7.18 %, R_{wp}=9.31 %, χ^2=91.34.

For comparison, Rietveld refinement with the $P2_1/m$ symmetry was also performed. As shown in **Table 3-2** and **Figure 3-3**, although such a model fits well with the experimental XRD patterns, the goodness of fitting does not improve significantly. Therefore, as above mentioned, given that both the C2/c and the $P2_1/m$ symmetries had been widely adopted to depict its structure, the former was selected for structural analyses in the following part of this chapter.

Table 3-2. Structural parameters of pristine Li_2RuO_3 - $P2_1/m$ symmetry

Phase: Li_2RuO_3	**Space group: $P2_1/m$**				
Atom	Fractional coordinates			Wyckoff symbol	Occupancy
	x	y	z		
Li1	0.7334(5)	0.25	0.9594(5)	2	0.86
Ru1	0.7334(5)	0.25	0.9594(5)	2	0.14
Li2	0.2193(3)	0.0654(3)	0.4593(3)	4	0.96
Ru2	0.2193(3)	0.0654(3)	0.4593(3)	4	0.04
Li3	0.772(1)	0.25	0.513(1)	2	0.96
Ru3	0.772(1)	0.25	0.513(1)	2	0.04
Li4	0.2671(2)	0.0768(7)	0.9911(8)	4	0.1
Ru4	0.2671(2)	0.0768(7)	0.9911(8)	4	0.9
O1	0.7621(9)	0.0526(9)	0.2650(4)	4	1.00
O2	0.8008(8)	0.1043(4)	0.7709(9)	4	1.00
O3	0.3004(1)	0.25	0.229(1)	2	1.00
O4	0.2295(8)	0.25	0.7506(9)	2	1.00
Lattice parameters: a=4.94247(20) Å, b=8.76095(35) Å, c=5.88840(28) Å; α=90°, β=124.4379(27)°, γ=90°; $V_{unit\ cell}$=210.286(17) $Å^3$, Rp=6.26 %, Rwp=8.36 %, χ2=73.91					

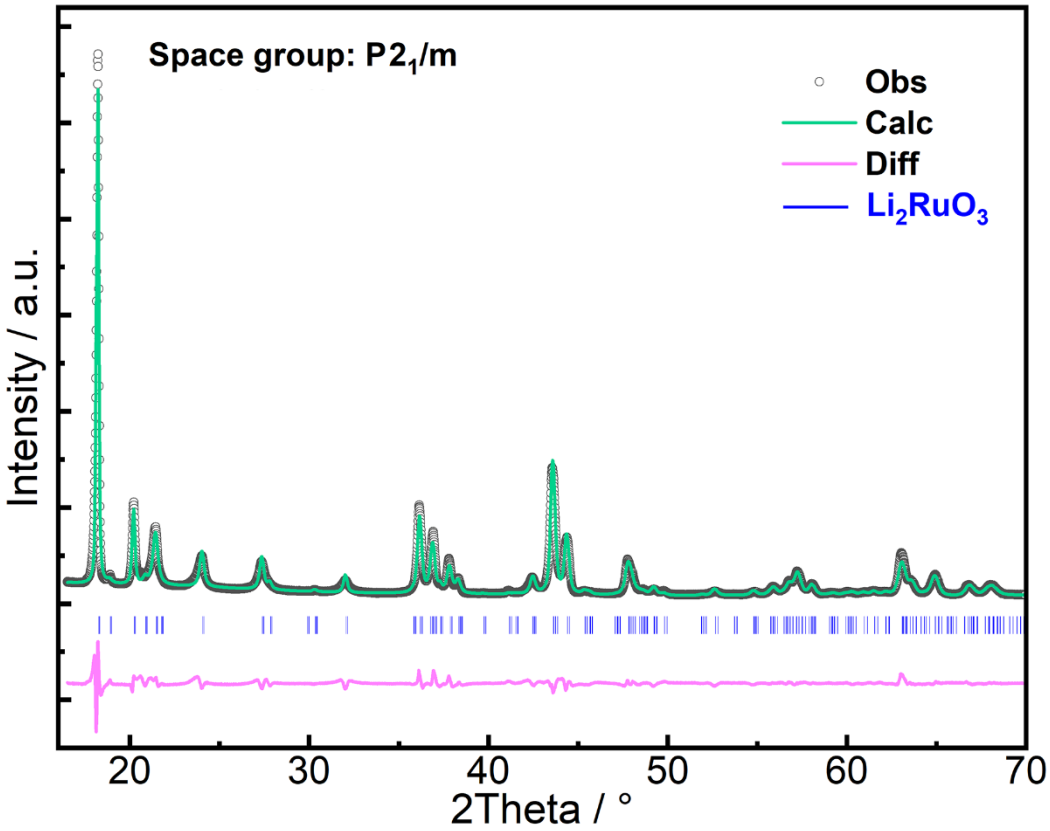


Figure 3-3. XRD patterns and Rietveld refinement results of Li_2RuO_3 ($P2_1/m$ symmetry).

Figure 3-4 exhibits the Raman spectrum of the powder Li_2RuO_3. The unique Ru-Ru dimerization results in Raman active Ru-Ru motions (peaks in the range of 150-350 cm^{-1}), which are absent in its counterpart Li_2MnO_3 (C2/m phase) because it has no Mn-Mn dimers.[22] According to its experimental and theoretical Raman spectrum reported by Ponosov et al,[23,24] the sharp Raman peaks at around 188.6 cm^{-1} and 250.7 cm^{-1} represent the in-plane (*ab*-plane) vibration modes, while small peaks at around 220.3 cm^{-1} and 325.3 cm^{-1} belong to the out-of-plane motions, which are weak because the fully occupied Li layers hinder their vibrations along the *c*-axis. **Figure 3-5** schematically illustrates the Raman active motions of the Ru-Ru dimers.

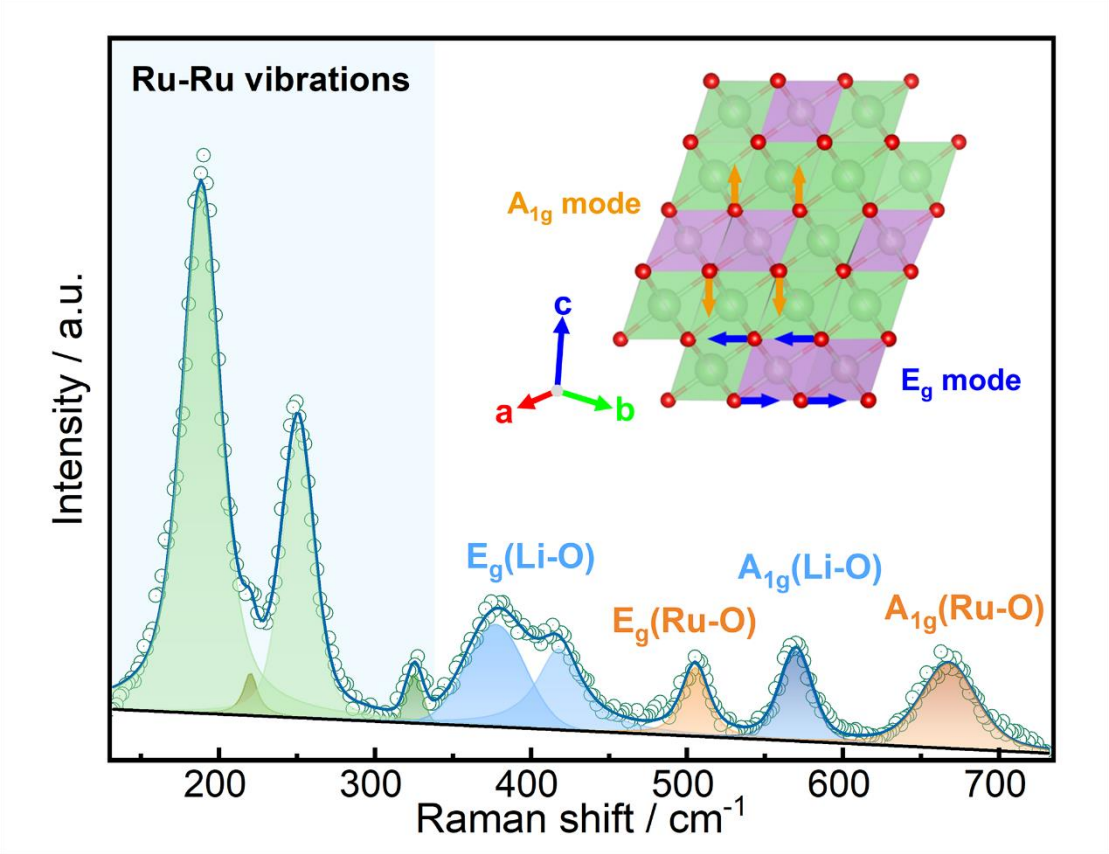


Figure 3-4. Raman spectrum of the powder Li_2RuO_3. The inset depicts two major Raman modes in the layered metal oxides, wherein the E_g mode and the A_{1g} mode represent an opposite motion of oxygens along adjacent O-layers (blue arrows) and a symmetrical movement of oxygen along the *c*-axis (orange arrows), respectively.

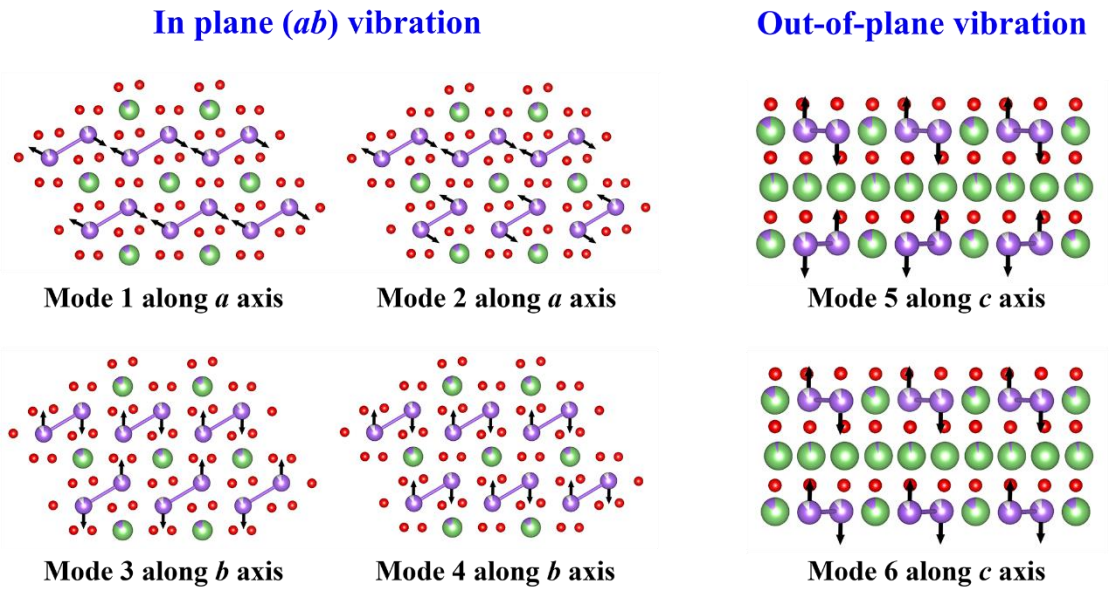


Figure 3-5. Schematic Raman active motions of the Ru-Ru dimers.

In the range of 350-750 cm^{-1}, Raman peaks at 505.3 cm^{-1} and 667.8 cm^{-1} are signatures of the symmetric deformation (E_g) and the symmetric stretching (A_{1g}) of the Ru-O bonding, respectively (inset of **Figure 3-4**). Peaks at 377.5 cm^{-1}, 418.2 cm^{-1} and 567.8 cm^{-1} arise from the Li-O vibrations in the $LiRu_6$ honeycomb patterns, widely seen in lithium rich layered oxides.[25,26]

3.3. General electrochemical properties of Li_2RuO_3

When tested as the cathode material in coin cells, the Li_2RuO_3 electrode presents electrochemical properties as similar to those previously reported.[27,28] Specifically, three pairs of redox peaks (i.e., 3.59/ 3.33 V, 3.70/ 3.40 V, and 4.30/ 4.0 V vs. Li/Li^+) in the 1st cyclic voltammetry (CV) curves (0.05 mV/s, 2.0 - 4.5 V vs. Li/Li^+), suggesting three main stages during de-/lithiation (**Figure 3-6a**). Correspondingly, the 1st charging profile contains a slope at around 3.5 V, a plateau at 3.67 V and a slope above 3.9 V vs. Li/Li^+ (**Figure 3-6b**).

Based on capacity calculations, the first two processes (< 3.9 V vs. Li/Li^+) result from the removal of the 1st Li^+, while the final one (> 3.9 V vs. Li/Li^+) is related to the extraction of the 2nd Li^+. In discharge, the Li_2RuO_3 electrode delivers an initial capacity of 224 mAh/g (20 mA/g, 2.0 - 4.5 V vs. Li/Li^+), which is higher than the theoretical capacity solely upon the Ru redox activities (Ru^{4+}-to-Ru^{5+}, 164 mAh/g), and the extra capacity is thought to be contributed by the oxygen redox reactions.[29] In the following cycles, the slope at around 3.5 V vs. Li/Li^+ decays to lower potentials and the plateau

at 3.67 V vs. Li/Li$^+$ shortens, which along with changes in both of its CV and dQ/dV curves imply irreversible structural rearrangements during the initial cycles (**Figure 3-6c** and **3-6d**).

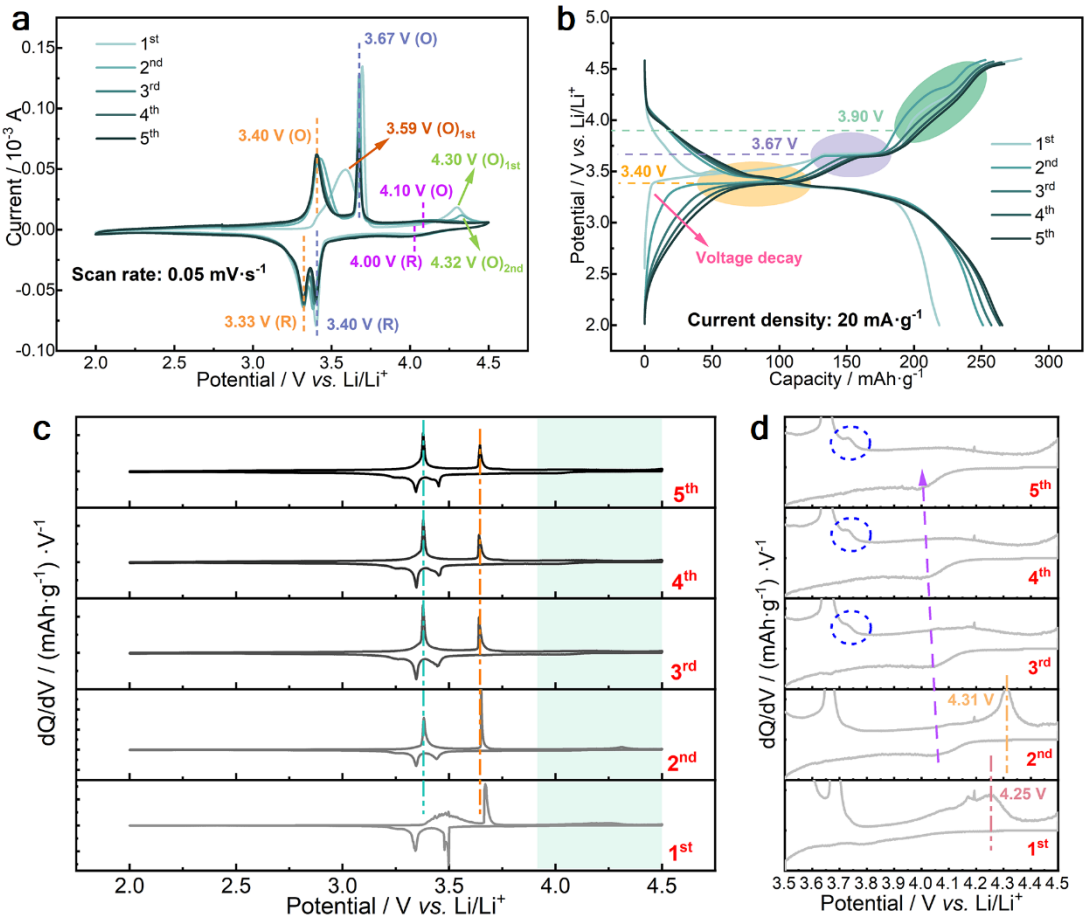


Figure 3-6. Electrochemistry of the Li_2RuO_3 electrode. **(a)** 1-5th CV curves at the scan rate of 0.05 mV/s. **(b)** 1-5th GCD curves at the current density of 20 mA/g. **(c** and **d)** The corresponding dQ/dV vs. V curves. The potential window is 2.0 - 4.5 V vs. Li/Li$^+$.

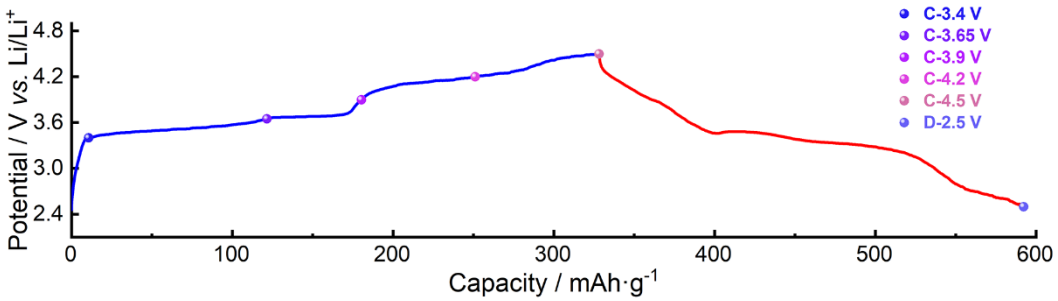


Figure 3-7. Typical GCD curves of the Li_2RuO_3 electrode during the 1st cycle. The current density is 10 mA/g, and the potential window is 2.5 - 4.5 V vs. Li/Li$^+$.

3.4. Structural evolutions of Li_2RuO_3 upon de-/lithiation

To correlate the electrochemistry with general structural changes, we firstly conducted both ex-situ and in-situ XRD studies on the Li_2RuO_3 electrode. Specifically, ex-situ XRD patterns were collected on Li_2RuO_3 electrodes dis-/charged to different voltages at 10 mA/g. As shown in **Figure 3-7**, nearly all Li^+ ions can be extracted at such a low current density as the charging capacity reaches its theoretical value (i.e., 328 mAh/g).

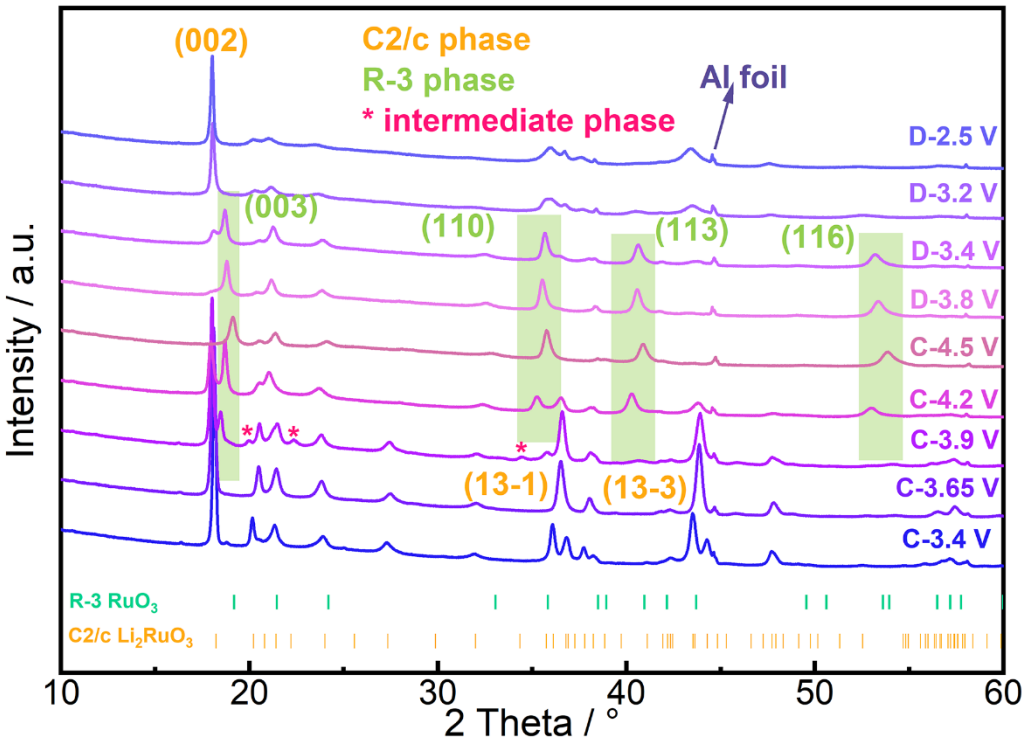


Figure 3-8. Ex-situ XRD patterns of the Li_2RuO_3 electrodes during the 1st cycle.

According to the ex-situ XRD patterns in **Figure 3-8**, upon charging to above 3.9 V vs. Li/Li^+ ($Li_{2-x}RuO_3$ where $x > 1$), new peaks at around 2θ = 18.9°, 35.5°, 40.2° and 52.9° can be indexed to (003), (110), (113) and (116) lattice planes in the newly formed R-3

phase, respectively. The transformation from C2/c to R-3 requires the ccp to hcp rearrangement of the oxygen arrays, during which the intermediate P3-phase appears (labeled by asterisks), as previously reported by Xie et al.[30] Upon deep de-lithiation, Rietveld refinement reveals that the lattice *c*-parameter decreases from 14.3576(11) Å in $Li_{0.6}RuO_3$ to 13.87733(11) Å in $RuO_{2.95}$, resulting from the Ru migration from the $LiRu_2$ layers to the Li layers (details in **Appendix A**), as proven by Zheng et al.[31] In discharge, the lithiation follows reverse processes to produce the monoclinic C2/c phase. However, both the (002) peak and superstructure-related peaks decline in intensity, implying irreversible structural changes such as the loss of the ordered $LiRu_6$ patterns caused by the Li/Ru mixing. As shown in **Figure 3-9**, such reversible phase transformations are captured via in-situ XRD tests as well. Accordingly, **Figure 3-10** schematically depicts the structural evolutions of Li_2RuO_3 upon the 1st cycle.

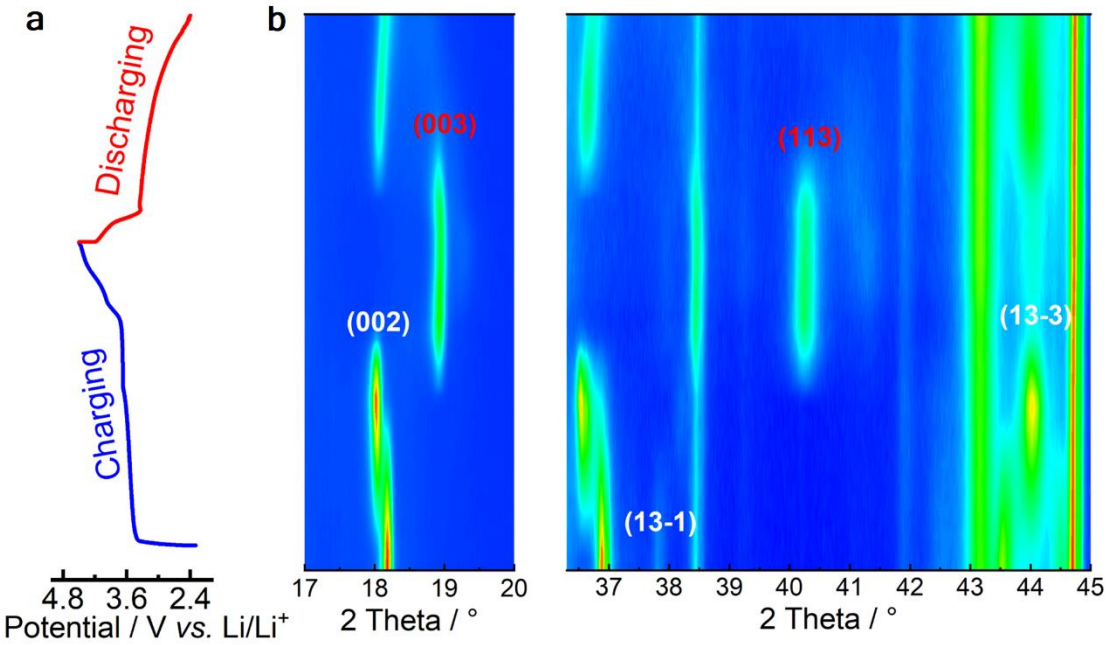


Figure 3-9. In-situ XRD patterns of the Li_2RuO_3 electrode. **(a)** GCD curves of the in-situ cell at the current density of 50 mA/g within a potential window of 2.5 - 4.5 V vs. Li/Li^+. **(b)** Contour maps revealing the evolution of major diffraction peaks.

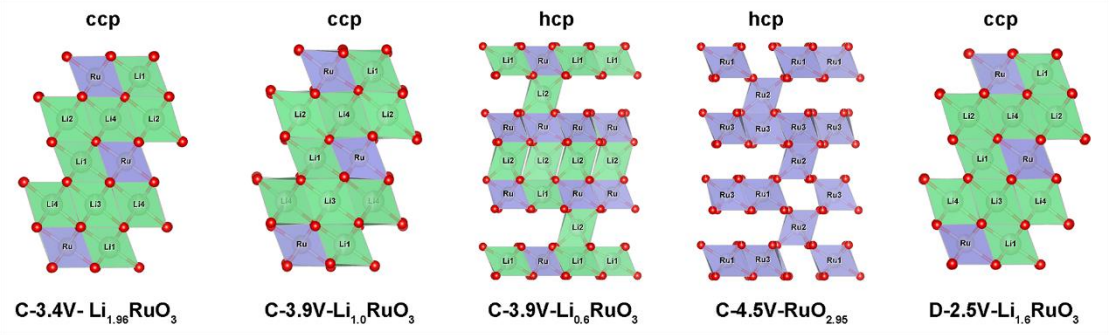


Figure 3-10. Structural changes of Li_2RuO_3 upon 1st de-/ lithiation.

3.5. Chemical evolutions of Li_2RuO_3 upon de-/lithiation

To study the chemical evolutions at a local level, both ex-situ XAS and ex-situ XPS studies were carried out on Li_2RuO_3 electrodes at various electrochemical states during the 1st cycle. As shown in **Figure 3-11a**, the O-K pre-edge first shifts to lower energy (529.9 eV) and remains steady on charge up to 4.2 V vs. Li/Li^+, indicating that the oxidation of Ru^{4+}-to-Ru^{5+} accounts for charge compensation during the 1st Li^+ removal (i.e., Li_2RuO_3 to $Li_{1.0}RuO_3$).[28] In the O 1s XPS spectra (**Figure 3-11b**), the peak appearing at 529.5 eV indicates the formation of electron holes in the rehybridized Ru 4d-O 2p orbitals, which shifts to 530.0 eV at 4.2 V vs. Li/Li^+, intrinsic to the formation of peroxide-like species (O_2^{2-}), consistent with previous XPS results.[16,32] Upon further charging to 4.5 V vs. Li/Li^+, the leading edge of the O-K pre-edge moves to a higher energy position (530.1 eV) and the lattice oxygen peak in the O 1s spectrum shifts to a lower energy (529.1 eV), probably resulting from O_2 loss and Ru^{5+}-to-Ru^{4+} reduction on the surface.[33]

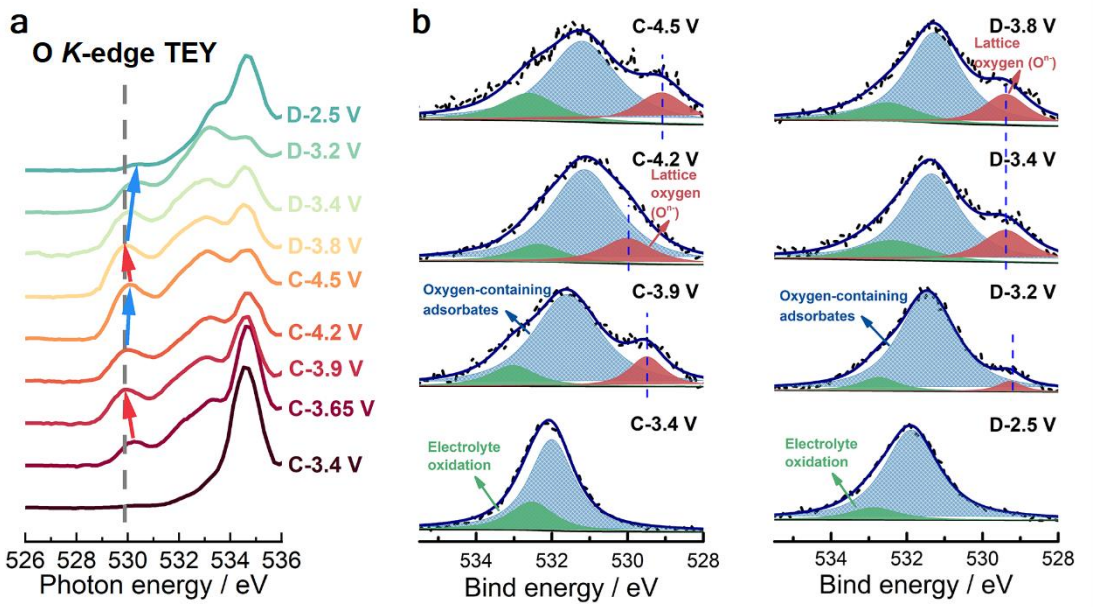


Figure 3-11. (a) Ex-situ O-K edge XAS spectra (TEY mode), and **(b)** ex-situ XPS spectra of Li_2RuO_3 electrodes at different voltages.

Upon discharging to 3.8 V vs. Li/Li^+, the pre-edge shifts back to a lower energy (529.9 eV), indicating that the O_2 is reduced and incorporated back into the lattice, consistent with the trapped O_2 theory (i.e., the oxygen redox activities involve reversible transformations between O^{2-} and O_2).[34] After discharge, the broadened pre-edges indicate the rehybridization of the Ru-O bonding and local rearrangement around O.[19] In summary, in Li_2RuO_3, Ru and O redox reactions take place in sequence for charge compensations upon de/ lithiation, wherein the lattice oxygen O^{2-} could be oxidized to form O_2^{n-} dimers and even O_2 molecules.

3.6. Li^+ transfer dynamics of Li_2RuO_3

Galvanostatic intermittent titration technique (GITT) tests were performed on the Li_2RuO_3 electrode to study its Li^+ ion transfer dynamics, which had not been well investigated previously.

As shown in **Figure 3-12a,** during either the low-voltage slope (3.5 V vs. Li/Li^+) or the middle plateau (3.67 V vs. Li/Li^+), the value of Li^+ diffusion coefficient (D, cm^2/s) firstly drops by 2-3 orders of magnitude to the minimum and then increases gradually, identical to the bi-phasic process as in $LiFePO_4$.[35] It is noteworthy that the lithium diffusivity in single-phase state, no matter with the C2/c or R-3 structure, is at the level of 10^{-10} cm^2/s, meaning that removing the 1st Li^+ barely affects lithium transfer dynamics notwithstanding the oxygen array rearrangement. However, upon the extraction of the 2nd Li^+, the D value gradually drops to 10^{-13} cm^2/s, indicating sluggish dynamics in the highly de-lithiated state. Moreover, both the iR drop and the overpotential increase sharply when the electrode is charged to above 4.2 V vs. Li/Li^+ ($Li_{2-x}RuO_3$ where $x > 1.5$), wherein the oxygen redox reactions dominate, and the Ru migration is inevitable.[31] Those processes are not reversible because even the equilibrium potential profiles (the dashed lines) exhibit the S-shape rather than the staircase-like shape in the 1st discharge and the 2nd cycle. Consequently, the corresponding changes of Li^+ diffusion coefficients exhibit characteristics different from those in the 1st charge. Besides, voltage decays are clearly observed in slopes in both the low-voltage (3.5 V vs. Li/Li^+) and the high-voltage (> 3.9 V vs. Li/Li^+) regions.

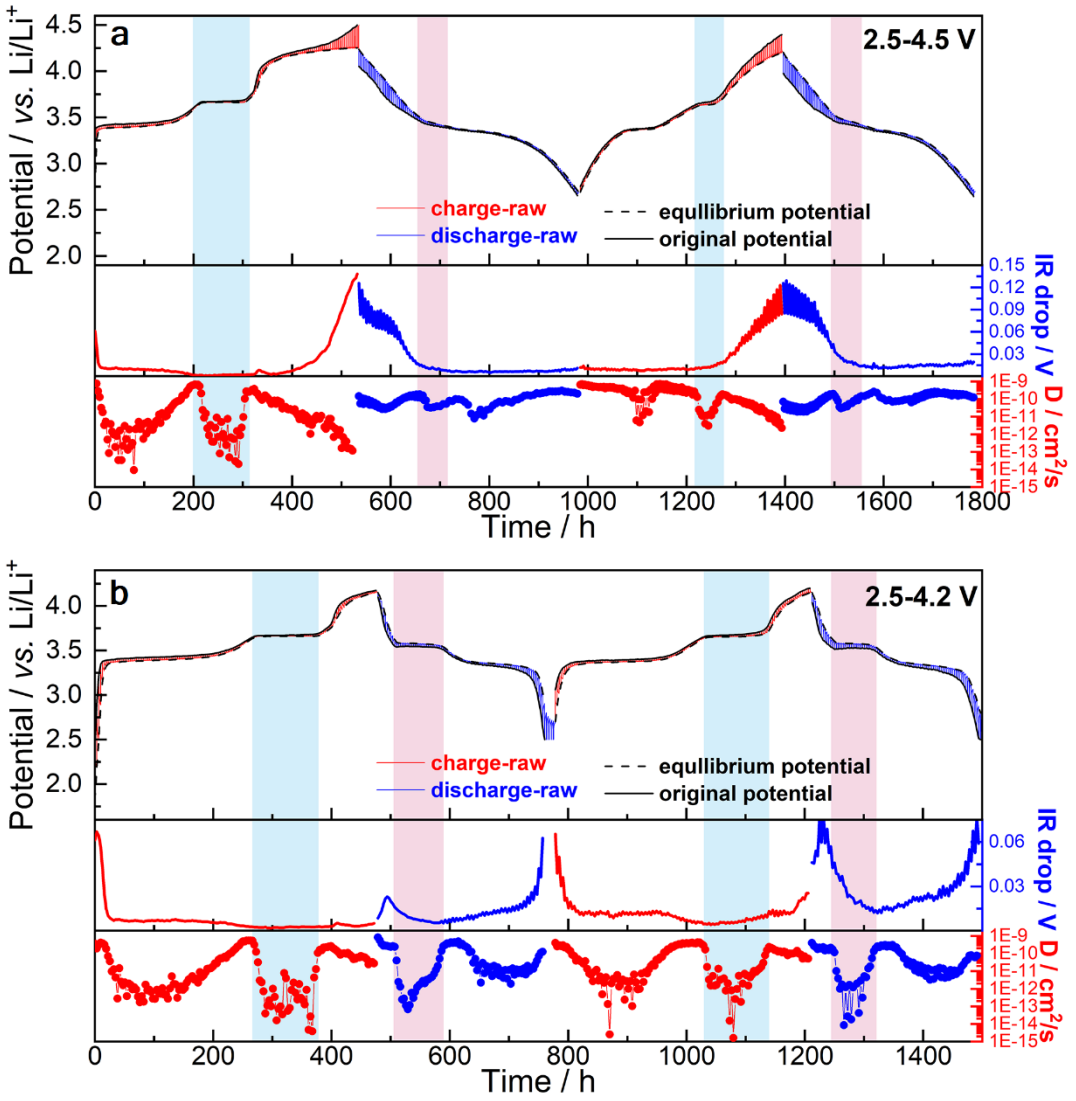


Figure 3-12. GITT results of the Li_2RuO_3 electrode within the potential windows of **(a)** 2.5 - 4.5 V vs. Li/Li^+, and **(b)** 2.5 - 4.2 V vs. Li/Li^+. Corresponding iR drops and calculated lithium diffusion efficient are presented in the middle and bottom, respectively.

Upon discharging to 3.4 V vs. Li/Li^+, the large overpotential might relate to the structural rearrangement and the bond cleavage, necessary for the reduction of O-O dimers (e.g., super-/ peroxide or O_2 molecule).[36,37] The oxygen reduction takes place at such a low potential not only because of the electrochemical polarization but also due to the rehybridization of O 2p and Ru 4d orbitals in the first charge to 4.5 V vs. Li/Li^+.[20]

On the contrary, for the GITT test performed within the potential window of 2.5 - 4.2 V vs. Li/Li^+ (**Figure 3-12b**). The staircase-like equilibrium potential profiles are well maintained in the first 2 cycles and the lithium diffusivity changes reversibly. Therefore, the local structural changes are supposed to be largely reversible when less than 1.5 Li^+ ions are extracted from Li_2RuO_3.

3.7. Local coordination evolutions in Li_2RuO_3 upon de-/lithiation

Although Raman spectroscopy sensitive to lattice vibrations is an ideal tool to probe the evolution of short-range patterns such as the RuO_6 distortion and the O-O dimerization, it has not been thoroughly utilized to study Li_2RuO_3. Therefore, one of the major contributions of this work to the understanding of Li_2RuO_3 is the demonstration of using in-situ Raman spectroscopy to monitor the local environment changes induced by both Ru and O redox activities upon de-/ lithiation.

The in-situ Raman spectra of the Li_2RuO_3 electrode were firstly recorded during the initial de-/ lithiation (**Figure 3-13**), experimental details in Chapter 2. Considering first the vibrations of the Ru-Ru dimers (i.e., Raman peaks in the region of 150 - 350 cm^{-1}). For the Li_2RuO_3 electrode at the beginning of the 1st charge (i.e., 3.4 V vs. Li/Li^+), the superimposed Raman bands at around 193 cm^{-1} and 251 cm^{-1} relate to the Ru-Ru motions within the *ab*-plane. Upon charging to 3.9 V vs. Li/Li^+, the former shifts leftwards to 185 cm^{-1} with a lower intensity and the latter shifts rightwards to 264 cm^{-1} with a higher intensity, respectively (**Figure 3-14**), consistent with the opposite

changes in the lattice parameters of *a* and *b*, as revealed by structural analyses in **Appendix A**.

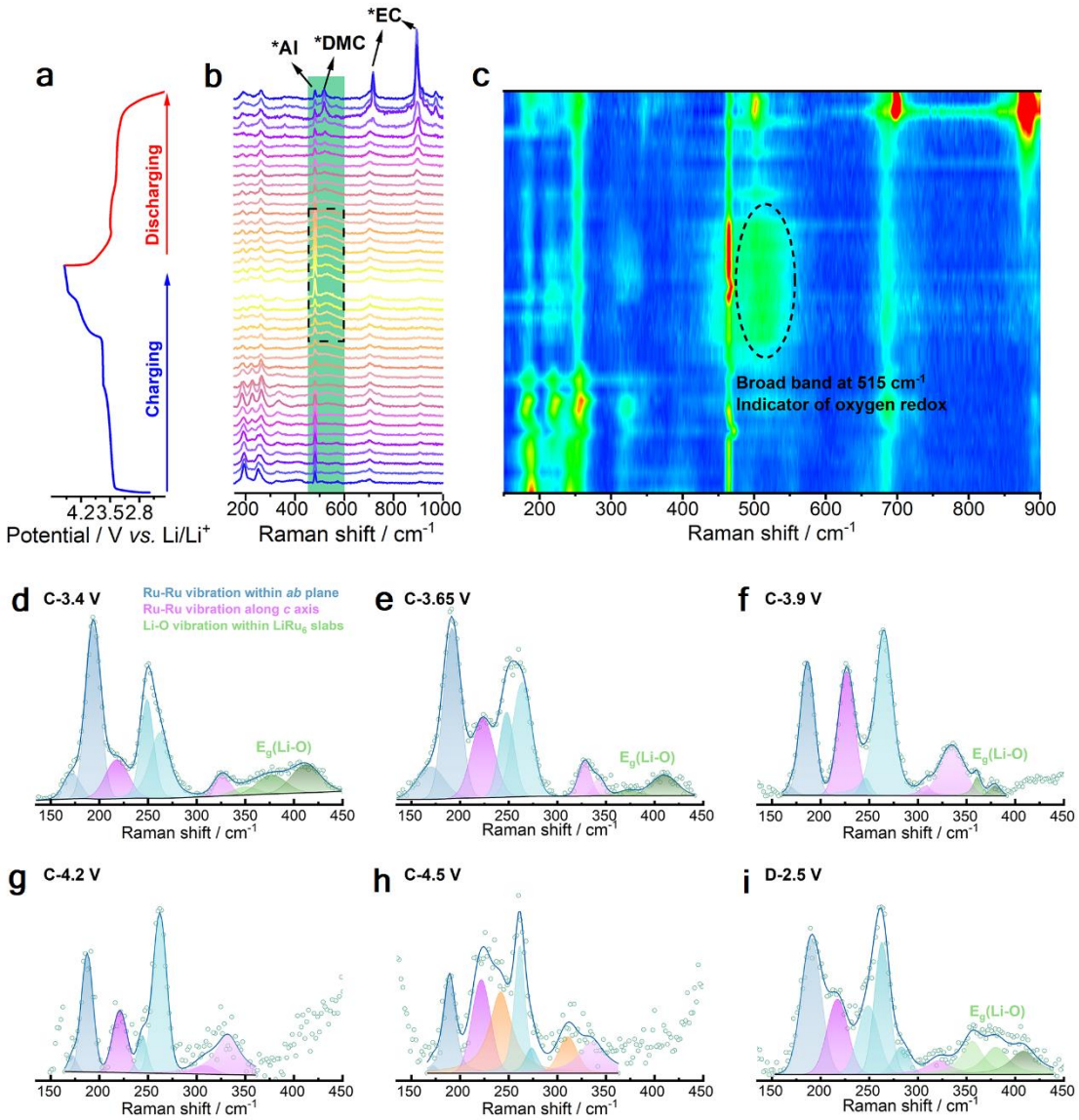


Figure 3-13. In-situ Raman spectra of the Li_2RuO_3 electrode upon the initial cycle. **(a)** GCD curves of the in-situ cell, **(b)** in-situ Raman spectra, and **(c)** contour maps. The current density is 50 mA/g, and the potential window is 2.5 - 4.5 V vs. Li/Li^+. **(d-i)** Fitted Raman spectra (150 - 450 cm^{-1}) of the Li_2RuO_3 electrode upon the 1st charge to **(d)** 3.4 V, **(e)** 3.65 V, **(f)** 3.9 V, **(g)** 4.2 V, **(h)** 4.5 V vs. Li/Li^+ and the 1st discharge to **(j)** 2.5 V vs. Li/Li^+. The superimposed peaks in blue and pink are attributed to the in-plane (ab) and out-of-plane Ru-Ru motions, while those green peaks are intrinsic to the Li-O vibrations (E_g mode). In **(h)**, peaks at around 241.8 cm^{-1} and 310.9 cm^{-1} (in orange) imply the formation of new local coordination around Ru-Ru dimers.

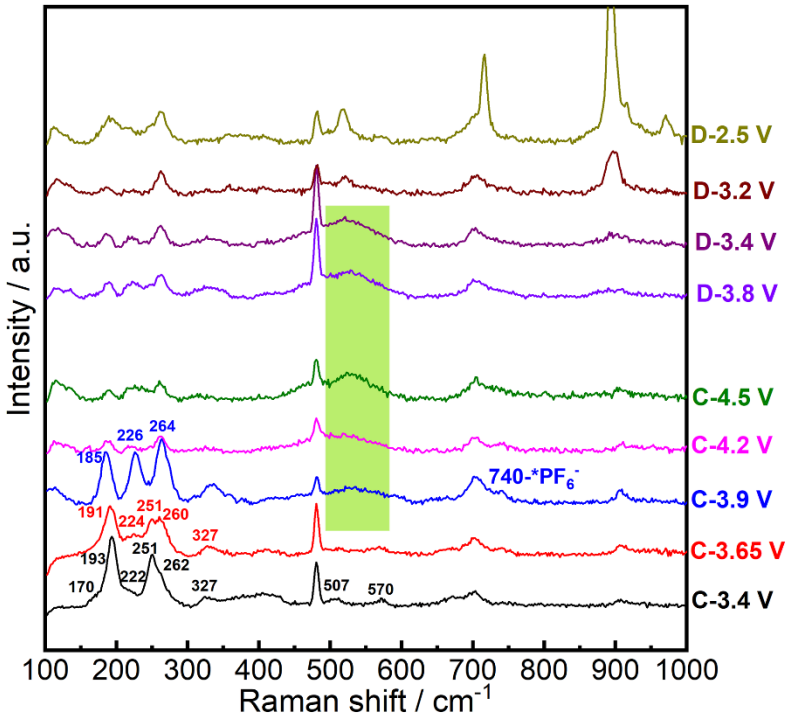


Figure 3-14. Raman spectra of the Li_2RuO_3 electrode at different potentials in the 1st cycle. All spectra are selected from the database of the in-situ Raman results.

As to the peaks at around 220 cm^{-1} and 325 cm^{-1} (i.e., the Ru-Ru motions along the *c*-axis), their intensities largely increase after the removal of the 1st Li^+ (**Figure 3-13f**). Meanwhile, Raman peaks belonging to the $LiRu_6$ honeycomb-like patterns (i.e., the Li-O E_g modes) are maintained, meaning that the Li^+ ions are mainly extracted from the Li layers. Therefore, the more favorable out-of-plane Ru-Ru vibrations potentially result from the increasing number of vacancies in the Li layers and the lattice expansion along the *c*-axis. Upon further charging to 4.2 V vs. Li/Li^+, the Raman peaks of the Li-O E_g modes decay, while the relative peak intensities of the in-plane Ru-Ru motions increase because removing Li^+ ions out of the $LiRu_2$ layers eases the Ru-Ru vibrations within the *ab*-plane. Despite those changes, the local coordination is

suggested to be largely maintained because no new Raman peaks appear. However, in the deeply de-lithiated state (**Figure 3-13h**), two new peaks could be deconvoluted at around 241.8 cm^{-1} and 310.9 cm^{-1}, implying the emergence of new local environments. In discharge, although those Raman peaks generally restore (**Figure 3-13i**), irreversible rearrangements around the Ru-Ru dimers could be implied by the remaining changes: i) the intensity ratio between peaks at around 193 cm^{-1} and 251 cm^{-1} reverses; ii) the intensity of the peak at around 220 cm^{-1} increases; and iii) the relative intensities of the Li-O E_g peaks differ from those in the pristine state.

As to the Ru-O vibrations (i.e., the Raman peaks in the region of 450 – 750 cm^{-1}), they are stable during the extraction of the 1st Li^+ (i.e., < 3.9 V vs. Li/Li^+), meaning that the local environment around O does not charge largely even after the C2/c to R-3 phase transformation (i.e., the plateau at around 3.67 V vs. Li/Li^+).[3,31] However, further de-lithiation produces a broad Raman band at around 515 cm^{-1}, which could be attributed to the new local environment induced by the oxygen redox activities, as indicated by ex-situ XPS and ex-situ XAS results. Upon discharging, such a Raman band gradually disappears, meaning that the local rearrangement around O is generally reversible.

It is noteworthy that, in the deeply lithiated state (i.e., 2.5 V vs. Li/Li^+), peaks at around 519 cm^{-1} could be assigned to DMC, while peaks at 716 cm^{-1} and 893 cm^{-1} could be assigned to EC (**Figure 3-15**).[38,39] The sudden increases in electrolyte signals result from the flow of the electrolyte caused by the electrode swelling and shrinking upon

charging and discharging, respectively. As show in **Figure 3-16**, the dark areas surrounded by dot lines represent defocus areas lower than the bright areas in the direction parallel to the incident laser. Upon charging, the dark area shrinks probably because of the expansion of the electrode. Further discharging induces the recovery of the dark area, implying the breath-like changes of the electrode. In the fully discharged state (i.e., 2.5 V vs. Li/Li^+), because the selected Li_2RuO_3 particle for in-situ Raman study (i.e., the particle in the middle of optic images) is immersed by the electrolyte, Raman signals from the electrolyte become stronger.

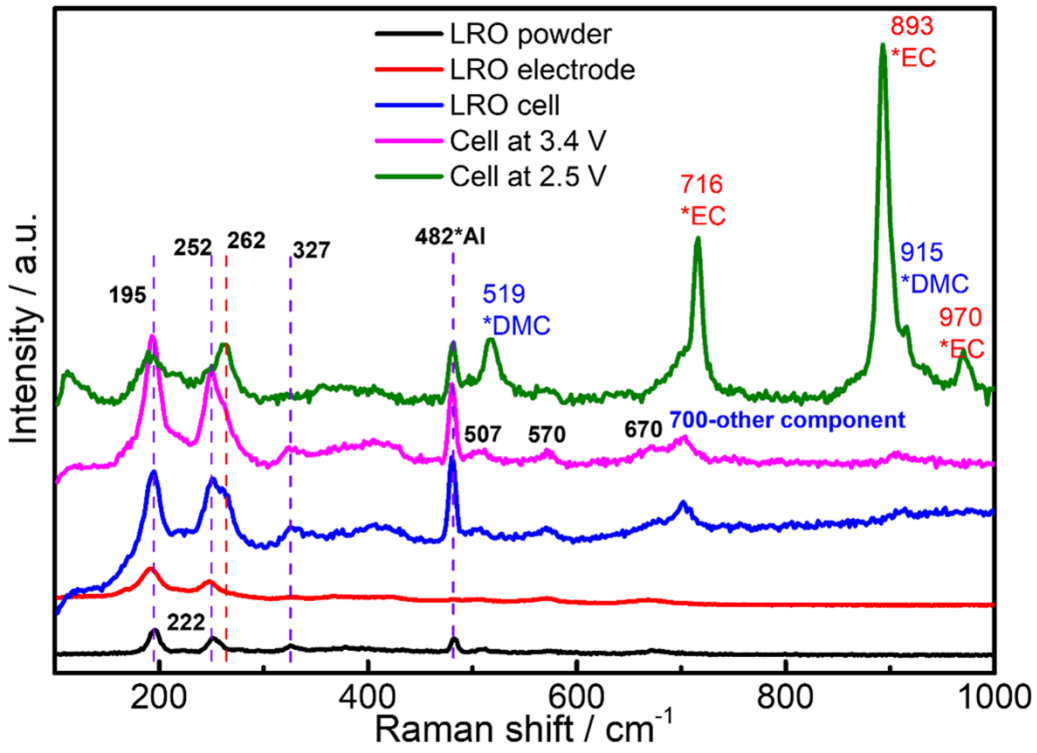


Figure 3-15. Raman spectra of the Li_2RuO_3 powder and Li_2RuO_3 electrodes. The cell at 3.4 V vs. Li/Li^+ represents the electrode at the beginning of the 1st charge, while the cell at 2.5 V vs. Li/Li^+ represents the deeply lithiated electrode after the 1st discharge. The sharp peak at around 482 cm^{-1} could be assigned to the Al foil as it is absent in the powder sample, while peaks at around 519 cm^{-1}, 716 cm^{-1} and 893 cm^{-1} originate from different components in the electrolyte.

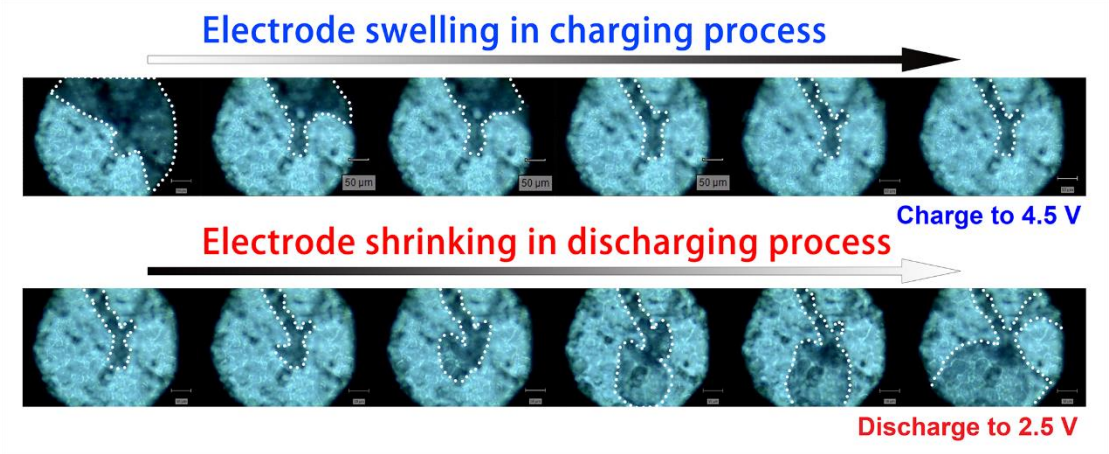


Figure 3-16. Optical images illustrating changes of the electrode during the 1st cycle.

In-situ Raman tests were repeatedly conducted during the 1st-3rd cycles of the Li_2RuO_3 electrode (**Figure 3-17**). Similarly, upon removing the 1st Li^+ (< 3.9 V vs. Li/Li^+), Raman peaks belonging to the Ru-O vibrations (both E_g and A_{1g} modes) change slightly due to the mild distortions of the octahedral RuO_6, whereas no new peaks appear, implying stable Ru-O coordination upon the Ru redox reactions. On the contrary, triggering the anion redox reactions (ARRs) leads to the emergence of the broad Raman band at around 500 cm^{-1}, which decreases and disappears in discharge, proving that it is intrinsic to the local coordination induced by the O redox activities. Because such a broad Raman band is asymmetric, it could be deconvoluted into several superimposed peaks, manifesting the coexistence of multiple local environments around O. Specifically, as shown in **Figure 3-17i** and **3-17j**, apart from the peak at round 513 cm^{-1} (Ru-O E_g mode), peaks at lower wavenumbers might be attributed to the potential coordination between Ru and O-O dimers ($Ru\text{-}O_2^{n-}$, $0 < n < 4$).

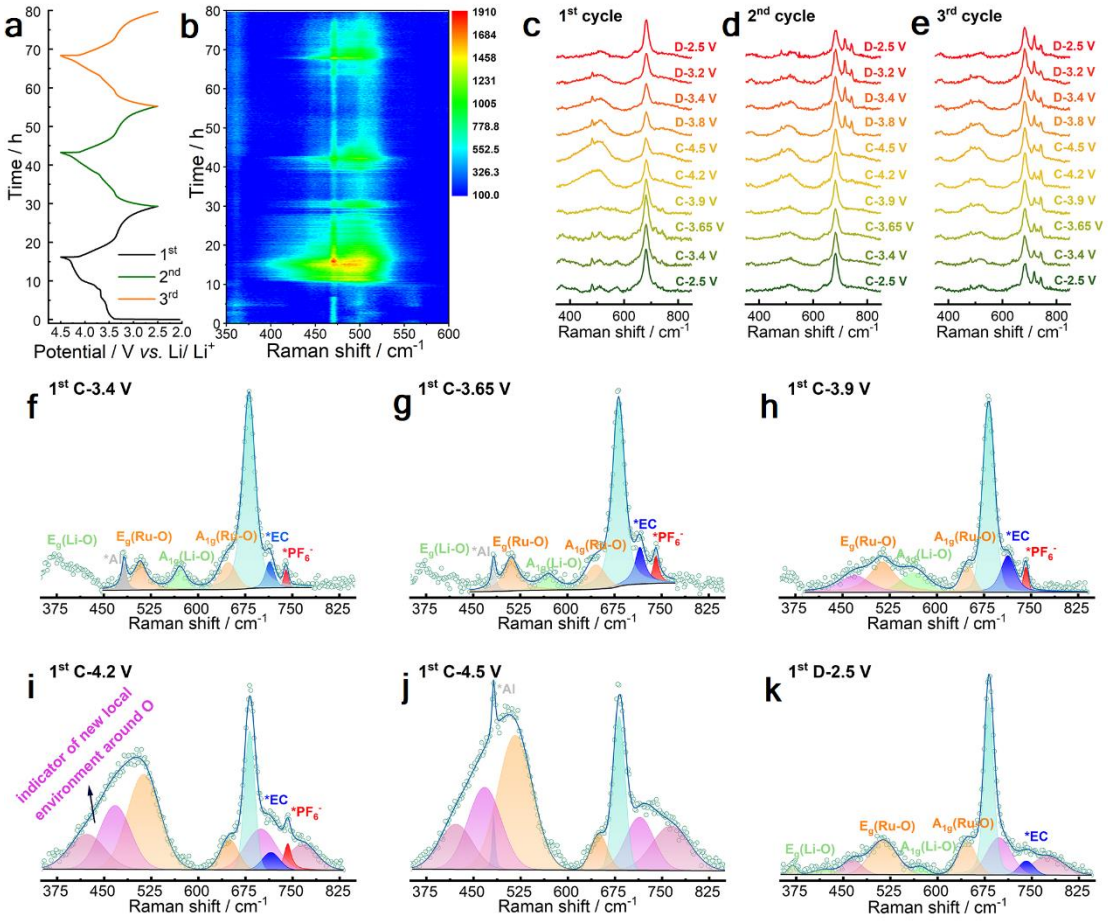


Figure 3-17. In-situ Raman spectra of the Li_2RuO_3 electrode upon the 1st-3rd cycles. **(a)**, GCD curves of the in-situ cell at the current density of 20 mA/g within the potential window of 2.5 - 4.5 V vs. Li/Li^+. **(c-e)**, Raman spectra at different voltages in the 1st, 2nd, and 3rd cycles, respectively. In the region of 700-800 cm^{-1}, sharp peaks belonging to Raman signals of the electrolyte appear in the 2nd discharge. **(f-k)**, Fitted Raman spectra of Li_2RuO_3 electrodes charged to **(f)** 3.4 V, **(g)** 3.65 V, **(h)** 3.9 V, **(i)** 4.2 V, **(j)** 4.5 V vs. Li/Li^+ and discharged to **(k)** 2.5 V vs. Li/Li^+. Peaks at around 482 cm^{-1} (in grey), 682 cm^{-1} (in light blue), 714 cm^{-1} (in blue) and 740 cm^{-1} (in red) are attributed to Raman signals from the Al foil, the window of the in-situ cell, EC and PF_6^-, respectively.

Likewise, as to the peaks related to the Ru-O A_{1g} mode vibrations, the emerging shoulders at around 715.5 cm^{-1} and 764.1 cm^{-1} also reveal the new Ru-O coordination. Meanwhile, after discharge, the shoulders at around 464.7 cm^{-1} and 775.5 cm^{-1} indicate irreversible local environment evolutions because they are not observed in

the pristine state (**Figure 3-17k**), consistent with the previous analyses. Similar evolutions are observed in both the 2nd and the 3rd cycles, meaning that the above-mentioned results are reliable to depict the picture of the local coordination evolutions in Li_2RuO_3 upon de-/ lithiation.

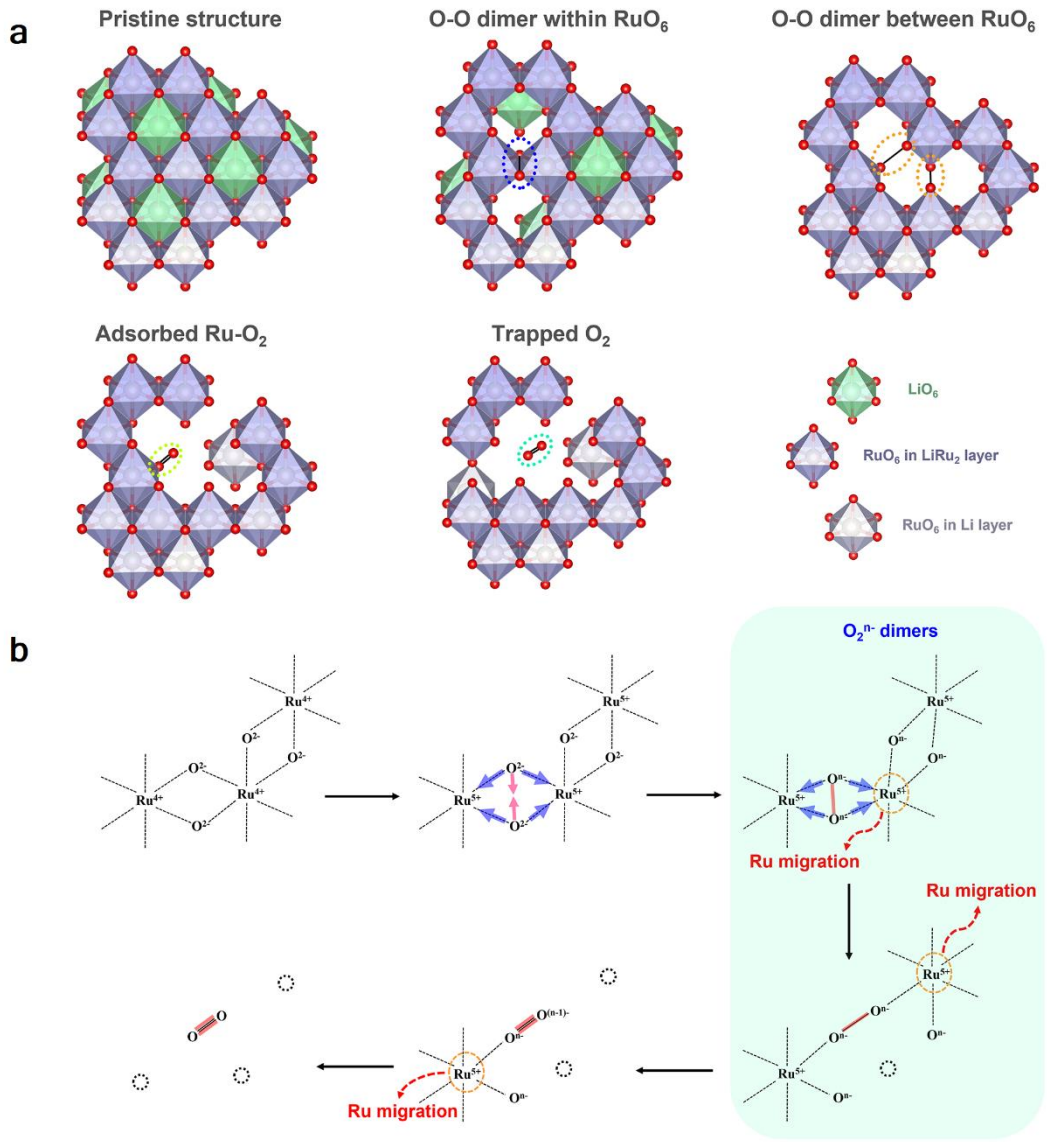


Figure 3-18. Schematic diagram of the local coordination evolutions in Li_2RuO_3 upon de-lithiation. **(a)** Changes of the LiRu6 patterns in the $LiRu_2$ layers. View of the [001] projection. **(b)** The mechanism of O-O dimerization and O_2 formation upon Ru and O redox reactions.

3.8. Summary and outlook

Generally, in Li_2RuO_3, cationic and anionic redox reactions take place in sequence for charge compensations upon de-lithiation, wherein the lattice oxygen O^{2-} could be ultimately oxidized to the molecular O_2 via the intermediate O_2^{n-} dimers (**Figure 3-18**).[40]

Specifically, upon the removal of the 1st Li^+, the Ru^{4+}-to-Ru^{5+} oxidation induces the distortion of the octahedral RuO_6 with close O-O pairs. Because of the high covalency of the Ru-O bonding, the O-O dimerization within the RuO_6 octahedra is energetically unfavorable in the well-ordered honeycomb arrangement.[20] Therefore, Raman peaks intrinsic to Ru-O vibrations merely change, whereas the out-of-plane motions of the Ru-Ru dimers (i.e., along the *c*-axis) become favorable due to the deceasing steric effect from the Li^+ ions.

Upon the following oxygen redox reactions, the Ru migration breaks the well-ordered structure and creates the Ru_{Li}-V_{Ru} anti-sites (i.e., Ru ions in Li vacancies), thereafter producing the O-O dimers bridging the adjacent RuO_6 octahedra. Further cation migration could even result in the formation of O_2 molecules either being absorbed on the Ru sites or trapped in the lattice. From this perspective, the ARR-induced Raman band at around 500 cm^{-1} could be assigned to the Ru-O_2^{n-} ($0 < n < 4$) coordination and regarded as the indicator of the O-O dimerization.

In summary, to investigate the nature of the oxygen redox activities, we demonstrate the ability of the in-situ Raman spectroscopy to monitor the local coordination evolutions during electrochemical processes in the archetypal Li_2RuO_3. The specific Raman-active vibrations of the Ru-Ru dimers were analyzed to reconcile the structural evolutions revealed by multimodal characterizations. Besides, the unique Raman band induced by the ARRs (at around 500 cm^{-1}) was captured and assigned to the newly formed Ru-O_2^{n-} ($0 < n < 4$) coordination, thereby making it an ideal signature to indicate the emergence of the O-O dimerization.

Looking forward, given that the Raman spectroscopy uses visible light as the probe, it is easily available in ordinary labs and feasible for real time and long-term operations with low, if any, sample damages. In addition, considering its high sensitivity towards lattice vibrations, we believe that the potential of the Raman spectroscopy demonstrated in this work is of sufficiently widespread appeal and could inspire more Raman-based investigations in a wide range of fields.

3.9. References

1. J.-M. Dulac, *C. R. Acad. Sc. Paris*, 1970, **270**, 223-226.
2. A. C. W. P. James, and J. B. Goodenough, *J. Solid State Chem.*, 1988, **74**, 287-294.
3. H. Kobayashi, R. Kanno, Y. Kawamoto, M. Tabuchi, O. Nakamura, and M. Takano, *Solid State Ionics*, 1995, **82**, 25-31.
4. H. Kobayashi, R. Kanno, Y. Kawamoto, M., Tabuchi, and O. Nakamura, *Solid State Ionics*, 1996, **86-88**, 859-863.
5. H. Kobayashi, R. Kanno, M., Tabuchi, H. Kageyama, O. Nakamura, and M. Takano, *J. Power Sources*, 1997, **68**, 686-691.
6. G. J. Moore, C. S. Johnson, and M. M. Thackeray, *J. Power Sources*, 2003, **119-121**, 216-220.

7. Y. Zheng, S. Taminato, Y. Xu, K. Suzuki, K. Kim, M. Hirayama, and R. Kanno, *J. Power Sources*, 2012, **208**, 447-451.
8. Felner, and I. M., Bradarić, *Physica B*, 2002, **311**, 195-199.
9. M. Soma, and H. Sato, *J. Phys. Soc. Jpn.*, 2006, **75**, 124802.
10. Y. Miura, Y. Yasui, M. Sato, N. Igawa, and K. Kakurai, *J. Phys. Soc. Jpn.*, 2007, **76**, 033705.
11. G. Jackeli, and D. I. Khomskii, *Phys. Rev. Lett.*, 2008, **100**, 147203.
12. M. D. Johannes, A. M. Stux, and K. E. Swider-Lyons, *Phys. Rev. B*, 2008, **77**, 075124.
13. Y. Miura, M. Sato, Y. Yamakawa, T. Habaguchi, and Y. Ōno, *J. Phys. Soc. Jpn.*, 2009, **78**, 094706.
14. S. A. J. Kimber, I. I. Mazin, J. Shen, H. O. Jeschke, S. V. Streltsov, D. N. Argyriou, R. Valentí, and D. I. Khomskii, *Phys. Rev. B*, 2014, **89**, 081408.
15. P. J. Reeves, I. D. Seymour, K. J. Griffith, and C. P. Grey, *Chem. Mater.*, 2019, **31**, 2814-2821.
16. M. Sathiya, K. Ramesha, G. Rousse, D. Foix, D. Gonbeau, A. S. Prakash, M. L. Doublet, K. Hemalatha, and J.-M. Tarascon, *Chem. Mater.*, 2013, **25**, 1121-1131.
17. M. Sathiya, G. Rousse, K. Ramesha, C. P. Laisa, H. Vezin, M. T. Sougrati, M. L. Doublet, D. Foix, D. Gonbeau, W. Walker, A. S. Prakash, M. Ben Hassine, L. Dupont, and J. M. Tarascon, *Nat. Mater.*, 2013, **12**, 827-835.
18. M. Sathiya, A. M. Abakumov, D. Foix, G. Rousse, K. Ramesha, M. Saubanère, M.-L. Doublet, H. Vezin, C. P. Laisa, A. S. Prakash, D. Gonbeau, G. Van Tendeloo, and J.-M. Tarascon, *Nat. Mater.*, 2015, **14**, 230-238.
19. Y. Yu, P. Karayaylali, S. H. Nowak, L. Giordano, M. Gauthier, W. Hong, R. Kou, Q. Li, J. Vinson, T. Kroll, D. Sokaras, C.-J. Sun, N. Charles, F. Maglia, R. Jung, and Y. Shao-Horn, *Chem. Mater.*, 2019, **31**, 7864-7876.
20. Y. Yu, P. Karayaylali, D. Sokaras, L. Giordano, R. Kou, C.-J. Sun, F. Maglia, R. Jung, F. S. Gittleson, and Y. Shao-Horn, *Energy Environ. Sci.*, 2021, **14**, 2322-2334.
21. R. A. House, J.-J. Marie, J. Park, G. J. Rees, S. Agrestini, A. Nag, M. Garcia-Fernandez, K.-J. Zhou, and P. G. Bruce, *Nat. Commun.*, 2021, **12**, 2975.
22. Q. Wu, V. A. Maroni, D. J. Gosztola, D. J. Miller, D. W. Dees, and W. Lu, *J. Electrochem. Soc.*, 2015, **162**, A1255-A1264.
23. Y. S. Ponosov, E. V. Komleva, and S. V. Streltsov, *Phy. Rev. B*, 2019, **100**, 134310.
24. Y. S. Ponosov, and S. V. Streltsov, *Phy. Rev. B*, 2020, **101**, 245142.
25. F. Amalraj, M. Talianker, B. Markovsky, D. Sharon, L. Burlaka, G. Shafir, E. Zinigrad, O. Haik, D. Aurbach, J. Lampert, M. Schulz-Dobrick, and A. Garsuch, *J. Electrochem. Soc.*, 2012, **160**, A324-A337.
26. P. Lanz, C. Villevieille, and P. Novák, *Electrochim. Acta*, 2013, **109**, 426-432.
27. B. Li, R. Shao, H. Yan, L. An, B. Zhang, H. Wei, J. Ma, D. Xia, and X. Han. *Adv. Funct. Mater.*, 2016, **26**, 1330-1337.
28. F. Ning, B. Li, J. Song, Y. Zuo, H. Shang, Z. Zhao, Z. Yu, W. Chu, K. Zhang, G. Feng, X. Wang, and D. Xia, *Nat. Commun.*, 2020, **11**, 4973.
29. M. Han, Z. Liu, X. Shen, L. Yang, X. Shen, Q. Zhang, X. Liu, J. Wang, H.-J. Lin, C.-T. Chen, C.-W. Pao, J.-L. Chen, Q. Kong, X. Yu, R. Yu, L. Gu, Z. Hu, X. Wang, Z. Wang, and L. Chen, *Adv. Energy Mater.*, 2020, **10**, e2002631.

30. Y. Xie, H. Gao, R. Harder, L. Li, J. Gim, H. Che, H. Wang, Y. Ren, X. Zhang, L. Li, Z. Chen, K. Amine, and Z.-F. Ma, *ACS Appl. Energy Mater.*, 2020, **3**, 6107-6114.
31. F. Zheng, S. Zheng, P. Zhang, X. Zhang, S. Wu, Y. Yang, and Z.-H. Zhu, *J. Phys. Chem. C*, 2019, **123**, 13491-13499.
32. M. Oishi, R. Imura, T. Ueki, K. Shimoda, H. Yamagishi, and I. Watanable, *Mod. Phy. Lett. B,* 2020, **34**, 7-9.
33. Z. Zhuo, K. Dai, J. Wu, L. Zhang, N. Tamura, Y.-D. Chuang, J. Feng, J. Guo, Z.-X. Shen, G. Liu, F. Pan, and W. Yang, *ACS Energy Lett.,* 2021, **6**, 3417-3424
34. R. A. House, J.-J. Marie, M. A. Pérez-Osorio, G. J. Rees, E. Boivin, and P. G. Bruce, *Nat. Energy*, 2021, **6**, 781-789.
35. Tang, X. Yu, J. Sun, H. Li, and X. Huang, *Electrochim. Acta*, 2011, **56,** 4869-4875.
36. G. Choi, J. Lee, S. Koo, S. Park, and D. Kim, *Cell Rep. Phys. Sci.*, 2021, **2**, 100508.
37. K., Kawai, X.-M. Shi, N. Takenaka, J. Jang, B. Mortemard de Boisse, A. Tsuchimoto, D. Asakura, J. Kikkawa, M. Nakayama, M. Okubo, and A. Yamada, *Energy Environ. Sci.*, 2022, **15**, 2591-2600.
38. G. Bouteau, A. N. Van-Nhien, M. Sliwa, N. Sergent, J. C. Lepretre, G. Gachot, I. Sagaidak, and F. Sauvage, *Sci. Rep.*, 2019, **9**, 135.
39. E. Miele, W. M. Dose, I. Manyakin, M. H. Frosz, Z. Ruff, M. F. L. De Volder, C. P. Grey, J. J. Baumberg, and T. G. Euser, *Nat. Commun.*, 2022, **13**, 1651.
40. A. Grimaud, W. T. Hong, Y. Shao-Horn, and J.-M. Tarascon, *Nat. Mater.*, 2016, **15**, 121-126.

CHAPTER 4. MITIGATING STRAIN ACCUMULATION IN LITHIUM RUTHENATE VIA FLUORINE DOPING

Traditionally, for Li_2RuO_3, triggering the O redox activities is thought to be the origin of its performance degradation in long-term cycling due to the irreversible oxygen loss and Ru migration. However, in this chapter, we find that solely tapping into the Ru redox activities (from Li_2RuO_3 to $Li_{1.0}RuO_3$) unexpectedly worsens its cyclability (i.e., 16.2 % capacity retention after 325 cycles within the potential window of 2.5 - 3.9 V vs. Li/Li^+), thereby unveiling the detrimental yet underestimated structural degradation induced by the cation redox activities. To solve this problem, we demonstrate that even trace amount of F-doping could effectively prohibit the capacity decay in $Li_{1.95}RuO_{2.95}F_{0.05}$, resulting in the superior long-term stability, i.e., 91.4 % capacity retention after 439 cycles within the potential window of 2.5 - 3.9 V vs. Li/Li^+.

4.1. Introduction

Generally speaking, two major challenges hindering the practical applications of lithium rich cathode materials (LRCMs) are the rapid capacity decay and the voltage fading upon long-term cycling, which have been widely attributed to the irreversible structural degradations (e.g., oxygen loss and TM migration) induced by the oxygen redox activities.[1-3]

Recently, the origin of such structural degradations has been proven to be in close relationship with the de-/lithiation-induced heterogeneities within single particles, namely nanoscale strain accumulation and lattice displacement, as revealed via using multimodal characterization techniques by Liu et al.[4] In detail, in typical lithium-rich manganese-rich oxides (LRMOs, $xLiTMO_2 \cdot 1\text{-}xLi_2MnO_3$, TM = Ni, Co, Mn, Ti, etc.), there are two kinds of domains (i.e., $LiTMO_2$ and Li_2MnO_3) which are supposed to be active in different potentials. Specifically, the initial de-lithiation takes place in $LiTMO_2$ domains and leads to anisotropic lattice expansion, while Li_2MnO_3 domains are largely intact, thereby creating nano-strains with lattice displacement at domain boundaries. Upon further de-lithiation to trigger anion redox reactions (ARRs), such severe strains could be relaxed via oxygen release, which lowers the energy penalty of TM migration and adversely accelerates the performance degradation.

In fact, even in the lithium stoichiometric single-phase crystals (e.g., $LiCoO_2$), the accumulation of nano-strains induced by non-equilibrium electrochemical activities is considered to be the driving force of structural degradation especially under fast charging conditions.[5] For instance, no matter following the shrinking core or the intercalation wave mechanisms,[6] nanodomains with different crystal orientations appear in the de-lithiated $Li_{0.5}CoO_2$, while the nonuniform volume change of primary particles induces intergranular cracks in polycrystalline nickel-rich cathode materials (NMC, $LiNi_xMn_yCo_{1-x-y}O_2$, $x > 0.6$).[7]

In this chapter, we have firstly studied electrochemical performances of the Li_2RuO_3 electrode in various depths of de-/ lithiation. Interestingly, although the irreversible ARRs are widely regarded as the origin of its performance decay, solely exploiting the Ru redox reactions unexpectedly worsens its long-term stability. Such a phenomenon is suggested to originate from the important yet overlooked strain accumulation induced by the Ru redox activities.

Considering that the strain-induced structural degradation is basically a bulk issue, doping is a potential way out of this.[8] For Li_2RuO_3, although various TM ions (e.g., Ti, Sn, etc.) were used for bulk doping,[1,3] F doping has not been thoroughly investigated. Therefore, we have prepared F-doped samples and studied the effects of F-doping systematically. Traditionally, F-doping has been widely used in conventional layered oxides (e.g., NCMs) and LRCMs,[9,10] demonstrating the ability to stabilize their structures in long-term cycling. Recently, F-doped lithium rich disordered rock-salts (DRXs) have attracted intense research interests because the F dopants could reduce TM ions to lower valence states, meaning that more cation redox activities could be exploited.[11] For example, reversible Mn^{2+}/Mn^{4+} double redox reactions were achieved in $Li_2Mn_{2/3}Nb_{1/3}O_2F$, delivering capacities higher than 300 mAh/g.[12] Meanwhile, theoretical calculations revealed that a small amount of F doping could prevent O-O dimerization in the F-doped Li_2MnO_3.[13]

Herein, in the F-doped Li_2RuO_3, upon triggering both the Ru and O redox reactions, F-

doping leads to poor cyclability. On the contrary, when only the Ru redox reactions are utilized, even trace amount of F-doping can largely improve the cycling performance of Li_2RuO_3 thanks to the effect of F dopants on mitigating strain accumulation. Firstly, because the repulsive interaction between O layers tends to increase along with the removal of the screening Li^+ ions, the weak O-F interaction could potentially buffer the interlayer repulsion. Meanwhile, F dopants lead to local disordering and suppress the preferential orientation along the *c*-axis, thereby mitigating the strain accumulation along the basal plane. Notwithstanding the widespread interests in exploiting the ARRs, this work highlights the importance of the cation redox reactions and provides a new perspective to rationally design LRCMs.

4.2. Structures of Li_2RuO_3 and $Li_{1.83}RuO_{2.83}F_{0.17}$

Both the pristine Li_2RuO_3 and the F-doped samples were prepared via solid-state reactions, as detailed in Chapter 2. Specifically, the F-doped sample was annealed at 900 °C and termed as $Li_{1.83}RuO_{2.83}F_{0.17}$. The composition was calculated based on the ratio between different precursors. The Ru was assumed to be in the valence state of +4 because the high temperature annealing process in the air was unlikely to produce Ru^{3+}.[14] Therefore, to balance the charge changes from the O^{2-} replacement by F^-, lithium vacancies were suggested to form in the F-doped samples. As indicated in Chapter 3, both the C2/c and the $P2_1/m$ symmetries could be used to depict the structure of Li_2RuO_3. Herein, the latter was adopted for the structural refinements of both the pristine Li_2RuO_3 and F-doped $Li_{1.83}RuO_{2.83}F_{0.17}$.

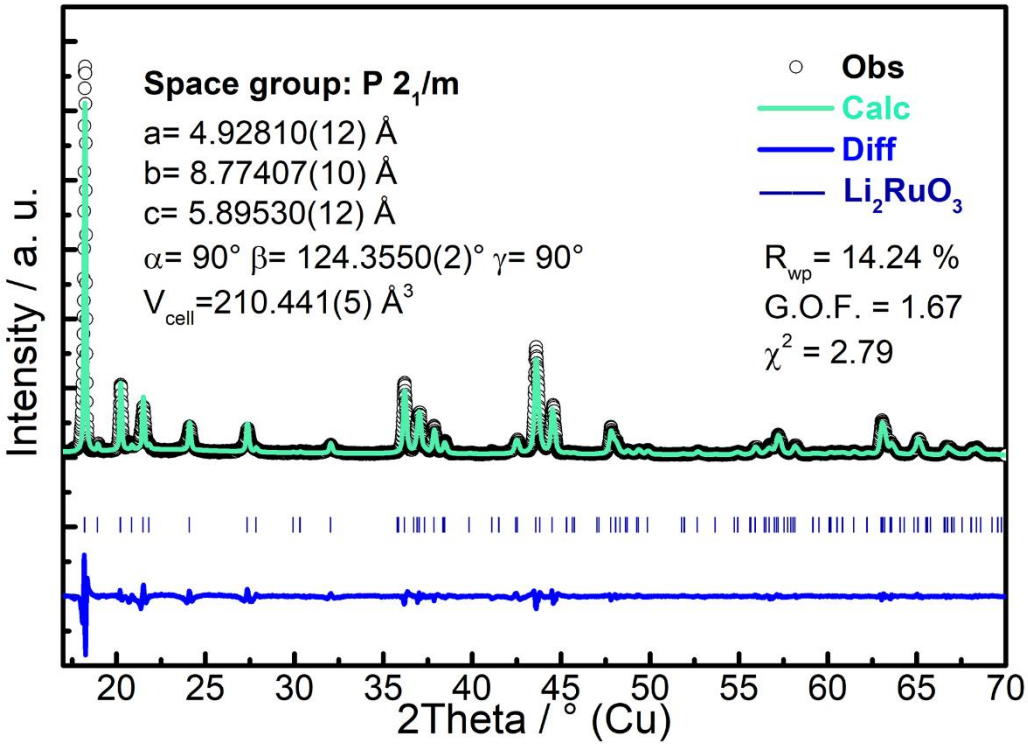


Figure 4-1. XRD patterns and Rietveld refinement results of Li_2RuO_3 ($P2_1/m$ symmetry).

For the pristine Li_2RuO_3, Rietveld refinement of its XRD patterns fits well with the $P2_1/m$ model (unique axis-*b*, **Figure 4-1**).[15] Peaks in the region of 2θ = 20 - 30° (Cu K_α, λ = 1.54 Å) could be attributed to the honeycomb-like superstructures.[16] Besides, the sharp (001) peak at 18.2° indicates its strong preferential orientation along the *c*-axis. It is noteworthy that, to improve the quality of the refinement, both the interlayer Li/Ru mixing (~4 %) and the intralayer Li/Ru mixing (~7 %) have been taken into consideration (details in **Table 4-1**).

Table 4-1. Structural parameters of pristine Li_2RuO_3 - $P2_1/m$ symmetry

Phase: Li_2RuO_3	**Space group: $P2_1/m$**				
Atom	Fractional coordinates			Multiplicity	Occupancy
	x	y	z		
Li1	0.7216(3)	0.25	0.9631(4)	2	0.86
Li2	0.2193(3)	0.0654(3)	0.4593(3)	4	0.96
Li3	0.772(1)	0.25	0.513(1)	2	0.96
Li4	0.2731(2)	0.0743(5)	0.9955(9)	4	0.10
Ru1	0.7216(3)	0.25	0.9631(4)	2	0.14
Ru2	0.2193(3)	0.0654(3)	0.4593(3)	4	0.04
Ru3	0.772(1)	0.25	0.513(1)	2	0.04
Ru4	0.2731(2)	0.0743(5)	0.9955(9)	4	0.90
O1	0.7445(1)	0.0512(7)	0.2614(8)	4	1.00
O2	0.7600(1)	0.1010(1)	0.7712(7)	4	1.00
O3	0.2683(3)	0.25	0.2160(6)	2	1.00
O4	0.2695(1)	0.25	0.7652(3)	2	1.00
Lattice parameters: a=4.92810(12) Å, b=8.77407(10) Å, c=5.89530(12) Å; α=90°, β=124.3550(2)°, γ=90°; $V_{unit\ cell}$=210.441(5) Å^3, R_{wp}=14.24 %, χ^2=2.79, G.O.F.=1.67					

For the F-doped $Li_{1.83}RuO_{2.83}F_{0.17}$, although its XRD patterns fit well with the $P2_1/m$ symmetry (unique axis-*b*, **Figure 4-2**), F dopants partially occupy the O sites and inevitably induce lattice distortions. Specifically, the unit cell anisotropically expands from 210.441(5) Å^3 to 211.202(4) Å^3, i.e., 1.07 % expansion along the *a*-axis, 0.40 % contraction along the *b*-axis, and 0.04 % shrinkage along the *c*-axis. Meanwhile, the ratio of the intralayer Li/Ru mixing increases to ~12 % (details in **Table 4-2**), which

indicates the loss of the ordered arrangement within the $LiRu_2$ layers and results in those weakened superstructure-related peaks.

Besides, the intensity ratio of (001)/ (13-2) decreases from 3.67 as in Li_2RuO_3 to 3.08 as in $Li_{1.83}RuO_{2.83}F_{0.17}$. Considering that the intragranular cracks induced by the interlayer repulsions mostly accumulate along the basal-plane (i.e., the (001) lattice plane perpendicular to the *c*-axis), such a weaker preferential orientation might favor the strain relaxation upon de-lithiation.[17]

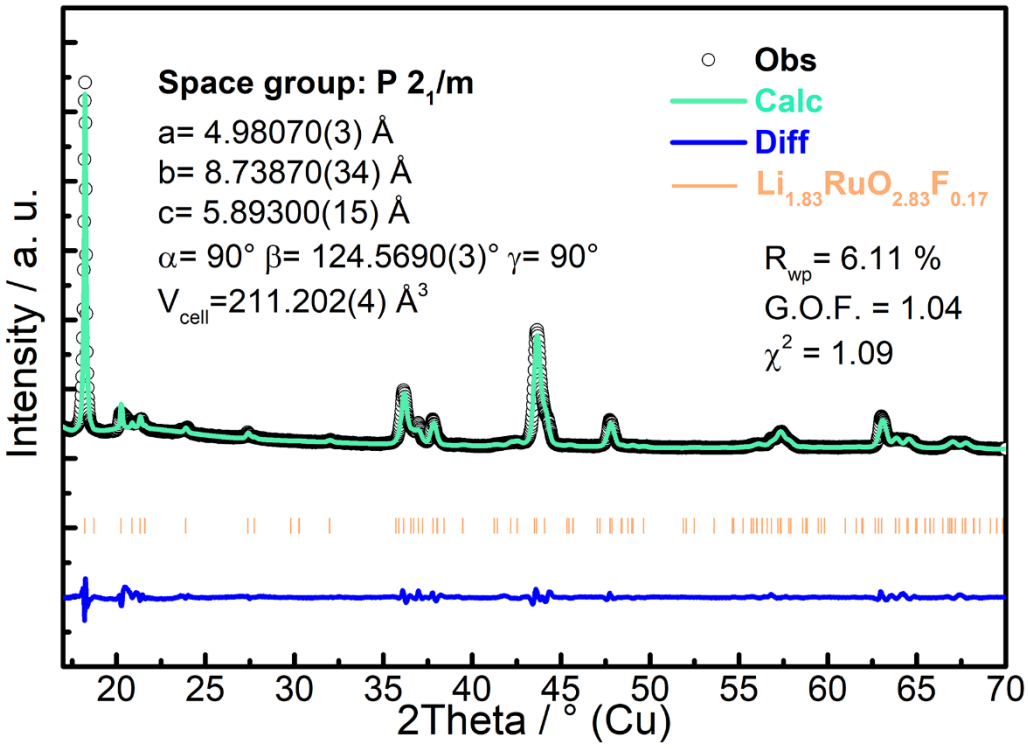


Figure 4-2. XRD patterns and Rietveld refinement results of $Li_{1.83}RuO_{2.83}F_{0.17}$.

Table 4-2. Structural parameters of pristine $Li_{1.83}RuO_{2.83}F_{0.17}$ - $P2_1/m$ symmetry

Phase: $Li_{1.83}RuO_{2.83}F_{0.17}$	**Space group: $P2_1/m$**				
Atom	Fractional coordinates			Multiplicity	Occupancy
	x	y	z		
Li1	0.7154(6)	0.25	0.9657(1)	2	0.695(8)
Li2	0.2388(3)	0.0701(4)	0.4689(5)	4	0.878(4)
Li3	0.7940(3)	0.25	0.5330(2)	2	0.878(4)
Li4	0.2684(7)	0.0756(1)	0.9940(5)	4	0.164(5)
Ru1	0.7154(6)	0.25	0.9657(1)	2	0.239(6)
Ru2	0.2388(3)	0.0701(5)	0.4689(6)	4	0.04
Ru3	0.7940(3)	0.25	0.5330(2)	2	0.04
Ru4	0.2684(7)	0.0756(1)	0.9940(6)	4	0.820(2)
O1	0.7036(9)	0.0881(6)	0.2507(7)	4	0.943
O2	0.7320(9)	0.1056(7)	0.7342(4)	4	0.943
O3	0.0997(1)	0.25	0.1102(3)	2	0.943
O4	0.2535(3)	0.25	0.7344(6)	2	0.943
F1	0.7036(9)	0.0881(6)	0.2507(7)	4	0.057
F2	0.7320(9)	0.1056(7)	0.7342(4)	4	0.057
F3	0.0997(1)	0.25	0.1102(3)	2	0.057
F4	0.2535(3)	0.25	0.7344(1)	2	0.057

Lattice parameters:

a=4.98070(3) Å, b=8.73870(34) Å, c=5.89300(15) Å; α=90°, β=124.5690(3)°, γ=90°;

$V_{unit\ cell}$=211.202(4) $Å^3$, R_{wp}=6.11 %, χ^2=1.09, G.O.F.=1.04

4.3. Electrochemical properties of Li_2RuO_3 and $Li_{1.83}RuO_{2.83}F_{0.17}$

As shown in the 1st GCD curves (**Figure 4-3a**), the Li_2RuO_3 electrode presents typical voltage profiles with an initial charging capacity of 311.1 mAh/g (20 mA/g, 2.5 - 4.5 V vs. Li/Li^+), namely a slope at around 3.5 V, a flat plateau at 3.67 V and a slope above 3.9 V vs. Li/Li^+.[18] Specifically, the first two processes could be attributed to cation redox

reactions, following solid-solution and biphasic mechanisms, respectively, as proven in the previous chapter. In contrast, given that the theoretical capacity of Ru^{4+}-to-Ru^{5+} oxidation is 164 mAh/g, the extra capacity contributed by the slope above 3.9 V vs. Li/Li^+ originates from the oxidation of oxygen.[19] Noteworthily, the sharp potential rise to trigger the oxygen redox activities indicates the large energy gap between energy bands of Ru and O.[20] In discharge, it delivers a capacity of 284.8 mAh/g, i.e., 8.5% capacity loss. Meanwhile, the initial staircase-like charging profile disappears in the 1st discharge and the following cycles, resulting from the loss of the ordered $LiRu_6$ patterns.[21] Besides, such a structural evolution lowers the potential to activate ARRs,[22] consistent with the left-ward shift of the anodic peaks in the CV curves (**Figure 4-3b**).

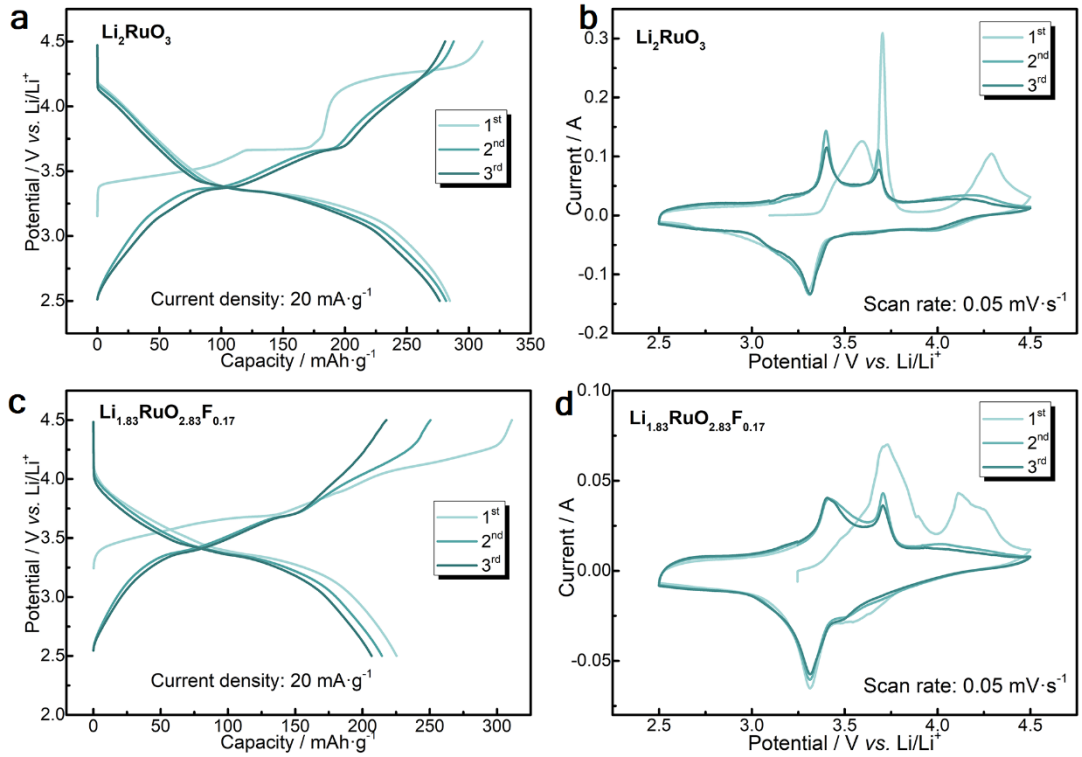


Figure 4-3. (a), The 1st-3rd GCD curves, and **(b)** CV curves of the Li_2RuO_3 electrode. **(c)** The 1st-3rd GCD curves, and **(d)** CV curves of the $Li_{1.83}RuO_{2.83}F_{0.17}$ electrode. The current density is 20 mA/g, the scan rate is 0.05 mV/s, and the potential window is 2.5-4.5 V vs. Li/Li^+.

As to the $Li_{1.83}RuO_{2.83}F_{0.17}$ electrode, although it delivers a comparable capacity of 311.1 mAh/g in the 1st charge, F-doping changes its electrochemistry (**Figure 4-3c**). Specifically, in the 1st GCD curves, a sloping plateau rather than a sharp potential rise bridges cation and anion redox processes. To understand this, the higher level of local disordering (i.e., Li/Ru mixing) might play part of the role because the above-mentioned structural rearrangement generally involves the order-to-disorder evolution.[19] Besides, F-doping could potentially alter O 2p and Ru 4d orbitals to higher and lower energy levels, respectively, thereby increasing the overlap between O and Ru bands.[23] Consequently, the anodic peaks of Ru and O oxidations shift to higher and lower potentials, respectively (**Figure 4-3d**). Notwithstanding the liability of facilitating ARRs, F-doping reduces the reversibility of oxygen redox as the $Li_{1.83}RuO_{2.83}F_{0.17}$ electrode bears a 27.6% capacity loss in the 1st discharge (85.8 mAh/g).

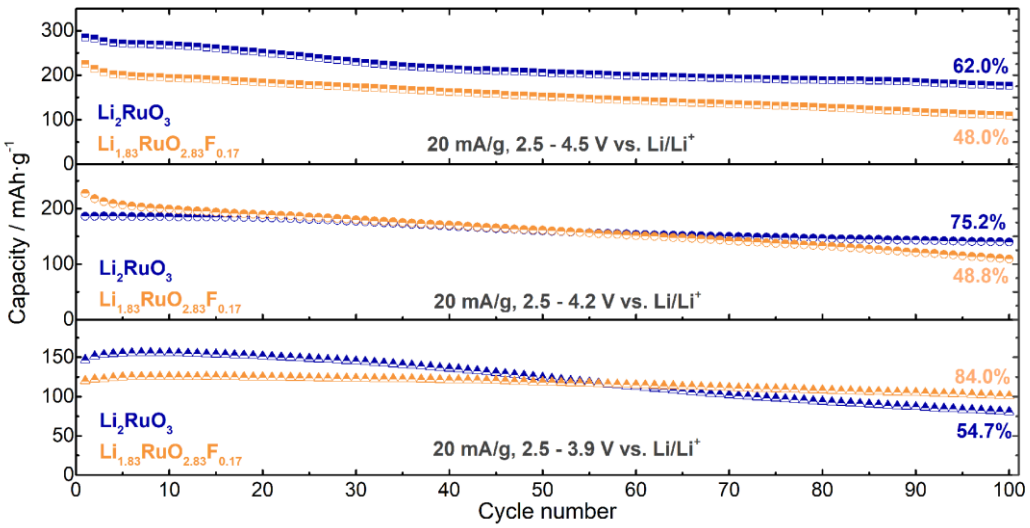


Figure 4-4. Cycling performances of Li_2RuO_3 and $Li_{1.83}RuO_{2.83}F_{0.17}$ electrodes within different potential windows.

To further investigate the effects of F-doping on long-term stability, both the Li_2RuO_3 and the $Li_{1.83}RuO_{2.83}F_{0.17}$ electrodes were cycled at the current density of 20 mA/g within different potential windows, i.e., 2.5 - 4.5 V, 2.5 - 4.2 V and 2.5 - 3.9 V vs. Li/Li^+ (**Figure 4-4**). Specifically, as displayed in **Figure 4-5**, upon cycling for 100 cycles in the potential window of 2.5 - 4.5 V vs. Li/Li^+, the capacity of the Li_2RuO_3 electrode declines from 284.8 to 176.4 mAh/g (i.e., 62.0% capacity retention), while that of the $Li_{1.83}RuO_{2.83}F_{0.17}$ electrode decays from 225.3 to 109.4 mAh/g (i.e., 48.0% capacity retention). Considering that both cation and anion redox reactions could be fully activated upon charging to 4.5 V vs. Li/Li^+, the rapid capacity decay potentially arises from the irreversible oxygen loss and TM migration.[24]

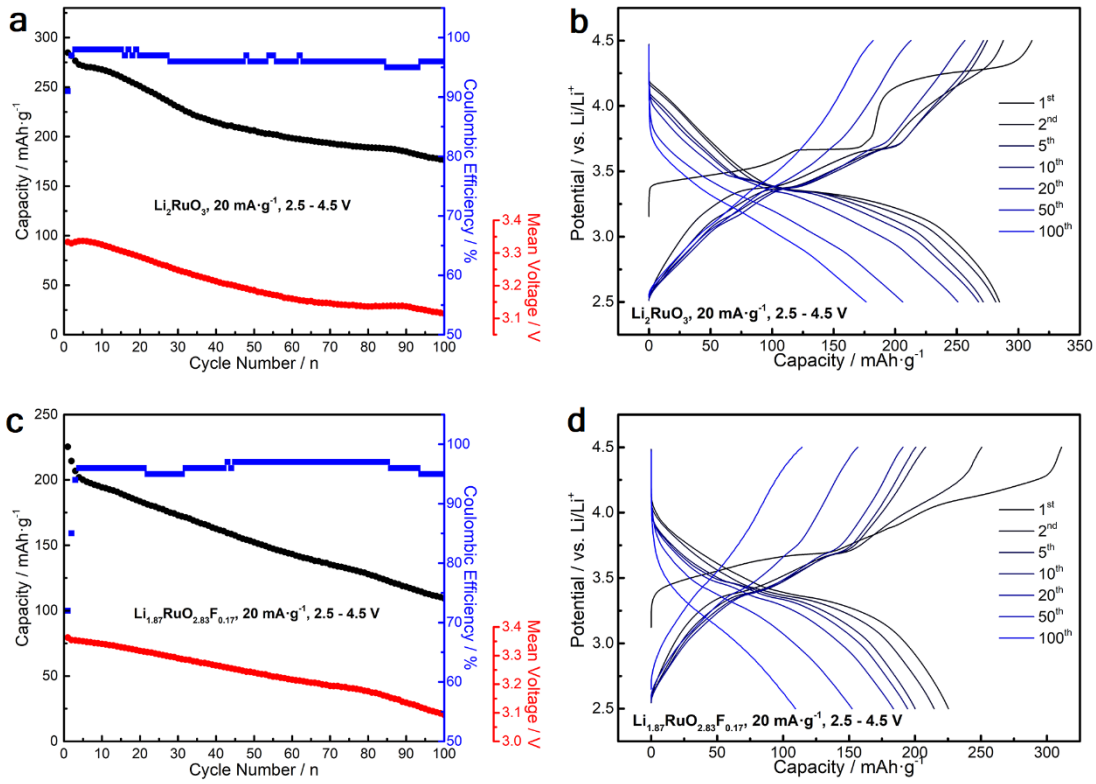


Figure 4-5. (a) Cycling performance of the Li_2RuO_3 electrode at 20 mA/g within the potential window of 2.5 - 4.5 V vs. Li/Li^+, and **(b)** corresponding GCD curves in different cycles. **(c)** Cycling performance of the $Li_{1.83}RuO_{2.83}F_{0.17}$ electrode at 20 mA/g within the potential window of 2.5 - 4.5 V vs. Li/Li^+, and **(d)** corresponding GCD curves.

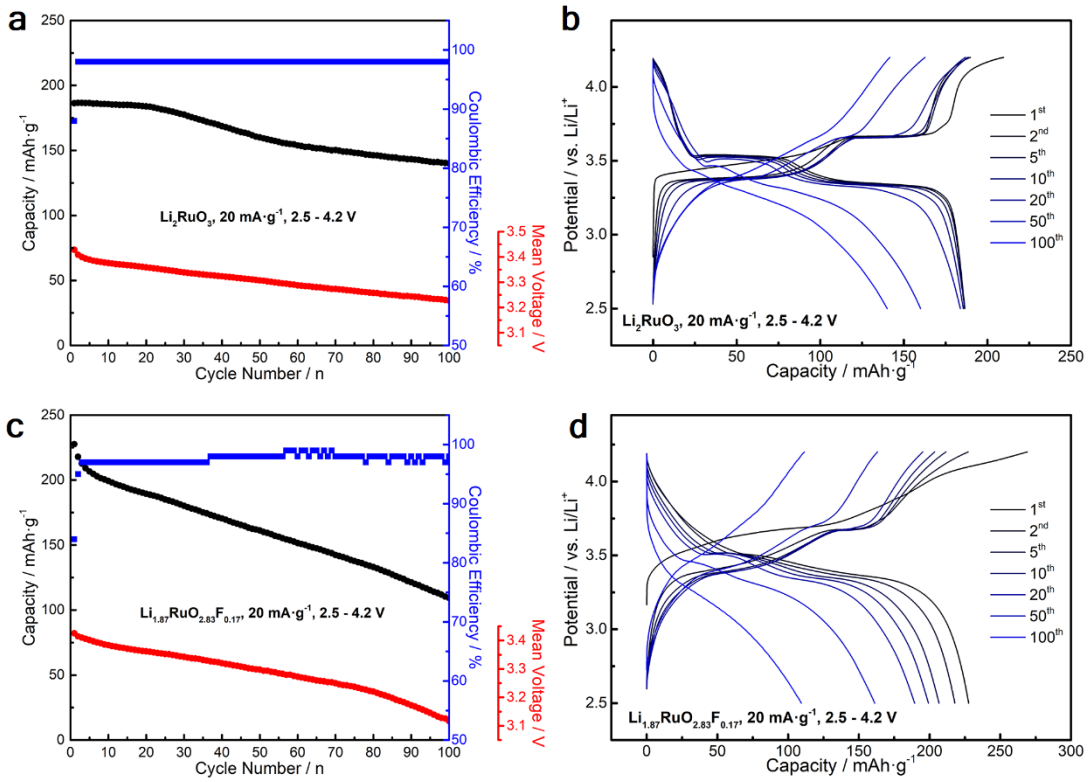


Figure 4-6. (a) Cycling performance of the Li_2RuO_3 electrode at 20 mA/g within the potential window of 2.5 - 4.2 V vs. Li/Li^+, and **(b)** corresponding GCD curves in different cycles. **(c)** Cycling performance of the $Li_{1.83}RuO_{2.83}F_{0.17}$ electrode at 20 mA/g within the potential window of 2.5 - 4.2 V vs. Li/Li^+, and **(d)** corresponding GCD curves.

In the potential window of 2.5 - 4.2 V vs. Li/Li^+, the $Li_{1.83}RuO_{2.83}F_{0.17}$ electrode delivers an initial capacity (227.7 mAh/g) higher than that of the Li_2RuO_3 electrode (186.3 mAh/g), probably resulting from the larger amount of activated oxygen for charge compensation (**Figure 4-6**). However, after 100 cycles, its capacity decays to 109.4 mAh/g with a capacity retention of 48.8%, inferior to that of the Li_2RuO_3 electrode (i.e., 140.1 mAh/g, 75.2% retention). Therefore, although F-doping energetically favors the oxygen oxidation in the deeply de-lithiated states, it unfortunately weakens the covalency of Ru-O bond, resulting in the irreversible de-coordination between Ru and O, namely the O-O dimerization and the formation of molecular O_2.[25]

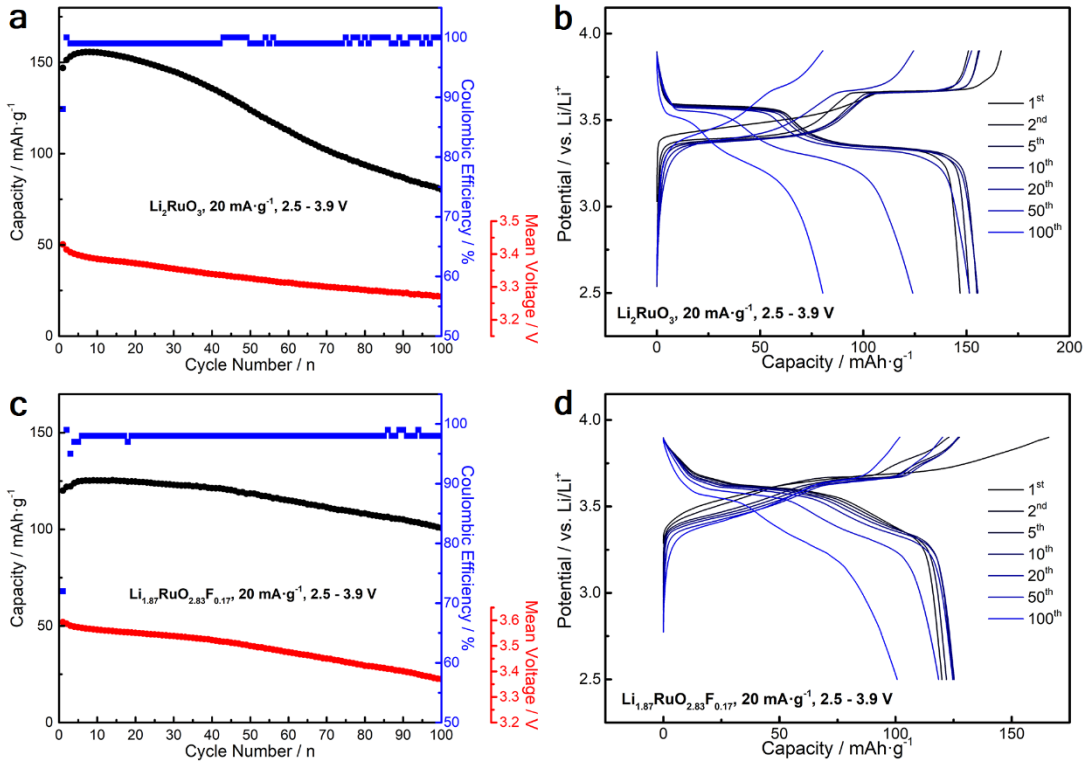


Figure 4-7. (a) Cycling performance of the Li_2RuO_3 electrode at 20 mA/g within the potential window of 2.5 - 3.9 V vs. Li/Li^+, and **(b)** corresponding GCD curves in different cycles. **(c)** Cycling performance of the $Li_{1.83}RuO_{2.83}F_{0.17}$ electrode at 20 mA/g within the potential window of 2.5 - 3.9 V vs. Li/Li^+, and **(d)** corresponding GCD curves.

Peculiar results were observed for electrodes cycled with the upper limit potential of 3.9 V vs. Li/Li^+, below which the oxygen redox activities are supposed to be untriggered or limited. As shown in **Figure 4-7**, the Li_2RuO_3 electrode exhibits reversible voltage profiles with a slope at around 3.5 V and a flat plateau at 3.67 V vs. Li/Li^+, corresponding to two-steps structural evolution upon the Ru redox activities.[26] Unexpectedly, it delivers an initial capacity of 146.9 mAh/g, which rapidly decays to 80.4 mAh/g after 100 cycles (i.e., 54.7% capacity retention). In contrast, the $Li_{1.83}RuO_{2.83}F_{0.17}$ electrode exhibits an initial capacity of 120.0 mAh/g and a much better capacity retention of 84.0 % after 100 cycles.

4.4. The effect of trace amount of F-doping in $Li_{1.95}RuO_{2.95}F_{0.05}$

To further verify the effectiveness of F-doping, $Li_{1.95}RuO_{2.95}F_{0.05}$ was prepared, in which only 1.7 % O sites are occupied by F dopants.

4.4.1. Preparation of $Li_{1.95}RuO_{2.95}F_{0.05}$

For F-doping, the raw materials were annealed at various temperatures in the range of 800 - 900 °C, details in Chapter 2. The main phase of the sample prepared at 800 °C could be indexed to the monoclinic Li_2RuO_3, both RuO_2 and LiF residues exist, though (**Figure 4-8**). In contrast, for samples annealed at 825, 850, 875, and 900 °C, all their XRD patterns exhibit no impure diffraction peaks, implying the successful F-doping.

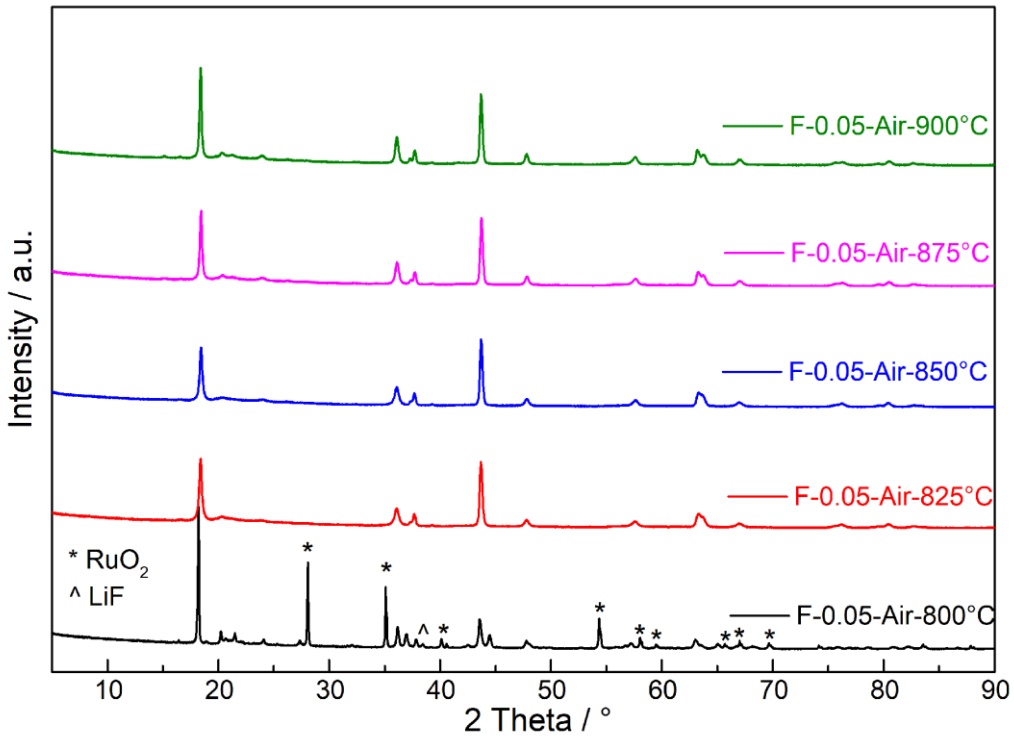


Figure 4-8. XRD patterns of $Li_{1.95}RuO_{2.95}F_{0.05}$ samples prepared at various temperatures. Impure phases in the sample prepared at 800 °C could be indexed to residual RuO_2 and LiF.

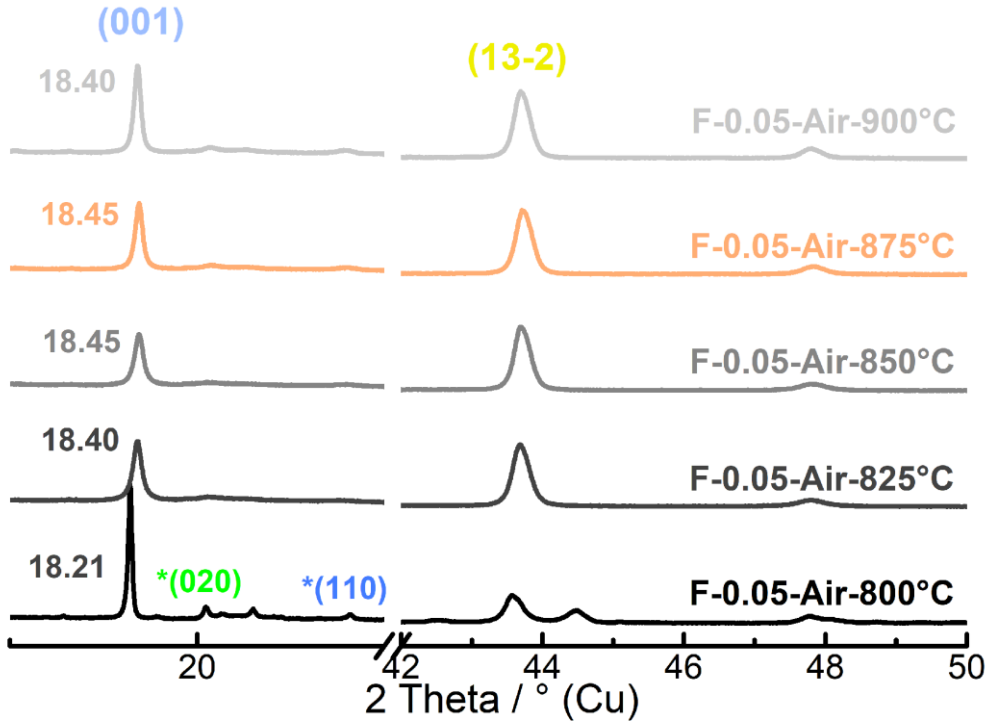


Figure 4-9. XRD patterns of $Li_{1.95}RuO_{2.95}F_{0.05}$ samples prepared at various temperatures.

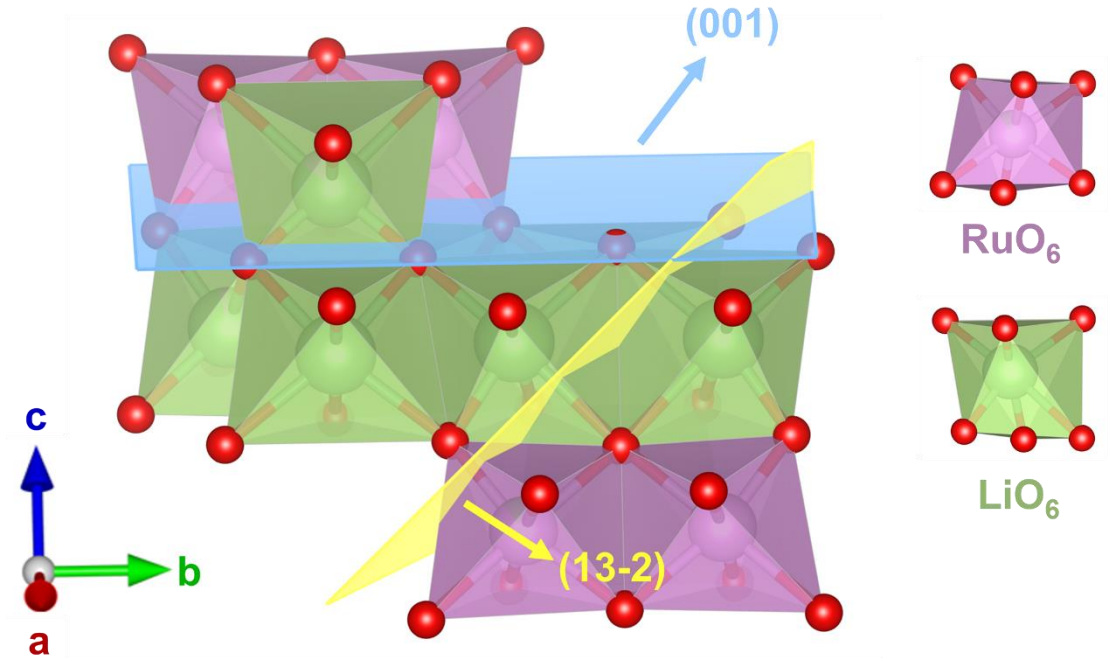


Figure 4-10. Schematic of (001) and (13-2) lattice places in the unit cell of Li_2RuO_3 with the $P2_1/m$ symmetry.

As shown in **Figure 4-9**, for those F-doped samples, (001) peaks shift to the right, revealing the decreasing interlayer spacings. Besides, F-doping alters the preferential orientation as the intensity ratio of (001)/ (13-2) decreases from 4.79 to 0.97, 0.80, 1.05, 1.30 for samples annealed at 800, 825, 850, 875, and 900 °C, respectively (**Figure 4-10** and **Table 4-3**). In addition, the decline of the superstructural peaks (e.g., *(020) and *(110)) indicates the loss of the ordered honeycomb-like local patterns.

Table 4-3. Selected XRD peak intensities in the F-doped samples

	I(001)	**I(*020)**	**I(*110)**	**I(13-2)**	**I(001)/ I(13-2)**
F-0.05-air-800	34539 (18.21°)	3123 (20.23°)	1480 (24.07°)	7214 (43.57°)	**4.79**
F-0.05-air-825	15555 (18.42°)	1398 (20.4°)	781 (23.8°)	16009 (43.68°)	**0.97**
F-0.05-air-850	13242 (18.44°)	982.5 (20.4°)	747.2 (24.01°)	16465 (43.7°)	**0.80**
F-0.05-air-875	17334 (18.45°)	1478.2 (20.37°)	1051 (23.99°)	16546 (43.71°)	**1.05**
F-0.05-air-900	22535 (18.4°)	1621.3 (20.32°)	1156.3 (23.91°)	17349 (43.69°)	**1.30**

Notes: Peak intensity refers to the background-subtracted intensity.

4.4.2. Morphology and structure of $Li_{1.95}RuO_{2.95}F_{0.05}$

Herein, the sample prepared at 875 °C was selected for further study and simply denoted as $Li_{1.95}RuO_{2.95}F_{0.05}$ in the following part. Morphologically, it is composed of polyhedral particles with sizes of several hundred nanometers (**Figure 4-11**), while all elements disperse uniformly within single particles (**Figure 4-12)**.

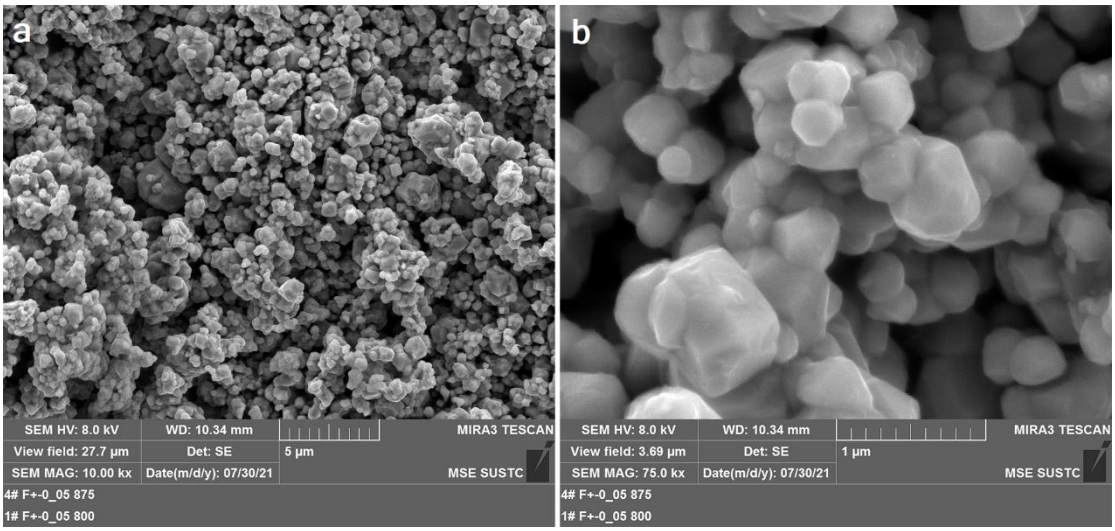


Figure 4-11. SEM images of the $Li_{1.95}RuO_{2.95}F_{0.05}$ prepared at 875 °C in air. The sale bars in **(a)** and **(b)** are 5 µm and 1 µm, respectively.

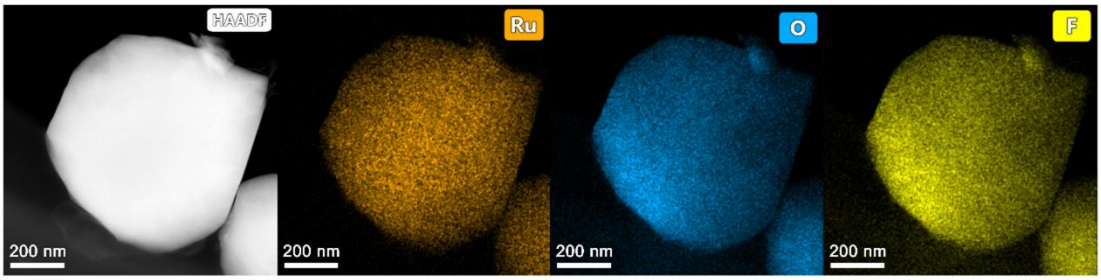


Figure 4-12. High-angle annular dark field-scanning transmission electrode microscope (HAADF-STEM) images and EDX mappings of $Li_{1.95}RuO_{2.95}F_{0.05}$ prepared at 875 °C in air. The scale bars are 200 nm.

Structural refinements manifest the increasing ratio of the intralayer Li/Ru mixing (~23 %) and the anisotropic unit cell expansion in $Li_{1.95}RuO_{2.95}F_{0.05}$, i.e., 2.78 % expansion along the *a*-axis, 0.50 % contraction along the *b*-axis, and 0.07 % shrinkage along the *c*-axis (**Table 4-4** and **Figure 4-13**).

Table 4-4. Structural parameters of pristine $Li_{1.95}RuO_{2.95}F_{0.05}$ - $P2_1/m$ symmetry

Phase: $Li_{1.95}RuO_{2.95}F_{0.05}$	**Space group: $P2_1/m$**				
Atom	Fractional coordinates			Multiplicity	Occupancy
	x	y	z		
Li1	0.7202(6)	0.25	0.9698(5)	2	0.527(9)
Li2	0.2388(3)	0.0701(4)	0.4689(5)	4	0.936(1)
Li3	0.7940(3)	0.25	0.5330(1)	2	0.936(1)
Li4	0.2639(1)	0.0768(1)	0.9955(9)	4	0.282(1)
Ru1	0.7202(6)	0.25	0.9698(5)	2	0.458(6)
Ru2	0.2388(3)	0.0701(5)	0.4689(6)	4	0.04
Ru3	0.7940(3)	0.25	0.5330(2)	2	0.04
Ru4	0.2639(2)	0.0768(1)	0.9955(9)	4	0.717(1)
O1	0.7335(7)	0.0483(7)	0.2531(7)	4	0.983
O2	0.7354(4)	0.0695(9)	0.7432(9)	4	0.983
O3	0.2164(1)	0.25	0.2189(5)	2	0.983
O4	0.2631(1)	0.25	0.7821(9)	2	0.983
F1	0.7335(8)	0.0483(7)	0.2531(7)	4	0.017
F2	0.7354(4)	0.0695(9)	0.7432(8)	4	0.017
F3	0.2164(1)	0.25	0.2189(6)	2	0.017
F4	0.2631(1)	0.25	0.7821(9)	2	0.017

Lattice parameters:

a=5.06500(17) Å, b=8.73056(10) Å, c=5.89120(39) Å;

α=90°, β=125.0584(2)°, γ=90°;

$V_{unit\ cell}$=213.247(5) Å^3, R_{wp}=4.81 %, χ^2=1.03, G.O.F.=1.02

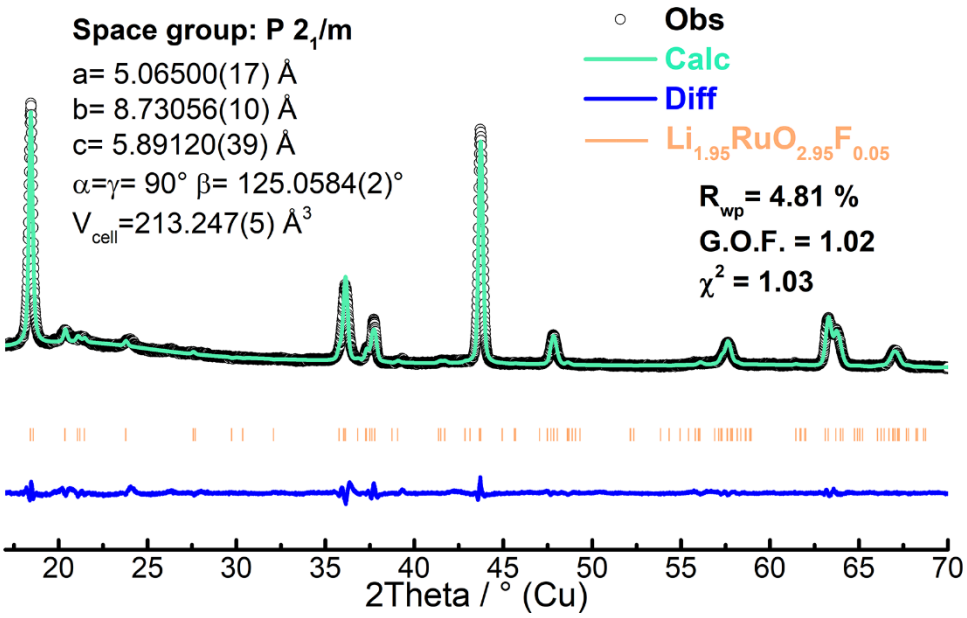


Figure 4-13. XRD patterns and Rietveld refinement results of $Li_{1.95}RuO_{2.95}F_{0.05}$.

4.4.3. Electrochemical properties of $Li_{1.95}RuO_{2.95}F_{0.05}$

Albeit trace amount, F-doping in $Li_{1.95}RuO_{2.95}F_{0.05}$ effectively changes its electrochemistry. **Figure 4-14a** displays the initial GCD and dQ/dV curves of the $Li_{1.95}RuO_{2.95}F_{0.05}$ electrode within the potential windows of 2.5 - 3.9 V and 2.5 - 4.2 V vs. Li/Li$^+$. Clearly, F-doping lowers the potential of oxygen oxidation because the sloping plateau at around 3.9 V vs. Li/Li$^+$ indicates the concurrent Ru and O redox reactions. The sharp anodic peak in dQ/dV curves implies the irreversible structural rearrangement, analogous to that in the undoped Li_2RuO_3 electrode.

When cycled in the potential window of 2.5 - 3.9 V vs. Li/Li$^+$, the capacity of the $Li_{1.95}RuO_{2.95}F_{0.05}$ electrode decreases from 149.5 to 127.0 mAh/g after 5 cycles, while the coulombic efficiency (C.E.) increases from 82.8 % to 99.0 %. Given that the capacity of the Li_2RuO_3 electrode even increases in the initial five cycles (i.e., from 146.9 to

155.1 mAh/g), such a capacity loss might originate from the irreversible oxygen activities promoted by the F dopants. As shown in **Figure 4-14b**, upon further cycling, although the Li_2RuO_3 electrode presents C.E. higher than 99.5 %, its capacity rapidly decays to 53.4 mAh/g in the first 150 cycles, which decreases to 25.1 mAh/g after 325 cycles (i.e., 16.2 % capacity retention) accompanied by the drop of C.E. to lower than 95.0 %. On the contrary, the $Li_{1.95}RuO_{2.95}F_{0.05}$ electrode displays superb long-term stability after the initial activation. Specifically, it delivers a capacity of 116.1 mAh/g after 439 cycles (i.e., 91.4 % capacity retention) with C.E. higher than 99.8 %.

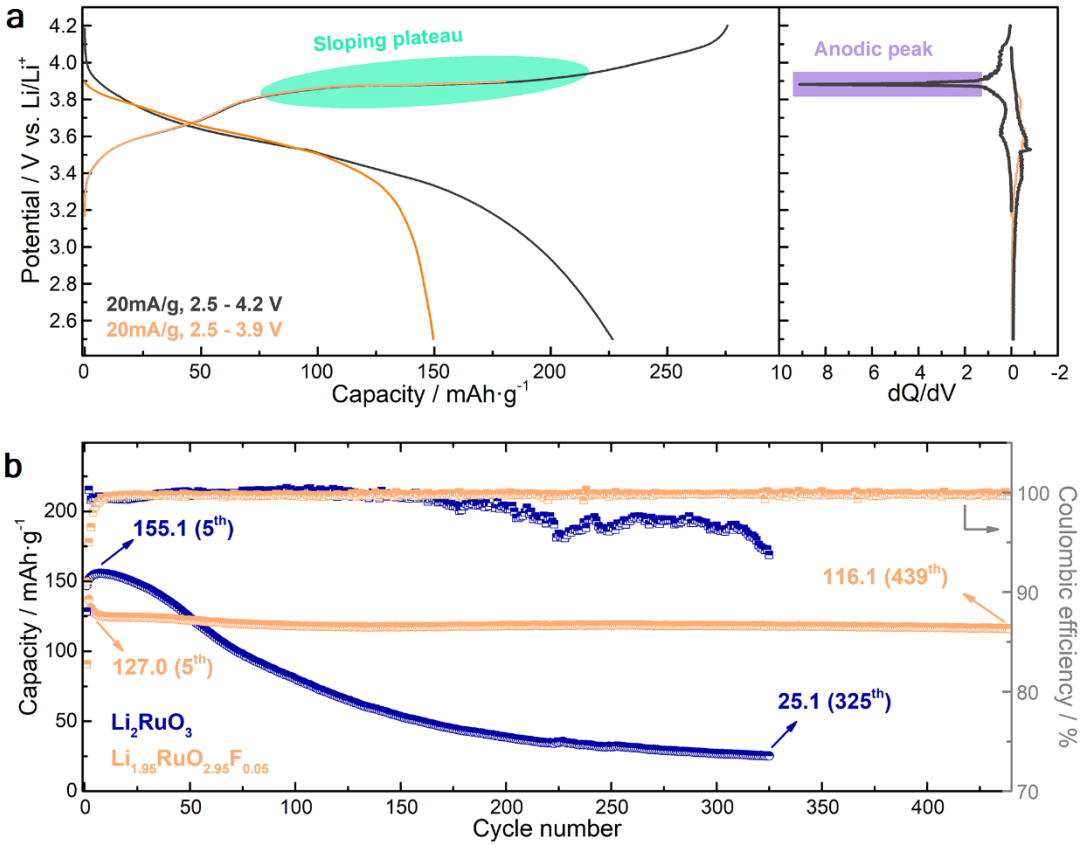


Figure 4-14. (a) GCD (left) and dQ/dV curves (right) of the $Li_{1.95}RuO_{2.95}F_{0.05}$ electrode within potential windows of 2.5 - 3.9 V and 2.5 - 4.2 V vs. Li/Li^+. The current density is 20 mA/g. **(b)** Cycling performances of Li_2RuO_3 and $Li_{1.95}RuO_{2.95}F_{0.05}$ electrodes at 20 mA/g within the potential window of 2.5 - 3.9 V vs. Li/Li^+.

4.5. The origin of stable Ru redox activities in F-doped Li_2RuO_3

The inferior stability of the pristine Li_2RuO_3 upon Ru redox activities might be attributed to the accumulation of strong interlayer repulsions and stacking faults caused by the incomplete phase transformation, as revealed in TEM and in-situ XRD studies by Han et al.[27] Generally, in the pristine Li_2RuO_3, the interlayer spacing is determined by the attractive Li-O and the repulsive O-O interactions, analogous to the layered $LiCoO_2$.[28]

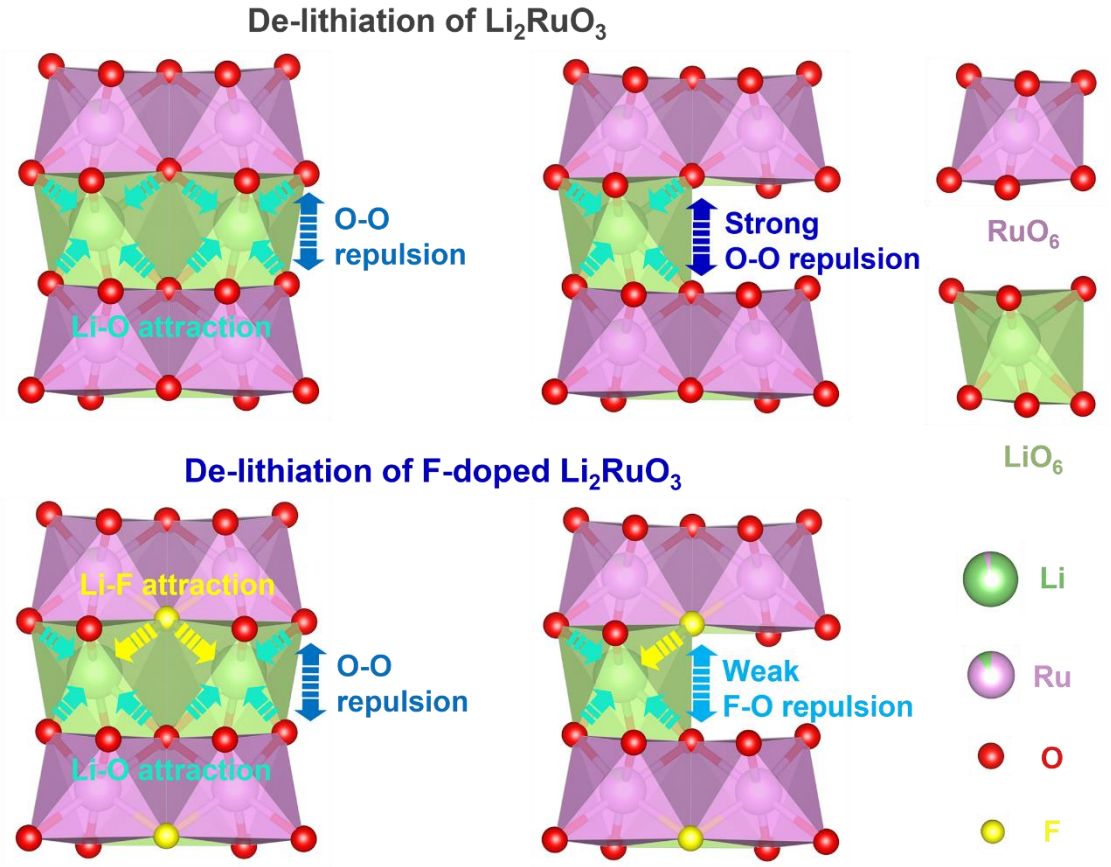


Figure 4-15. Illustrations of the interlayer interactions in the pristine and de-lithiated Li_2RuO_3 (top) and the F-doped Li_2RuO_3 (bottom). Views are from the [100] projection.

As illustrated in **Figure 4-15**, upon the Ru^{4+}-to-Ru^{5+} oxidation, the stronger interaction between Ru^{5+}-O^{2-} leads to the contraction of the RuO_2 slabs. Meanwhile, with the decreasing screening effects from the Li^+ ions, the interlayer spacing between the RuO_2 slabs tends to increase because of the strong repulsion between the O layers. Commonly, to relax the increasing interlayer repulsion, the RuO_2 slabs tend to glide along the basal plane (ab-plane), while the space group changes from monoclinic to rhombohedral (i.e., the flat plateau at around 3.67 V vs. Li/Li^+).[29] Such a biphasic process inevitably results in nano-strains at phase boundaries, which gradually accumulate and cause structural degradation upon cycling.

By contrast, in the F-doped samples, for the Ru redox activities, notwithstanding the loss of the counteracting Li-O attraction upon de-lithiation, having F dopants on O sites weakens the repulsive interaction between the O layers. Besides, as revealed by the structural analyses, F-doping induces local disordering (e.g., Li/Ru mixing) and decreases the intensity ratio of (001)/ (13-2) diffraction peaks. From this perspective, both the weak F-O repulsion and the altered preferential orientation could mitigate the strain accumulation along the *c*-axis, thereby suppressing the formation of nano-cracks along the basal plane (ab-plane). Therefore, despite its ineffectiveness in stabilizing ARRs, F-doping turns out to be beneficial to improving the stability of Li_2RuO_3 during the Ru redox reactions.

4.6. Summary and outlook

Traditionally, in LRCMs, triggering the ARRs is believed to be the origin of capacity decay and voltage fading due to the parasitic oxygen loss and TM migration. However, not activating the oxygen redox activities does not necessarily guarantee better long-term performances.

In this chapter, we find that the pristine Li_2RuO_3 electrode shows the worst capacity retention solely upon the Ru redox reactions. Such an inferior property is suggested to originate from the strain accumulation upon the removal of the 1^{st} Li^+, which has been overlooked. In addition, we demonstrate that F-doping is an effective way to prohibit such Ru redox-induced structural degradations. Firstly, the weaker F-O repulsion could buffer the strong repulsive interaction between O layers, which is supposed to be the driving force of strain formation. Besides, F-doping increases the level of local disordering as evidenced by the loss of superstructure peaks and suppresses the preferential growth along the *c*-axis, thereby mitigating the strain accumulation along the basal plane (*ab*-plane).

In terms of future work, in-situ XRD tests should be conducted to investigate the structural evolutions in real time. Besides, the strain accumulation might be quantitively evaluated via Rietveld refinement of XRD patterns. Moreover, as demonstrated in Chapter 3, Raman spectroscopy sensitive to local patterns should be a good tool to monitor the local coordination evolutions in those F-doped samples.

Finally, although F-doping favors the stability of Ru redox, it unfortunately deteriorates the stability of ARRs. From this perspective, striking the balance between liability and stability of the oxygen redox activities is still a long-lasting dilemma in exploiting the extra capacity from LRCMs.

4.7. References

1. M. Sathiya, G. Rousse, K. Ramesha, C. P. Laisa, H. Vezin, M. T. Sougrati, M. L. Doublet, D. Foix, D. Gonbeau, W. Walker, A. S. Prakash, M. Ben Hassine, L. Dupont, and J.-M. Tarascon, *Nat. Mater.*, 2013, **12**, 827-835.
2. Q. Li, D. Ning, D. Zhou, K. An, G. Schuck, D. Wong, W. Kong, C. Schulz, G. Schumacher, and X. Liu, *Chem. Mater.*, 2020, **32**, 9404-9414.
3. M. Sathiya, A. M. Abakumov, D. Foix, G. Rousse, K. Ramesha, M. Saubanere, M. L. Doublet, H. Vezin, C. P. Laisa, A. S. Prakash, D. Gonbeau, G. VanTendeloo, and J. M. Tarascon, *Nat. Mater.*, 2015, **14**, 230-238.
4. T. Liu, J. Liu, L. Li, L. Yu, J. Diao, T. Zhou, S. Li, A. Dai, W. Zhao, S. Xu, Y. Ren, L. Wang, T. Wu, R. Qi, Y. Xiao, J. Zheng, W. Cha, R. Harder, I. Robinson, J. Wen, J. Lu, F. Pan, and K. Amine, *Nature*, 2022, **606**, 305-312.
5. X. Liu, G.-L. Xu, V. S. C. Kolluru, C. Zhao, Q. Li, X. Zhou, Y. Liu, L. Yin, Z. Zhuo, A. Daali, J.-J. Fan, W. Liu, Y. Ren, W. Xu, J. Deng, I. Hwang, D. Ren, X. Feng, C. Sun, L. Huang, T. Zhou, M. Du, Z. Chen, S.-G. Sun, M. K. Y. Chan, W. Yang, M. Ouyang, and K. Amine, *Nat. Energy*, 2022, **7**, 808-817.
6. A. J. Merryweather, C. Schnedermann, Q. Jacquet, C. P. Grey, and A. Rao, *Nature*, 2021, **594**, 522-528.
7. Y. Bi, J. Tao, Y. Wu, L. Li, Y. Xu, E. Hu, B. Wu, J. Hu, C. Wang, J.-G. Zhang, and J. Xiao, *Science*, 2020, **370**, 1313-1317.
8. Z. Wu, Y. Ni, S. Tan, E. Hu, L. He, J. Liu, M. Hou, P. Jiao, K. Zhang, F. Cheng, and J. Chen, *J. Am. Chem. Soc.*, 2023, **145**, 9596-9606.
9. C. L., W. Kan, H. Xie, Y. Jiang, Z. Zhao, C. Zhu, Y. Xia, J. Zhang, K. Xu, D. Mu, and F. Wu, *Adv. Sci.*, 2019, **6**, 1801406.
10. P. Vanaphuti, J. Chen, J. Cao, K. Bigham, B. Chen, L. Yang, H. Chen, and Y. Wang, *ACS Appl. Mater. Interfaces*, 2019, **11**, 37842-37849.
11. Z. Lun, B. Ouyang, D. Kwon, Y. Ha, E. E. Foley, T. Huang, Z. Cai, H. Kim, M. Balasubramanian, Y. Sun, J. Huang, Y. Tian, H. Kim, B. D. McCloskey, W. Yang, R. J. Clément, H. Ji, and G. Ceder, *Nat. Mater.*, 2021, **20**, 214-221.
12. J. Lee, D. A. Kitchaev, D. Kwon, C. Lee, J. K. Papp, Y. Liu, Z. Lun, R. J. Clément, T. Shi, B. D. McCloskey, J. Guo, M. Balasubramanian, and G. Ceder, *Nature*, 2018, **556**, 185-190.
13. J. Lee, and D. Kim, *Energy Environ. Sci.*, 2022, **15**, 4554-4560.

14. P. H. Duvigneaud, and D. Reinhard-Derie, *Thermochim. Acta*, 1981, **51**, 307-314.
15. Y. Miura, Y. Yasui, M. Sato, N. Igawa, and K. Kakurai, *J. Phys. Soc. Jpn.*, 2007, **76**, 033705.
16. Y. Zuo, H. Shang, J. Hao, J. Song, F. Ning, K. Zhang, L. He, and D. Xia, *J. Am. Chem. Soc.*, 2023, **145**, 5174-5182.
17. P. Yan, J. Zheng, M. Gu, J. Xiao, J.-G. Zhang, and C. Wang, *Nat. Commun.*, 2017, **8**, 14101.
18. B. Li, R. Shao, H. Yan, L. An, B. Zhang, H. Wei, J. Ma, D. Xia, and X. Han. *Adv. Funct. Mater.,* 2016, **26**, 1330-1337.
19. F. Ning, B. Li, J. Song, Y. Zuo, H. Shang, Z. Zhao, Z. Yu, W. Chu, K. Zhang, G. Feng, X. Wang, and D. Xia, *Nat. Commun.*, 2020, **11**, 4973.
20. Y. Yu, P. Karayaylali, D. Sokaras, L. Giordano, R. Kou, C.-J. Sun, F. Maglia, R. Jung, F. S. Gittleson, and Y. Shao-Horn, *Energy Environ. Sci.*, 2021, **14**, 2322-2334.
21. M. Sathiya, K. Ramesha, G. Rousse, D. Foix, D. Gonbeau, A. S. Prakash, M. L. Doublet, K. Hemalatha, and J.-M. Tarascon, *Chem. Mater.,* 2013, **25**, 1121-1131.
22. Y. Yu, P. Karayaylali, S. H. Nowak, L. Giordano, M. Gauthier, W. Hong, R. Kou, Q. Li, J. Vinson, T. Kroll, D. Sokaras, C.-J. Sun, N. Charles, F. Maglia, R. Jung, and Y. Shao-Horn, *Chem. Mater.*, 2019, **31**, 7864-7876.
23. T. Seaby, T.-E. Lin, Y.-X. Hu, Q.-H. Yuan, and L.-Z. Wang, *Rare Metals*, 2022, **41**, 1771-1796.
24. W. Hua, S. Wang, M. Knapp, S. J. Leake, A. Senyshyn, C. Richter, M. Yavuz, J. R. Binder, C. P. Grey, H. Ehrenberg, S. Indris, and B. Schwarz, *Nat. Commun.*, 2019, **10**, 5365.
25. R. A. House, J.-J. Marie, J. Park, G. J. Rees, S. Agrestini, A. Nag, M. Garcia-Fernandez, K.-J. Zhou, and P. G. Bruce, *Nat. Commun.*, 2021, **12**, 2975.
26. G. Choi, J. Lee, S. Koo, S. Park, and D. Kim, *Cell Rep. Phys. Sci.*, 2021, **2**, 100508.
27. M. Han, Z. Liu, X. Shen, L. Yang, X. Shen, Q. Zhang, X. Liu, J. Wang, H.-J. Lin, C.-T. Chen, C.-W. Pao, J.-L. Chen, Q. Kong, X. Yu, R. Yu, L. Gu, Z. Hu, X. Wang, Z. Wang, and L. Chen, *Adv. Energy Mater.,* 2020, **10**, e2002631.
28. J. Li, C. Lin, M. Weng, Y. Qiu, P. Chen, K. Yang, W. Huang, Y. Hong, J. Li, M. Zhang, C. Dong, W. Zhao, Z. Xu, X. Wang, K. Xu, J. Sun, and F. Pan, *Nat. Nanotechnol.*, 2021, **16**, 599-605.
29. F. Zheng, S. Zheng, P. Zhang, X. Zhang, S. Wu, Y. Yang, and Z.-H. Zhu, *J. Phys. Chem. C*, 2019, **123**, 13491-13499.

CHAPTER 5. A METASTABLE O6-PHASE WITH STABLE CATION AND ANION REDOX REACTIONS

Although Li_2RuO_3 studied in the previous two chapters is a good model to investigate the mechanisms of the oxygen redox activities, the 4d Ru is expensive and unlikely to be widely used for commercial purposes. Therefore, from the perspective of practical applications, the 3d Mn-based lithium rich manganese oxides (LRMOs) are more promising. However, one of the major drawbacks of triggering the anion redox reactions (ARRs) in LRMOs is the irreversible Mn migration in the deeply de-lithiated state, which is energetically favorable in traditional O3-type structures.

In this chapter, to solve this problem, we have demonstrated a metastable O6-type structure, in which the face-sharing local geometry suppresses the interlayer Mn migration and favors the structural stability. Specifically, the O6-type $Li_{0.693}[Li_{0.153}Ni_{0.190}Mn_{0.657}]O_2$ shows stable cation and anion redox reactions and exhibits excellent cycling performances without severe capacity fading or voltage decay. To understand the hidden mechanisms of its superior stability, multimodal characterization techniques and tests have been carried out, including Rietveld refinement, TEM, in-situ/ ex-situ XRD, in-situ Raman, ex-situ XPS, ex-situ XAS, ex-situ EPR and electrochemical tests.

5.1. Introduction

Lithium rich manganese oxides (LRMOs) are promising candidates for cathode materials in next generation batteries because of their high capacities (>250 mAh/g) contributed by both cation and anion redox reactions (ARRs).[1,2] Nonetheless, triggering the ARRs in LRMOs jeopardizes their long-term stabilities due to irreversible oxygen loss and transition metal (TM) migration.[3-5]

In typical O3-type LRMOs, the lattice oxygen (O^{2-}) can be oxidized ultimately to molecular O_2 upon de-lithiation, which releases from bulk particles.[6] Meanwhile, because some TM sites are occupied by Li ions to activate oxygen redox via forming Li-O-Li or Li-O-vacancy configurations,[7,8] TM ions are prone to migrate either within the TM layers or into the Li layers, both of which are thermodynamically favorable in the deeply de-lithiated states.[9] For the intralayer migration, TM ions tend to migrate to adjacent octahedral Li vacancies, thereby destroying the ordered local patterns (e.g., honeycomb-like superstructures) and inducing voltage hysteresis in the 1st discharge.[10] Approaches to tuning TM/Li arrangement, e.g., tailoring ribbon-like superstructures and building totally disordered local patterns,[11,12] have been demonstrated to be effective in mitigating the intralayer TM/Li mixing. For the interlayer TM migration, once TM ions have entered the intermediate tetrahedral sites in the Li layers, their migration into adjacent octahedral sites to form TM_{Li}-V_{TM} anti-site defects is inevitable and irreversible.[13] Therefore, TM ions trapped in the Li layers lead to the layered-to-spinel phase transformation, which is thought to be the origin of voltage decay.[14]

Although various methods, e.g., local structure design, cation/ anion doping and surface coating, have been conducted to improve the electrochemical performance of O3-type LRMOs,[15-17] preventing the cumulative spinel phase formation is still challenging upon long-term cycling.

Recently, reversible interlayer migrations of TM ions have been demonstrated in O2-type LRMOs thanks to their face-sharing local structures.[18] Although both O3-type and O2-type structures are similarly built up via the layer-by-layer stacking of LiO_2 and TMO_2 slabs, LiO_6 octahedra only share edges with adjacent TMO_6 octahedra in the former, whereas they share both edges and faces with TMO_6 octahedra in the latter (**Figure 5-1**).[19] Therefore, in O2-type LRMOs, it needs to overcome higher energy penalties for TM ions to migrate from intermediate tetrahedral sites to octahedral sites, owing to the large electrostatic repulsion between face-sharing TM ions.[20]

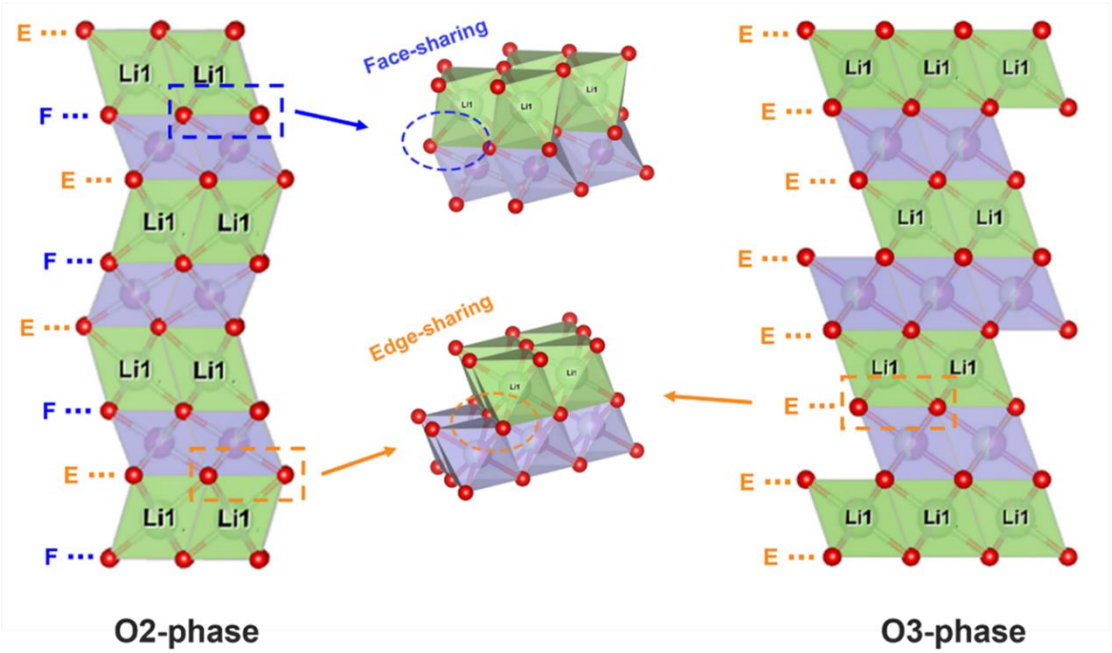


Figure 5-1. Schematic illustration of O2-type and O3-type structures. E and F denote edge-sharing and face-sharing planes between octahedral LiO_6 and octahedral TMO_6.

In this chapter, we report an O6-type $Li_{0.693}[Li_{0.153}Ni_{0.190}Mn_{0.657}]O_2$, which is an isoform of the O2-type structure and also contains shared faces between adjacent TMO_6 octahedra and LiO_6 octahedra. The O6-phase has been captured as an intermediate phase upon de-/lithiation or thermal treatment of O2-type cathode materials.[21,22] However, because it is metastable, this is, to our knowledge, the first demonstration of using a directly synthesized O6-type as a cathode material to investigate both cation and anion redox reactions. Specifically, when tested as the cathode material, this material delivers a capacity of around 250 mAh/g (10 mA/g, 2.0 - 4.8 V vs. Li/Li^+). Furthermore, upon cycling at the current density of 100 mA/g in the fluorinated electrolyte, it shows an initial capacity of 194.9 mAh/g and 96.0 % capacity retention after 100 cycles without severe voltage decay and spinel phase formation.

Careful examinations reveal that the metastable O6-type structure potentially converts to O2-type structures in either deeply de-lithiated or deeply lithiated states. Interestingly, the as-suggested O6-to-O2 phase transformations are highly reversible because they only involve the gliding of TMO_2 slabs without breaking TM-O bonds, meaning that the face-sharing geometry is retained in the full de-/lithiation process. Considering that the formation of TM vacancies potentially favors the release of gaseous O_2 and vice versa, mitigating irreversible TM migrations is critically important when tapping into ARRs in LRMOs. Therefore, we believe that the O6-type structure reported in this work provides another degree of freedom for designing other cathode materials with ARRs.

5.2. Preparation and characterization of the O6-phase

As illustrated in **Figure 5-2**, the metastable O6-type $Li_{0.693}[Li_{0.153}Ni_{0.190}Mn_{0.657}]O_2$ was prepared via a facile ion-exchange process followed by a thermal treatment at a medium temperature, as detailed in Chapter 2. Multiple techniques have been used to characterize the properties of the as-prepared materials, namely XRD, neutron diffraction (ND), ICP-MS, SEM, TEM, XPS, TGA-DSC, and Rietveld refinement.

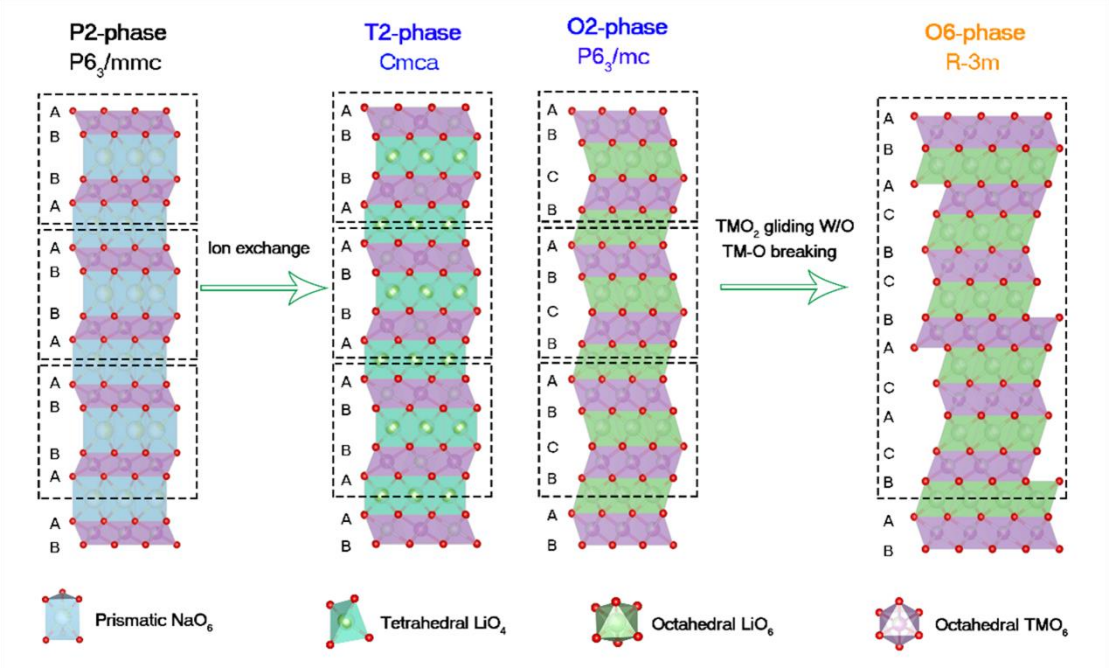


Figure 5-2. Schematic illustration of preparing the metastable O6-phase.

5.2.1. Preparation in three steps

Firstly, the P2-type precursor was synthesized through a traditional solid reaction method. Its composition and structure were determined by ICP-MS test and Rietveld refinement of its XRD patterns, respectively (details in **Figure 5-3**, **Table 5-1** and **5-2**). In the P2-type structure ($P6_3/mmc$ symmetry), NaO_6 prisms stack alternately with TMO_6 octahedra in the ABBA pattern along the *c*-axis.[23]

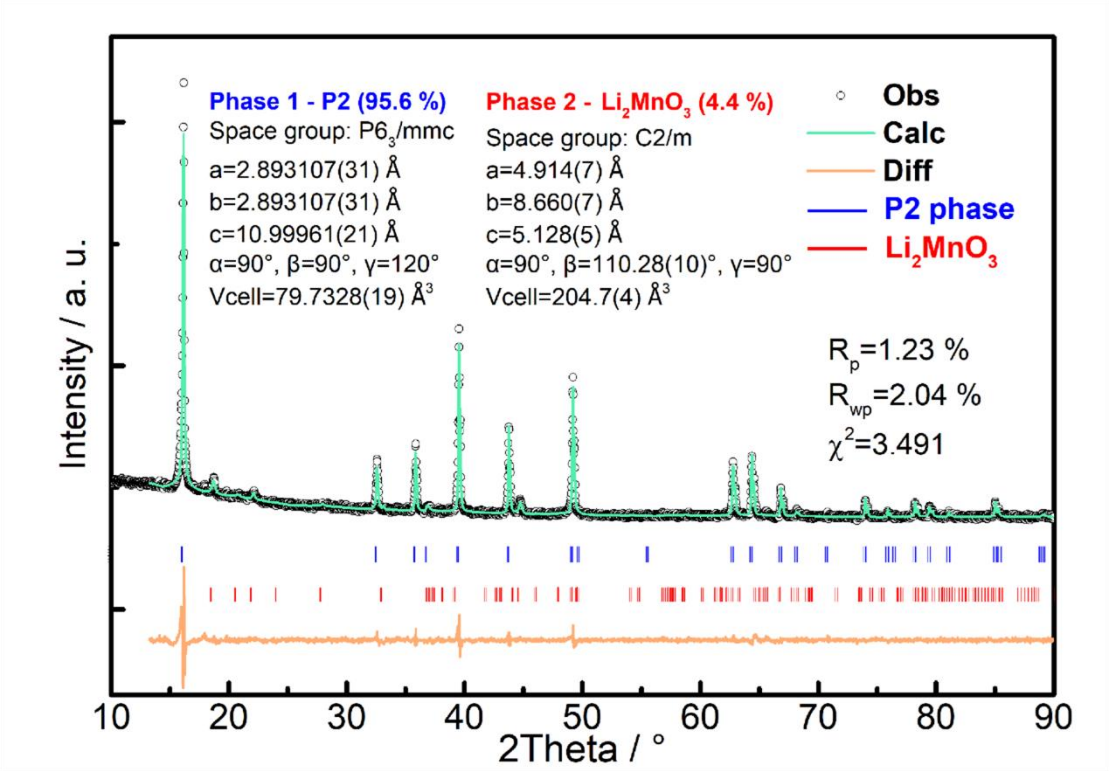


Figure 5-3. Rietveld refinement of XRD patterns of the P2-type precursor.

Table 5-1. ICP-MS results

	7 Li [He]		**23 Na [He]**		**55 Mn [He]**		**60 Ni [He]**	
	Conc. [ppb]	Conc. RSD	Conc. [ppb]	Conc. RSD	Conc. [ppb]	Conc. RSD	Conc. [ppb]	Conc. RSD
P2-precursor	59.856 1(9)	4.8649 (2)	610.98 16(5)	3.1460 (6)	1291.0 716(5)	2.5362 (7)	405.14 08(8)	2.5272 (8)
O6-phase	278.38 24(9)	1.0964 (1)	<0.000	N/A	1697.2 955(5)	0.8950 (5)	537.53 92(7)	0.8659 (2)

Table 5-2. Structural parameters of the P2-type precursor

Phase 1: P2-$Na_{0.745}[Li_{0.153}Ni_{0.194}Mn_{0.626}]O_2$			Space group: $P6_3/mmc$		wt=95.6%
Atom	Fractional coordinates			Multiplicity	Occupancy
	x	y	z		
Na1	0	0	1/4	2	0.237(1)
Na2	1/3	2/3	1/4	2	0.475(1)
Li1	0	0	0	2	0.191(1)
Li2	0	0	1/4	2	0.039(1)
Mn1	0	0	0	2	0.628(1)
Ni1	0	0	0	2	0.181(1)
O1	2/3	1/3	0.0861(5)	4	1
Lattice parameters: a=2.893107(31) Å, b=2.893107(31) Å, c=10.99961(21) Å; α=90°, β=90°, γ=120°; $V_{unit\ cell}$=79.7328(19) $Å^3$					

Phase 2: Li_2MnO_3			Space group: C2/m		wt=4.4%
Atom	Fractional coordinates			Multiplicity	Occupancy
	x	y	z		
Li1	0	1/2	0	2	1
Li2	0	0	1/2	2	1
Li3	0	0.6606(1)	1/2	4	1
Mn1	0	0.1670(8)	0	4	1
O1	0.2189(1)	0	0.2273(1)	4	1
O2	0.2541(1)	0.3211(9)	0.2233(1)	8	1
Lattice parameters: a=4.914(7) Å, b=8.660(7) Å, c=5.128(5) Å; α=90°, β=110.28(10)°, γ=90°; $V_{unit\ cell}$=204.7(4) $Å^3$					

Secondly, via a facile Na^+/Li^+ ion-exchange method, the O2+T2-type $Li_{0.673}[Li_{0.162}Ni_{0.188}Mn_{0.650}]O_2$ was synthesized from the sodium-deficient P2-phase (**Figure 5-4**). Usually, upon Na^+/Li^+ ion-exchange, P2-type precursors can transform into either T2- or O2-type structures, depending on the interlayer spacing between TMO_2 slabs.[24] The former has a Cmca structure with tetrahedral LiO_4 and octahedral TMO_6 stacking along the *c*-axis in the pattern of ABBA, while the latter has a $P6_3/mc$ structure with LiO_6 and TMO_6 octahedra stacking in the ABCB pattern.[25-27]

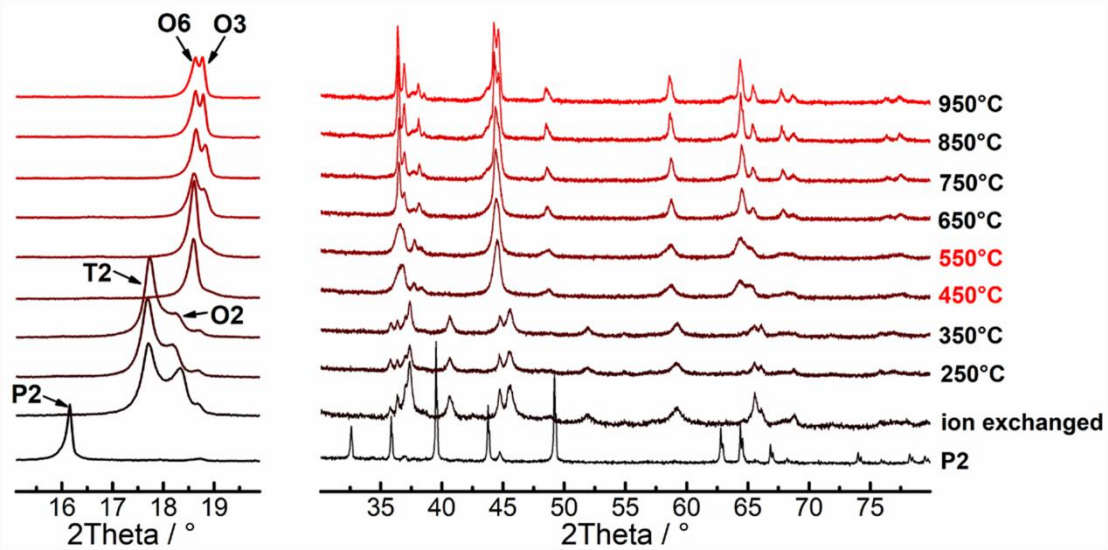


Figure 5-4. XRD patterns of P2-type precursor, the ion-exchanged T2+O2 mixture and the reannealed samples at various temperatures.

Finally, to obtain the metastable O6-phase, the O2+T2 mixture was reheated at a moderate temperature (550 °C), which was selected via thermal and structural analyses. Upon heating up to 350 °C, the O2+T2 mixture lost 0.7 % weight according to the thermogravimetric (TG) curve presumably due to the evaporation of adsorbed water (**Figure 5-5**). Meanwhile, XRD results reveal that the annealed sample is still mainly composed of T2- and O2-phases. However, upon further heating up to 550 °C,

although no weight loss was observed, an endothermic peak appeared at around 400 °C in the differential scanning calorimetry (DSC) curve. According to XRD patterns, such a process is accompanied by a phase transformation to form a new phase (i.e., the O6-phase). The new phase is metastable and tends to decompose at higher temperatures (i.e., > 550 °C) with 3.8 % weight loss upon heating up to 1000 °C, probably resulting from O_2 release and the O3-phase formation.[21,28]

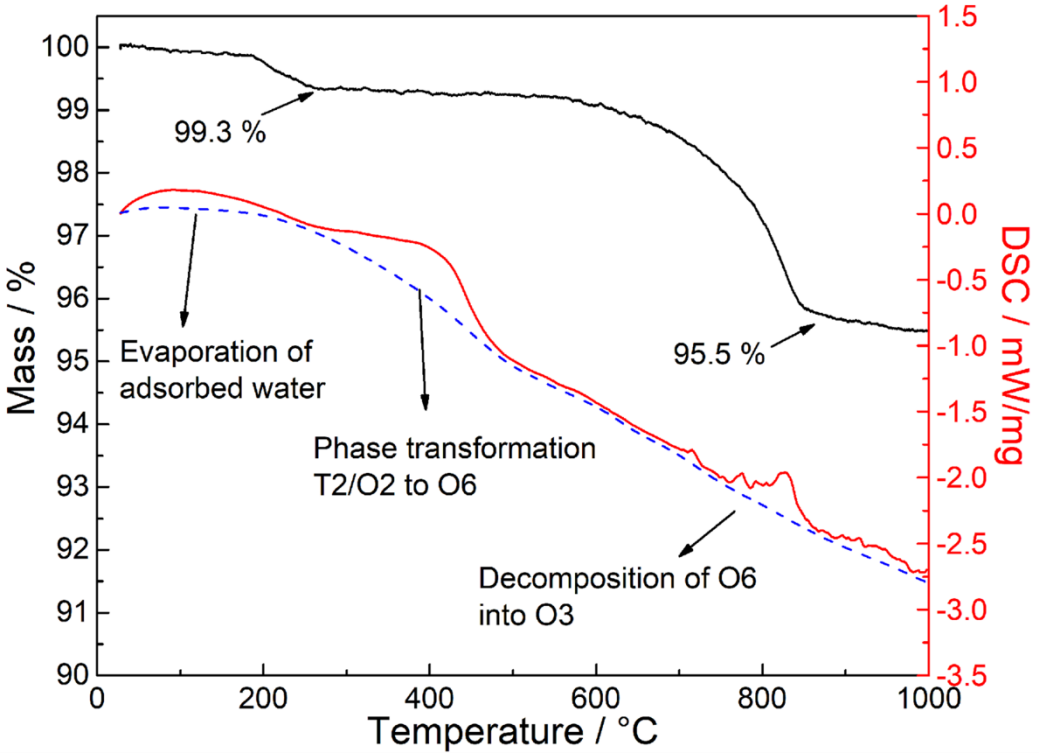


Figure 5-5. Thermal analysis of the O2+T2 mixed phase. The black solid line represents the thermogravimetric (TG) curve. The red solid line represents the differential scanning calorimetry (DSC) curve, while the blue dashed line represents the baseline. Those tests were performed in the protective argon atmosphere at the heating rate of 5°C/min.

As illustrated in **Figure 5-6**, although both O6- and O3-phases have R-3m symmetries, the former involves the ABACBCBACACB pattern with alternative LiO_2 and TMO_2 slabs stacking along the *c*-axis, while in the latter, LiO_6 octahedra and TMO_6 octahedra stack

alternatively along the *c*-axis in the pattern of ABCABC. Moreover, in the O6-type structure, along the *c*-axis, LiO_6 octahedra share edges with adjacent TMO_6 octahedra on one side and share faces with TMO_6 octahedra on the other side. However, in the O3-type structure, along the *c*-axis, LiO_6 octahedra only share edges with adjacent TMO_6 octahedra. Therefore, the O6-to-O3 phase transformation involves the cleavage of TM-O bonds during the gliding of TMO_2 slabs and releases O_2.

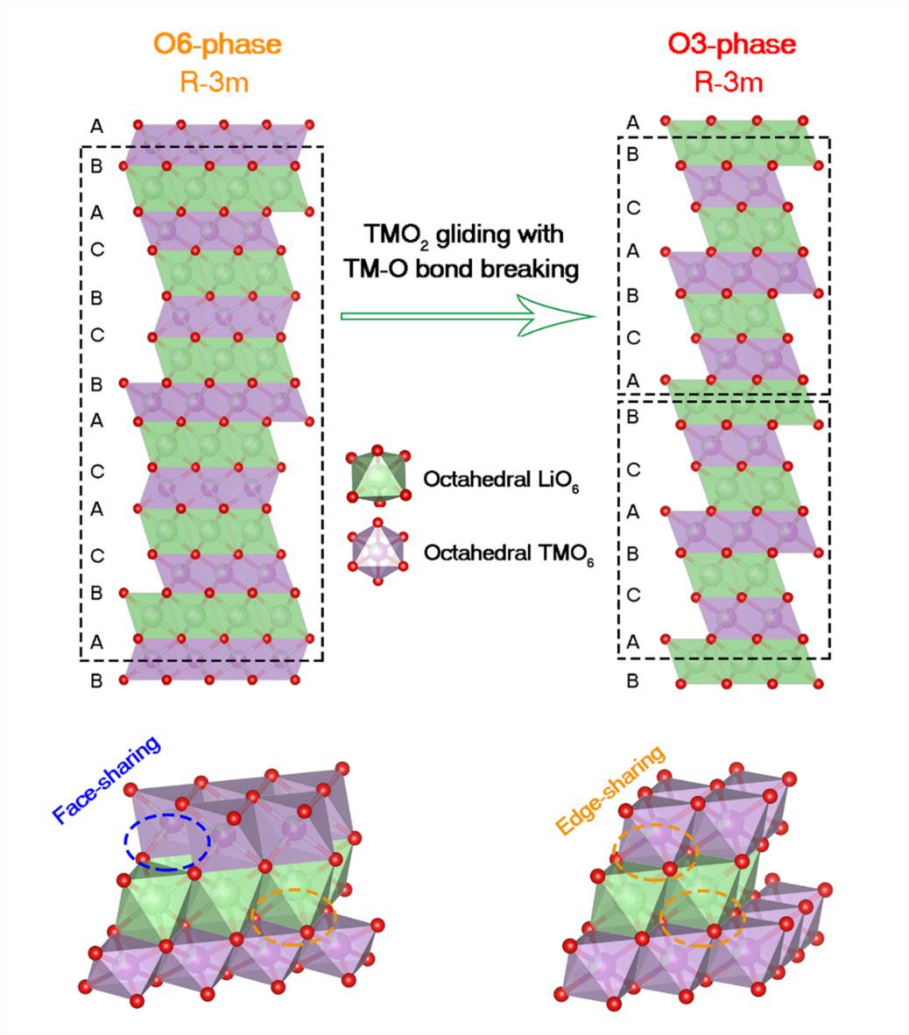


Figure 5-6. Schematic illustration of the O6-to-O3 phase transformation.

5.2.2. Formation mechanisms

Herein, to better understand the formation of the O6-phase, its relationship with the

O2-phase is introduced. As illustrated in **Figure 5-7**, to form the O2-phase from the P2-type precursor, every the other TMO_2 slab glides toward the (1/3, 2/3, c) direction, while Na^+ ions at prismatic sites are replaced by Li^+ ions at octahedral sites. It is noteworthy that every the other TMO_2 slabs possibly glide toward the (2/3, 1/3, c) direction, producing the O2'-phase (**Figure 5-8**). Both the O2- and the O2'-phases are superimposed with each other via rotating 180° with the axis of symmetry, meaning that they are crystallographically identical. In the ideal O2- and O2'-phases, a LiO_6 octahedron shares a face with a TMO_6 octahedron on the one side and shares three edges with three TMO_6 octahedra on the other side, and vice versa.

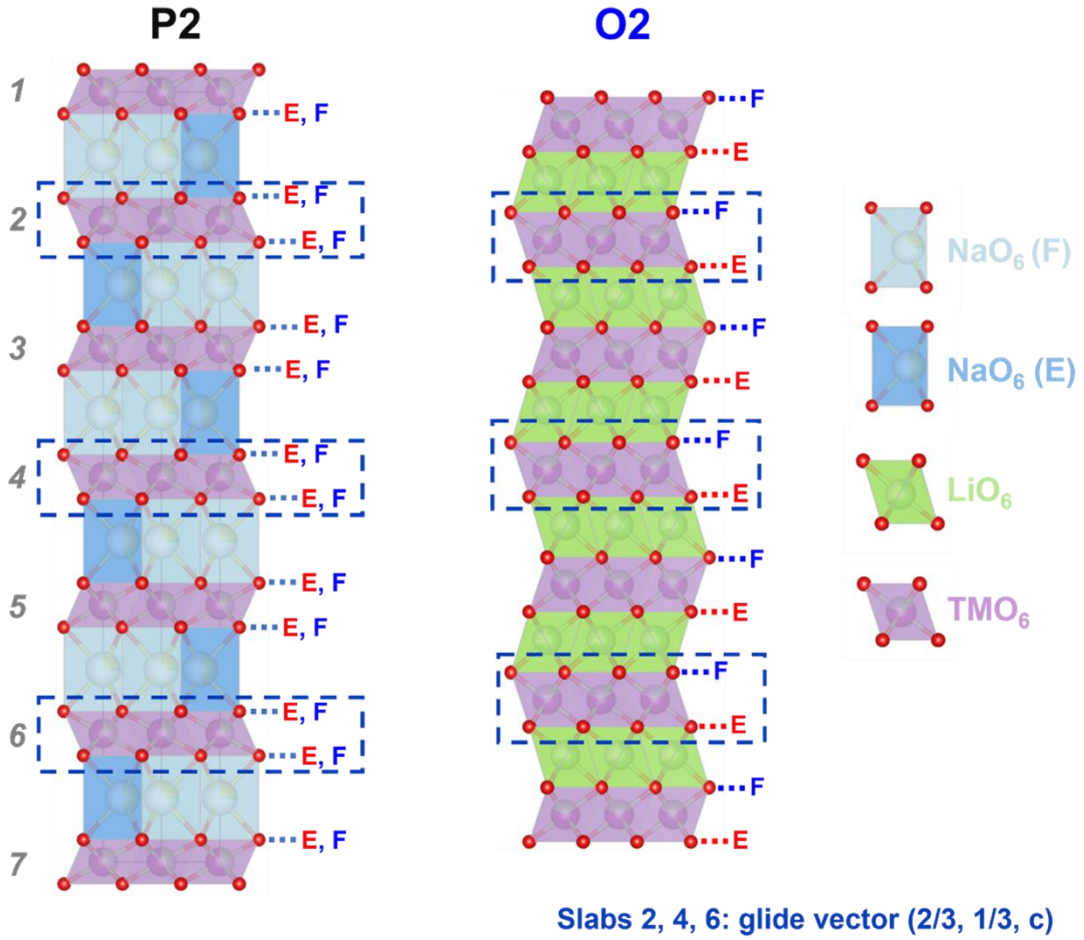


Figure 5-7. Schematic illustration of the P2-to-O2 phase transformation. Via Na^+/Li^+ ion exchange, TMO_2 slabs with odd numbers (*i.e.*, 1, 3, 5) stay at their original positions, whereas those with even numbers (*i.e.*, 2, 4, 6) glide towards the (2/3, 1/3, c) direction. E and F denote edge-sharing and face-sharing planes, respectively.

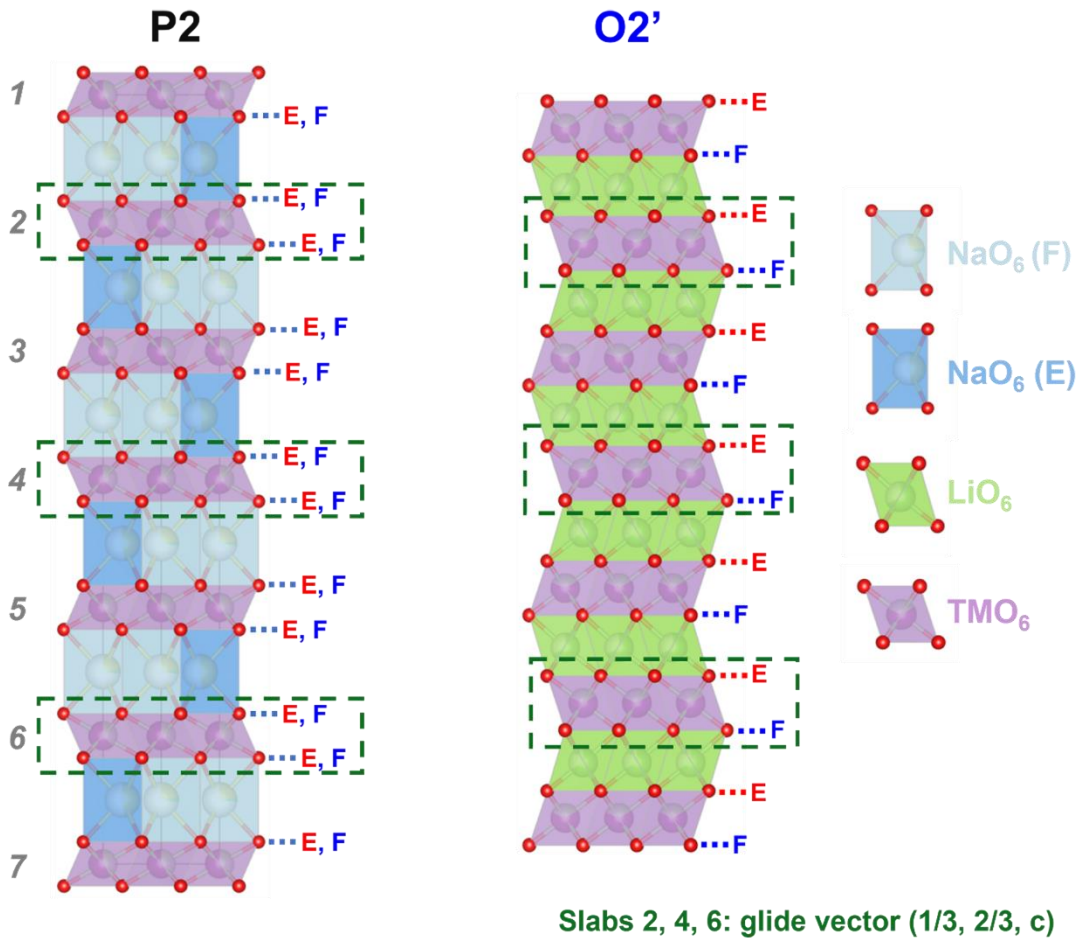


Figure 5-8. Schematic illustration of the P2-to-O2' phase transformation. Via Na^+/Li^+ ion exchange, TMO_2 slabs with odd numbers (*i.e.*, 1, 3, 5) stay at their original positions, whereas those with even numbers (*i.e.*, 2, 4, 6) glide towards the (1/3, 2/3, c) direction. E and F denote edge-sharing and face-sharing planes, respectively.

As for the O6-phase, it is arguably an ordered intergrowth of O2- and O2'-phases.[23] As illustrated in **Figure 5-9**, for every three adjacent TMO_2 slabs, every the second TMO_2 slabs glide toward the (1/3, 2/3, c) direction and every the third TMO_2 slabs glide toward the (2/3, 1/3, c) direction. Specially, although a LiO_6 octahedron still shares three edges with three TMO_6 octahedra on the one side and shares a face with another TMO_6 octahedron on the other side, a TMO_6 octahedron either shares six edges with six LiO_6 octahedra or shares two faces with two LiO_6 octahedra on both sides.

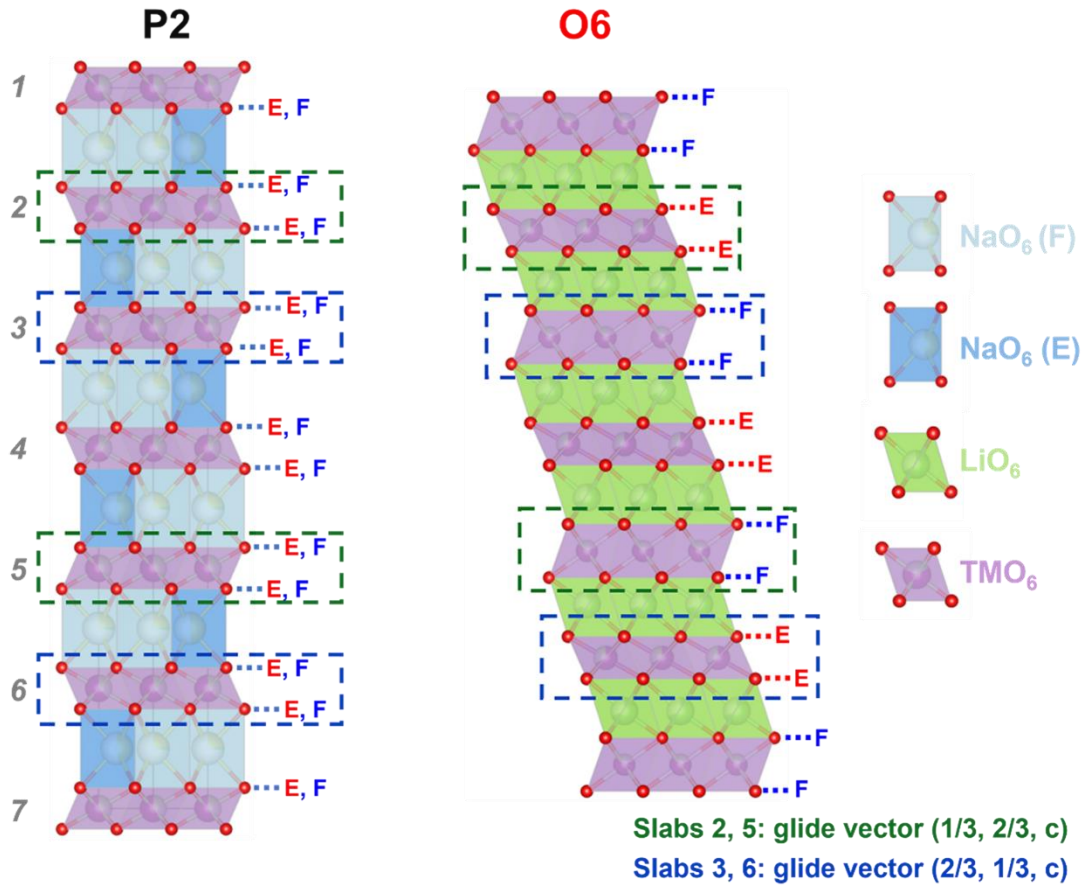


Figure 5-9. Schematic illustration of the P2-to-O6 phase transformation. TMO_2 slabs numbered as 1 and 4 stay at their original positions; TMO_2 slabs numbered as 2 and 5 glide towards the (1/3, 2/3, c) direction; TMO_2 slabs numbered as 3 and 6 glide towards the (2/3, 1/3, c) direction. E and F denote edge-sharing and face-sharing planes, respectively.

The formation of these two different TMO_2 slabs was firstly attributed to the ordering arrangements of cations in different valences. For example, in the O6-phase formed upon lithium deintercalation of the O2-$LiCoO_2$, $Co^{3+}O_6$ octahedra and $Co^{4+}O_6$ octahedra were supposed to only share faces and edges with LiO_6 octahedra, respectively, to minimize the face-sharing Li^+-Co^{4+} repulsion.[29] However, the formation mechanism of the O6-type structure is still controversial because such a charge ordering cannot explain the formation of O6-phases with multiple cations. Specifically, in this work, the T2/O2-to-O6 phase transformation is mainly driven by the thermal

expansion. Anyhow, as for these two types of TMO_2 slabs in the O6-type structure, the ones sharing only faces with LiO_2 slabs are supposed to be destabilized, while the others are stabilized with respect to the O2-type structure. Phase transformations between O2-type and O6-type structures could happen via the gliding of TMO_2 slabs without breaking the TM-O bonds, which are commonly induced by the changes of interlayer interactions.

5.2.3. Rietveld refined structure

A combined Rietveld refinement with both synchrotron XRD (λ=0.16167 Å) and time-of-flight (TOF) neutron diffraction data proves that is has an O6-type structure (R-3m) with a small impurity of Li_2MnO_3 (4.4 wt%) (**Figure 5-10**, **5-11** and **Table 5-3**).[30]

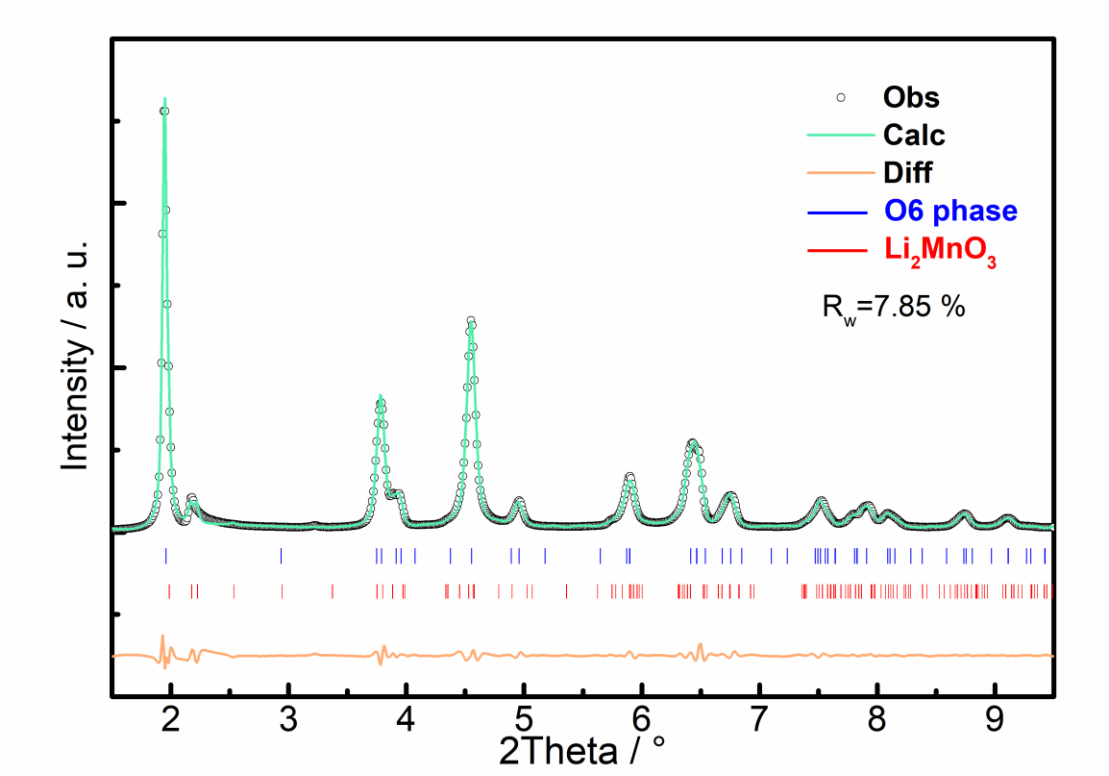


Figure 5-10. Rietveld refinement of XRD patterns (λ=0.16167 Å).

Table 5-3. Rietveld refined structural parameters of the O6-phase

Phase 1: O6-$Li_{0.693}[Li_{0.153}Ni_{0.190}Mn_{0.657}]O_2$	Space group: R-3m			wt=95.6%	
Atom	Fractional coordinates			Multiplicity	Occupancy
	x	y	z		
Li1	0	0	1/12	6	0.693
Li2	0	0	0	3	0.153
Li3	0	0	1/2	3	0.153
Mn1	0	0	0	3	0.657
Mn2	0	0	1/2	3	0.657
Ni1	0	0	0	3	0.19
Ni2	0	0	1/2	3	0.19
O1	0	0	0.2016(1)	6	1
O2	0	0	0.3685(4)	6	1

Lattice parameters:

a=2.86804(4) Å, b=2.86804(4) Å, c=28.4310(1) Å; α=90°, β=90°, γ=120°;

$V_{unit\ cell}$=202.53(2) $Å^3$

Phase 2: Li_2MnO_3	Space group: C2/m			wt=4.4%	
Atom	Fractional coordinates			Multiplicity	Occupancy
	x	y	z		
Li1	0	1/2	0	2	1
Li2	0	0	1/2	2	1
Li3	0	0.6606(1)	1/2	4	1
Mn1	0	0.1671(8)	0	4	1
O1	0.2169(1)	0	0.2283(9)	4	1
O2	0.2552(1)	0.3214(2)	0.2237(5)	8	1

Lattice parameters:

a=5.03790(7) Å, b=8.51294(2) Å, c=4.9254(8) Å; α=90°, β=108.747(1)°, γ=90°;

$V_{unit\ cell}$=200.03(4) $Å^3$

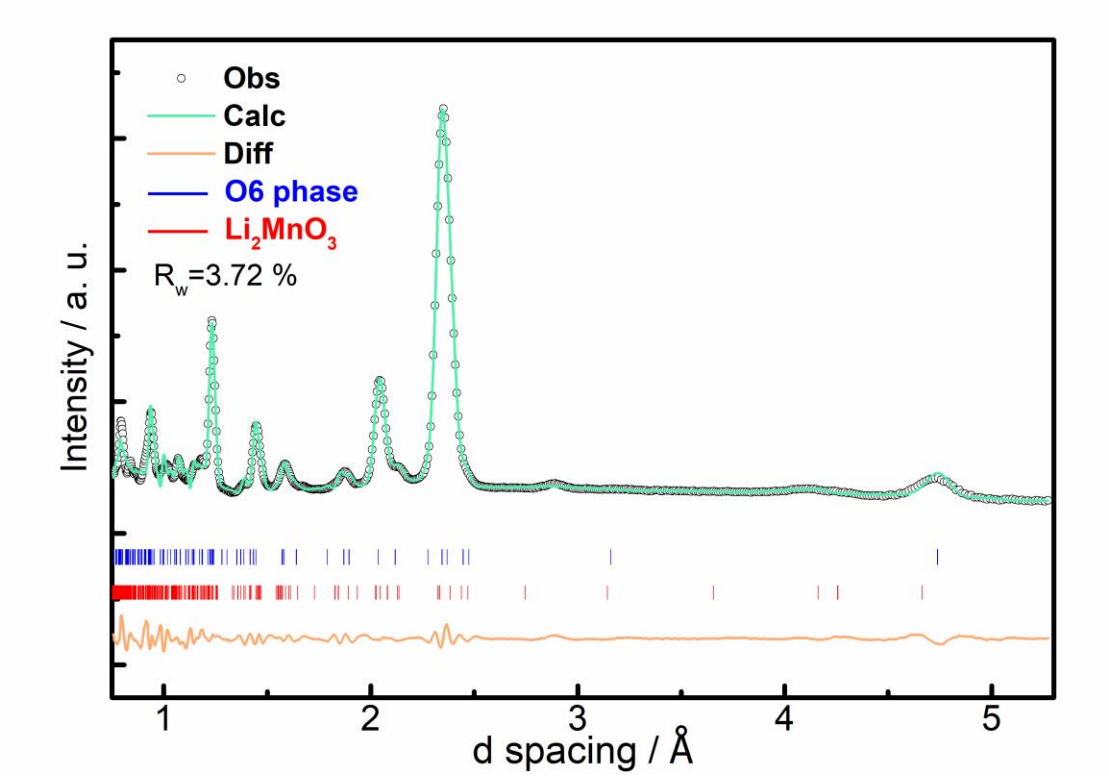


Figure 5-11. Rietveld refinement of TOF neutron diffraction patterns.

5.2.4. Morphology

The as-prepared O6-type material exhibits spherical secondary particles, which are composed of many platelike primary particles, while all elements disperse uniformly (**Figure 5-12**). As shown in Cs-corrected HAADF-STEM images (**Figure 5-13)**, those platelike primary particles display ordered structures with randomly distributed stacking-faulted layers, meaning that they could be regarded as single crystals with strong preferential orientations. Considering that the T2/O2-to-O6 phase transformation involves the gliding of TMO_2 slabs without breaking TM-O bonds, forming stacking faults is inevitable and is an issue of probability. Interlayer spacings of the (006) and the (018) lattice planes are measured to be around 4.85 Å and 2.10 Å, respectively, consistent with the refined structure.

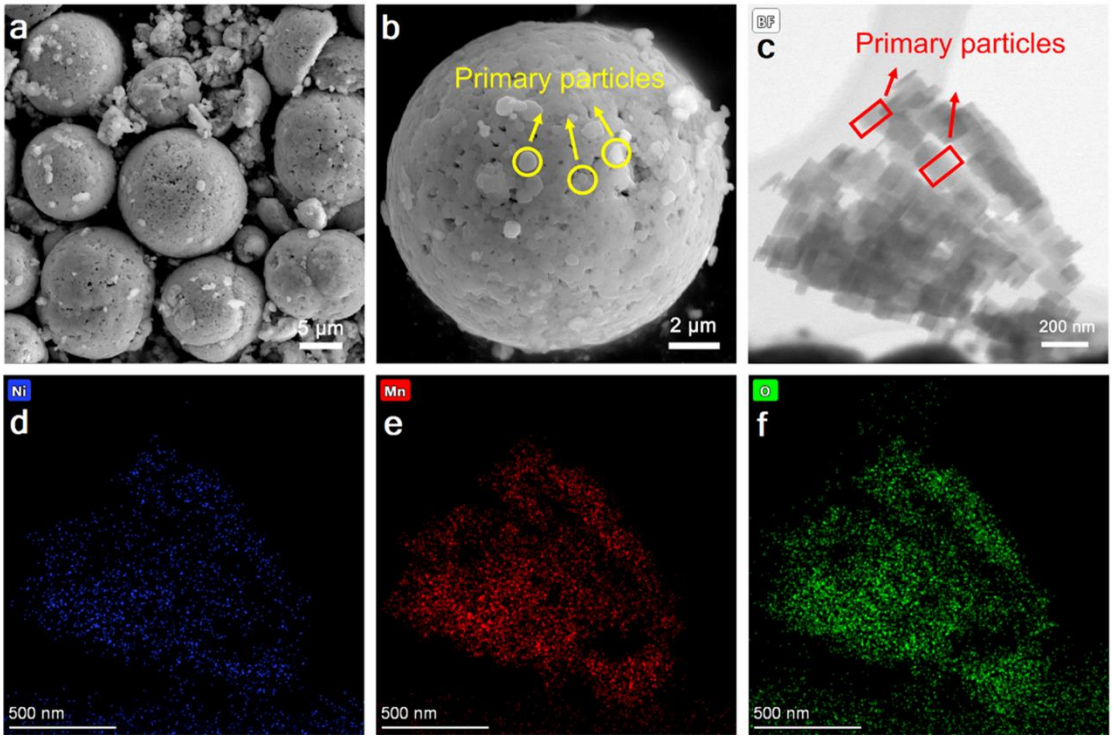


Figure 5-12. Morphology of the O6-type material. **(a** and **b)** SEM, and **(c)** TEM images. EDX mappings of **(d)** Ni, **(e)** Mn, and **(f)** O.

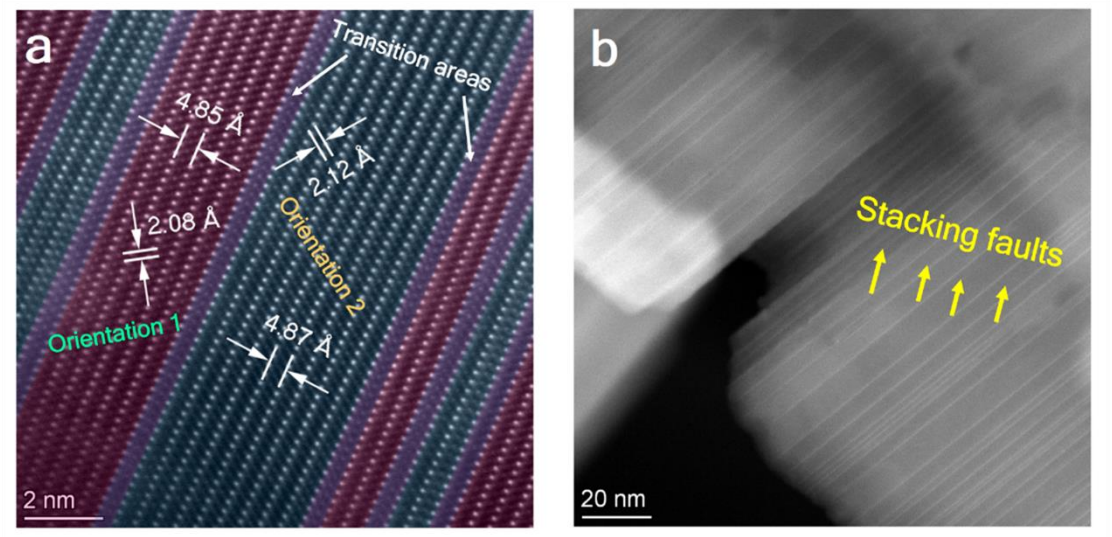


Figure 5-13. Cs-corrected HAADF-STEM images of the O6-phase material. In **(a)**, regions colored in dull red and light blue represent different lattice orientations, while the violet ones represent corresponding transition areas (i.e., stacking-faulted layers). In **(b)**, areas marked by yellow arrows indicate stacking faults caused by the gliding of TMO_2 slabs.

5.2.5. Electronic structures

The valence state of Mn

To determine the valence state of Mn in the O6-phase, we reperformed XPS tests on MnO, Mn_2O_3, MnO_2, the P2-type precursor and the O6-phase. As shown in **Figure 5-14**, the center of the Mn $2p_{1/2}$ peak shifts from 653.4 to 653.7 and 654.2 eV for MnO, Mn_2O_3, and MnO_2, respectively. Although the Mn $2p_{3/2}$ peaks similarly shift to higher binding energies upon Mn oxidization, they are rather broad, and the shifts are not large enough to clearly distinguish between different oxides. Specifically, the Mn $2p_{3/2}$ spectrum of MnO is centered at the same position (marked by blue dashed line) with that of Mn_2O_3 except for a shoulder at a lower binding energy (marked by pink dashed line), probably manifesting the oxidization of Mn^{2+} in the near-surface area. As for the Mn $2p_{3/2}$ spectrum of the MnO_2, the shoulder at a higher binding energy (marked by red dashed line) reveals the existence of Mn^{4+}, while the sharp peak represents the coexistence of Mn^{3+}, which might result from oxygen vacancies in the near-surface area. For the P2-type precursor and the O6-phase, both of their Mn $2p_{3/2}$ peaks are asymmetric, indicating the coexistence of multiple valence states. Specifically, the binding energies of the former are lower than those of the latter, meaning that the average valence state of Mn in the P2-type precursor is lower than that in the O6-phase.

To quantitively investigate the valence states of Mn in the above-mentioned materials, their Mn 2p spectra are fitted by using XPSPEAK41 (**Figure 5-15**). Specifically, for the

Mn_2O_3, peaks at 641.5 and 653.3 eV are assigned to spin orbitals of $2p_{3/2}$ and $2p_{1/2}$ of Mn^{3+}, respectively, while peaks at 642.9 and 654.3 eV are assigned to $2p_{3/2}$ and $2p_{1/2}$ of Mn^{4+}, respectively.[31] The appearance of a large amount of Mn^{4+} in the near-surface area might result from surface oxidization upon air exposure. For the MnO_2, two main peaks at 642.6 and 654.1 eV are attributed to spin orbitals of $2p_{3/2}$ and $2p_{1/2}$ of Mn^{4+}, respectively, while deconvoluted shoulders at 642.1 and 653.7 eV indicate the co-existence of Mn^{3+}.[32] For the P2-type precursor, the shape of its Mn 2p spectrum is similar to that of the MnO_2, which could be deconvoluted into mixed spectra of both Mn^{3+} and Mn^{4+}. For the O6-phase, the average valence state of Mn is higher than that in the P2-type precursor because the deconvoluted Mn^{3+} $2p_{1/2}$ and Mn^{3+} $2p_{3/2}$ peaks decrease. Therefore, according to the XPS results, Mn^{3+} and Mn^{4+} coexist in the P2-type precursor and the O6-phase, and Mn^{4+} dominates in the O6-phase with a small amount of Mn^{3+} at least in the near-surface area.

In addition, we collected Mn K edge X-ray absorption spectroscopy data of the P2-type precursor and the O6-phase. As shown in **Figure 5-16**, the Mn K edge of the P2-type precursor lies in between that of the Mn_2O_3 and that of the MnO_2, indicating that the mixed valence state of Mn is between +3 and +4. The Mn K edge of the O6-phase almost superimposes with that of MnO_2, meaning that the main valence state of Mn is +4. Meanwhile, the Mn K pre-edge of the O6-phase lies at the energy slightly higher than that of the P2-type precursor and slightly lower than that of the MnO_2, probably suggesting the coexistence of a small amount of Mn^{3+}.

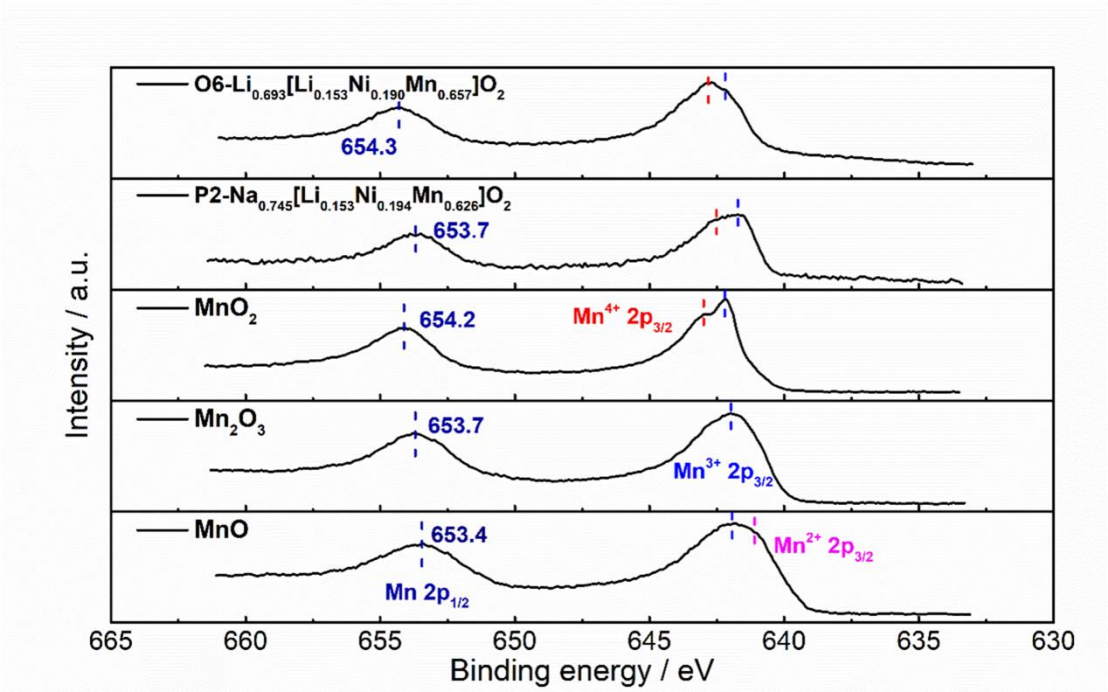


Figure 5-14. Mn 2p XPS spectra. The peak position correction was applied based on the C 1s peak (284.8 eV).

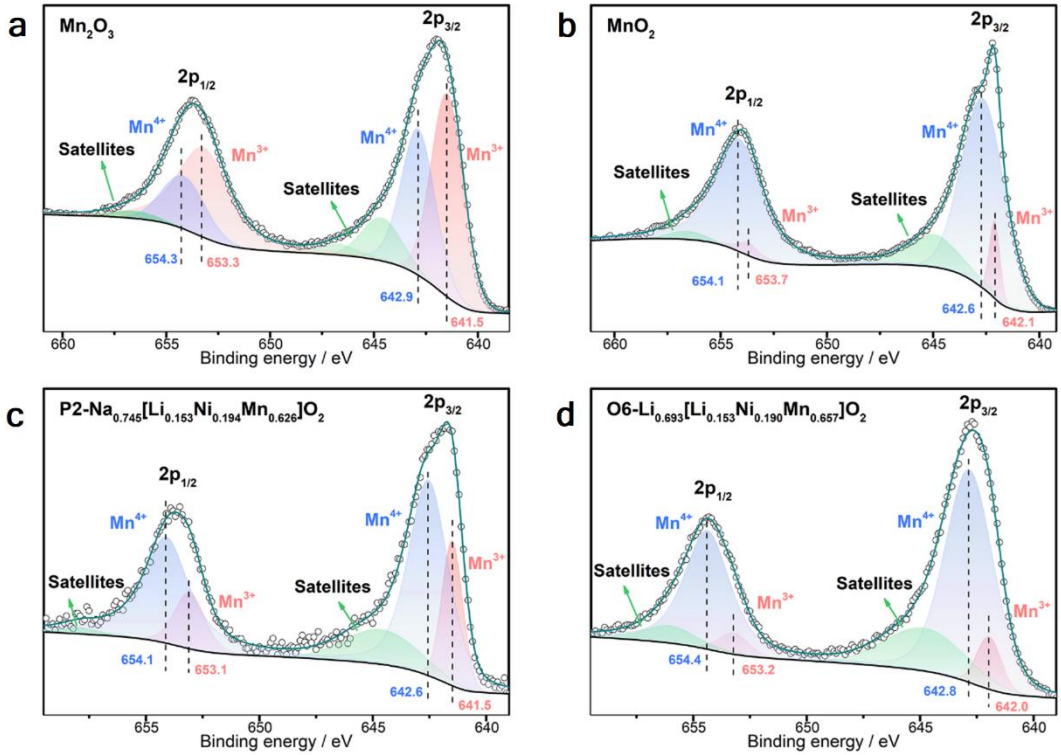


Figure 5-15. Mn 2p XPS spectra. Fitted Mn 2p XPS spectra of **(a)** Mn_2O_3, **(b)** MnO_2, **(c)** the P2-type precursor, and **(d)** the O6-phase. The peak position correction was applied based on the C 1s peak (284.8 eV).

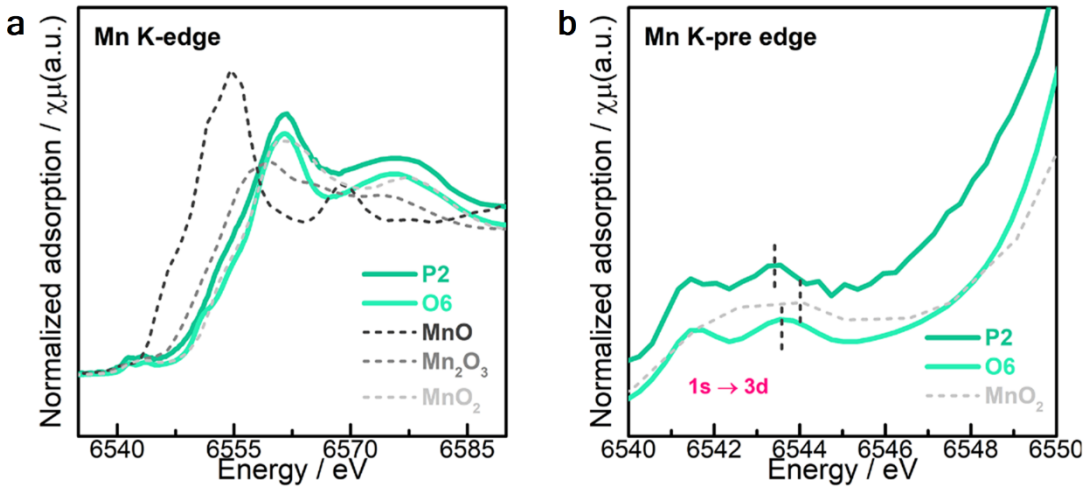


Figure 5-16. XAS spectra of Mn. **(a)** Mn K-edge XANES results of MnO, Mn_2O_3, MnO_2, the P2-type precursor and the O6-phase. **(b)** Mn K pre-edge XANES results of MnO_2, the P2-type precursor and the O6-phase.

The valence state of Ni

To interpret the valence state of Ni in the O6-phase, we further collected XPS data of NiO, Ni_2O_3, the P2-type precursor and the O6-phase. As displayed in **Figure 5-17**, even NiO presents a large amount of Ni^{3+} as there is a strong peak at the higher binding energy in the Ni $2p_{3/2}$ spectrum (marked by red dashed line). As for the P2-type precursor and the O6-phase, the $2p_{1/2}$ and $2p_{3/2}$ peaks of Ni in the former are centered at the binding energies lower than those of the latter, meaning that the valence state of Ni increases after ion exchange and thermal annealing.

Figure 5-18 shows the fitted Ni 2p spectra of NiO, Ni_2O_3, the P2-type precursor and the O6-phase. For the NiO, peaks at 853.6 and 871.0 eV are assigned to spin orbitals of $2p_{3/2}$ and $2p_{1/2}$ of Ni^{2+}, respectively, while peaks at 855.4 and 872.8 eV are assigned to $2p_{3/2}$ and $2p_{1/2}$ of Ni^{3+}, respectively.[33] It is common to see strong peaks from Ni^{3+} in XPS

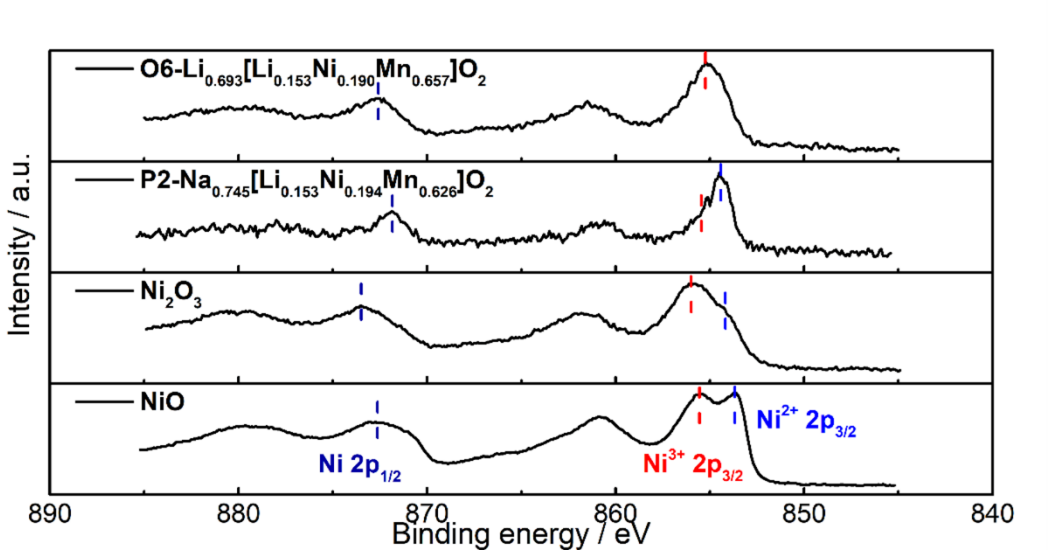


Figure 5-17. Ni 2p XPS spectra. The peak position correction was applied based on the C 1s peak (284.8 eV).

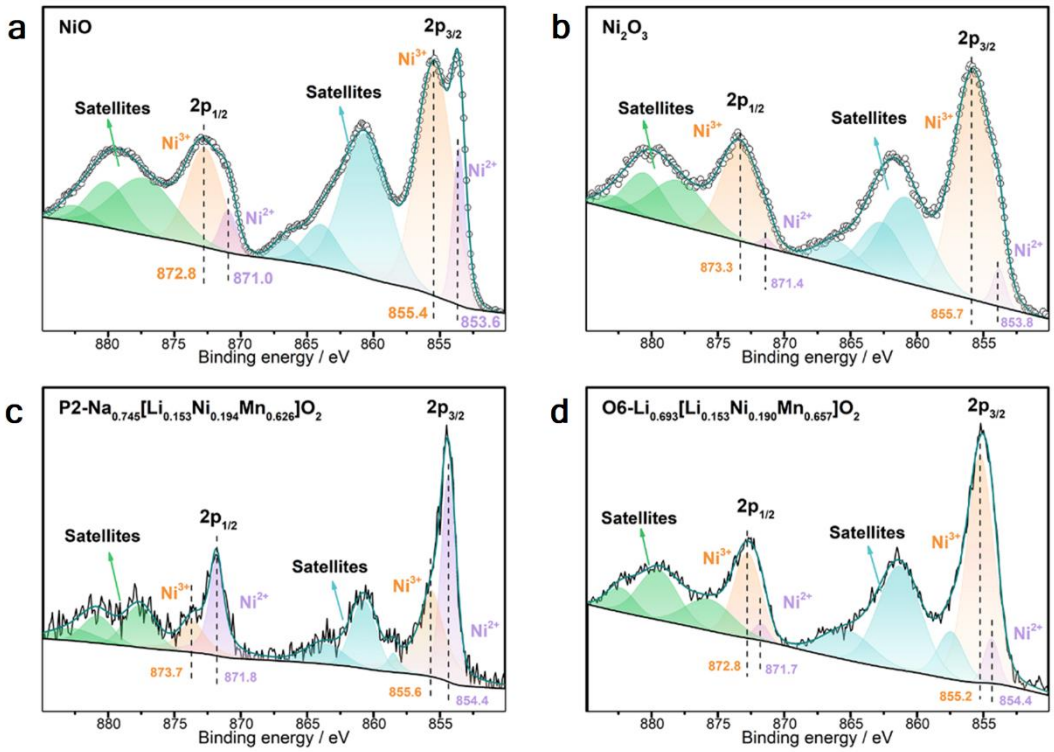


Figure 5-18. Ni 2p XPS spectra. Fitted Ni 2p XPS spectra of **(a)** NiO, **(b)** Ni_2O_3, **(c)** the P2-type precursor, and **(d)** the O6-phase. The peak position correction was applied based on the C 1s peak (284.8 eV).

results of NiO because of surface oxidization. For the Ni_2O_3, two main peaks at 855.7 and 873.3 eV are attributed to spin orbitals of $2p_{3/2}$ and $2p_{1/2}$ of Ni^{3+}, respectively, while deconvoluted shoulders at 853.8 and 871.4 eV indicate the co-existence of Ni^{2+}.[34] The appearance of a small amount of Ni^{2+} might result from oxygen vacancies in the near-surface area. For the P2-type precursor, the sharp main peaks centered at 854.4 and 871.8 eV are assigned to $2p_{3/2}$ and $2p_{1/2}$ of Ni^{2+}, respectively, while the shoulders at 855.6 and 873.7 eV are assigned to $2p_{3/2}$ and $2p_{1/2}$ of Ni^{3+}, respectively. Therefore, Ni^{2+} dominates in the P2-$Na_{0.745}[Li_{0.153}Ni_{0.194}Mn_{0.626}]O_2$, and a small amount of Ni is in the valence state of Ni^{3+} to compensate the charge deficiency caused by sodium vacancies. For the O6-phase, the main valence state of Ni is +3 as the main peaks at 855.2 and 872.8 eV could be assigned to $2p_{3/2}$ and $2p_{1/2}$ of Ni^{3+}, respectively, while deconvoluted shoulders at 854.4 and 871.7 eV indicate the co-existence of Ni^{2+}. Therefore, according to the XPS results, Ni^{2+} and Ni^{3+} coexist in both the P2-type precursor and the O6-phase, while Ni^{2+} and Ni^{3+} dominates in the former and the latter, respectively.

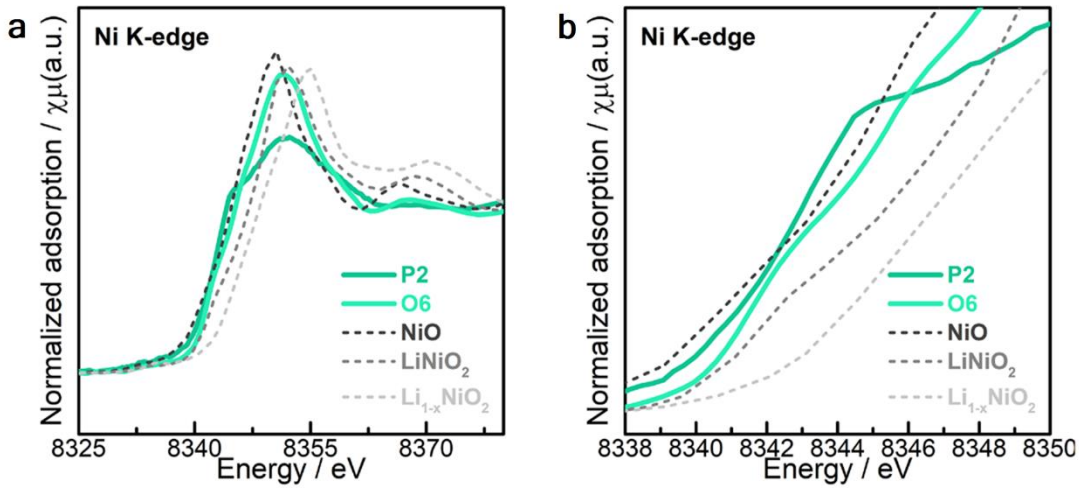


Figure 5-19. XAS spectra of Ni. **(a)** Ni K edge XANES results of NiO, $LiNiO_2$, $Li_{1-x}NiO_2$, the P2-type precursor and the O6-phase. **(b)** Enlarged Ni K edge XANES results of NiO, $LiNiO_2$, $Li_{1-x}NiO_2$, the P2-type precursor and the O6-phase.

In addition, we collected Ni K edge X-ray absorption spectroscopy data for the P2-type precursor and the O6-phase. As displayed in **Figure 5-19**, the Ni K edges of the P2-type precursor and the O6-phase almost superimpose with the Ni K edge of NiO. Specifically, the Ni K edge of the O6-phase lies at higher energy than that of the P2-type precursor, suggesting Ni oxidization upon ion exchange and thermal treatment. Actually, the Ni K edge of the O6-phase lies in between that of the NiO and that of the $LiNiO_2$, meaning that Ni^{2+} and Ni^{3+} coexist in the O6-phase. Yet, Ni^{3+} is unlikely to dominate as it is closer to the K edge of NiO, which contradicts with XPS results. However, considering the strong Ni 2p peaks from Ni^{3+} in XPS results of NiO, Ni^{2+} might be partially oxidized to Ni^{3+} in the near-surface area. Therefore, based on both XPS and XAS results, we suggest that Ni is in the mixed valence state between +2 and +3.

The overall valence states of Mn and Ni

Taking both the valence states of Mn and Ni into consideration, in the high-temperature synthesized P2-$Na_{0.745}[Li_{0.153}Ni_{0.194}Mn_{0.626}]O_2$, Mn^{3+} and Mn^{4+} coexist, while Ni^{2+} dominates with a small amount of Ni^{3+}, probably resulting from the sodium-deficient environment. Upon Na^+/Li^+ ion-exchange and the following thermal treatment, both Mn and Ni are oxidized to higher valence states to compensate charge deficiency in the O6-$Li_{0.693}[Li_{0.153}Ni_{0.190}Mn_{0.657}]O_2$ because the amount of Li^+ in the O6-phase is lower than the combined amount of Na^+ and Li^+ in the P2-type precursor. Consequently, Mn^{4+} dominates in the O6-phase with a small amount of Mn^{3+}, while Ni^{2+} and Ni^{3+} coexist with the amount of Ni^{3+} higher than that in the P2-type precursor.

Traditionally, in lithium/sodium layered nickel manganese oxides (*e.g.*, $Li_xNi_yMn_{1-y}O_2$ or $Na_xNi_yMn_{1-y}O_2$), the valence states of Ni and Mn are widely reported as +2 and +4, respectively, which originate from the deliberate design of the ratio between Ni and Mn. For instance, Ni^{2+} and Mn^{4+} are prone to exist in the ordered honeycomb-like superstructure in the TM layers as in P2-$Na_{2/3}[Ni_{1/3}Mn_{2/3}]O_2$.[35] Ideally, upon de-/lithiation, Ni redox is responsible for the capacity and Mn remains in +4, thereby avoiding the detrimental Jahn-Teller deformation of $Mn^{3+}O_6$ octahedra. However, in O3-$LiNi_{0.5}Mn_{0.5}O_2$ without the ordered honeycomb-like superstructure, the coexistence of Ni^{2+}, Ni^{3+}, Mn^{3+}, and Mn^{4+} have been proven.[36]

Accordingly, as for the O6-$Li_{0.693}[Li_{0.153}Ni_{0.190}Mn_{0.657}]O_2$ that we demonstrated in this work, having both [Ni^{2+}-Mn^{4+}] and [Ni^{3+}-Mn^{3+}] configurations is reasonable. Firstly, because it is lithium-deficient, a lithium vacancy would create a Ni^{3+} ion. Having a Ni^{3+} at the next-near-neighbor promotes the electron transfer from a Ni^{2+} to a near-neighbor Mn^{4+} thanks to the cooperative Jahn-Teller distortions between $Ni^{3+}O_6$ and $Mn^{3+}O_6$ octahedra. Besides, as proven by the weak superstructural peaks in XRD patterns, the arrangement of Li, Ni and Mn in the transition metal layer is largely disordered. Therefore, the presence of Ni^{3+} contributes to the local disordering, while anti-site disorder further favors the formation of [Ni^{3+}-Mn^{3+}] configurations.

5.3. Electrochemical properties of the O6-phase

The as-prepared O6-type $Li_{0.693}[Li_{0.153}Ni_{0.190}Mn_{0.657}]O_2$ was firstly tested as the cathode material in coin cells using the commercial electrolyte (1M $LiPF_6$ in EC/DMC, 1: 1 in volume), as detailed in Chapter 2.

In the 1st charge, the irreversible anodic peak in CV curves and the plateau in GCD curves at around 4.5 V vs. Li/Li^+ indicate local rearrangement induced by initial oxygen oxidization, widely seen in Mn-based cathode materials when the valence state of Mn reaches +4 (**Figure 5-20**).[37] Uniquely, apart from redox peaks in the low potential region (2.5 - 3.0 V vs. Li/Li^+) and the high potential region (3.5 - 4.5 V vs. Li/Li^+), two pairs of redox peaks appear in the region of 4.5 - 4.8 V vs. Li/Li^+ in its CV curves.

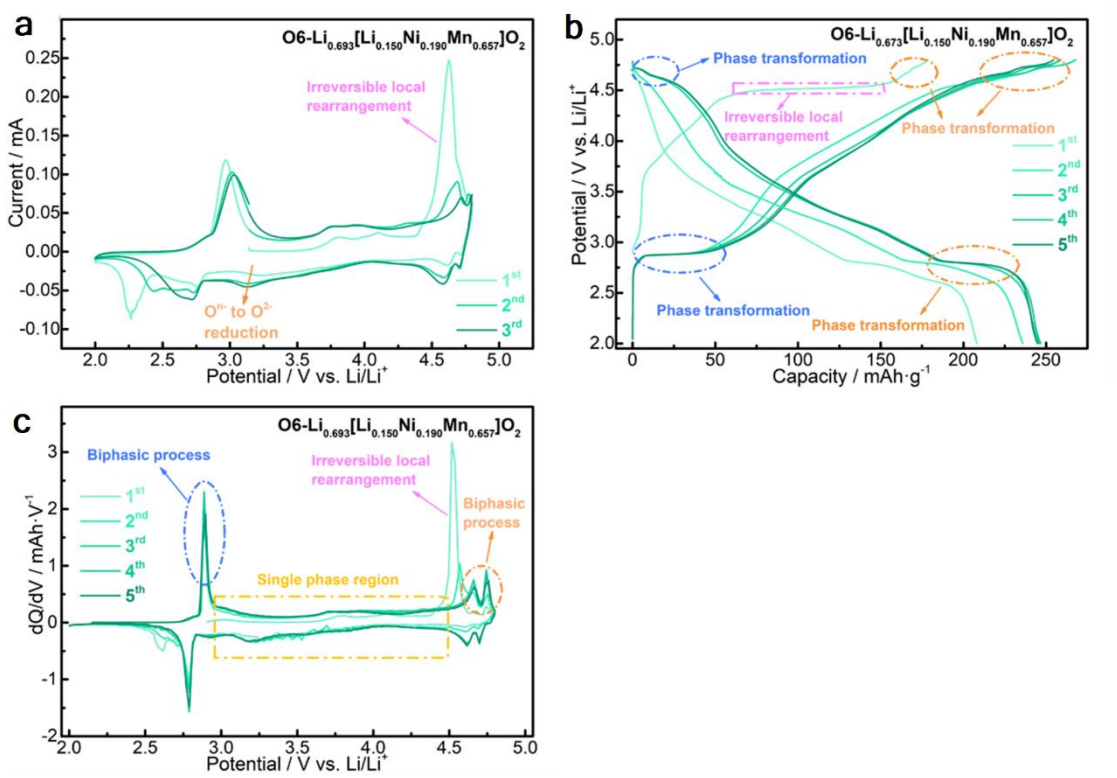


Figure 5-20. Electrochemistry of the O6-phase. **(a)** 1st-3rd CV curves at the scan rate of 0.05 mV/s. **(b)** 1st-5th GCD curves, and **(c)** corresponding dQ/dV curves at the current density of 10 mA/g within the potential window of 2.0 - 4.8 V vs. Li/Li^+.

Specifically, corresponding plateaus in GCD profiles and sharp peaks in dQ/dV curves imply biphasic processes, like the O6-to-O2 phase transformation and the subsequent order-to-disorder transition seen in O2-type $LiCoO_2$. [29,38,39] Upon de-/lithiation, while broad redox peaks in the potential region (3.0 - 4.5 V vs. Li/Li^+) imply single-phase processes, sharp redox peaks in the low potential region (2.5 - 3.0 V vs. Li/Li^+) manifest the occurrence of another first-order phase transformation in the deeply lithiated state. Therefore, the O6-phase is suspected to convert into other phases at either low or high lithium concentrations. Noteworthily, because the pristine material is lithium deficient, the discharging capacity (208.4 mAh/g) is higher than the charging capacity (178.2 mAh/g) in the 1st cycle, which increases in the following cycles to reach a stable capacity of around 250 mAh/g at 10 mA/g.

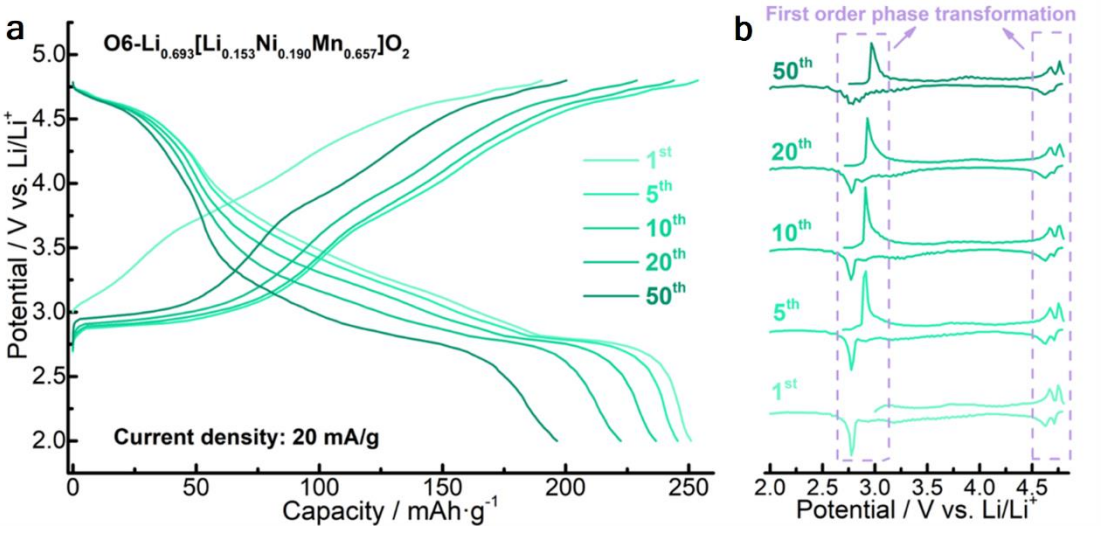


Figure 5-21. Cycling performance of the O6-phase electrode. **(a)** GCD curves, and **(b)** corresponding dQ/dV curves at the 1st, 5th, 10th, 20th and 50th cycles. The current density is 20 mA/g, and the potential window is 2.0 - 4.8 V vs. Li/Li^+.

Upon cycling at the current density of 20 mA/g within the potential window of 2.0 - 4.8 V vs. Li/Li^+, the O6-type electrode deliver initial discharge capacities of 250.9 mAh/g, decreasing to 196.6 mAh/g after 50 cycles (**Figure 5-21a**). Specifically, the initial coulombic efficiency (C.E.) is above 100 % due to the lithium-deficient environment in pristine material, while the C.E. decreases to around 98 % in the following cycles. Despite the gradual capacity loss and voltage decay, no peaks at around 3.0 V vs Li/Li^+ are observed in the dQ/dV curves (**Figure 5-21b**), which would indicate the formation of the spinel phase.[40] On the contrary, upon cycling, the O3-type $Li_{1.2}Ni_{0.2}Mn_{0.6}O2$ prepared via a traditional solid-state reaction presents redox peaks identical to the spinel phase because of the cumulative interlayer TM migration,[41] accompanied by both capacity fading and voltage decay (details in **Appendix B**). Moreover, for the O6-phase, those phase transformation related plateaus in GCD curves and redox peaks in corresponding dQ/dV curves remain, revealing that those biphasic processes are reversible even in long-term operation. Therefore, the performance degradation probably results from the continuous consumption of the electrolyte rather than from the structural degradation.

5.4. Cation and anion redox mechanisms of the O6-phase

To elucidate the charge compensation mechanisms in the O6-phase, multiple analyses were performed to investigate the chemical states of transition metal and oxygen during the initial de-/lithiation, including ex-situ XAS, ex-situ XPS, and ex-situ CW-EPR.

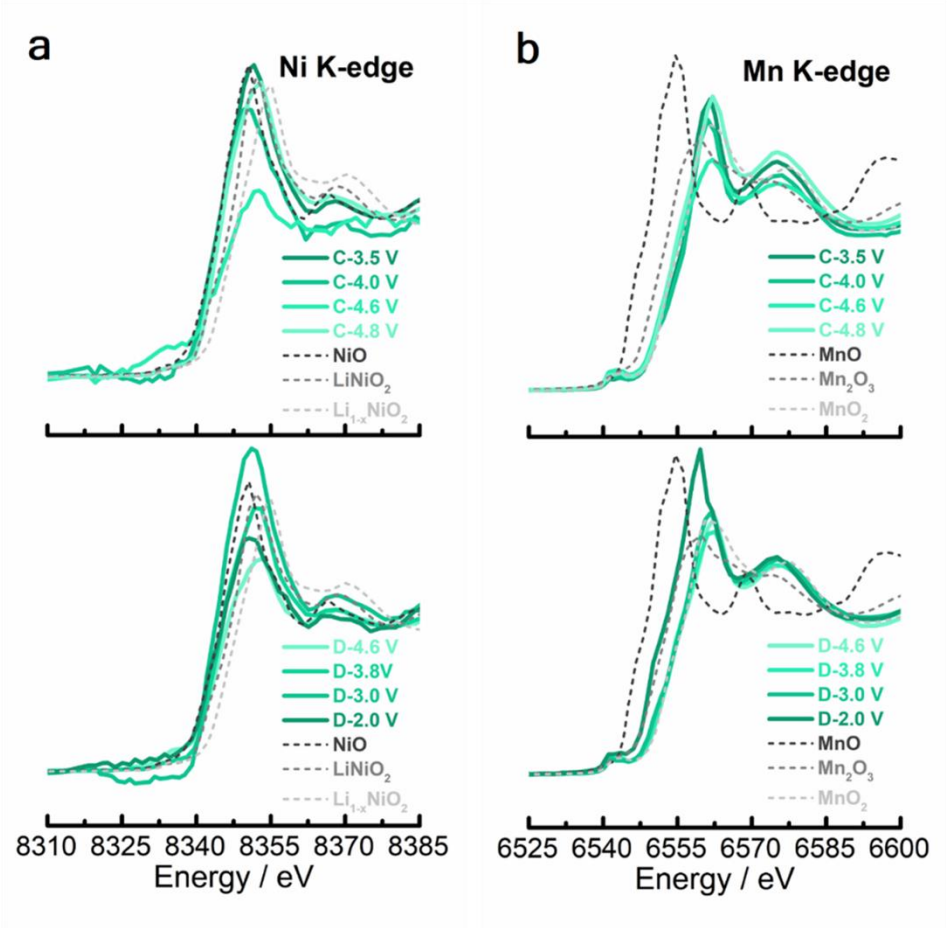


Figure 5-22. Ex-situ XAS results. **(a)** Ni K-edge and, **(b)** Mn K-edge spectra of O6-phase electrodes at different potentials during the initial cycle.

As shown in **Figure 5-22a**, the Ni K-edge moves to higher energies upon charging to 4.8 V vs. Li/Li^+ and shifts back after discharging to 3.0 V vs. Li/Li^+, indicating the reversible oxidation and reduction of Ni within the potential window of 3.0 - 4.8 V vs. Li/Li^+. In contrast, the Mn XANES spectra demonstrate the stability of Mn^{4+} within such a potential window because the shift of Mn K-edge is negligible (**Figure 5-22b**). After discharging to 2.0 V vs. Li/Li^+, the Mn pre-edge moves to lower energy, demonstrating that the Mn^{4+}-to-Mn^{3+} reduction is responsible for the dQ/dV peak at around 2.8 V vs. Li/Li^+.

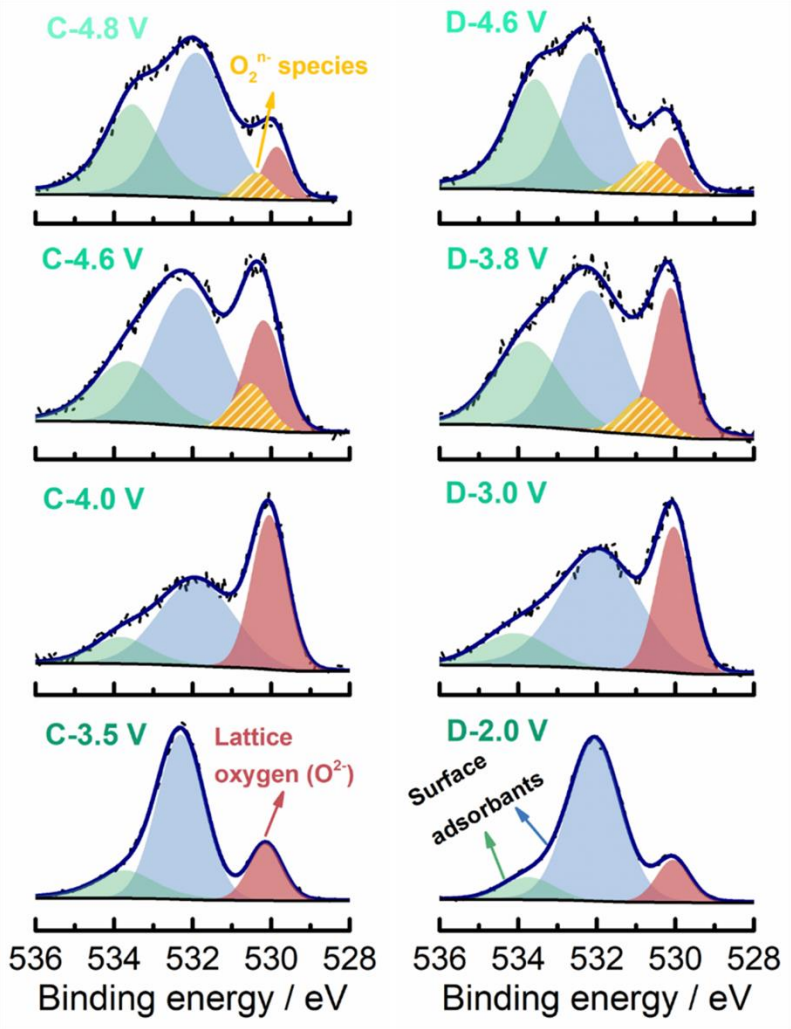


Figure 5-23. Ex-situ O 1s XPS spectra of O6-phase electrodes at different potentials during the initial cycle.

In the O 1s XPS spectra (**Figure 5-23**), after charging to 4.6 V vs. Li/Li^+, a shoulder appears at the binding energy (530.5 eV) higher than that of the lattice oxygen (O^{2-}), indicating the formation of O_2^{n-} species caused by anion redox reactions.[14] The signal retains even after discharging to 3.8 V vs. Li/Li^+ but disappears after discharging to 3.0 V vs. Li/Li^+, revealing the polarizing O_2^{n-}-to-O^{2-} reduction.[42] It is noteworthy that XPS is a surface technique, RIXS tests will be conducted in the future to reveal the oxygen redox activities in the bulk.

The mechanisms revealed by XAS and XPS spectra are well supported by EPR results. **Figure 5-24** presents the normalized ex-situ CW-EPR spectra. At the beginning of the initial charge (i.e., C-3.5 V vs. Li/Li^+), the broad symmetric peak originates from the paramagnetic Mn^{4+} and the sharp peak is attributed to the conductive carbon.[43] The broad peak increases after charging to 4.0 V vs. Li/Li^+ (**Figure 5-25a**), implying the oxidation of residual Mn^{3+} to Mn^{4+}. However, it decreases dramatically upon further charging to 4.6 V vs. Li/Li^+ because the activation of oxygen redox induces anisotropic distortions of TMO_6 octahedra and disturbs the magnetic exchange interaction between TM and oxygen atoms.[44]

Additionally, removing Li from the TM layer creates vacancies and favors the formation of O-O dimers (O_2^{n-}), thereby breaking the percolating network mediated by oxygen and producing six-fold hyperfine patterns (marked by pink ellipses). Specifically, such six-fold hyperfine patterns reveal the TM^{4+}-O_2^{n-} coupling in the vacancy-mediated structure (the right part of **Figure 5-24**), which could be regarded as the indicator of oxygen redox.[45] Those patterns become sharper after charging to 4.8 V vs. Li/Li^+ and even remain after discharging to 3.8 V vs. Li/Li^+, meaning that reducing the dimerized O_2^{n-} back to lattice oxygen (O^{2-}) is thermodynamically polarized. They finally disappear after discharging to 3.0 V vs. Li/Li^+ and the broad symmetric peak of Mn^{4+} restores, which is much weaker than that of the original state because of the irreversible local rearrangement. The signal further decreases after discharging to 2.0 V vs. Li/Li^+ (**Figure 5-25b**), due to the reduction of Mn^{4+} to Mn^{3+}.

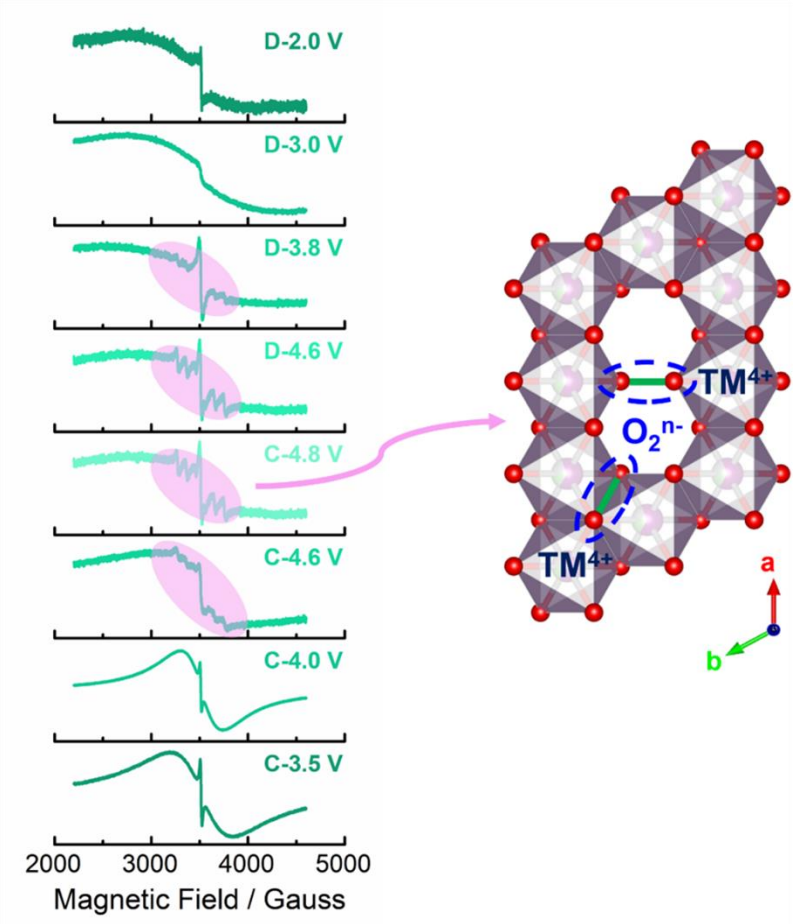


Figure 5-24. Normalized ex-situ CW-EPR results of O6-phase electrodes at different potentials during the initial cycle. All spectra are normalized based on mass. The right shows local patterns of the de-lithiated O6-phase with Li vacancies and O-O dimers.

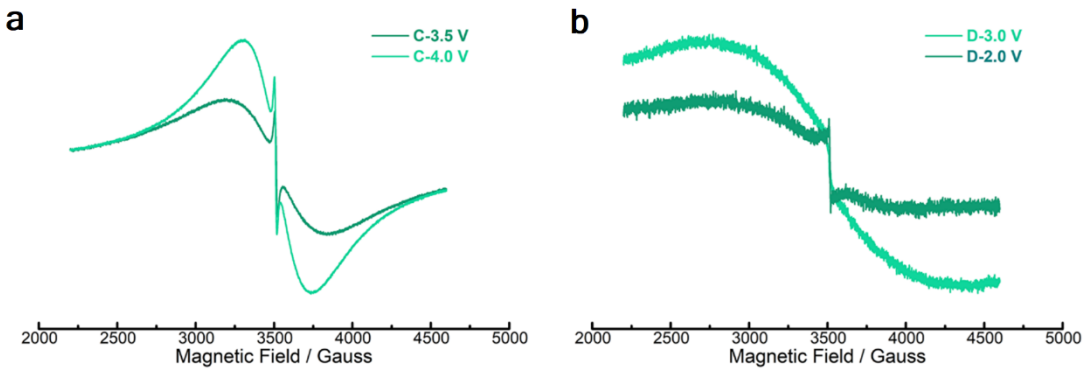


Figure 5-25. (a) Ex-situ CW-EPR results of O6-phase electrodes collected at 3.5 V and 4.0 V vs. Li/Li^+ upon the initial charge. **(b)** Ex-situ CW-EPR results of O6-phase electrodes collected at 3.0 V and 2.0 V vs. Li/Li^+ upon the initial discharge.

Accordingly, both cationic and anionic redox reactions take place upon de/lithiation in the O6-type $Li_{0.693}[Li_{0.153}Ni_{0.190}Mn_{0.657}]O_2$. Specifically, the oxidization and reduction of Ni mainly occur within the potential window of 3.0 - 4.8 V vs. Li/Li^+, while the redox reactions between Mn^{3+} and Mn^{4+} mostly happen in the potential window of 2.0 - 3.0 V vs. Li/Li^+. As to the anion redox reactions, oxygen is prone to be oxidized at high potentials (> 4.6 V vs. Li/Li^+) to form the oxidized species such as the dimerized O_2^{n-} ($0 < n < 4$), yet the O_2^{n-}-to-O^{2-} reduction is polarized to as low as 3.0 V vs. Li/Li^+.

5.5. Structural evolutions of the O6-phase upon de-/lithiation

5.5.1. In-situ and ex-situ XRD results of the O6-phase upon de-/lithiation

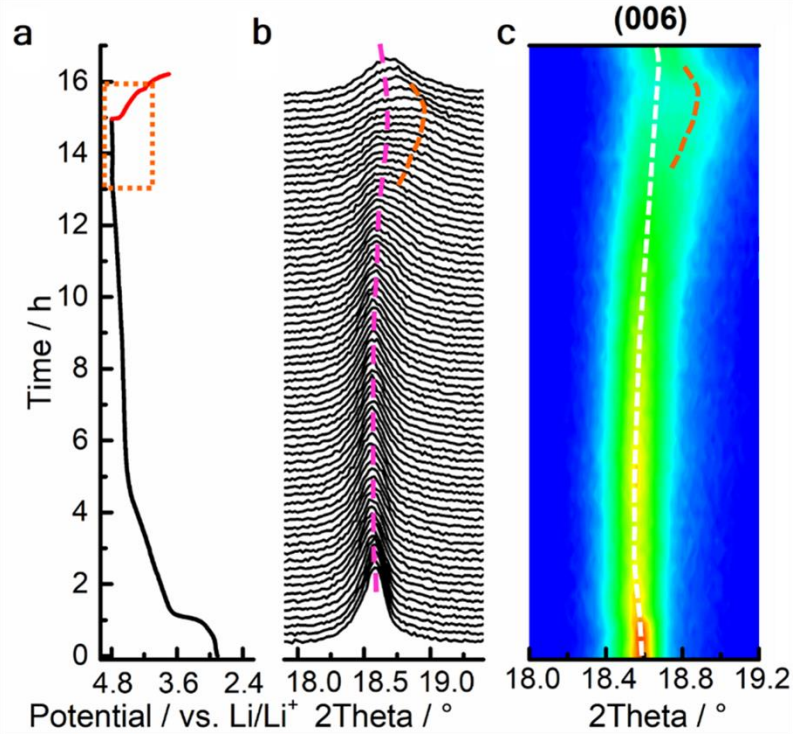


Figure 5-26. (a) GCD curves of the in-situ cell collected at the current density of 20 mA/g during the first charge to 4.8 V and discharge to 3.8 V vs Li/Li^+. XRD patterns of the electrode were collected with steps of 15 min (i.e., 5 mAh/g in capacity). **(b)** Evolutions of the (006) peak, and **(c)** corresponding contour map.

To uncover the structural evolution of the O6-type $Li_{0.693}[Li_{0.153}Ni_{0.190}Mn_{0.657}]O_2$ during de-/lithiation, both in-situ and ex-situ XRD tests were performed (**Figure 5-26** and **5-27**). Specifically, for in-situ XRD tests, a customized coin cell with a beryllium window was used, as detailed in Chapter 2. For ex-situ XRD tests, the O6-phase electrodes were charged and discharged (if needed) at the current density of 5 mA/g (~ 1/50 C). **Figure 5-28** displays the typical GCD curves of the O6-phase electrode during the 1st cycle and the 2nd charge, on which the selected potential points for ex-situ XRD tests are labeled by hollow circles.

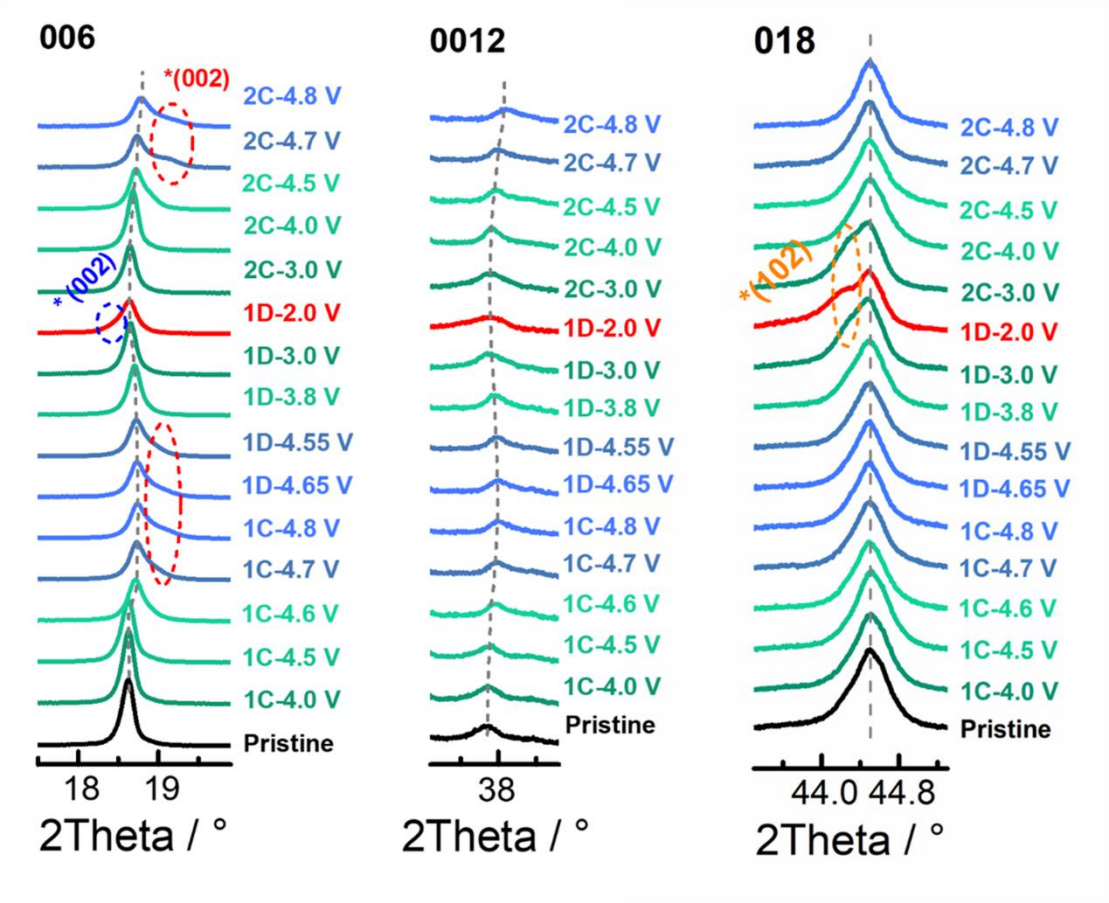


Figure 5-27. Ex-situ XRD patterns of the O6-type electrodes at different potentials. C and D denote charge and discharge, respectively.

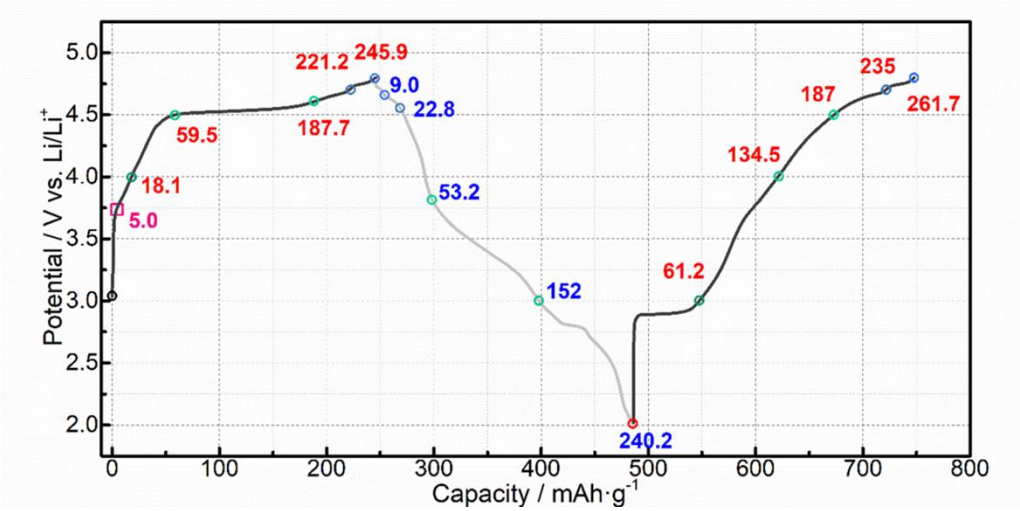


Figure 5-28. Typical GCD curves of the O6-phase electrode. the current density is 5 mA/g, and the potential window is 2.0 - 4.8 V vs. Li/Li^+.

5.5.2. Interlayer interactions in O3- and O6-type structures

Generally, for layered oxides composed of LiO_2 and TMO_2 slabs, the position of the first diffraction peak (00x) is related to the interlayer spacing between adjacent TMO_2 slabs, determined by interlayer interactions. In the typical O3-type structure (e.g., $LiCoO_2$), LiO_6 octahedra share edges with CoO_6 octahedra along the *c*-axis, meaning that the interaction between Li^+ and Co^{3+} is weak. Therefore, its interlayer spacing is mainly determined by two competing forces, i.e., the attractive Li^+-O^{2-} interaction and the repulsive O^{2-}-O^{2-} interaction (**Figure 5-29a**). Upon charging, the removal of Li^+ reduces the attraction between Li^+ and O^{2-}, thereby diminishing the screening effect. Hence, the interlayer spacing increases due to the stronger electrostatic repulsion between the O layers. Commonly, upon further de-lithiation, the interlayer spacing keeps increasing until the repulsion is large enough to drive the change of the stacking patterns (e.g., the O3-to-O1 phase transformation in the deeply de-lithiated $LiCoO_2$).[46]

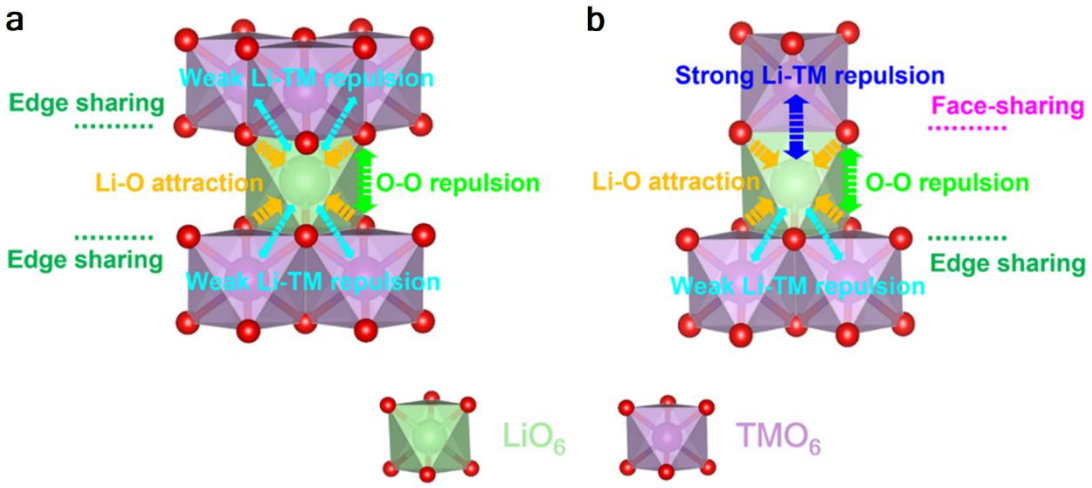


Figure 5-29. Interlayer interactions in **(a)** O3-type, and **(b)** O6-type structures.

However, in the O6-type structure, LiO_6 octahedra not only share edges but also share faces with TMO_6 octahedra along the *c*-axis. Because the repulsion between the face-sharing Li^+ and TM^{n+} ions is strong, it should be considered when investigating the evolution of the interlayer spacing (**Figure 5-29b**).

5.5.3. Structural evolutions upon the 1st charging to 4.5 V vs. Li/Li^+

Specifically, upon charging to 4.5 V vs. Li/Li^+ (i.e., cation redox processes), the O6-type electrode undergoes solid solution reactions because no new peaks appear. The (006) peak ($2\theta = 18.63°$) merely changes because the increasing repulsive O^{2-}-O^{2-} interaction and the decreasing Li^+-TM^{n+} repulsion counteract with each other (**Figure 5-30**), indicating the superior lattice stability.

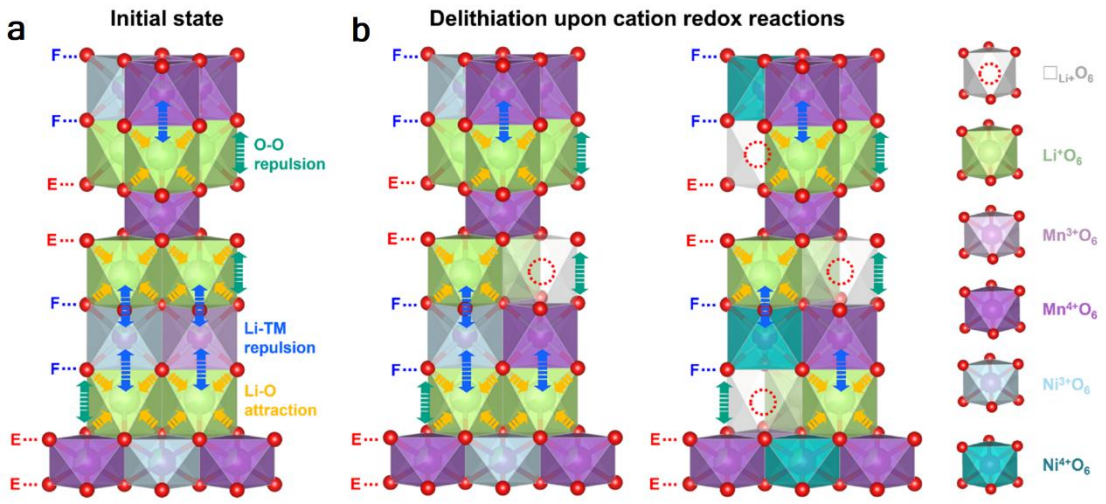


Figure 5-30. Schematic illustrations of the interlayer interactions **(a)** in the pristine O6-type structure, and **(b)** upon cation redox reactions in the 1st charging to 4.5 V vs. Li/Li$^+$. E and F denote edge-sharing and face-sharing planes of LiO_6-TMO_6, respectively.

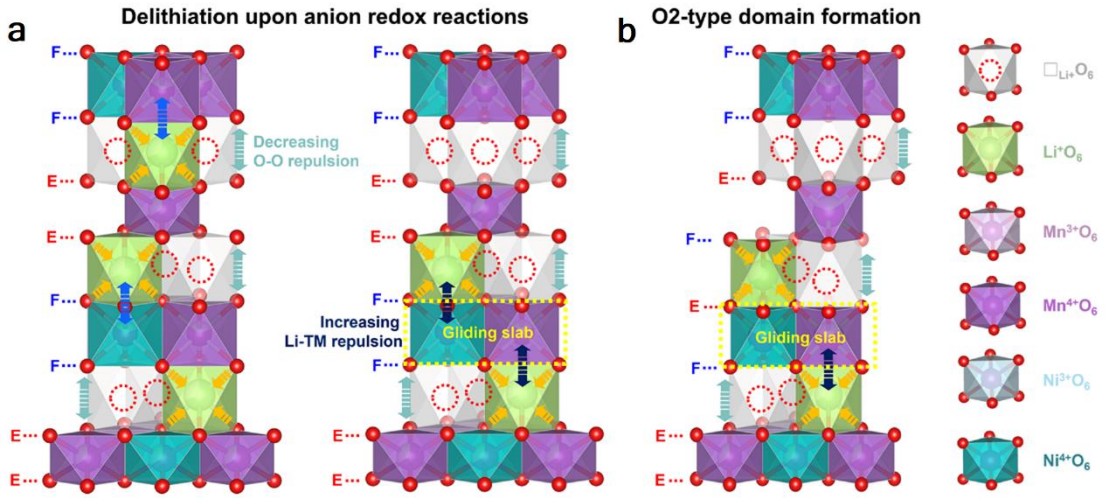


Figure 5-31. Schematic illustrations of the interlayer interactions **(a)** upon anion redox reaction in the 1st charging from 4.5 V to 4.8 V vs. Li/Li$^+$, and **(b)** the O6-to-O2 phase transformation via the gliding of TMO_2 slabs. E and F denote edge-sharing and face-sharing planes of LiO_6-TMO_6, respectively.

5.5.4. Structural evolutions upon the 1st charging from 4.5 V to 4.8 V vs. Li/Li$^+$

The following charging plateau at around 4.5 V vs. Li/Li$^+$ is usually attributed to the activation of lattice oxygen, during which irreversible local rearrangement takes place.[47] Correspondingly, after charging up from 4.5 to 4.6 V vs. Li/Li$^+$, the interlayer

spacing decreases as the (006) peak shifts to a higher angle (2θ = 18.72°), resulting from the reduced repulsion between O layers caused by the O^{2-}-to-O^{n-} (n < 2) oxidization (**Figure 5-31a**). No new peaks form during such a process, indicating that it follows a single phase deintercalation mechanism. Upon further lithium extraction to 4.7 V and 4.8 V vs. Li/Li^+, the (006) peak becomes asymmetrical and a shoulder at a higher angle appears (2θ ≈ 19.13°, marked by the red dashed circle), indicating the formation of a new phase with a smaller interlayer spacing.

Generally, in the O6-type structure, there are two kinds of TMO_2 slabs sharing either faces or edges with adjacent LiO_2 slabs on both sides. During this deep de-lithiation process, anion redox reactions dominate and the interlayer interactions of these two kinds of TMO_2 slabs are supposed to evolve in different ways. Specifically, for TMO_2 slabs sharing edges with adjacent LiO_2 slabs, the repulsion between O layers is prone to increase because removing Li^+ ions further weakens their screening effects. On the contrary, the oxygen oxidization reduces the charge density on O^{n-} (n < 2), thereby decreasing the repulsive O^{n-}-O^{n-} interaction. Those two competing factors govern the evolution of the interlayer spacing and even the phase transformation. Generally, three scenarios should be discussed: (i) if the decreasing O^{n-}-O^{n-} repulsion induced by oxygen oxidization outperforms the decreasing screening effect of Li^+, the overall repulsion between O layers decreases; (ii) the overall repulsion does not change when one of them could balance out the other one; (iii) the overall repulsion between O layers increases. In both the 1st and the 2nd scenarios, the edge-sharing structure is

stable. In the 3rd scenario, the interlayer spacing tends to increase and the gliding of TMO_2 slabs could happen for structural relaxation. Considering that there are large amounts of lithium vacancies ($\square_{Li+}$) in the deeply de-lithiated state, the O2-phase with face-sharing $\square_{Li+}$-TM^{4+} sites might form, thereby suggesting a O6-to-O2 phase transformation. However, the final scenario is unlikely to be the case because the new phase has a smaller interlayer spacing (i.e., the new XRD peak appears at a higher angle). On the other hand, for TMO_2 slabs sharing faces with adjacent LiO_2 slabs, the face-sharing Li^+-TM^{4+} repulsion should be considered. Considering that further oxygen oxidization reduces the repulsion between O layers and narrows the interlayer distancing between TMO_2 slabs, the distance between face-sharing Li^+-TM^{4+} ions decreases, leading to a stronger cationic repulsion. Such a repulsion could be relaxed by reducing the amount of face-sharing Li^+-TM^{4+} ions, which is achievable via the gliding of the TMO_2 slabs, i.e., the O6-to-O2 phase transformation (**Figure 5-31b**). The as formed O2-phase is supposed to have a smaller interlayer spacing, which is consistent with XRD results. Therefore, the final de-lithiated product could be regarded as the intergrowth of O6-type and O2-type structures (**Figure 5-32**). For other XRD peaks, the (0012) peak evolves similarly to the (006) peak, while the (018) peak merely changes, suggesting that TMO_6 octahedra do not distort severely within the basal plane (*ab*-plane). Admittedly, although the as-proposed O6-to-O2 phase transformation mechanism seems reasonable, synchrotron XRD tests and structural refinements are needed to further prove the structure of the newly formed phase in the deeply de-lithiated state.

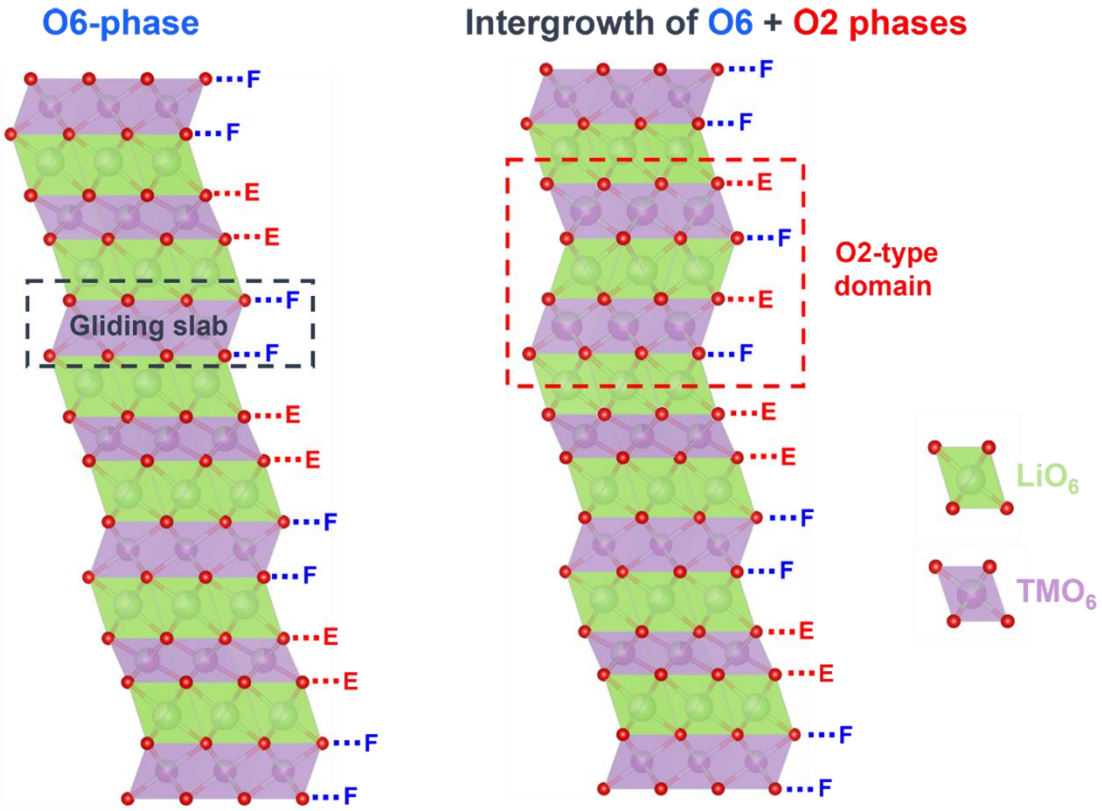


Figure 5-32. Schematic illustration of the O6-to-O2 phase transformation in the deeply de-lithiated state via the gliding of the TMO_2 slab sharing faces with adjacent LiO_2 slabs. E and F denote edge-sharing and face-sharing planes of LiO_6-TMO_6, respectively.

5.5.5. Structural evolutions upon the 1st discharge to 2.0 V vs. Li/Li^+

Upon lithium intercalation, the peak at 2θ ≈ 19.13° gradually disappears and the (006) peak centered at 2θ = 18.73° becomes more symmetrical at 4.55 V vs. Li/Li^+, meaning that such a O6-to-O2 phase transformation is reversible. Upon further discharging to 3.8 and 3.0 V vs. Li/Li^+, the (006) peak shifts to 18.7° and 18.65°, respectively, while no new peaks appear, intrinsic to the single-phase solid solution mechanism. In the deeply discharged electrode at 2.0 V vs. Li/Li^+, a shoulder appears in XRD patterns (2θ ≈ 18.45°, marked by the blue dashed circle) and gives evidence of another biphasic process leading to the discharging plateau at around 2.8 V vs. Li/Li^+. The newly formed

phase has an interlayer spacing larger than that of the O6-phase. During this deep lithiation process, the dominant electrochemical reaction is the Mn^{4+}-to-Mn^{3+} reduction. Similarly, interlayer interactions of TMO_2 slabs sharing edges with LiO_2 slabs change differently from those sharing faces with LiO_2 slabs. Specifically, for TMO_2 slabs sharing edges with adjacent LiO_2 slabs, having more screening Li^+ ions weakens the repulsion between O layers, thereby favoring the decrease of the interlayer spacing. Conversely, without considering the uneven Jahn-Teller distortions, the MnO_6 octahedra are prone to expand in volume because of the weaker covalency of the Mn^{3+}-O^{2-} bond than that of the Mn^{4+}-O^{2-} bond. From this perspective, the charge density on O^{2-} increases and the distance between TMO_2 slabs narrows, both of which contribute to the stronger repulsion between O layers. To release the increasing repulsion, TMO_2 slabs could glide to increase the interlayer spacing via forming more face-sharing structures, i.e., the O6-to-O2 phase transformation (**Figure 5-33**).

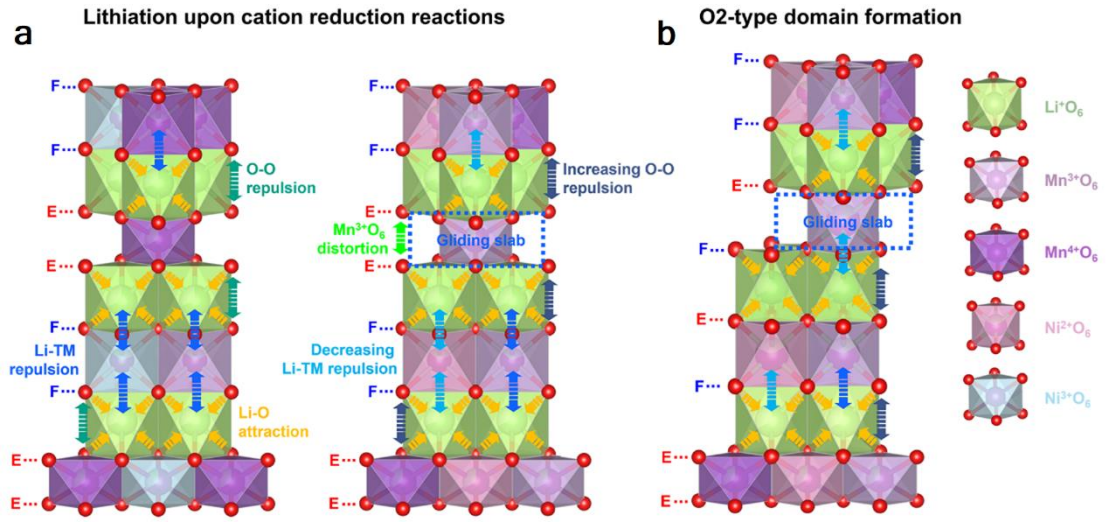


Figure 5-33. Schematic illustrations of the interlayer interactions **(a)** upon cation reduction reactions in the 1st discharging to 2.0 V vs. Li/Li^+, and **(b)** the O6-to-O2 phase transformation via the gliding of TMO_2 slabs. E and F denote edge-sharing and face-sharing planes of LiO_6-TMO_6, respectively.

Such a process is possible because the cationic repulsion between face-sharing Li^{+}-Mn^{3+} ions is weaker than that of the Li^{+}-Mn^{4+} ones. On the other hand, for TMO_2 slabs sharing faces with adjacent LiO_2 slabs, the increasing repulsion between O layers counteracts with the decreasing repulsion between face-sharing Li^{+}-TM^{3+} ions, thereby allowing the persistence of original face-sharing structures.

Therefore, the final lithiated product could also be regarded as the intergrowth of O6-type and O2-type structures (**Figure 5-34**). For other XRD peaks, the (0012) peak changes similarly to the (006) peak. As for the (018) peak (2θ = 44.5°), its position merely changes, indicating that the O6-phase is stable. However, a new peak emerges at a lower angle (2θ ≈ 44.25°, marked by the orange dashed circle), which could be indexed to the (102) peak of the O2-phase.[48] Therefore, the Mn^{4+}-to-Mn^{3+} reduction not only increases the interlayer spacing along the *c*-axis but also induces structural rearrangement within the basal plane (*ab*-plane), resulting from the expansion of $Mn^{3+}O_6$ octahedra. Such a peak split has not been observed in the O6-to-O2 phase transformation in deeply de-lithiated regions because no cation redox reactions take place. Similarly, the as-proposed O6-to-O2 phase transformation is suggested upon present XRD results and interlayer interaction analyses. Whether the newly formed phase in the deeply lithiated state has an O2-type structure needs further evidence from high resolution diffraction patterns and structural refinements.

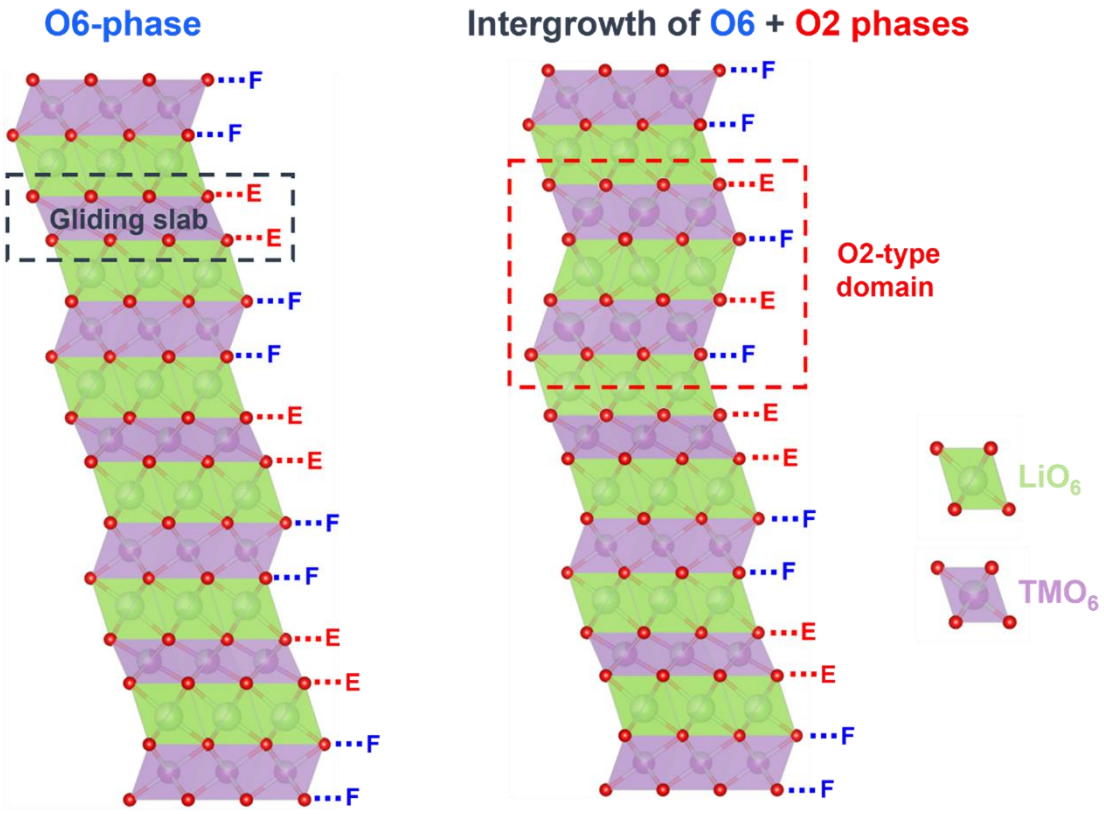


Figure 5-34. Schematic illustration of the O6-to-O2 phase transformation in the deeply lithiated state via the gliding of the TMO_2 slab sharing faces with adjacent LiO_2 slabs. E and F denote edge-sharing and face-sharing planes of LiO_6-TMO_6, respectively.

5.5.6. Structural evolutions upon the 2nd charging to 4.8 V vs. Li/Li+

In the 2nd charging to 4.0 V vs. Li/ Li+, both the shoulder at 2θ ≈ 18.4° and the peak at 2θ ≈ 44.25° gradually disappear, revealing the reversible phase transformation. Thereafter, the O6-type electrode undergoes solid solution processes until reaching the high potential plateaus (i.e., 4.6 - 4.8 V vs. Li/Li+), which again witness the possible O6-to-O2 phase transformation with the emerging peak at 2θ ≈ 19.13°. Again, the formation of the O2-phase needs to be further proven with more solid evidence in the future.

5.5.7. Overall lattice changes of the O6-phase upon de-/lithiation

To prove the reliability of those analyses, ex-situ XRD tests were performed repeatedly on another two groups of electrodes (**Figure 5-35** and **5-36**).

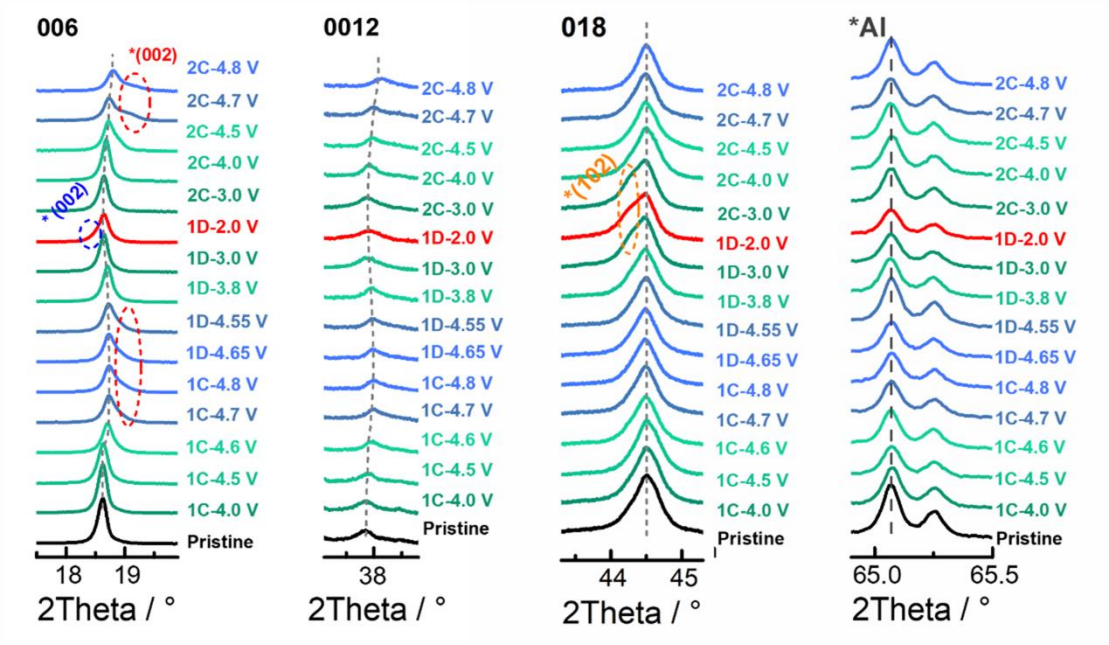


Figure 5-35. Ex-situ XRD patterns of the 2nd group of O6-type electrodes at different potentials. C and D denote charge and discharge, respectively.

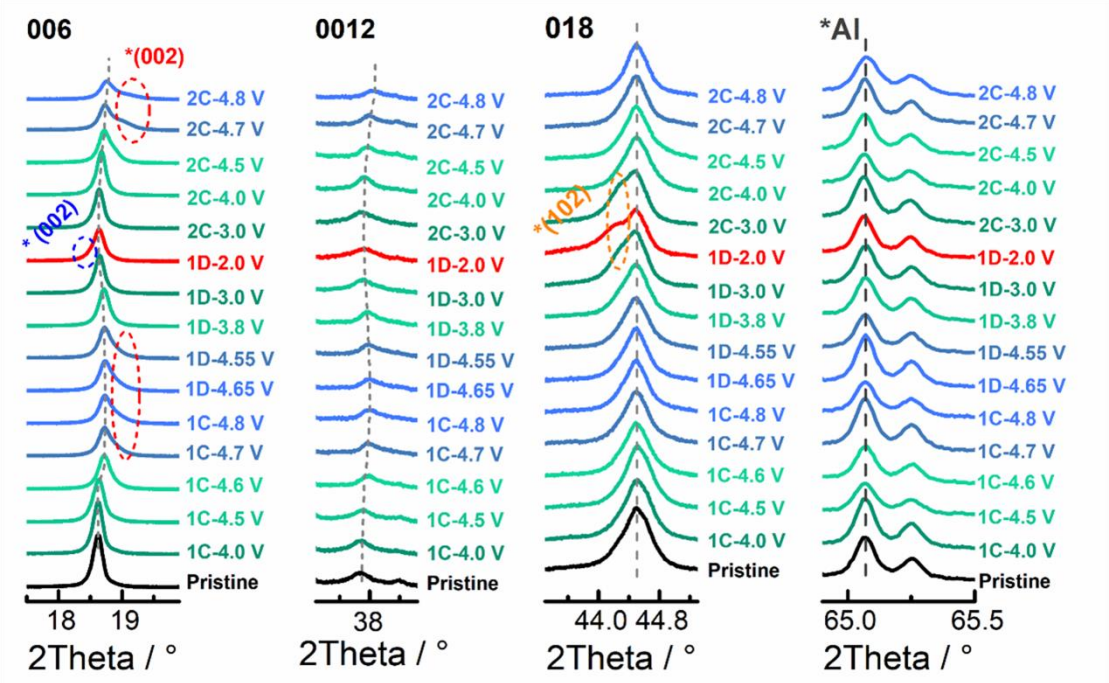


Figure 5-36. Ex-situ XRD patterns of the 3rd group of O6-type electrodes at different potentials. C and D denote charge and discharge, respectively.

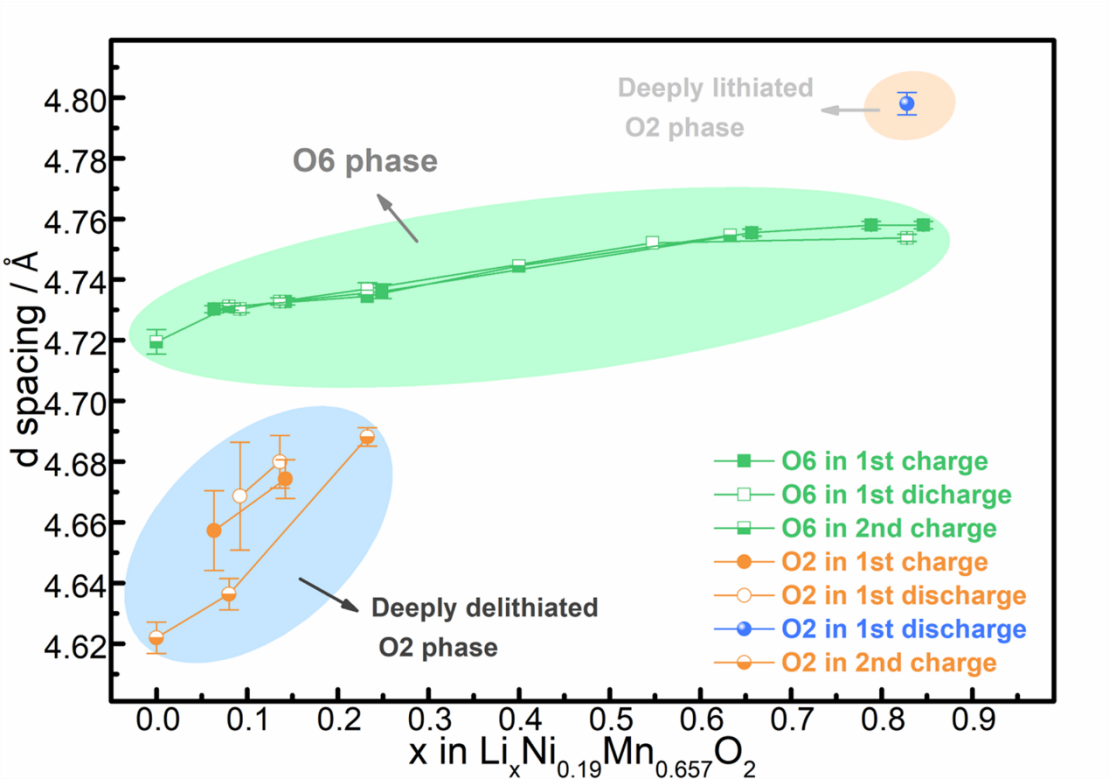


Figure 5-37. The evolution of the interlayer spacing of the (006)/ (002) lattice plane as a function of lithium content.

To quantitatively evaluate the lattice changes along the *c*-axis, all those three groups of ex-situ XRD data are used to calculate the interlayer spacings at different potentials. **Figure 5-37** presents the evolution of the interlayer spacing as a function of lithium content. Upon charging, without considering side reactions, the lithium content x in $Li_xNi_{0.190}Mn_{0.657}O_2$ is calculated according to the equation:

$$x = 0.846 \times (1 - \frac{C}{C_0}) \qquad (5-1)$$

where C is the charging capacity (mAh/ g), C_0 is the theoretical capacity of the O6-type $Li_{0.693}[Li_{0.153}Ni_{0.190}Mn_{0.657}]O_2$ (i.e., 265.9 mAh/g). The amount of lithium in the following discharge and the 2nd charge could be obtained in similar ways.

Accordingly, the O6-type structure is always the main phase within the lithium content region of $0 < x < 0.85$. Upon lithiation, the interlayer spacing of the (006) lattice plane increases from 4.719 (±0.004) Å to 4.758 (±0.001) Å as in $Li_0Ni_{0.190}Mn_{0.657}O_2$ and $Li_{0.846}Ni_{0.190}Mn_{0.657}O_2$, respectively, corresponding to a 0.83 % expansion along the *c*-axis. Meanwhile, in the deeply lithiated $Li_{0.828}Ni_{0.190}Mn_{0.657}O_2$, the as-suggested O6-to-O2 phase transformation further increases the interlayer spacing from 4.753 (±0.001) Å to 4.798 (±0.004) Å, corresponding to a 0.94 % expansion along the *c*-axis. On the contrary, in the deeply de-lithiated state, the potential O6-to-O2 phase transformation is accompanied by the decrease of the interlayer spacing from 4.719 Å (±0.004) to 4.622 Å (±0.005) (i.e., a 2.05 % contraction along the *c*-axis). Therefore, although the pristine O6-phase undergoes multiple phase transformations upon de-/ lithiation, the largest volume change along the *c*-axis is less than 4 %, which is superior to typical O3-type materials because the corresponding O3-to-O1 phase transformation usually involves much more drastic lattice changes (e.g., > 10 % in $LiCoO_2$).[42]

In summary, upon present results, the O6-phase is suggested to undergo reversible O6-to-O2 phase transformations during both the high potential (i.e., 4.6 - 4.8 V vs. Li/Li^+) and the low potential (i.e., 2.8 V vs. Li/Li^+) plateaus. Although both are resulting from the relaxation of interlayer repulsions, the former is accompanied by anion redox reactions and the latter is closely related to the Mn^{4+}-to-Mn^{3+} reduction. Notably, those phase transformations only require the gliding of the TMO_2 slabs without breaking the TM-O bonds, thereby resulting in moderate lattice changes and high

structural stability. To prove the as-suggested O6-to-O2 phase transformations, more solid evidence will be provided in the future.

5.6. Electrochemical properties of O6-phase in the fluorinated electrolyte

Given both the structural stability and the possible formation of active oxygen species upon ARRs, the capacity fading of the O6-phase is likely to result from the continuous consumption of the electrolyte to form thick cathode electrolyte interphase (CEI) films, thereby implying that its cycling performance could be improved in electrolytes being able to promote the formation of stable CEIs. Therefore, to evaluate the intrinsic long-term stability of the O6-phase and to avoid the parasitic performance decay induced by continuous electrolyte depletion, the O6-type $Li_{0.693}[Li_{0.153}Ni_{0.190}Mn_{0.657}]O_2$ was further tested in an self-made fluorinated electrolyte (details in Chapter 2).

As shown in **Figure 5-38**, changing the electrolyte does not affect the number and type of redox processes taking place in the O6-type electrode: both redox pairs in the middle potential region (i.e., 3.5 - 4.5 V vs. Li/Li^+) and sharp peaks relating to the as-suggested O6-to-O2 phase transformations are clearly seen in CV curves and dQ/dV curves, similar to those observed in the commercial electrolyte. However, in the fluorinated electrolyte, the cathodic peak assigned to the O^{n-}-to-O^{2-} reduction stabilizes after the 1st discharge, whereas it gradually increases upon initial cycles in the commercial electrolyte.

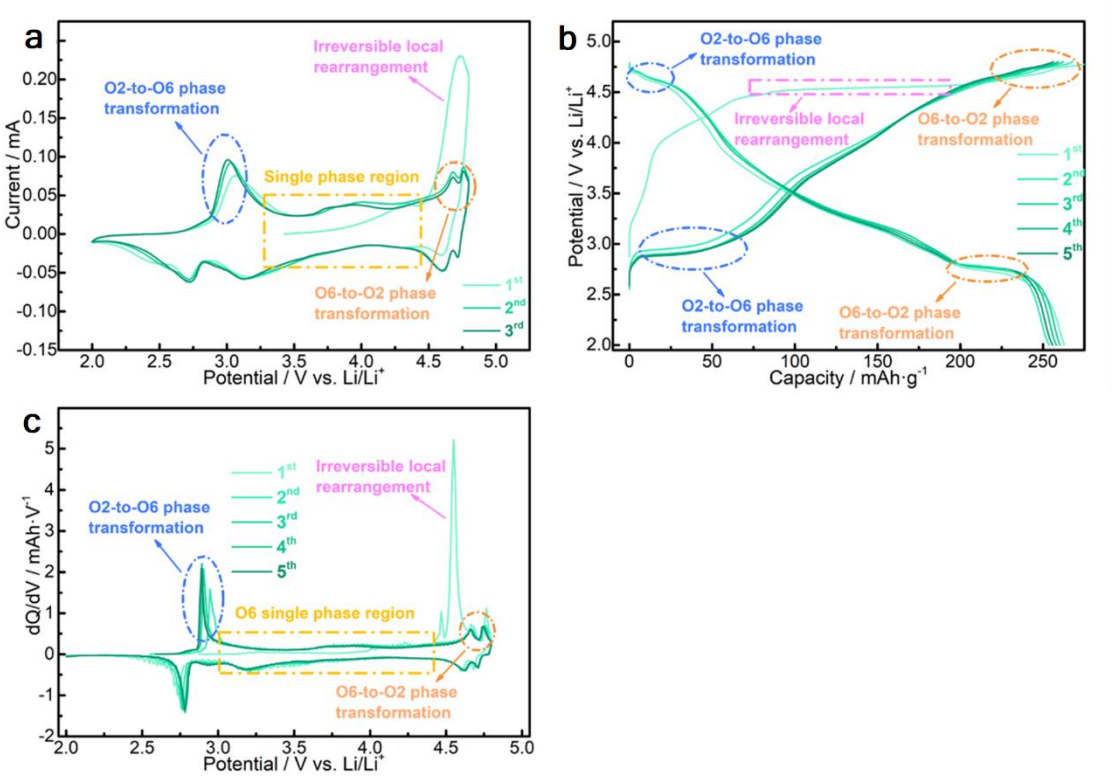


Figure 5-38. Electrochemistry of the O6-phase in the fluorinated electrolyte. **(a)** 1st-3rd CV curves at the scan rate of 0.05 mV/s. **(b)** 1st-5th GCD curves, and **(c)** corresponding dQ/dV curves at the current density of 10 mA/g within the potential window of 2.0 - 4.8 V. vs Li/Li^+.

5.6.1. Long-term cycling performance

Upon cycling in the fluorinated electrolyte, its 1st charging capacity reaches 281.0 mAh/g at a current density of 10 mA/g, which even surpasses its theoretical capacity (265.1 mAh/g) upon the complete removal of 0.846 Li^+. Presumably, this extra capacity and the prolonged plateau at around 4.5 V vs. Li/Li^+ originate from severe electrolyte decomposition in the initial activation process. In addition, compared to the commercial electrolyte, the high voltage biphasic process shows full reversibility with low voltage hysteresis from the first cycle. The capacity and voltage-hysteresis advantages bestowed by the fluorinated electrode are even more apparent at higher

current densities: 194.9 mAh/g is achieved in the first discharge with 96.0 % capacity retention after 100 cycles at the current density of 100 mA/g within the potential window of 2.0 - 4.8 V vs. Li/Li^+ (**Figure 5-39**).

By contrast, in the commercial electrolyte, its capacity decays from 194.3 mAh/g to 143.5 mAh/g after 100 cycles, i.e., 73.8 % capacity retention, with a significantly larger voltage hysteresis which increases upon cycling. Specifically, the anodic peak at around 3.0 V vs. Li/Li^+ shifts rightwards with potential changes of 0.13 V and 0.05 V in the commercial and fluorinated electrolytes, respectively. Considering that coulombic efficiencies in the fluorinated electrolyte and the commercial electrolyte are around 99.8 % and 98.8 %, respectively, the inferior performance of the O6-type electrode in the latter probably originates from cumulative side reactions between the electrolyte and the activated electrode at high potentials.

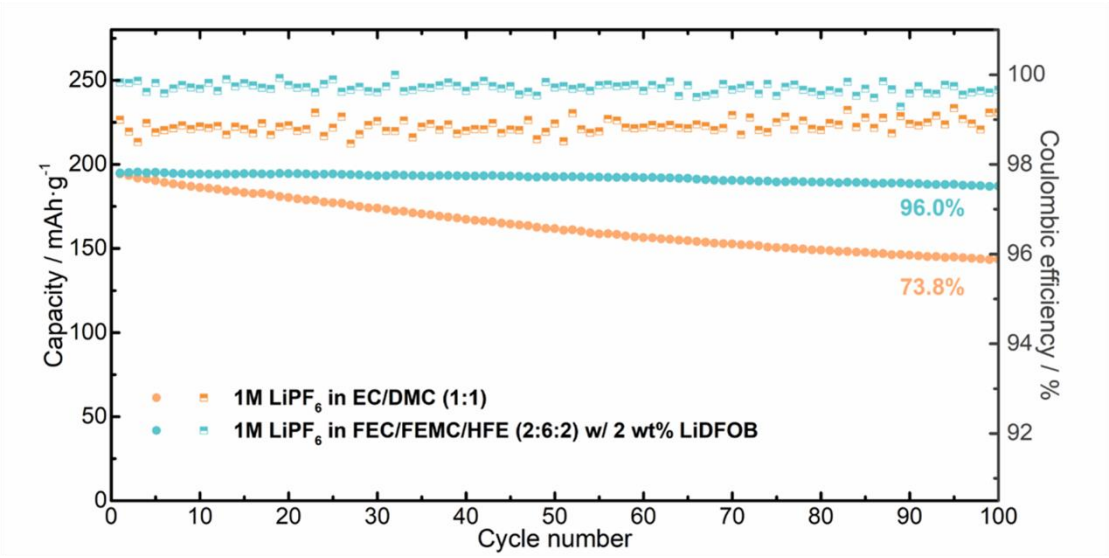


Figure 5-39. Cycling performances of the O6-phase electrodes in different electrolytes. Filled circles and half-filled squares represent capacities and coulombic efficiencies at certain cycles, respectively.

The O6-phase electrode cycled in the fluorinated electrolyte also presents slight voltage decay and those phase transformation related peaks are still sharp, whereas the one cycled in the commercial electrolyte shows severe voltage decay and broadened redox peaks (**Figure 5-40**). Specifically, after 100 cycles, the middle voltage drops from 3.16 V to 3.08 V and 2.80 V vs. Li/Li^+ in the fluorinated electrolyte and in the commercial electrolyte, respectively.

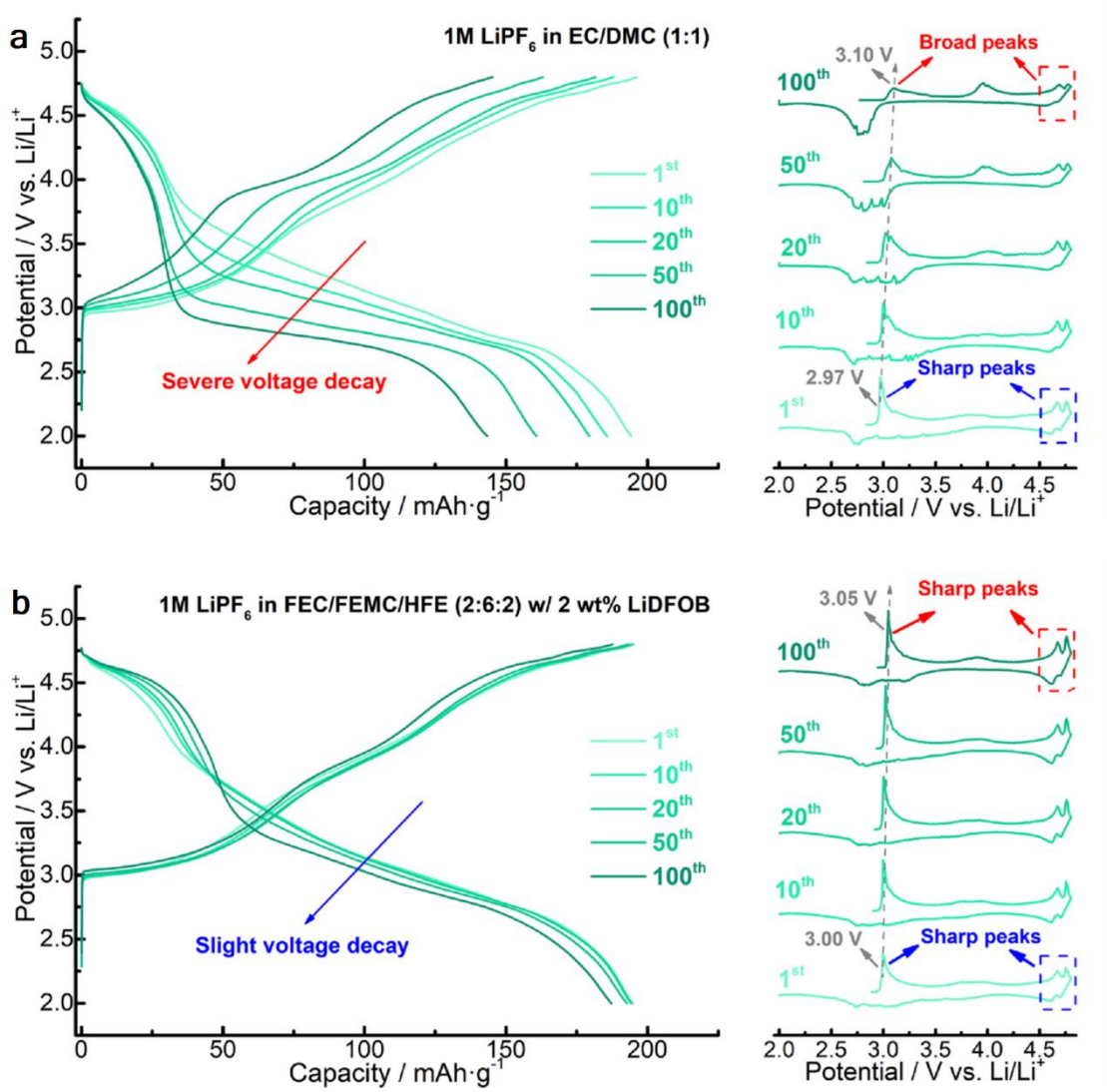


Figure 5-40. GCD curves and corresponding dQ/dV curves at the 1^{st}, 10^{th}, 20^{th}, 50^{th} and 100^{th} cycles in **(a)** the commercial electrolyte, and **(b)** the fluorinated electrolyte. The current density is 100 mA/g, and the potential window is 2.0 - 4.8 V vs. Li/Li^+. The grey dashed arrows imply the increasing polarizations upon 100 cycles.

5.6.2. The origin of the cycling stability in the fluorinated electrolyte

As shown in the Nyquist plots collected at 3.0 V vs. Li/Li^+ in the 1st discharge (**Figure 5-41**), the electrode tested in the fluorinated electrolyte presents a larger semicircle in the high frequency region than that of the electrode tested in the commercial electrolyte, indicating a larger resistance of the CEI (R_{CEI}). Upon further cycling, for the electrode tested in the fluorinated electrolyte, the value of R_{CEI} gradually decreases and stabilizes after 5 cycles, whereas it keeps increasing in the commercial electrolyte, suggesting continuous electrolyte consumption.

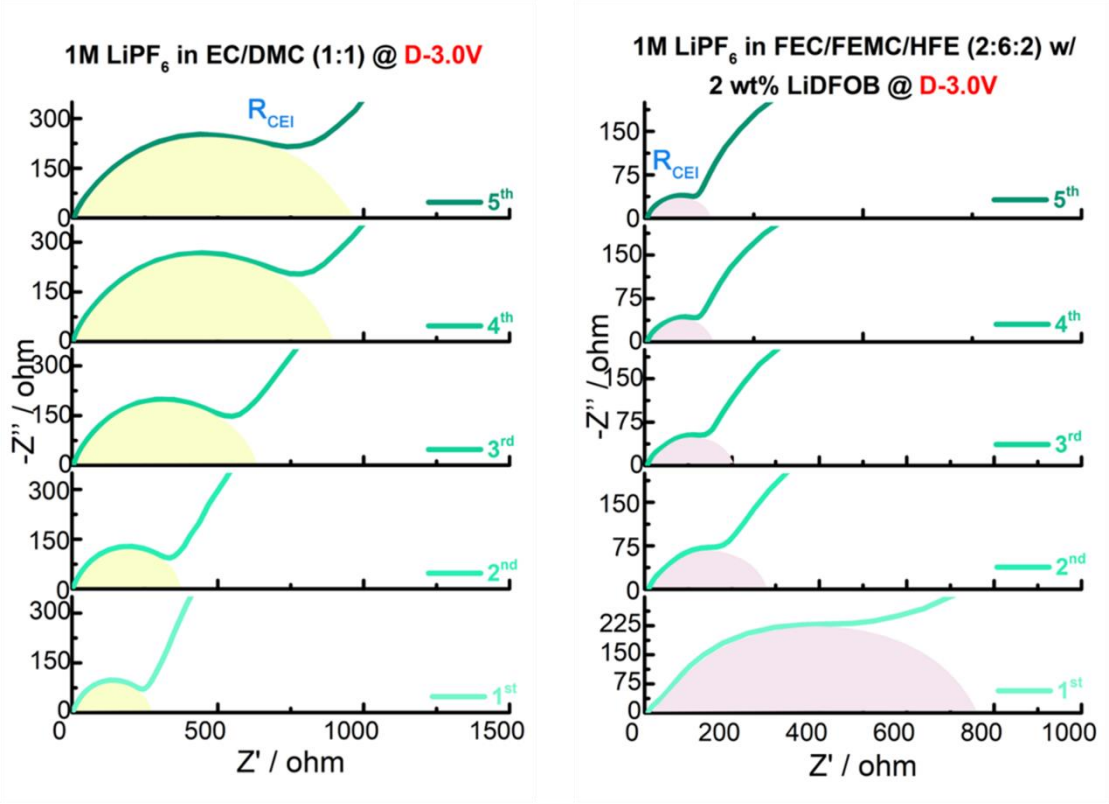


Figure 5-41. Nyquist plots of the O6-phase electrodes tested in different electrolytes at 3.0 V vs. Li/Li^+ during the 1st-5th cycles. Solid lines are fitted from experimental results and colored semicircles depict resistances of surface films (R_{CEI}).

The depth profiling XPS spectra of cycled electrodes also suggest the formation of uniform and dense CEI in the fluorinated electrolyte (**Figure 5-42**). In the O 1s spectrum, the shoulder at 529.8 eV reveals the bare lattice oxygen for the electrode cycled in the commercial electrolyte, whereas it is not observed for the one cycled in the fluorinated electrolyte. Via etching, both electrodes show increasing amounts of bare lattice oxygen, yet the intensity of the peak at 529.8 eV is much higher for the electrode cycled in the commercial electrolyte than that of the one cycled in the fluorinated electrolyte. In addition, the much stronger LiF peaks (684.7 eV) compared to the C-F bonds (687.4 eV) demonstrate that the CEI formed in the fluorinated electrolyte is LiF-enriched,[49] meaning that they can protect the electrode from being continuously corroded by the electrolyte especially when ARRs take place.

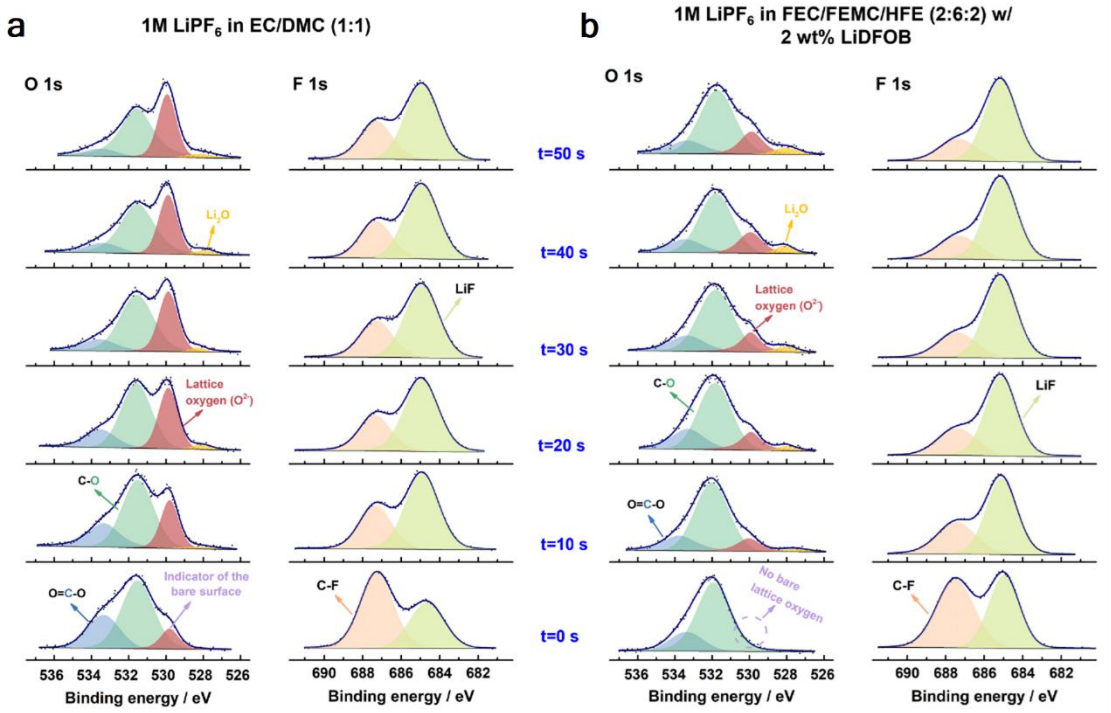


Figure 5-42. Depth profiling XPS spectra of electrodes cycled **(a)** in the commercial electrolyte, and **(b)** in the fluorinated electrolyte. From bottom to top, electrodes were etched by Ar^+ beam for 0, 10, 20, 30, 40 and 50 s, respectively.

5.7. Summary and outlook

This work demonstrates the potential of O6-type materials for stable high-capacity and long-life cathode materials. A metastable O6-phase lithium-deficient layered cathode material was prepared via Na^+/Li^+ ion-exchange of the P2-type precursor followed by the low-temperature thermal treatment. Although the O6-type structure has been observed as a metaphase in lithium-based layered materials since its first observation in $Li_{0.62}CoO_2$,[22] this is the first demonstration of a directly synthesized lithium-deficient and manganese-rich O6-type cathode material with both stable cation and (at least surface) anion redox reactions for lithium-ion batteries. Detailed multimodal characterization has demonstrated that the metastable O6-phase undergoes first-order phase transformations in both highly de-lithiated states and highly-lithiated states, potentially forming O2-phases via the gliding of TMO_2 slabs. The absence of TM-O bond cleavage means that those phase transformation processes show excellent dynamics resulting in low potential polarizations, and superior long-term stability, with the retention of sharp differential peaks even after 100 cycles.

When tested as the cathode material in the fluorinated electrolyte, the O6-type $Li_{0.693}[Li_{0.153}Ni_{0.190}Mn_{0.657}]O_2$ electrode delivers a capacity of 194.9 mAh/g and a capacity retention of 96.0 % after 100 cycle (100 mA/g, 2.0-4.8 V vs. Li/Li^+). Additionally, neither severe voltage decay nor the formation of the spinel phase is observed upon long-term cycling. Although the protective CEI formed in the fluorinated electrolyte is helpful for initiating the reversibility of the O6-O2 transition in lower cycle numbers,

the intrinsic reason for its superior performance lies in the stable O6-type structure itself especially considering its manganese-rich local environment. It has been widely reported that the Jahn-Teller effect induced by the reduction of Mn^{4+} to Mn^{3+} easily causes distortions of $Mn^{3+}O_6$ octahedra, thereby leading to irreversible layered-to-spinel phase transformations and the parasitic voltage decay.[50] Even worse, upon anion redox reactions, extracting electrons from the O 2p orbital produces localized electron holes, O_2^{n-} dimers or even molecular O_2, all of which inevitably induce local distortions.[51-53] Lithium vacancies formed upon de-lithiation make interlayer or intralayer TM migrations possible. However, because of the face-sharing geometry between TMO_6 and LiO_6 octahedra in the O6-type structure, the irreversible TM migration is largely suppressed due to electrostatic repulsion. Even though O6-to-O2 phase transformations taking place over the high potential (i.e., 4.6 - 4.8 V vs. Li/Li^+) and low potential plateaus (i.e., 2.8 V vs. Li/Li^+) appear undesirable at first glance, those processes do not involve the breaking of TM-O bonds, thereby leaving the face-sharing local structure intact and suppressing TM migration.

Finally, while there is no doubt that mitigating the irreversible TM migration is beneficial for achieving long-term stability in lithium-stoichiometric cathode materials, it is critically important when tapping into the additional capacity afforded by anion redox reactions in lithium-rich cathode materials. Upon the oxidation of oxygen, the lattice oxygen (O^{2-}) ultimately transforms to molecular O_2 via the O-O dimerization, which ideally should be trapped in the lattice and reduced back to O^{2-} upon

discharging.[54] However, the TM migration creates isolated O_2 molecules no longer anchoring to the nearby TM sites, which thereafter escape from the lattice and cause performance deterioration.[55] On the other hand, the oxygen loss further eases the detrimental TM migration and vice versa. Although many O2-type structures have been reported to demonstrate stable anion redox reactions and mitigated TM migrations due to similar local structures, directly ion-exchanged materials might contain a multitude of defects and nanodomains as characterized in this work, which do not promote the formation of uniform surface films especially under circumstances of anion redox reactions. It has been shown that forming uniform and dense CEIs is of great importance when pushing the charging limit to higher potentials, e.g., monocrystal cathode materials with lower surface areas are attracting more and more attentions recently than their polycrystal counterparts.[56] From this perspective, because the thermal treatment even at a moderate temperature favors crystallization without destroying face-sharing local patterns, the O6-type structure should be an ideal candidate in designing advanced cathode materials with anion redox reactions. We hope this work could inspire future talented ideas to build more unique metastable phases different from traditional O3-type structures.

5.8. References

1. A. Grimaud, W. T. Hong, Y. Shao-Horn, and J.-M. Tarascon, *Nat. Mater.*, 2016, **15**, 121-126.
2. Z. Zhuo, K. Dai, J. Wu, L. Zhang, N. Tamura, Y. Chuang, J. Feng, J. Guo, Z. X. Shen, G. Liu, F. Pan, and W. Yang, *ACS Energy Lett.*, 2021, **6**, 3417-3424.

3. M. Sathiya, G. Rousse, K. Ramesha, C. P. Laisa, H. Vezin, M. T. Sougrati, M.-L. Doublet, D. Foix, D. Gonbeau, W. Walker, A. S. Prakash, M. Ben Hassine, L. Dupont, J.-M. Tarascon, *Nat. Mater.*, 2013, **12**, 827-835.
4. Y. Yu, P. Karayaylali, D. Sokaras, L. Giordano, R. Kou, C.-J. Sun, F. Maglia, R. Jung, F. S. Gittleson, and Y. Shao-Horn, *Energy Environ. Sci.*, 2021, **14**, 2322-2334.
5. E. Hu, X. Yu, R. Lin, X. Bi, J. Lu, S. Bak, K.-W. Nam, H. L. Xin, C. Jaye, D. A. Fischer, K. Amine, and X.-Q. Yang, *Nat. Energy*, 2018, **3**, 690-698.
6. R. A. House, J.-J. Marie, M. A. Pérez-Osorio, G. J. Rees, E. Boivin, and P. G. Bruce, *Nat. Energy*, 2021, **6**, 781-789.
7. D.-H. Seo, J. Lee, A. Urban, R. Malik, S. Y. Kang, and G. Ceder, *Nat. Chem.*, 2016, **8**, 692-697.
8. X. Cao, H. Li, Y. Qiao, P. He, Y. Qian, X. Yue, M. Jia, J. Cabana, and H. Zhou, *Joule*, 2022, **6**, 1-14.
9. D. Eum, B. Kim, S. J. Kim, H. Park, J. Wu, S.-P. Cho, G. Yoon, M. H. Lee, S.-K. Jung, W. Yang, W. M. Seong, K. Ku, O. Tamwattana, S. K. Park, I. Hwang, and K. Kang, *Nat. Mater.*, 2020, **19**, 419-427.
10. Y. Idemoto, R. Yamamoto, N. Ishida, and N. Kitamura, *Electrochim. Acta*, 2015, **153**, 399-408.
11. R. A. House, U. Maita, M. A. Pérez-Osorio, J. G. Lozano, L. Jin, J. W. Somerville, L. C. Duda, A. Nag, A. Walters, K.-J. Zhou, M. R. Roberts, and P. G. Bruce, *Nature*, 2020, **577**, 502-508.
12. F. Ning, B. Li, J. Song, Y. Zuo, H. Shang, Z. Zhao, Z. Yu, W. Chu, K. Zhang, G. Feng, X. Wang, and D. Xia, *Nat. Commun.*, 2020, **11**, 4973.
13. Y. Yang, H. Su, T. Wu, Y. Jiang, D. Liu, P. Yan, H. Tian, and H. Yu, *Sci. Bull.*, 2019, **64**, 553-561.
14. M. Sathiya, A. M. Abakumov, D. Foix, G. Rousse, K. Ramesha, M. Saubanère, M. L. Doublet, H. Vezin, C. P. Laisa, A. S. Prakash, D. Gonbeau, G. VanTendeloo, and J.-M. Tarascon, *Nat. Mater.*, 2015, **14**, 230-238.
15. X. Ding, D. Luo, J. Cui, H. Xie, Q. Ren, and Z. Lin, *Angew. Chem. Int. Ed.*, 2020, **59**, 7778-7782.
16. Q. Li, D. Ning, D. Zhou, K. An, G. Schuck, D. Wong, W. Kong, C. Schulz, G. Schumacher, and X. Liu, *Chem. Mater.*, 2020, **32**, 9404-9414.
17. Z. Zhu, R. Gao, I. Waluyo, Y. Dong, A. Hunt, J. Lee, and J. Li, *Adv. Energy Mater.*, 2020, **10**, 202001120.
18. B. Mortemard de Boisse, J. Jang, M. Okubo, and A. Yamada, *J. Electrochem. Soc.*, 2018, **165**, A3630-A3633.
19. N. Yabuuchi, Y. Kawamoto, R. Hara, T. Ishigaki, A. Hoshikawa, M. Yonemura, T. Kamiyama, and S. Komaba, *Inorg. Chem.*, 2013, **52**, 9131-9142.
20. H. Liu, C. Zhao, Q. Qiu, B. Hu, F. Geng, J. Li, W. Tong, B. Hu, and C. Li, *J. Phys. Chem. Lett.*, 2021, **12**, 8740-8748.
21. S. Komaba, L. Croguennec, F. Tournadre, P. Willmann, and C. Delmas, *J. Phys. Chem. C*, 2013, **117**, 3264-3271.
22. A. Mendiboure, C. Delmas, and P. Hagenmuller, *Mat. Res. Bull.*, 1984, **19**, 1383-1392.

23. N. Yabuuchi, R. Hara, M. Kajiyama, K. Kubota, T. Ishigaki, A. Hoshikawa, and S. Komaba, *Adv. Energy Mater.*, 2014, **4**, 1301453.
24. Z. Lu, R. A. Donaberger, C. L. Thomas, and J. R. Dahn, *J. Electrochem. Soc.*, 2002, **149**, A1083-A1091.
25. C. Delmas, J.-J. Braconnier, and P. Hagenmuller, *Mat. Re. Bull.*, 1981, **17**, 117-123.
26. F. Tournadre, L. Croguennec, I. Saadoune, F. Weill, Y. Shao-Horn, P. Willmann, and C. Delmas, *Chem. Mater.*, 2014, **16**, 1411-1417.
27. J. M. Paulsen, and J. R. Dahn, *Solid State Ionics*, 1999, **126**, 3-24.
28. D. Carlier, I. Saadoune, L. Croguennec, M. Ménétrier, E. Suard, and C. Delmas, *Solid State Ionics*, 2001, **144**, 263-276.
29. J. N. Reimers, and J. R. Dahn, *J. Electrochem. Soc.*, 1992, **139**, 2091-2097.
30. Z. Lu, and J. R. Dahn, *Chem. Mater.*, 2001, **13**, 2078-2083.
31. M. A. Stranick, *Surf. Sci. Spectra*, 1999, **6**, 39-46.
32. M. A. Stranick, *Surf. Sci. Spectra*, 1999, **6**, 31-38.
33. A. M. Mansour, *Surf. Sci. Spectra*, 1994, **3**, 231-238.
34. A. M. Mansour and C. A. Melendres, *Surf. Sci. Spectra*, 1994, **3**, 263-270.
35. Z. Lu and J. R. Dahn, *J. Electrochem. Soc.*, 2001, **148**, A1225.
36. X. Liu, D. Zhang, M. Zhang, Y. Yan, Z. Li, P. Wang, and R. Murakami, *J. Phys. Chem. Lett.*, 2022, **13**, 6181-6186.
37. P. K. Nayak, J. Grinblat, M. Levi, E. Levi, S. Kim, J. W. Choi, and D. Aurbach, *Adv. Energy Mater.*, 2016, **6**, 1502398.
38. D. Carlier, I. Saadoune, M. Ménétrier, and C. Delmas, *J. Electrochem. Soc.*, 2002, **149**, A1310-A1320.
39. D. Carlier, A. Van der Ven, C. Delmas, and G. Ceder, *Chem. Mater.*, 2003, **15**, 2651-2660.
40. D. Eum, B. Kim, S. J. Kim, H. Park, J. Wu, S.-P. Cho, G. Yoon, M. H. Lee, S.-K. Jung, W. Yang, W. M. Seong, K. Ku, O. Tamwattana, S. K. Park, I. Hwang, and K. Kang, *Nat. Mater.*, 2020, **19**, 419-427.
41. H. Liu, C. Du, G. Yin, B. Song, P. Zuo, X. Cheng, Y. Ma, and Y. Gao, *J. Mater. Chem. A*, 2014, **2**,15640.
42. K. Kawai, X.-M. Shi, N. Takenaka, J. Jang, B. Mortemard de Boisse, A. Tsuchimoto, D. Asakura, J. Kikkawa, M. Nakayama, M. Okubo, and A. Yamada, *Energy Environ. Sci.*, 2022, **15**, 2591-2600.
43. M. Tang, A. Dalzini, X. Li, X. Feng, P.-H. Chien, L. Song, and Y. Hu, *J. Phys. Chem. Lett.*, 2017, **8**, 4009-4016.
44. H. Nguyen, and R. J. Clément, *ACS Energy Lett.*, 2020, **5**, 3848-3859.
45. B. Song, M. Tang, E. Hu, O. J. Borkiewicz, K. M. Wiaderek, Y. Zhang, N. D. Phillip, X. Liu, Z. Shadike, C. Li, L. Song, Y.-Y. Hu, M. Chi, G. M. Veith, X.-Q. Yang, J. Liu, J. Nanda, K. Page, and A. Huq, *Chem. Mater.*, 2019, **31**, 3756-3765.
46. J. Li, C. Lin, M. Weng, Y. Qiu, P. Chen, K. Yang, W. Huang, Y. Hong, J. Li, M. Zhang, C. Dong, W. Zhao, Z. Xu, X. Wang, K. Xu, J. Sun, and F. Pan, *Nat. Nanotechnol.*, 2021, **16**, 599-605.

47. W. Hua, S. Wang, M. Knapp, S. J. Leake, A. Senyshyn, C. Richter, M. Yavuz, J. R. Binder, C. P. Grey., H. Ehrenberg, S. Indris, and B. Schwarz, *Nat. Commun.*, 2019, **10**, 5365.
48. J. M. Paulsen, C. L. Thomas, and J. R. Dahn, *J. Electrochem. Soc.*, 2000, **147**, 861-868.
49. C. Cui, X. Fan, X. Zhou, J. Chen, Q. Wang, L. Ma, C. Yang, E. Hu, X.-Q. Yang, and C. Wang, *J. Am. Chem. Soc.*, 2020, **142**, 8918-8927.
50. R. Tackett, G. Lawes, B. C. Melot, M. Grossman, E. S. Toberer, and R. Seshadri, *Phys. Rev. B*, 2007, **76**, 024409.
51. K. Luo, M. R. Roberts, N. Guerrini, N. Tapia-Ruiz, R. Hao, F. Massel, D. M. Pickup, S. Ramos, Y.-S. Liu, J. Guo, A. V. Chadwick, L. C. Duda, and P. G. Bruce, *J. Am. Chem. Soc.*, 2016, **138**, 11211-11218.
52. Z. Chen, J. Li, and X. C. Zeng, *J. Am. Chem. Soc.*, 2019, **141**, 10751-10759.
53. R. A. House, J.-J. Marie, J. Park, G. J. Rees, S. Agrestini, A. Nag, M. Garcia-Fernandez, K.-J. Zhou, and P. G. Bruce, *Nat. Commun.*, 2021, **12**, 2975.
54. R. A. House, G. J. Rees, M. A. Pérez-Osorio, J.-J. Marie, E. Boivin, A. W. Robertson, A. Nag, M. Garcia-Fernandez, K.-J. Zhou, and P. G. Bruce, *Nat. Energy*, 2020, **5**, 777-785.
55. J. Hong, W. E. Gent, P. Xiao, K. Lim, D.-H. Seo, J. Wu, P. M. Csernica, C. J. Takacs, D. Nordlund, C.-J. Sun, K. H. Stone, D. Passarello, W. Yang, D. Prendergast, G. Ceder, M. F. Toney, and W. C. Chueh, *Nat. Mater.*, 2019, **18**, 256-265.
56. Y. Bi, J. Tao, Y. Wu, L. Li, Y. Xu, E. Hu, B. Wu, J. Hu, C. Wang, J.-G. Zhang, Y. Qi, and J. Xiao, *Science*, 2020, **370**, 1313-1317.

CHAPTER 6. CONCLUSIONS AND FUTURE WORK

The overall aim of this thesis was to improve the stability of ARRs in LRCMs via (i) gaining a greater understanding about the ARR-induced local coordination evolutions and (ii) tailoring rational local structures to suppress the detrimental oxygen loss and TM migration. The main conclusions drawn from this project and implications for future work are summarized as follows.

6.1. Conclusions

Chapter 3 demonstrates the potential of using in-situ Raman spectroscopy to decipher the local environment changes upon both cation and anion redox activities in the archetypal Li_2RuO_3. Because of the unique Ru-Ru dimerization in Li_2RuO_3, it presents Raman active Ru-Ru motions in the region of 150-300 cm^{-1}. The evolutions of such Ru-Ru dimers have been monitored and interpreted in combination with multimodal characterizations. Moreover, a unique Raman band is captured at around 500 cm^{-1} upon triggering the oxygen redox activities, which is suggested to originate from the Ru-O_2^{n-} ($0 < n < 4$) coordination and regarded as the indicator of O-O dimerization. Accordingly, a general picture about the redox activities in Li_2RuO_3 has been drawn, which is consistent with present theories, thereby manifesting the capability of the Raman spectroscopy to study local environment changes under electrochemical conditions.

In Chapter 4, F-doping turns out to be ineffective in stabilizing ARRs in Li_2RuO_3. However, even trace amount of F-doping largely improves the cycling performance of Li_2RuO_3 solely upon the Ru redox reactions. Such a performance enhancement is attributed to the effects of F-dopants to mitigate the strain accumulation during the extraction of the 1st Li^+ (i.e., Li_2RuO_3 to $Li_{1.0}RuO_3$). Specifically, because the repulsive interaction between the O layers tends to increase along with the removal of the screening Li^+ ions, the weak O-F interaction could potentially buffer the interlayer repulsion. Meanwhile, F dopants lead to local disordering and suppress the preferential orientation along the *c*-axis, thereby mitigating the strain accumulation along the basal plane. In further work, in-situ XRD tests should be conducted to investigate the structural evolutions in real time. Besides, the strain accumulation might be quantitively evaluated via Rietveld refinement of XRD patterns. Traditionally, in LRCMs, triggering the ARRs is believed to be the origin of performance degradation. However, this work reveals that not activating the oxygen redox activities does not necessarily guarantee better long-term performances. Therefore, notwithstanding the widespread interests in exploiting the ARRs, this work highlights the importance of being aware of potential structural degradations during the cation redox reactions and provides a new perspective to rationally design LRCMs.

Chapter 5 demonstrates that tailoring local structures is an effective way to improve the stability of ARRs in LRCMs. Specifically, a metastable O6-type material with the face-sharing local geometry was prepared, which presents stable cation and anion

redox reactions. Careful examinations suggest that the metastable O6-type structure potentially converts to O2-type structures in either deeply de-lithiated or deeply lithiated states. In further work, whether the newly formed phases are O2-phases need to be proven via collecting high quality diffraction data and performing structural refinements. Interestingly, the as-suggested O6-to-O2 phase transformations are highly reversible because they only involve the gliding of TMO_2 slabs without breaking TM-O bonds, meaning that the face-sharing geometry retains in the full de-/lithiation process. Upon cycling, it shows superior long-term stability in terms of both capacity and voltage retentions. Therefore, the O6-type structure reported in this work provides another degree of freedom for designing other cathode materials with ARRs.

The main chapters of this thesis mainly focus on investigating mechanisms of anion redox reactions (ARRs) in multiple materials and improving their electrochemical properties. In Appendix C, we have tentatively tried to build an interferometric scattering microscopy (iSCAT) setup, which has the potential to track single particle dynamics. Considering that iSCAT uses visible light as the incident wave, it is suitable for the in-situ/operando study of the ARR-induced structural changes via the light-matter scattering. A dedicated O6-phase $Li_{1.2}Mn_{0.8}O_2$ has been prepared and demonstrated unique electrochemical properties, making it a good candidate for further iSCAT test.

6.2. Future work

Looking forward, there are great potentials and opportunities that could be explored in the future.

Firstly, Raman spectroscopy is sensitive to the lattice vibration, and so is an ideal probe to study the short-range patterns. Therefore, in-situ Raman spectroscopy to investigate the local coordination evolutions around oxygen could be used in other LRCMs to track the oxygen redox activities and in a wide range of fields as well. Meanwhile, collecting data via using local sensitive techniques such as PDF and NMR will be useful to better interpret the findings from the in-situ Raman results. In addition, building reasonable models upon experimental observations and performing theoretical calculations will be very helpful in indexing or even visualizing the Raman-active motions. Moreover, as observed in Chapter 3, other than the Raman-active lattice vibrations, the other components such as the organic solvents and lithium salts in the electrolyte could be identified by Raman spectroscopy. Therefore, future work can also be devoted to using in-situ Raman spectroscopy to study the decomposition of the electrolyte or the formation of CEIs upon ARRs.

Secondly, as indicated in Chapter 5, building advanced LRCMs with ARRs does not necessarily focus on the well-studied structures (e.g., traditional O3-phases). The metastable O6-phase has demonstrated the potential to be a model structure for stable cation and anion redox reactions. The stability of such a metastable O6-phase is

considered to originate from its face-sharing local structures, which suppress the interlayer TM migration. In the future, the energy barriers for TM migrations in different phases should be quantitively compared via theoretical calculations. Similarly, the as-suggested O6-to-O2 phase transformations should be evaluated theoretically as well. From the perspective of building better LRCMs, more O6-phase materials can be designed based on this model, while finding other stable or metastable phases different from traditional O3-type structures is also of great potential.

Finally, developing in-situ/operando techniques has been and will be very important in understanding the nature of the ARRs. As indicated throughout the thesis, although the oxygen redox activities have been proven and monitored, there are still puzzles to be solved, e.g., whether the Mn^{5+}/Mn^{7+} species form or not? From this perspective, capturing the intermediate phases between the lattice oxygen (O^{2-}) and oxygen molecules (O_2) should be one of the main goals in future in-situ/operando studies, in which the temporal resolution of the technique should be considered because those intermediate states might only exist for a very short period.

Appendix A. Structural refinements of Li_2RuO_3 electrodes

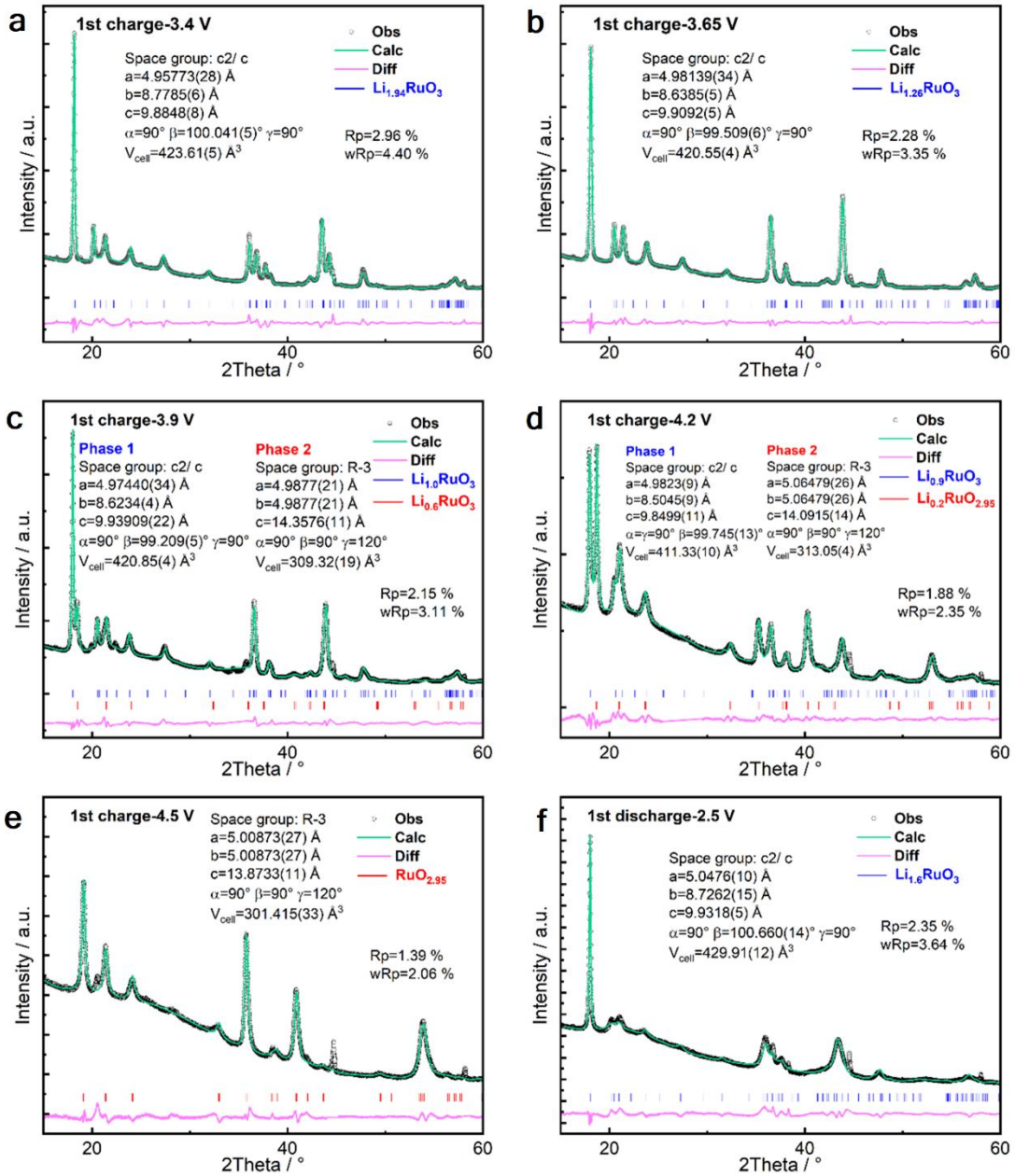


Figure A1. Rietveld refinement results of XRD patterns collected at different states in the initial cycle. **(a)** XRD patterns at the beginning of the first slope (3.4 V). The structure of $Li_{1.94}RuO_3$ fits well with the pristine monoclinic phase. The content of Li is calculated according to GCD profiles with a theoretical capacity of 328 mAh/g. **(b)**, XRD patterns at the beginning of the middle plateau (3.65 V). The $Li_{1.26}RuO_3$ presents a monoclinic phase with a distorted C2/c symmetry. **(c** and **d)** XRD patterns at the beginning and in the middle of the high-voltage slope. **(e)** XRD patterns at the end of 1st charge (4.5 V). The unfitted peak at around 2θ=20.5° is attributed to the ordered honeycomb-like patterns that are not involved in the R-3 model. **(f)**, XRD patterns after the 1st discharge. Although the structure changes back to c2/c phase, peaks relating to honeycomb-like superstructures decay in intensity and present larger full width at half maximums (FWHMs), indicating irreversible changes of the local environment.

Table A1. Structural parameters of C-3.4V-$Li_{1.94}RuO_3$

Phase: $Li_{1.94}RuO_3$	Space group: C2/c				
Atom	Fractional coordinates			Wyckoff symbol	Occupancy
	x	y	z		
Li1	0.25	0.25	0.50	4d	0.83
Ru1	0.25	0.25	0.50	4d	0.14
Li2	0	0.07	0.25	4e	0.93
Ru2	0	0.07	0.25	4e	0.04
Li3	0	0.389(1)	0.25	4e	0.97
Ru3	0	0.389(1)	0.25	4e	0.00
Li4	0	0.7374(1)	0.25	4e	0.96
Ru4	0	0.7374(1)	0.25	4e	0.04
Ru5	0.2386(9)	0.0783(4)	0.0025(9)	8f	0.90
Li5	0.2386(9)	0.0783(4)	0.0025(9)	8f	0.10
O1	0.1333(7)	0.25	0.118(1)	8f	1.00
O2	0.122(1)	0.577(1)	0.120(1)	8f	1.00
O3	0.128(1)	0.923(1)	0.117(1)	8f	1.00
Lattice parameters: a=4.95773(28) Å, b=8.7785(6) Å, c=9.8848(8) Å; α=90°, β=100.041(5)°, γ=90°; $V_{unit\ cell}$=423.61(5) $Å^3$					

Table A2. Structural parameters of C-3.65V-$Li_{1.26}RuO_3$

Phase: $Li_{1.26}RuO_3$	Space group: C2/c				
Atom	Fractional coordinates			Wyckoff symbol	Occupancy
	x	y	z		
Li1	0.25	0.25	0.50	4d	0.49
Ru1	0.25	0.25	0.50	4d	0.14
Li2	0	0.025	0.25	4e	0.59
Ru2	0	0.025	0.25	4e	0.04
Li3	0	0.4153(1)	0.25	4e	0.63
Ru3	0	0.4153(1)	0.25	4e	0.00
Li4	0	0.6758(4)	0.25	4e	0.59
Ru4	0	0.6758(4)	0.25	4e	0.04
Ru5	0.2306(1)	0.0827(1)	-0.0035(1)	8f	0.90
Li5	0.2306(1)	0.0827(1)	-0.0035(1)	8f	0.10
O1	0.132(1)	0.2501(2)	0.120(1)	8f	1.00
O2	0.120(1)	0.576(1)	0.1043(1)	8f	1.00
O3	0.132(1)	0.940(1)	0.1298(1)	8f	1.00
Lattice parameters: a=4.98139(34) Å, b=8.6385(5) Å, c=9.9092(5) Å; α=90°, β=99.509(6)°, γ=90°; $V_{unit\ cell}$=420.55(4) $Å^3$					

Table A3. Structural parameters of C-3.9V-$Li_{0.9}RuO_3$

Phase1: $Li_{1.0}RuO_3$	Space group: C2/c			wt=76.3%	
Atom	Fractional coordinates			Wyckoff symbol	Occupancy
	x	y	z		
Li1	0.25	0.25	0.50	4d	0.41
Ru1	0.25	0.25	0.50	4d	0.14
Li2	0	0.0250(1)	0.25	4e	0.51
Ru2	0	0.0250(1)	0.25	4e	0.04
Li3	0	0.4153(1)	0.25	4e	0.55
Ru3	0	0.4153(1)	0.25	4e	0.00
Li4	0	0.6758(4)	0.25	4e	0.51
Ru4	0	0.6758(4)	0.25	4e	0.04
Ru5	0.2446(3)	0.0833(4)	0.0009(6)	8f	0.90
Li5	0.2446(3)	0.0833(4)	0.0009(6)	8f	0.10
O1	0.1323(7)	0.2503(1)	0.1208(1)	8f	1.00
O2	0.1199(1)	0.5758(1)	0.1076(4)	8f	1.00
O3	0.1319(1)	0.9385(1)	0.1272(6)	8f	1.00
Lattice parameters: a=4.97440(34) Å, b=8.6234(4) Å, c=9.93909(22) Å; α=90°, β=99.209(5)°, γ=90°; $V_{unit\ cell}$=420.85(4) $Å^3$					
Phase2: $Li_{0.6}RuO_3$	Space group: R -3			wt=23.7%	
Atom	Fractional coordinates			Wyckoff symbol	Occupancy
	x	y	z		
Li1	0	0	0	3a	0.300(1)
Ru1	0	0	0	3a	0.180(9)
Li2	0	0	0.5	3b	0.408(4)
Ru2	0	0	0.5	3b	0.010(6)
Li3	0	0	0.3355(6)	6c	0.095(8)
Ru3	0	0	0.3355(6)	6c	0.904(2)
O1	0.3132(1)	-0.0358(2)	0.2610(9)	18f	1.00
Lattice parameters: a=4.9877(21) Å, b=4.9877(21) Å, c=14.3576(11) Å; α=90°, β=90°, γ=120°; $V_{unit\ cell}$=309.32(19) $Å^3$					

Table A4. Structural parameters of C-4.2V-$Li_{0.46}RuO_3$

Phase1: $Li_{0.9}RuO_3$	Space group: C2/c			wt=51.0%	
Atom	Fractional coordinates			Wyckoff symbol	Occupancy
	x	y	z		
Li1	0.25	0.25	0.50	4d	0.36
Ru1	0.25	0.25	0.50	4d	0.14
Li2	0	0.025	0.25	4e	0.46
Ru2	0	0.025	0.25	4e	0.04
Li3	0	0.4153(1)	0.25	4e	0.50
Ru3	0	0.4153(1)	0.25	4e	0.00
Li4	0	0.6758(4)	0.25	4e	0.46
Ru4	0	0.6758(4)	0.25	4e	0.04
Ru5	0.2134(7)	0.0815(7)	-0.0014(4)	8f	0.871(2)
Li5	0.2134(7)	0.0815(7)	-0.0014(4)	8f	0.10
O1	0.1278(1)	0.2505(1)	0.1280(1)	8f	1.00
O2	0.1200(1)	0.5760(1)	0.1012(5)	8f	1.00
O3	0.1320(1)	0.9466(1)	0.1301(1)	8f	1.00
Lattice parameters: a=4.9823(9) Å, b=8.5045(9) Å, c=9.8499(11) Å; α=90°, β=99.745(13)°, γ=90°; $V_{unit\ cell}$=411.33(10) $Å^3$					
Phase2: $Li_{0.2}RuO_3$	Space group: R -3			wt=49.0%	
Atom	Fractional coordinates			Wyckoff symbol	Occupancy
	x	y	z		
Li1	0	0	0	3a	0.150(1)
Ru1	0	0	0	3a	0.187(1)
Li2	0	0	0.5	3b	0.150(1)
Ru2	0	0	0.5	3b	0.033(1)
Li3	0	0	0.3382(9)	6c	0.050(1)
Ru3	0	0	0.3382(9)	6c	0.890(1)
O1	0.3132(1)	-0.0357(1)	0.2608(1)	18f	0.982(1)
Lattice parameters: a=5.06479(26) Å, b=5.06479(26) Å, c=14.0915(14) Å; α=90°, β=90°, γ=120°; $V_{unit\ cell}$=313.05(4) $Å^3$					

Table A5. Structural parameters of C-4.5V-$RuO_{2.95}$

Phase: $RuO_{2.95}$	Space group: R -3				
Atom	Fractional coordinates			Wyckoff symbol	Occupancy
	x	y	z		
Li1	0	0	0	3a	0
Ru1	0	0	0	3a	0.537(1)
Li2	0	0	0.5	3b	0
Ru2	0	0	0.5	3b	0.498(1)
Li3	0	0	0.3291(8)	6c	0
Ru3	0	0	0.3291(8)	6c	0.482(5)
O1	0.3166(4)	-0.0438(3)	0.2546(1)	18f	0.981(8)
Lattice parameters: a=5.00873(27) Å, b=5.00873(27) Å, c=13.8733(11) Å; α=90°, β=90°, γ=120°; $V_{unit\ cell}$=301.415(33) $Å^3$					

Table A6. Structural parameters of D-2.5V-$Li_{1.6}RuO_3$

Phase: $Li_{1.6}RuO_3$	Space group: C2/c				
Atom	Fractional coordinates			Wyckoff symbol	Occupancy
	x	y	z		
Li1	0.25	0.25	0.50	4d	0.70
Ru1	0.25	0.25	0.50	4d	0.173(2)
Li2	0	0.0700(1)	0.25	4e	0.80
Ru2	0	0.0700(1)	0.25	4e	0.04
Li3	0	0.4034(8)	0.25	4e	0.80
Ru3	0	0.4034(8)	0.25	4e	0.04
Li4	0	0.7376(1)	0.25	4e	0.80
Ru4	0	0.7376(1)	0.25	4e	0.04
Ru5	0.2341(2)	0.0751(6)	-0.0037(1)	8f	0.766(8)
Li5	0.2341(2)	0.0751(6)	-0.0037(1)	8f	0.05
O1	0.1350(1)	0.2520(1)	0.1190(1)	8f	1.00
O2	0.1223(1)	0.5700(1)	0.1199(9)	8f	1.00
O3	0.1280(1)	0.9015(1)	0.1133(8)	8f	1.00
Lattice parameters: a=5.0476(10)Å, b=8.7262(15) Å, c=9.9318(5) Å; α=90°, β=100.660(14)°, γ=90°; $V_{unit\ cell}$=429.91(12) $Å^3$					

Table A7. Comparison of lattice parameters at various states

Sample	Phase	Space group	a/ Å	b/ Å	c/ Å	Cell volume/ Å^3
C-3.4 V	$Li_{1.94}RuO_3$	C2/c	4.958	8.779	**9.885**	423.61
C-3.65 V	$Li_{1.26}RuO_3$	C2/c	4.981	8.639	**9.909**	420.55
C-3.9 V	$Li_{1.0}RuO_3$	C2/c (76.3%)	4.974	8.623	**9.939**	420.85
	$Li_{0.6}RuO_3$	R-3 (23.7%)	4.988	4.988	14.358	309.32
C-4.2 V	$Li_{0.9}RuO_3$	C2/c (51%)	4.982	8.505	**9.850**	411.33
	$Li_{0.2}RuO_{2.75}$	R-3 (49%)	5.065	5.065	14.092	313.05
C-4.5 V	$RuO_{2.95}$	R-3	5.009	5.009	13.874	301.43
D-2.5 V	$Li_{1.6}RuO_3$	C2/c	5.048	8.726	**9.932**	429.91

Appendix B. Properties of O3-type $Li_{1.2}Ni_{0.2}Mn_{0.6}O_2$

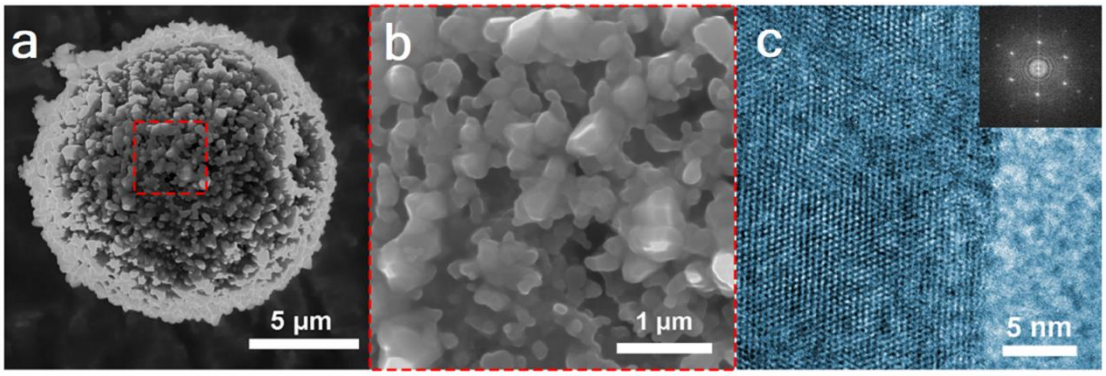


Figure B1. Morphology of the O3-phase. **(a** and **b)** SEM images of the O3-phase. **(c)** TEM image of the O3-phase. The inset shows the FFT SAED patterns.

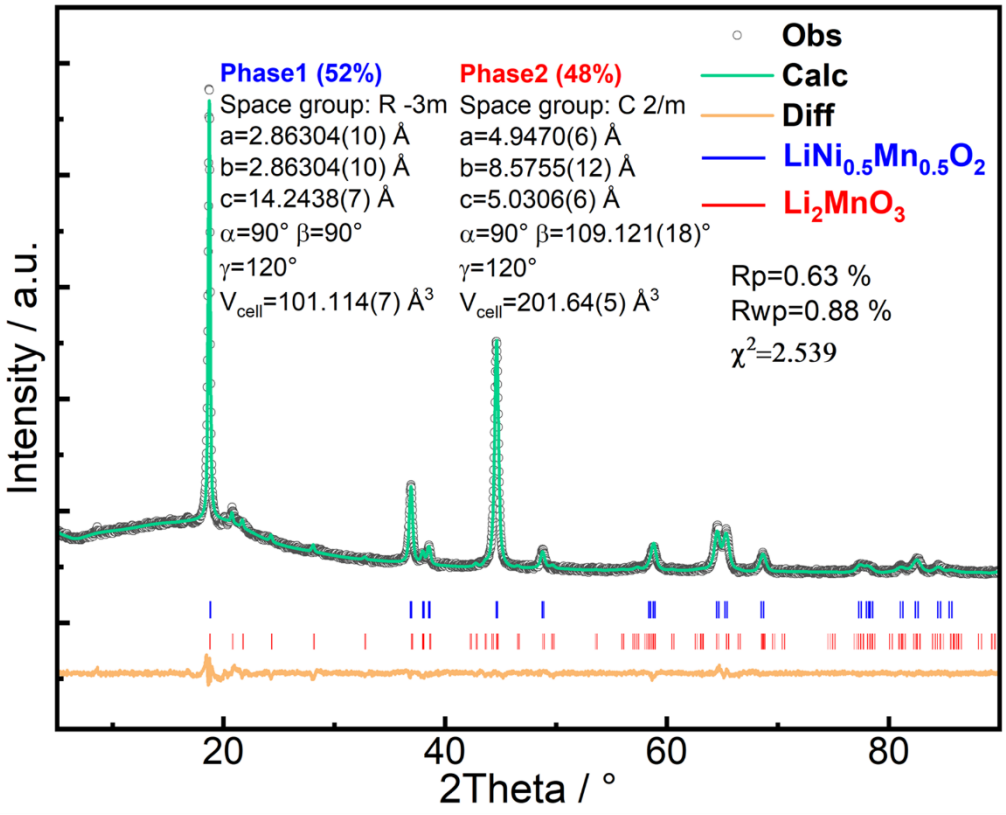


Figure B2. Rietveld refinement of XRD patterns of the O3-type material. The O3-type $Li_{1.2}Ni_{0.2}Mn_{0.6}O_2$ was prepared via a traditional solid-state reaction, consisting of a R-3m phase $LiNi_{0.5}Mn_{0.5}O_2$ (52 wt%) and a C2/m phase Li_2MnO_3 (48 wt%).

Table B1. Structural parameters of O3-type $Li_{1.2}Ni_{0.2}Mn_{0.6}O_2$

Phase1: O3-$LiNi_{0.5}Mn_{0.5}O_2$			Space group: R-3m		wt=52.0%
Atom	Fractional coordinates			Multiplicity	Occupancy
	x	y	z		
Li1	0	0	0	3	0.882(1)
Li2	0	0	1/2	3	0.118(1)
Mn	0	0	1/2	3	0.5
Ni1	0	0	0	3	0.118(1)
Ni2	0	0	1/2	3	0.381(1)
O1	0	0	0.2473(8)	6	1

Lattice parameters:

a=2.86304(10) Å, b=2.86304(10) Å, c=14.2438(7) Å; α=90°, β=90°, γ=120°;

$V_{unit\ cell}$=101.114(7) $Å^3$

Phase2: Li_2MnO_3			Space group: C2/m		wt=48.0%
Atom	Fractional coordinates			Multiplicity	Occupancy
	x	y	z		
Li1	0	1/2	0	2	0.6
Li2	0	0	1/2	2	1
Li3	0	0.7148(9)	1/2	4	1
Li4	0	0.1715(8)	0	4	0.2
Mn1	0	0.1715(8)	0	4	0.8
Mn2	0	1/2	0	2	0.4
O1	0.2171(9)	0	0.1989(5)	4	1.0
O2	0.1812(5)	0.3405(7)	0.1952(7)	8	1.0

Lattice parameters:

a=4.9470(6) Å, b=8.5755(12) Å, c=5.0306(6); α=90°, β=109.121(18)°, γ=120°;

$V_{unit\ cell}$=201.64(5) $Å^3$

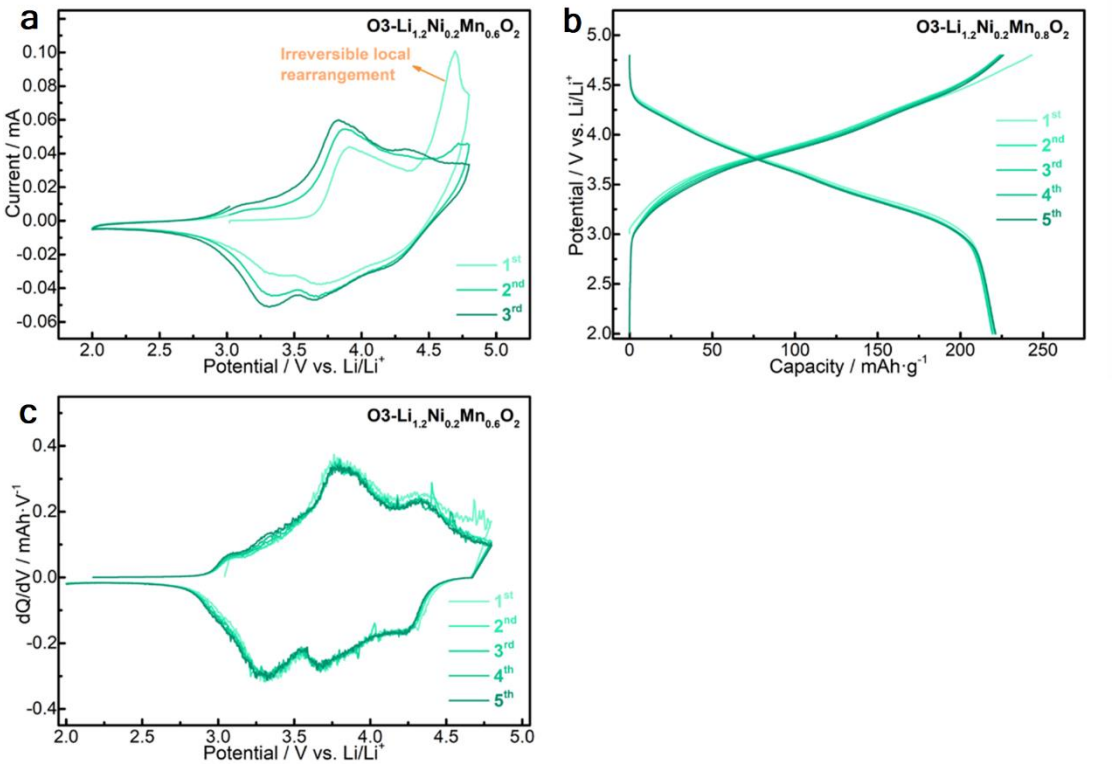


Figure B3. Electrochemistry of O3-type $Li_{1.2}Ni_{0.2}Mn_{0.6}O_2$. **(a)** 1^{st}-3^{rd} cyclic voltammetry (CV) curves at the scan rate of 0.05 mV/s within the potential window of 2.0 - 4.8 V vs. Li/Li^+. In the first anodic scan, the sharp peak at around 4.7 V vs. Li/Li^+ implies the irreversible local rearrangement, widely seen in lithium-rich cathode materials. **(b)** 1^{st}-5^{th} galvanostatic charge-discharge (GCD) curves at the current density of 20 mA/g within the potential window of 2.0 - 4.8 V vs. Li/Li^+. Noteworthy, the long charging plateau was not observed in the 1^{st} cycle because the cell had been used for CV test, meaning that the irreversible local rearrangement had taken place. **(c)** Corresponding 1^{st}-5^{th} dQ/dV curves.

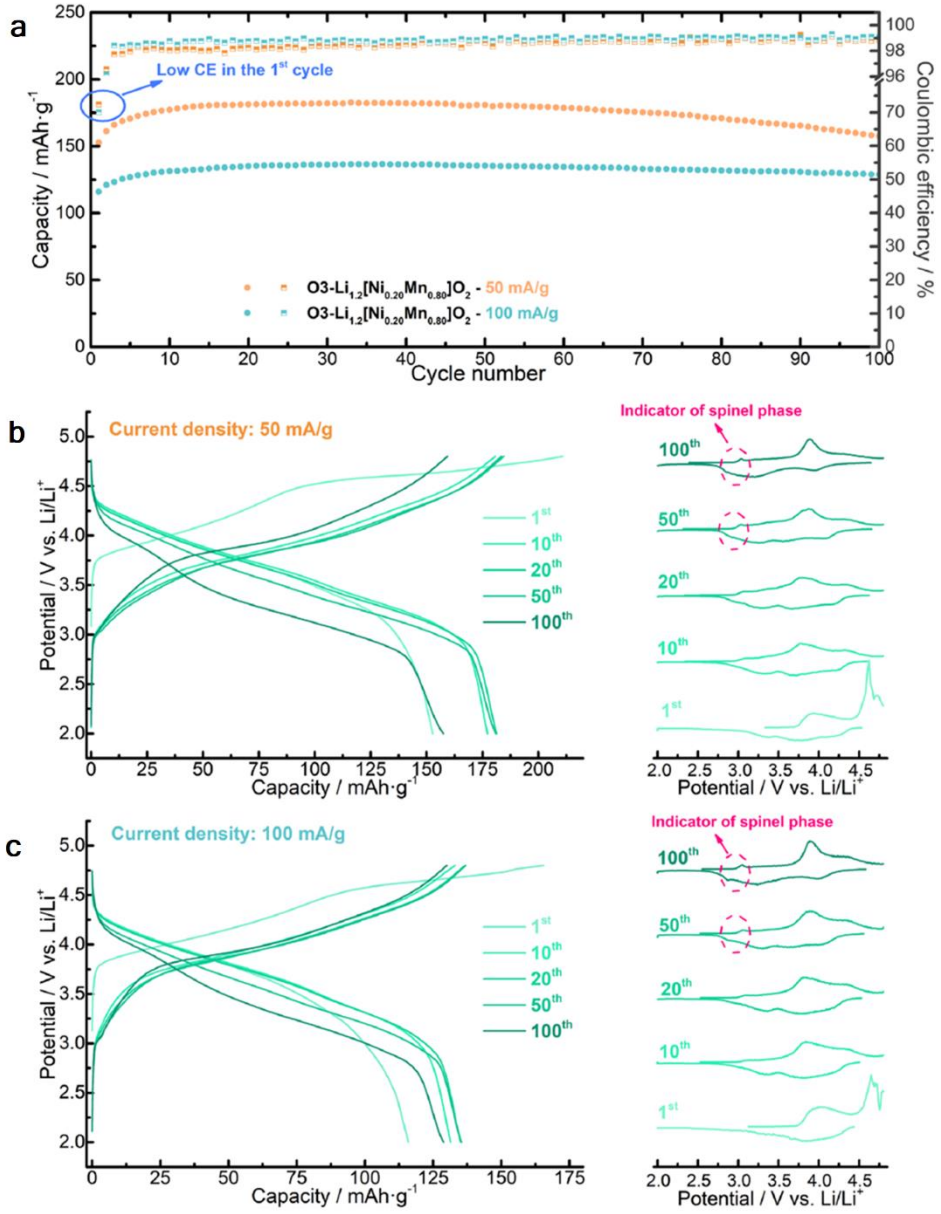


Figure B4. Cycling performance of O3-type $Li_{1.2}Ni_{0.2}Mn_{0.6}O_2$. **(a)** Capacity retention of the O3-type $Li_{1.2}Ni_{0.2}Mn_{0.6}O_2$ electrodes cycled at 50 mA/g and 100 mA/g within the potential window of 2.0-4.8 V vs Li/Li^+. Filled circles and half-filled squares represent capacities and coulombic efficiencies at certain cycles, respectively. The coulombic efficiency in the 1st cycle is low (i.e., around 70 %) because of irreversible local rearrangement and oxygen loss. Upon cycling, for both cells, the capacity increases firstly and declines gradually, probably resulting from the activation and degradation processes, respectively. GCD curves and corresponding dQ/dV curves at the 1st, 10th, 20th, 50th and 100th cycles for the O3-type $Li_{1.2}Ni_{0.2}Mn_{0.6}O_2$ electrodes cycled at **(b)** 50 mA/g, and **(c)** 100 mA/g within the potential window of 2.0-4.8 V vs Li/Li^+. For both cells, the long charging plateau in the 1st cycle is related to irreversible local rearrangement upon the activation of oxygen. In dQ/dV curves, redox pairs belonging to the spinel phase (i.e., peaks circled by pink dashed lines) increase gradually upon cycling, revealing the irreversible and cumulative TM migrations.

Appendix C. A taste of building interferometric scattering (iSCAT) microscopy to monitor single particle dynamics

Chapters 3-5 of this thesis mainly focus on investigating the mechanisms of anion redox reactions (ARRs) in multiple materials and improving their electrochemical properties. In this Appendix, we have tentatively tried to build an interferometric scattering microscopy (iSCAT) setup to monitor the ARRs at the single particle level. For future in-situ iSCAT tests, a suitable cathode material (i.e., O6-phase $Li_{1.2}Mn_{0.8}O_2$.) has been prepared and characterized.

C.1. Introduction

Upon decades of investigation, consensus has been made that, in lithium rich cathode materials (LRCMs), the lattice oxygen (O^{2-}) could be ultimately oxidized to the molecular O_2 via ARRs, as indicated by high-resolution RIXS and neutron PDF.[1,2] However, it is still debatable that in what ways do the oxygen redox activities occur. For example, in lithium rich manganese oxides (LRMOs), although theoretical calculations suggest that the intermediate Mn^{5+}/Mn^{7+} could form first and oxidize the lattice oxygen thereafter,[3,4] no experimental evidence supports such a mechanism.[5]

Therefore, finding ways to capture the intermediate states, no matter they are the overoxidized Mn^{5+}/Mn^{7+} species or the O-O dimers, could in no doubt enrich our understanding of the hidden mechanisms of ARRs. Developing advanced

characterization techniques suitable for in-situ or operando tests is of particular interest because such intermediate states might be metastable and change during sample preparations for ex-situ tests.

At present, the prevailing techniques to prove the occurrence of the oxygen redox activities can be divided into two types in terms of mechanisms. The first type captures the ARR-induced structural evolutions via the elastic diffractions or Rayleigh scatterings to decipher the structural evolutions, e.g., neutron with atomic nuclei, X-ray with electron cloud, and electron beam with electromagnetic field. The other type is usually based on the inelastic interactions between the incident waves and materials, e.g., spectroscopic methods such as XAS and RIXS. Generally, X-ray and neutron beams carry information from plenty of particles, while electron beams could probe small regions down to several square nanometers. However, we still lack tools to track them at the single particle level (i.e., several micrometers). Therefore, developing techniques to monitor single particle dynamics upon the ARRs is demanding.

Recent progresses in Bragg coherent diffraction imaging (BCDI) enrich our arsenal to monitor single-particle dynamics under operando conditions.[6,7] For example, thanks to the nanoscale sensitivity of BCDI, Amine et al. captured the accumulation of nanoscale strain and local displacement upon ARRs in single particles.[8] With the help of multiscale characterizations, such defects are suggested to be the origin of structural degradation and oxygen loss, thereby inducing both capacity fading and

voltage decay. Clearly, BCDI is a powerful and unique technique to decipher the poorly understood strain evolutions in single particles of battery materials. Considering that nano-strains usually originate from inhomogeneous electrochemical reactions, the heterogeneous nature of ARRs makes BCDI an ideal tool for investigating lithium rich materials. Albeit promising, the success of BCDI requires high-covalency and high-flux X-ray beams, which are only achievable in several of the most advanced synchrotron light sources. Therefore, the wide application of BCDI is unfortunately hindered by the availability of the sophisticated and costly synchrotron X-rays.

While looking for other feasible incident waves to monitor electrochemical activities at the single particle level, visible light is arguably the most ubiquitous candidate in terms of availability, low beam-induced sample damage, and real time monitoring. Actually, Rao et al have originally showcased brilliant attempts of using visible light to track single particle dynamics via introducing the optical interferometric scattering microscopy (iSCAT) into the battery field.[9-11] Specifically, by using iSCAT, heterogeneous lithium de-/intercalations have been visualized in single-particles of $LiCoO_2$, Ni-rich NMCs ($LiNi_xMn_yCo_{(1-x-y)}O_2$, $x>0.5$), and $Nb_{14}W_3O_{44}$, revealing its versatility towards various materials. Besides, it has demonstrated the power to quantitatively evaluate lithium diffusion kinetics under fast dis-/charging conditions, which makes it even more attractive with respect to present characterization techniques.

In this Appendix, considering the simple mechanisms of iSCAT, i.e., the elastic light-matter interaction and the interferometric light-light interaction, it has the potential to track the ARRs in LRCMs at the single-particle level. Therefore, we have tentatively tried to build an iSCAT setup according to the established protocols and designed a suitable cathode material for future in-situ tests.

C.2. Fundamentals of visible light imaging

Using visible light for imaging has been and continues to be of great interests thanks to its easy accessibility, relatively noninvasive nature, and capability for three-dimensional (3D) imaging. Basically, imaging with visible light is based on three contrast mechanisms, namely extinction, fluorescence, and interference. [12]

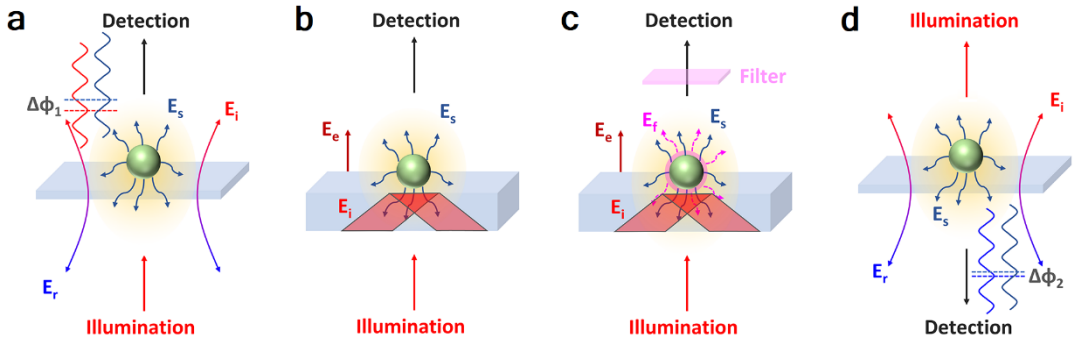


Figure C1. Schematic diagrams of signal generations in **(a)** the bright-field microscopy, **(b)** the dark-field microscopy, **(c)** the total internal reflection fluorescence (TIRF) microscopy, and **(d)** the interferometric scattering (iSCAT) microscopy. E_i, incident wave; E_r, reflected wave (or reference wave); E_s, scattered wave; E_e, evanescent wave; E_f, fluorescence wave; $\Delta\phi_1$, the phase difference between E_i and E_s; $\Delta\phi_2$, the phase difference between E_r and E_s.

C.2.1. Extinction imaging

The extinction of the incident light is arguably the most widely used contrast

mechanism in optical microscopies. Specifically, while interacting with the matter of interest, both absorption and scattering of the substance lead to the light extinction (in the Optical Theorem (OT), extinction = absorption + scattering).[13] For example, in the conventional bright-field microscopy, the incident plane-wave is partially scattered by the object to different directions, while the rest propagates forward to the detector (**Figure C1a**). Therefore, both the incident wave (E_i) and the scattered wave (E_s) contribute to the detected intensity (I_d),

$$I_d = |E_i + E_s|^2 = |E_i|^2 + |E_s|^2 + 2E_r E_s cos\Delta\varphi_1 \qquad (C-1)$$

where $\Delta\phi_1$ is the phase difference between E_i and E_s. The cross-term denotes the interference between E_i and E_s, which is negligible with the incoherent light as the illumination. The scattered wave (E_s) is directly related to the complex particle polarizability (α) via $E_s=\eta\alpha E_i$, where η denotes the collection efficiency of the detection system. Generally, the polarizability (α) is linearly proportional to the particle volume (V), meaning that the scattered intensity ($I_s=|E_s|^2$) scales with the square of its volume, i.e., six orders of magnitude of its diameter (D^6) for a spherical particle. Therefore, because the scattering effect drops rapidly with decreasing particle size, the conventional bright-field microscopy becomes incapable of distinguishing the scattered signals of nanoparticles from the dominant background.

However, despite its low distinguishability, the extinction signal itself might be still detectable even for nanoparticles. Hence, the idea of eliminating the bright background in the detection channel has led to a boom in dark-field microscopy.[14] As

shown in **Figure C1b**, the incident wave (E_i) is separated from the scattered wave (E_s) in the total internal reflection (TIR) geometry, and the latter propagates to the detector for imaging. The TIR dark-field microscopy has become a gold standard to effectively identify image features. Nonetheless, it is still challenging to achieve single-molecule or single-particle measurement solely upon extinction due to the weak scattering effect of nanoparticles.

C.2.2. Fluorescence imaging

Fluorescence microscopy has emerged as an alternative technique for ultrasensitive imaging thanks to its ability to suppress the background and to highlight the signal of interest.[15] For example, in the typical total internal reflection fluorescence (TIRF) microscopy, the fluorescence excitation laser (i.e., the incident wave, E_i) spurs the fluorescence emission (E_f) of the object itself or the dye adhered to the object. Via the TIR geometry and the fluorescence filter, both the illumination (E_i) and the scattered wave (E_s) could be separated from the detection channel, making the emitted fluorescence (E_f) the only signal on the detector (**Figure C1c**). Generally, the detected intensity scales with the number or the volume of the fluorescently labeled molecules rather than scaling with its square as in the pure scattering scenario. Therefore, ever since its inception, the fluorescence microscopy has prevailed in single-molecule or single-particle imaging, and it has been widely used in areas covering chemistry, life science, materials science and so on.[16,17] Despite such advantages, fluorescence microscopy suffers from photophysical limitations such as bleaching, saturation, and

blinking, thereby impairing its reliability to capture fast dynamics or to monitor long-term activities.[18] Moreover, the success of fluorescence-based imaging largely relies on using compatible dyes as fluorescence-labels, which could possibly perturb the intrinsic properties of the matter of interest.[19]

C.2.3. Interference imaging

Thanks to the advances in lasers and other optical components, scattering-based microscopy has been rejuvenated for label-free ultrasensitive imaging, which alternatively takes the interference rather than the pure scattering as the contrast mechanism.[20] With coherent illuminations (e.g., lasers), even in the transmissive configuration as in the typical bright-field microscopy, the cross-term in the equation 6-1 is ineligible due to the interference between the incident wave (E_i) and the scattered wave (E_s). Considering that the interference intensity decays linearly with decreasing particle volume, the detected signal drops much slower than that in the pure-scattering scheme. Therefore, interference-based microscopy has the potential to track single-molecule or single-particle dynamics.[21]

C.3. Theory and applications of iSCAT

The prototype of interferometric scattering (iSCAT) microscopy was originally demonstrated by Sandoghdar et al. in a reflective configuration.[22] As illustrated in **Figure C1d**, the illumination passes through the transparent substrate and interacts with the sample, producing the scattered wave (E_s) in all directions. Meanwhile, a small

portion of the incident wave (E_i) is reflected at the substrate-sample interface due to the abrupt change in refractive index, serving as the reference wave (E_r). Therefore, in the reflection mode, the detected intensity (I_d) consists of the reference wave (E_r), the scattered wave (E_s) and their interference,

$$I_d = |E_r + E_s|^2 = |E_r|^2 + |E_s|^2 + 2E_r E_s cos\Delta\varphi_2 \qquad (C-2)$$

where the cross-term denotes the interference between E_r and E_s, and $\Delta\phi_2$ is the phase difference between E_r and E_s. For a small scatter, the second term becomes insignificant, and the detected signal from the sample manifests itself as a small interference-induced variation on the top of a big reflection-induced background ($I_r=|E_r|^2$).

$$I_d \approx |E_r|^2 + 2E_r E_s cos\Delta\varphi_2 \qquad (C-3)$$

For Mie scattering of a spherical particle, the scattering follows the equation,

$$E_s = \eta\alpha E_i = \eta\varepsilon_m \pi \frac{D^3}{2} \frac{\varepsilon_p - \varepsilon_m}{\varepsilon_p + 2\varepsilon_m} E_i \qquad (C-4)$$

where η denotes the collection efficiency of the detection system; D is the diameter of the particle; ε_m and ε_p are the dielectric functions of the medium and the particle, respectively. Therefore, the interference-based contrast mechanism functions as long as the particle and the surrounding medium present different dielectric properties. Besides, without considering the perturbation of the system, the shot noise is theoretically the single origin of noise in iSCAT, meaning that its signal-to-noise ratio (SNR) could be improved solely by increasing the number of detected photons.

Moreover, the scattering-based method does not face challenges such as bleaching, saturation, and blinking as in the fluorescence-based scheme, thereby enabling it to perform in long-term operations with high temporal resolutions.

Therefore, it is not surprising that the iSCAT has been intensively investigated to track the high-speed single particle movements,[23] to monitor the dynamics of biological processes,[24] and to quantitatively measure the masses of small molecules or proteins (i.e., mass photometry).[25] Admittedly, the scattering-based mechanism generally lacks the specificity to differentiate characteristic behaviors other than the intensity, thereby making it challenging to deal with complex samples. Nonetheless, given that iSCAT is still in its infancy, advancing system designs and optimizing algorithms for data processing could in no doubt promote its further development, while applying it to investigate nanoscale activities in a wide range of fields is also of great potential.

C.4. The possibility of tracking ARRs via iSCAT

Although iSCAT had been widely used in many areas for more than a decade since its invention, it was not until recently that the technique was introduced into the battery field. The very first application of iSCAT to investigate real-time electrochemical activities was the successful observation of single-particle ion dynamics in a typical cathode material $LiCoO_2$.[9] Generally, upon de-lithiation, $LiCoO_2$ undergoes multiple processes, i.e., a biphasic transition from the semiconducting $Li_{0.95}CoO_2$ to the metallic $Li_{0.77}CoO_2$, a solid solution process to $Li_{0.5}CoO_2$, and a following biphasic process with

the lithium/vacancy ordering and the rhombohedral-to-monoclinic transition in symmetry. Because removing lithium ions promotes electronic delocalisation and thus induces a higher degree of polarizability, the overall intensity of the iSCAT image of a single particle increases in the de-lithiated states and decreases reversibly upon lithiation. In addition, the high sensitivity of iSCAT enables it to reveal the spatially resolved features within a single particle. Specifically, the iSCAT image of the pristine $LiCoO_2$ presents uniform intensity distributions. During solid solution processes, such a spatial homogeneity maintains, implying that the dielectric property of a specific phase changes evenly with increasing or decreasing amounts of lithium ions. On the contrary, upon phase-transformation processes, the newly formed phase displays abrupt changes in the scattering property with respect to that of the initial phase, resulting in bright and dark regions (i.e., different phases) within a single particle.

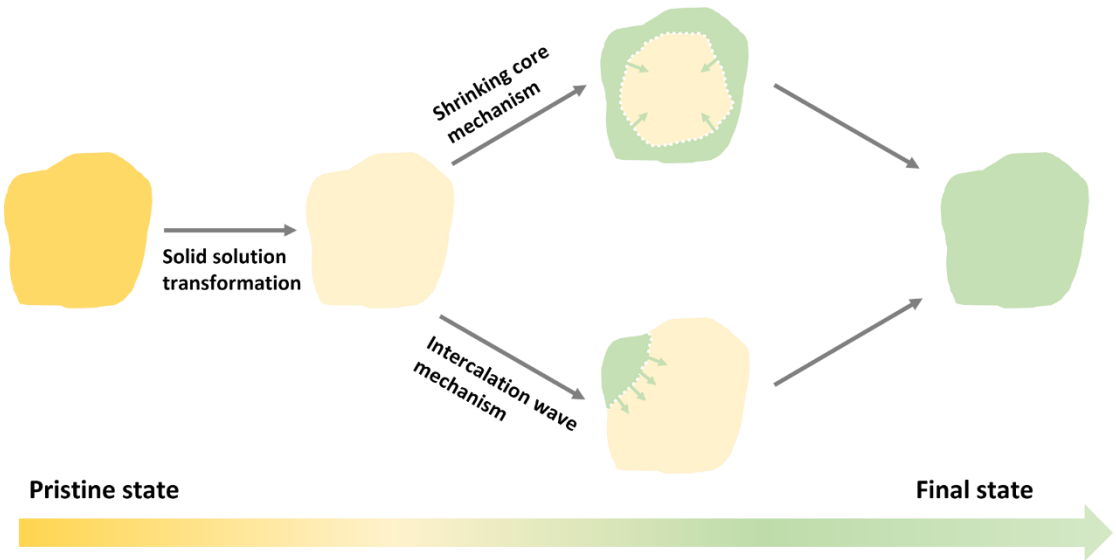


Figure C2. Schematic evolutions of single particle iSCAT images during solid solution and biphasic processes. The arrows indicate the propagation directions of the phase boundaries.

As illustrated in **Figure C2**, depending on the rate-limiting step (i.e., charge-transfer-limited, or diffusion-limited), the phase boundaries propagate either from one side to the other side or from the surface to the core, corresponding to the intercalation wave mechanism or the shrinking core mechanism, respectively. Moreover, iSCAT has demonstrated the capability of quantitatively monitoring the phase propagation in long-term operations, thereby making it a promising candidate to investigate operando single particle dynamics. Simply put, iSCAT is capable to distinguish any phase boundaries and to monitor biphasic dynamics as long as they are different in scattering properties. For instance, such phase-transition-induced heterogeneities have also been visualized in single particles of the fast-charging anode $Nb_{14}W_3O_{44}$ and Ni-rich NMCs.[10,11]

Commonly, for lithium rich cathode materials, in addition to cation redox reactions as the Co^{3+}-to-Co^{4+} oxidation in $LiCoO_2$, anion redox reactions (ARRs) get involved in the charge compensation and accounts for the extra capacities at high potentials (e.g., > 4.5 V vs. Li/Li^+). Under such conditions, extracting electrons from oxygen could inevitably alter the local electronic structure and thus the scattering property. Therefore, triggering oxygen redox activities is expected to drastically change the intensity of the iSCAT image. Meanwhile, any features induced by the change of lithium concentration or phase-transformation processes could be deciphered as what has been done in lithium-stoichiometric materials. Clearly, there is no doubt that iSCAT could be utilized to monitor single particle dynamics during the ARRs.

More excitingly, because iSCAT is a lab-available technique, it is convenient to investigate battery degradation mechanisms in long-term operation. For LRCMs, the longstanding puzzle is that, despite the extra capacities contributed by ARRs, both the oxygen loss and transition metal migration lead to the detrimental layered-to-spinel phase transformation.[26] Although the formation of the spinel phase has been proven according to TEM, XRD, Raman and electrochemical results,[27,28] monitoring its evolution at the single particle level is still challenging. Considering that the layered phase and the spinel phase might possess different dielectric properties, iSCAT could potentially distinguish the fatigued regions in the cycled single particles. This will enrich our understanding about the degradation mechanisms of LRCMs, provide clues to rationally design their structures, and thus pave the way for their practical applications.

C.5. Lab-made iSCAT setup

As illustrated in **Figure C3**, the iSCAT setup is adapted from previous work by Alice et al,[9,10] which generally consists of three parts, namely the illumination, the 4f system and the imaging section.

C.5.1. Illumination

A diode laser (633 ± 3 nm) is used because its coherence length is appropriate to enhance interferometric signals from the sample and to avoid strong interferences from the reflection of optics. The laser is firstly coupled into a polarization-maintaining

single-mode fiber (SMF) for spatial filtering. As shown in **Figure C4**, the output laser is collimated and the beam diameter is adapted by using a telescopic lens system (T), which includes a short-focus lens (f = 15.27 mm), an aspheric lens (f = 30 mm), a collimating lens (f = 75 mm) and a pinhole (d = 150 µm) for spatial filtering. The output beam is expected to present a better Gaussian profile with a beam diameter of ~ 7.5 mm.

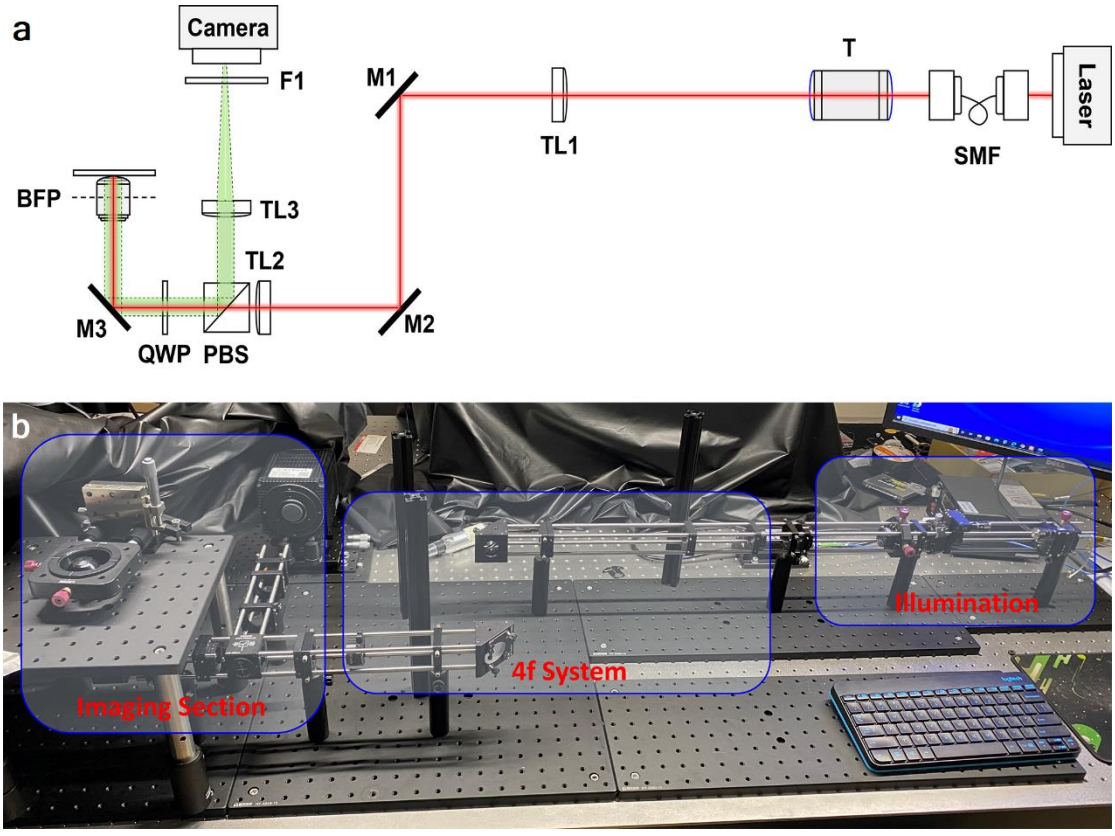


Figure C3. (a) Schematic of the iSCAT setup. Red lines represent incident beams; green lines represent scattering and reflecting signals. Note: SMF, single-mode fiber; T, telescope for beam diameter adjustment; MX, adjustable mirrors; TL: telecentric lens; PBS, polarizing beam splitter; QWP, quarter wave plate; BFP, back focal plane; F1, long-pass filter. **(b)** Image of the assembled iSCAT setup.

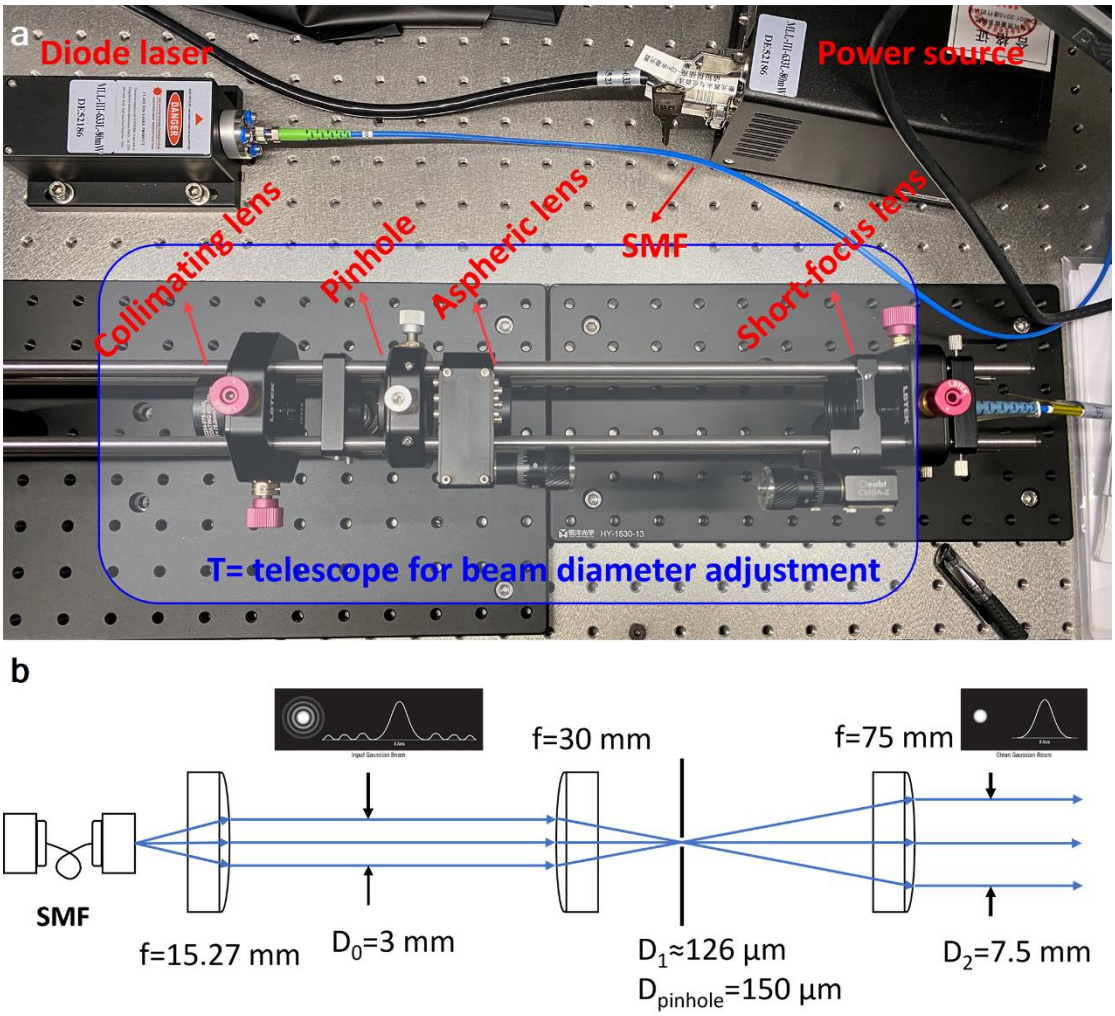


Figure C4. (a) Image of the illumination of the iSCAT setup. **(b)** Diagram of the beam adjustment by the telescopic lens system. The insets illustrate the beam profiles before (left) and after (right) the pinole spatial filtering process.

C.5.2. 4f system

The adjusted beam is directed into a 4f system, consisting of two plano-convex lenses (TL1 and TL2, f = 400 mm) and two mirrors (M1 and M2) to change the direction of the illumination. The beam is then imaged into the back focal plane (BFP) of an objective (Olympus PlanApo, 100×, 1.4 NA).

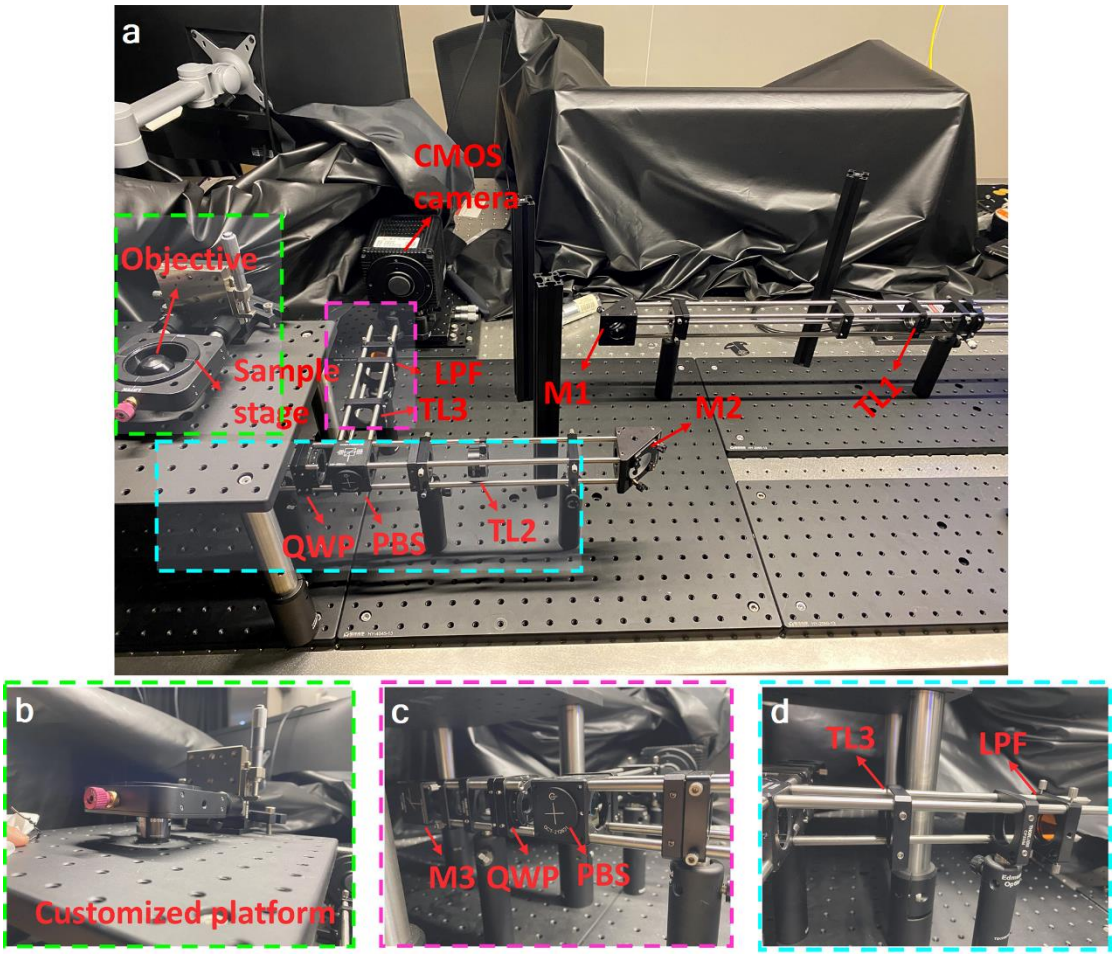


Figure C5. (a) Image of the 4f system and the imaging section of the iSCAT setup. Enlarged images of **(b)** the objective part, **(c)** the polarization regulation part, and **(d)** the final signal filtering part.

C.5.3. Imaging section

The key component of the imaging section is the high-numerical-aperture microscope objective, which focuses the beam on to the sample. The objective is mounted steadily on the customized platform to avoid unfavorable vibrations. As shown in **Figure C5**, there are several components between TL2 and the objective, i.e., a polarizing beam splitter (PBS), a quarter wave plate (QWP) and a mirror at 45° (M3) to direct the beam upwards (perpendicular to the stage). Specifically, the P-polarized beam out of the 4f system passes through the PBS and is then circularly polarized by the QWP before

being directed into the BFP of the objective by M3. The sample stage is mounted on a self-designed xyz transition stage, which is perpendicular to the incident beam out of the objective. The sample is placed on the glass plate, which is tightly mounted on the sample stage during the imaging. The incident beam is either reflected by the glass/sample interface or scattered by the sample itself, both of which are collected by the objective and direct reversely through the M3 and the QWP. The light becomes S-polarized after passing through the QWP twice, which is then reflected by the PBS into the detection channel. The detection channel is composed of the focusing lens (TL3), a long-pass filter (F1) and a complementary metal-oxide semiconductor (CMOS) camera.

C.6. The sample designed for iSCAT test

As introduced in previous sections, the phase difference between the reflected wave and the scattered wave largely determines the intensity of the interference. Therefore, to avoid the phase differences caused by inconsistent optical path differences, the sample for iSCAT test should have a flat surface perpendicular to the incident wave.

C.6.1. Morphology and structure of O6-$Li_{1.2}Mn_{0.8}O_2$

Herein, we synthesized a lithium-rich manganese oxide $Li_{1.2}Mn_{0.8}O_2$ according to the method provided in Chapter 5. As shown in **Figure C6a** and **C6b**, the as-prepared sample show plate-like shapes with several micrometers in size. Because of the strong preferential orientation inherited from the P2-precursor, it presents flat surfaces,

which are ideal for iSCAT tests. Rietveld refinement reveals that it mainly has an O6-type structure with a small amount of Li_2MnO_3 impurity (**Figure C6c** and **Table C1**). Although it has superstructure-related peaks in the region of 2θ = 20-30°, the $LiMn_6$ patterns disperse randomly rather that form the honeycomb-like superstructures, as illustrated in the HAADF-STEM image (**Figure C6d**).

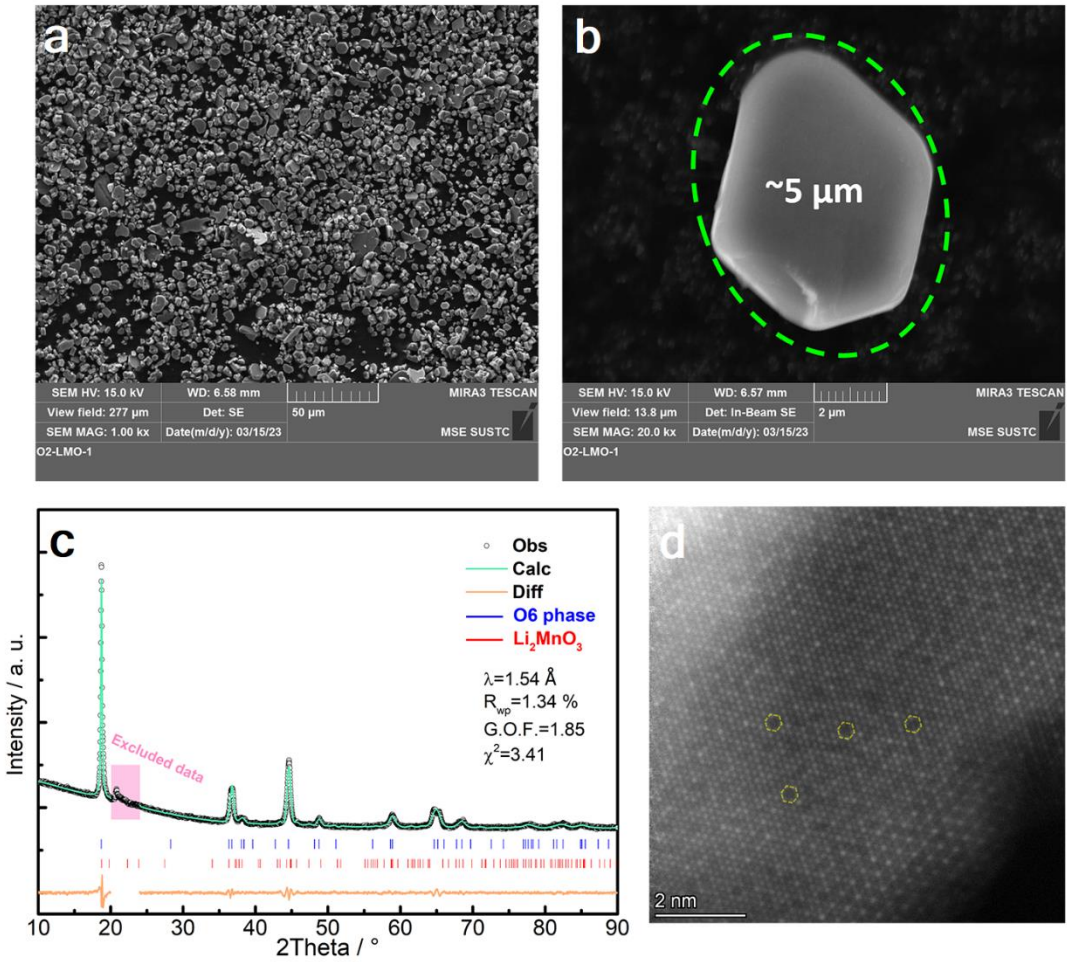


Figure C6. (a and **b)** SEM images, **(c)** XRD patterns, and **(d)** HAADF-STEM image ([001] projection) of the as-prepared $Li_{1.2}Mn_{0.8}O_2$.

Table C1. Rietveld refined structural parameters of the O6-phase $Li_{1.2}Mn_{0.8}O_2$

Phase1: O6-$Li_{1.2}Mn_{0.8}O_2$			Space group: R-3m		wt=95.2%
Atom	Fractional coordinates			Wyckoff symbol	Occupancy
	x	y	z		
Li1	0	0	1/12	6	1
Li2	0	0	0	3	0.2
Li3	0	0	1/2	3	0.2
Mn1	0	0	0	3	0.8
Mn2	0	0	1/2	3	0.8
O1	0	0	0.2065(7)	6	1
O2	0	0	0.3700(8)	6	1
Lattice parameters:					
a=2.85590(18) Å, b=2.85590(18) Å, c=28.2541(6) Å; α=90°, β=90°, γ=120°;					
$V_{unit\ cell}$=199.572(15) $Å^3$					

Phase2: Li_2MnO_3			Space group: C2/m		wt=4.8%
Atom	Fractional coordinates			Wyckoff symbol	Occupancy
	x	y	z		
Li1	0	1/2	0	2	1
Li2	0	0	1/2	2	1
Li3	0	0.6606(1)	1/2	4	1
Mn1	0	0.1670(8)	0	4	1
O1	0.2069(5)	0	0.2215(1)	4	1
O2	0.2680(3)	0.3252(5)	0.2277(1)	8	1
Lattice parameters:					
a=4.773(1) Å, b=8.897(9) Å, c=5.071(7) Å; α=90°, β=112.12(6)°, γ=90°;					
$V_{unit\ cell}$=199.536(34) $Å^3$					

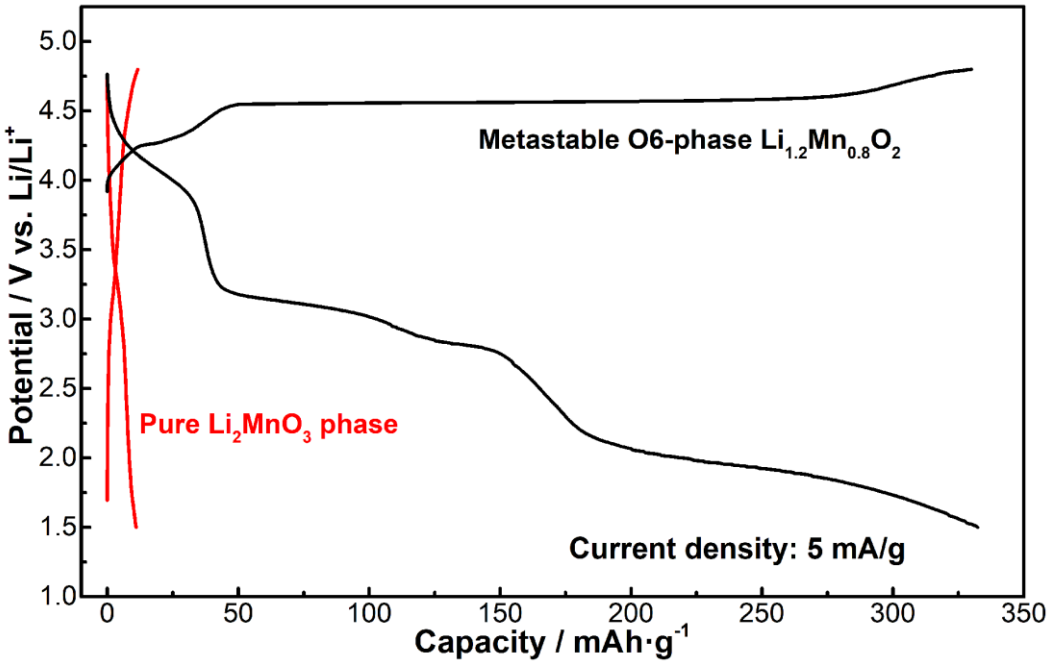


Figure C7. GCD curves of the pure Li_2MnO_3 phase and the O6-phase $Li_{1.2}Mn_{0.8}O_2$. The potential window is 1.5 - 4.8 V vs. Li/Li^+ and the current density is 5 mA/g.

C.6.2. Electrochemical properties of O6-$Li_{1.2}Mn_{0.8}O_2$

Both the as-prepared O6-phase $Li_{1.2}Mn_{0.8}O_2$ and the pure Li_2MnO_3 phase were tested as the active materials in coin cells, as detailed in Chapter 2. As shown in **Figure C7**, although Li_2MnO_3 is regarded as the active component with ARRs in traditional LRMOs,[29] the pure Li_2MnO_3 phase shows very low capacities. On the contrary, the as-prepared O6-phase $Li_{1.2}Mn_{0.8}O_2$ could deliver a reversible capacity of higher than 300 mAh/g in the potential window of 1.5 - 4.8 V vs. Li/Li^+ at 5 mA/g. Besides, in the 1st charging profile, it presents a long plateau at around 4.5 V vs. Li/Li^+, which even provides a capacity of around 250 mAh/g. Considering that the flat plateau is in close relationship with the ARRs, as indicated in previous chapters, the O6-phase $Li_{1.2}Mn_{0.8}O_2$ is a suitable candidate to study the oxygen redox activities.

C.7. Summary and future work

Developing in-situ techniques to monitor the oxygen redox activities at the single-particle level is promising. Herein, we have built an iSCAT setup according to established protocols. Also, the unique O6-phase $Li_{1.2}Mn_{0.8}O_2$ is prepared, whose electrochemistry is different from the well-known Li_2MnO_3 and deserves further study. By far, the in-situ iSCAT test has not been performed because of the lack of suitable in-situ cells. Looking forward, an in-situ cell should be designed to satisfy the requirements for the real-time iSCAT experiment, namely a transparent glass window for the laser, a steady sample/glass interface for stable reflection and the reliable tightness and conductivity for electrochemical tests.

C.8. References

1. R. A. House, U. Maitra, M. A. Perez-Osorio, J. G. Lozano, L. Jin, J. W. Somerville, L. C. Duda, A. Nag, A. Walters, K. J. Zhou, M. R. Roberts, and P. G. Bruce, *Nature*, 2020, **577**, 502-508.
2. R. A. House, H. Y. Playford, R. I. Smith, J. Holter, I. Griffiths, K.-J. Zhou, and P. G. Bruce, *Energy Environ. Sci.*, 2022, **15**, 376-383.
3. M. D. Radin, J. Vinckeviciute, R. Seshadri, and A. Van der Ven, *Nat. Energy*, 2019, **4**, 639-646.
4. Z. Zhang, S. Zhao, B. Wang, and H. Yu, *Cell Rep. Phys. Sci.*, 2020, **1**, 100061.
5. M. J. Zuba, A. Grenier, Z. Lebens-Higgins, G. J. Paez Fajardo, Y. Li, Y. Ha, H. Zhou, M. S. Wittingham, W. Yang, Y. S. Meng, K. W. Chapman, and L. F. J. Piper, *ACS Energy Lett.*, 2021, **6**, 1055-1064.
6. A. Ulvestad, A. Singer, J. N. Clark, H. M. Cho, J. W. Kim, R. Harder, J. Maser, Y. S. Meng, and O. G. Shpyrko, *Science*, 2015, **348**, 1344-1347.
7. A. Singer, M. Zhang, S. Hy, D. Cela, C. Fang, T. A. Wynn, B. Qiu, Y. Xia, Z. Liu, A. Ulvestad, N. Hua, J. Wingert, H. Liu, M. Sprung, A. V. Zozulya, E. Maxey, R. Harder, Y. S. Meng, and O. G. Shpyrko, *Nat. Energy*, 2018, **3**, 641-647.
8. T. Liu, J. Liu, L. Li, L. Yu, J. Diao, T. Zhou, S. Li, A. Dai, W. Zhao, S. Xu, Y. Ren, L. Wang, T. Wu, R. Qi, Y. Xiao, J. Zheng, W. Cha, R. Harder, I. Robinson, J. Wen, J. Lu, F. Pan, and K. Amine, *Nature*, 2022, **606**, 305-312.
9. A. J. Merryweather, C. Schnedermann, Q. Jacquet, C. P. Grey, and A. Rao, *Nature*,

2021, **594**, 522-528.
10. A. J. Merryweather, Q. Jacquet, S. P. Emge, C. Schnedermann, A. Rao, and C. P. Grey, *Nat. Mater.*, 2022, **21**, 1306-1313.
11. C. Xu, A. J. Merryweather, S. S. Pandurangi, Z. Lun, D. S. Hall, V. S. Deshpande, N. A. Fleck, C. Schnedermann, A. Rao, and C. P. Grey, *Joule*, 2022, **6**, 2535-2546.
12. G. Young, and P. Kukura, *Annu. Rev. Phys. Chem.*, 2019, **70**, 301-322.
13. R. W. Taylor, and V. Sandoghdar, *Nano Lett.*, 2019, **19**, 4827-4835.
14. X. Meng, A. Sonn-Segev, A. Schumacher, D. Cole, G. Young, S. Thorpe, R. W. Style, E. R. Dufresne, and P. Kukura, *ACS Photonics*, 2021, **8**, 3111-3118.
15. M. Orrit, and J. Bernard, *Phys. Rev. Lett.*, 1990, **65**, 2716-2719.
16. S. Weiss, *Science*, 1999, **283**, 1676-1683.
17. W. E. Moerner, and D. P. Fromm, *Rev. Sci. Instrum.*, 2003, **74**, 3597-3619.
18. J. O. Arroyo, D. Cole, and P. Kukura, *Nat. Protoc.*, 2016, **11**, 617-633.
19. J. O. Arroyo, and P. Kukura, *Nat. Photon.*, 2015, **10**, 11-17.
20. L. Priest, J. S. Peters, and P. Kukura, *Chem. Rev.*, 2021, **121**, 11937-11970.
21. D. Cole, G. Young, A. Weigel, A. Sebesta, and P. Kukura, *ACS Photonics*, 2017, **4**, 211-216.
22. K. Lindfors, T. Kalkbrenner, P. Stoller, and V. Sandoghdar, *Phys. Rev. Lett.*, 2004, **93**, No. 037401.
23. R. W. Taylor, R. G. Mahmoodabadi, V. Rauschenberger, A. Giessl, A. Schambony, and V. Sandoghdar, *Nat. Photonics*, 2019, **13**, 480-487.
24. A. Gemeinhardt, M. P. McDonald, K. Konig, M. Aigner, A. Mackensen, and V. Sandoghdar, *J. Vis. Exp.*, 2018, **141**, e58486.
25. G. Young, N. Hundt, D. Cole, A. Fineberg, J. Andrecka, A. Tyler, A. Olerinyova, A. Ansari, E. G. Marklund, M. P. Collier, S. A. Chandler, O. Tkachenko, J. Allen, M. Crispin, N. Billington, Y. Takagi, J. R. Sellers, C. Eichmann, P. Selenko, L. Frey, R. Riek, M. R. Galpin, W. B. Struwe, J. L. P. Benesch, and P. Kukura, *Science*, 2018, **360**, 423-427.
26. W. Hua, S. Wang, M. Knapp, S. J. Leake, A. Senyshyn, C. Richter, M. Yavuz, J. R. Binder, C. P. Grey, H. Ehrenberg, S. Indris, and B. Schwarz, *Nat. Commun.*, 2019, **10**, 5365.
27. D. Eum, B. Kim, S. J. Kim, H. Park, J. Wu, S. P. Cho, G. Yoon, M. H. Lee, S. K. Jung, W. Yang, W. M. Seong, K. Ku, O. Tamwattana, S. K. Park, I. Hwang, and K. Kang, *Nat. Mater.*, 2020, **19**, 419-427.
28. Z. Yang, J. Zhong, J. Feng, J. Li, and F. Kang, *Adv. Funct. Mater.*, 2021, **31**, 2103594.
29. J. Vinckeviciute, D. A. Kitchaev, and A. Van der Ven, *Chem. Mater.*, 2021, **33**, 1625-1636.